Jörg Petermann

A contribution to evaluate and predict the strength and life time of angle-ply CFRP laminates under static and cyclic loads

---

A contribution to evaluate and predict the strength and life time of angle-ply CFRP laminates under static and cyclic loads

Vom Promotionsausschuß der

Technischen Universität Hamburg-Harburg

zur Erlangung des akademischen Grades

Doktor-Ingenieur

genehmigte Dissertation

von

Dipl.-Ing. Jörg Petermann

aus Frankfurt/Oder

2004

1st member of committee : Prof. Dr.-Ing. Karl Schulte

                                      Technische Universität Hamburg-Harburg

                                      Hamburg, Germany

2nd member of committee : Prof. Alan Plumtree, PhD

                                      University of Waterloo

                                      Waterloo, Ontario, Canada

Date of oral examination: 30. January 2004

Ein Problem ist halb gelöst, wenn es klar formuliert ist.

John Dewey, Amerikanischer Philosoph (1859-1952)

Für die ungelöste Hälfte gilt jedoch:

Je planmäßiger ein Mensch vorgeht,
desto wirksamer vermag ihn der Zufall zu treffen.

Friedrich Dürrenmatt, Schweizer Schriftsteller (1921-1990)

Danksagung

Die vorliegende Arbeit ist im Rahmen meiner Tätigkeit als wissenschaftlicher Mitarbeiter im Arbeitsbereich Kunststoffe und Verbundwerkstoffe der Technischen Universität Hamburg-Harburg von April 1999 bis Juli 2003 entstanden.

Mein besonderer Dank gilt meinem Doktorvater Herrn Prof. Dr.-Ing. Karl Schulte, der mich stets in meiner persönlichen und fachlichen Entwicklung unterstützte und mir viele Freiräume und Entfaltungsmöglichkeiten für die Forschungsarbeiten gewährte.

Herrn Prof. Dr. Alan Plumtree (University of Waterloo, Kanada) danke ich für die Übernahme des Koreferats und insbesondere dafür, bereits während meines Studiums mein Interesse an Faserverbundwerkstoffen geweckt und gefördert zu haben.

Meinen Kollegen danke ich für das immer freundliche Arbeitsumfeld und die stete Hilfsbereitschaft. Insbesondere Andreas Gagel und Stephan Hinz haben durch vielfältige Anregungen und tatkräftige Unterstützung wesentlich zum Gelingen dieser Arbeit beigetragen. Den beteiligten studentischen Hilfskräften, Studienarbeitern und Diplomanden danke ich für Ihren persönlichen Einsatz bei der Durchführung der Arbeiten.

Dem Bundesministerium für Wirtschaft und der Firma Airbus Deutschland GmbH danke ich für die finanzielle Unterstützung im Rahmen des Luftfahrtforschungsprogramms II und die unentgeltliche Bereitstellung von Materialien.

Zu guter Letzt danke ich allen Freunden und meiner Familie für das entgegengebrachte Verständnis und den Beistand während des Entstehens dieser Arbeit. Besonders herzlich und nachdrücklich danke ich meinen Eltern, die mich seit meiner Kindheit gefördert und unermüdlich unterstützt haben.

Abstract

The mechanical degradation behaviour of matrix dominated, continuous ±45° carbon fibre reinforced epoxide laminates from HTA/6376 prepregs has been examined with particular regard to integrated load-property interactions.

The mechanisms of deformation and damage evolution were assessed by different experimental techniques such as stress-strain hysteresis measurements, microscopy and thermography. The fibre rotation effect was found to be negligible for all loadings.

With respect to the statistically distributed damage evolution, homogenised strain based approaches were developed and successfully applied to the predict strength and life time under static and cyclic loads. The material focus was directed towards, *first* the dependence of the (quasi-static and cyclic) material response on the load rate, *second*, the interaction of creep and fatigue, and *third*, the influence of load sequences and pre-loads in fatigue. The main findings are:

1. The quasi-static stress-strain behaviour exhibits a characteristic yielding with a load rate dependence. With increasing strain rate, the laminate becomes stiffer, stronger, and more brittle. The distribution of material defects does not affect stiffness and yield properties but determines whether the rupture process is dominated by local or global energy dissipation.

2. A threshold stress value for static creep could be determined and a parametric function to predict the stress and time dependent strain evolution given. Cyclic creep occurs once the mean stress in fatigue exceeds the threshold stress for static creep. The portions of creep and fatigue strain to the total strain under cyclic loading could be separated and well estimated.

3. The fatigue life and the damage accumulation behaviour under block load conditions are dependent on the load sequence and the load level. Strain based damage accumulation approaches could be developed and verified for different load sequences.

   Pre-loads (initial pulse or cyclic stresses, or creep and recovery) tend to prolong the subsequent fatigue life. This effect is believed to result from the reduction of stress intensities in the matrix by plastic deformation. The plastic deformations due to initial loads and due to cyclic creep are thereby competitive.

Contents

List of Notations

Abbreviations

2D	:	two-dimensional
3D	:	three-dimensional
AP	:	angle-ply
ASME	:	American Society of Mechanical Engineers
ASTM	:	American Society for Testing and Materials
BMI	:	bismaleimide
CAF	:	constant amplitude fatigue
CDT	:	cumulative damage theory
CFRP	:	carbon fibre reinforced polymer
CLT	:	classical lamination theory
CR	:	creep-recovery
CRF	:	creep-recovery-fatigue
CTE	:	coefficient of thermal expansion
DDS	:	diamino diphenyl sulfone
DGEBA	:	diglycidyl ether of bisphenol A
DMTA	:	dynamic mechanical thermal analyis
DSC	:	differential scanning calorimetry
EP	:	epoxide
FE(A)	:	finite element (analysis)
FRP	:	fibre reinforced polymer
GFRP	:	glass fibre reinforced polymer
H-L	:	high-low
ISO	:	International Standardisation Organisation
L-H	:	low-high
LM	:	light microscopy
MV	:	mean value
NCF	:	non-crimped fabrics
NDT	:	non-destructive testing
PAN	:	polyacrylonitrile
PEEK	:	polyetheretherketone
PM	:	Palmgren-Miner
PMMA	:	polymethylmethacrylate
PP	:	polypropylene
RH	:	relative humidity

RI	:	resin infusion
ROM	:	Rule of Mixtures
RSA	:	rate of stress application
RT	:	room temperature
RTM	:	resin transfer moulding
SD	:	standard deviation
SEM	:	scanning electron microscopy
SLERA	:	strength life equal rank assumption
TGMDA	:	tetraglycidylether of methylenedianiline
TTSP	:	time temperature superposition principle
UD	:	unidirectional
UTS	:	ultimate tensile strength
WLF	:	Williams, Landel, Ferry

Latin Symbols

a, b	:	geometric metrics, parameters
$2a$	:	crack spacing
a_T	:	time shift factor
A	:	cross-section
B	:	constant
$[A_{ij}]$	:	extensional stiffness matrix
c_p	:	specific heat capacity
C_1, C_2	:	WLF constants
$[C_{ijkl}]$	:	stiffness tensor
d	:	diameter
E	:	Young's modulus, stiffness
f	:	frequency
F	:	force
G	:	shear modulus, shear stiffness
G	:	energy release rate
h_k	:	z-coordinate of the kth layer
H	:	material history
i	:	summation counter
J	:	creep compliance
k, K	:	summation counter, total number of elements
K	:	Nutting parameter
l	:	length
Δl	:	elongation

m	:	stress exponent, Nutting parameter
m	:	total number of load stages
N	:	fatigue life, number of cycles to failure
$\{N\}$	:	resultant forces per unit length
n	:	time exponent, Nutting parameter
n	:	cycle number
Q	:	(activation) energy
$[Q_{ij}]$	:	reduced lamina stiffness matrix
$[\bar{Q}_{ij}]$	:	transformed global stiffness matrix
R	:	stress ratio
R	:	gas constant $(8.314 J/(mol \cdot K))$
$[S_{ijkl}]$	:	compliance tensor
$[S_{ij}]$	:	reduced lamina compliance matrix
$[\bar{S}_{ij}]$	:	transformed global compliance matrix
t	:	time, hold time
t	:	thickness, layer thickness
T	:	absolute temperature
T	:	duration time of one cycle
T	:	creep rupture time
$[T], [T']$	:	transformation matrices
T_g	:	glass transition temperature
v	:	velocity
V_f	:	fibre volume fraction
w	:	width
W	:	work

Greek Symbols

α	:	coefficient of thermal expansion
ε	:	strain
$\dot{\varepsilon}$	:	strain rate
η	:	dynamic viscosity
γ	:	shear strain
λ	:	thermal conductivity
Λ	:	internal damping
ν_{12}, ν_{21}	:	major and minor Poisson's ratio
ρ	:	specific electrical resistance
ϱ	:	density
σ	:	stress
τ	:	shear stress

τ :   retardation or relaxation time

Indices (combined with above symbols)

0	:	initial, reference
a	:	applied
amp	:	amplitude
b	:	bending
B	:	break
c	:	compression
cr	:	creep
C	:	critical
dyn	:	dynamic
el	:	elastic
exp	:	experimental
f	:	fibre
fat	:	fatigue
k	:	individual layer number
L	:	loss
m	:	matrix
max	:	maximum
$mean$	:	mean
min	:	minimum
$norm$	:	normalised
r	:	reversible
rec	:	recovery
S	:	store
sec	:	secant
t	:	tension
tan	:	tangent
th	:	threshold
ut	:	ultimate (for failure)
v	:	viscous
y	:	yield
$\parallel, \perp$	:	parallel and perpendicular
$1, 2, 3$	:	local cartesian coordinate system or counter
x, y, z	:	global (reference) cartesian coordinate system
$i, j, k, l (= 1, 2, 3)$	:	indices for constitutive equations

1

Introduction

1.1 Historical Background

Few things last forever. It would appear that most material things that respond to their environment change their form or function with time. Our technical understanding of the relationship of the history of response to engineering properties such as stiffness and strength is yet incomplete [1]. The safety, reliability, and durability of every engineering component rests directly on our understanding of what we might call 'materials response' after Kelvin [2], or what is more commonly, the subjects of elasticity, creep and fatigue[1].

  Most engineering components are subjected to load and environmental histories which vary in time over the period of service. The reduction of strength and the subsequent failure of materials subjected to repeated loading had been first addressed as a fundamental problem in 1837 by Albert [3] for repeated load proof tests on mine-hoist chains made of iron. A railway accident with extensive loss of life in 1842 gave reasons for further interest. A comprehensive description of the accident and its causes on the fatigue research is given by Smith [4]. Later, Wöhler started to investigate mechanical loads and (permanent) deflections of railroad axles in service [5, 6, 7]. These attempts were systematically continued with apparatus equipment at the Headquarter of the Niederschlesisch-Märkische Eisenbahn in Frankfurt/Oder with respect to the cycle, material and geometry dependent failure behaviour [7, 8, 9]. The results led to today's fatigue characterisation in terms of stress amplitude-life (S-N) curves, and to the concept of fatigue endurance limit. Based on these findings Gerber [10] and Goodman [11] developed methods of fatigue life calculations for different mean stress levels of cyclic stresses. By the 1920s,

---

[1]The word *fatigue* originated from the Latin expression *fatigare* means 'to tire'.

fatigue had evolved as a major field for scientific research [12]. Investigations in this time period also led to the development of damage accumulation models for fatigue failure by Palmgren [13] and Miner [14]. With the rapid development of the aircraft industry in the 1930s, multi-level loads had to be considered for dimensioning and Gassner [15] subsequently introduced the concept of service strength.

1.2   Overview

Although the subject of fatigue has attracted numerous scientists and engineers over a period of more than 150 years, the US Ministry of Energy estimates that today 90% of all cases of failure are due to fatigue [16]. This has to do with the increasing complexity under which materials must serve their engineering purposes. As our technologies advance, traditional and modern materials like composites, especially fibre reinforced polymers (FRPs), are being used under increasingly extreme conditions, mechanical loads, temperatures, environments, et cetera. Moreover, economic matters and performance requirements become more pressing [1].

FRPs have unique advantages over monolithic materials, such as a high specific[2] stiffness and strength related to a superior structural performance and adaptability to the intended function of the structure by affording the particular possibility of designing the material and structure in one unified and concurrent process [17]. Additional improvements can be realised in corrosion and wear resistance, appearance, temperature-dependent behaviour, electrical conductivity [18], thermal conductivity and stability, and acoustic insulation. Today, the aircraft, automobile, wind power, leisure, electronic and medical industries are quite dependent on FRPs as Figure 1.1 exemplary shows. These composites are routinely designed, manufactured and used [19].

The anisotropic and heterogeneous character of the material provides composite systems with many degrees of freedom for optimum configuration of the material but requires a high degree of know-how for design, computation, manufacturing, and life-prediction. Visible expression of the existing uncertainties and the non-utilised material potential is the often criticised yet used design criterion that only allows for 0.3% ultimate strain. An understanding of the micro-mechanisms of failure and their dominance under service conditions is important in engineering design, because for a particular application, they determine design allowables and the damage accumulation rate which affects damage tolerance, residual strength and stiffness, and life time of the component [20].

---

[2] property to density ratio
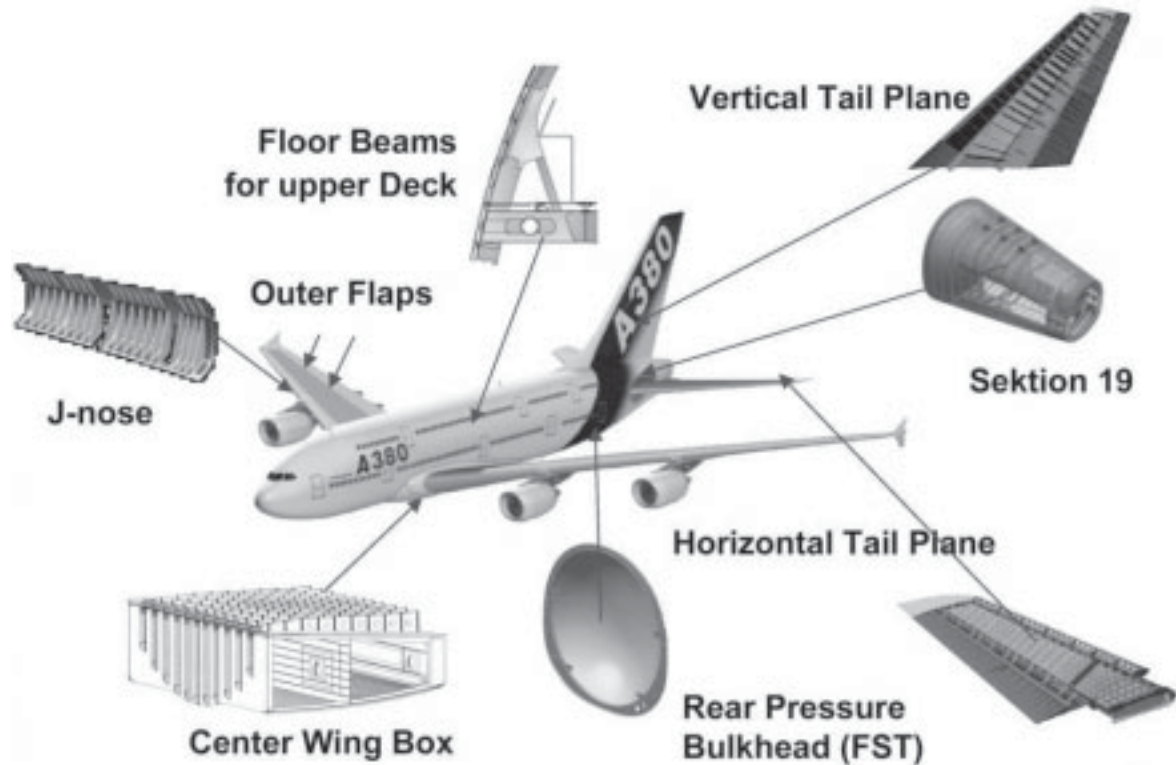
Figure 1.1: Example illustrating the various components of the Airbus A380 aircraft made of CFRP. (Source: Airbus Germany)

1.3 Significance of ± 45°-layers in FRPs

Applications from fibre reinforced polymers (FRPs) are normally designed in a way that tensile and compressive loads are carried by layers those fibres are parallel to the loading axes. The reinforcement to carry and withstand shear loads is ideally achieved by angle-plied ±45°-layers [21]. Typical engineering components which are highly subjected to shear loads, thus ideally containing very high percentages of ±45°-layers are drive shafts and the webs in I-sections of beams and spars. These structures have in common that the loads are carried by the geometrical shape rather than by additional reinforcing stringers and ties, e.g. as in fuselage panels to prevent global compressive and shear buckling. The components may additionally be subjected to radial and hoop stresses, e.g. as in pressurised lines and vessels, as well as tensile, compressive, and bending stresses, e.g. from dead and service loads.

To control stress concentrations and the damage behaviour [22], and to account for uncertainties in the load assumption and for the use in multipurpose applications, also multidirectional laminates are designed to contain a considerable fraction of ±45° reinforcement layers, varying from 5 to 80%. The popular quasi-isotropic laminate contains 50% ± 45°-layers, as much as

0° and 90°-layers together. Although the angle-ply (AP) layers in multidirectional laminates are constrained by the mutual agreement with the other layers, their inherent characteristics are included [23].

The above examples point up the significance of ±45°-layers for structural applications from FRPs. Therefore, the fundamental understanding of the time, load and temperature dependent material behaviour of ±45°-layers is indispensable for the material comprehension of ±45°- and other multidirectional laminates.

1.4   Homogenisation approaches

A flowchart to select the appropriate choice of the modelling and characterisation method for FRPs is presented in Figure 1.2. The upper part describes the (visco)elastic properties of the FRP on the constituent level, e.g. by the classical lamination theory (CLT) whereas the absence of microscopic damage is assumed. The inquiry box in the lower part selects, how the durability, i.e. the load, time, and strength dependent properties of the material can be appropriately modelled and characterised. The potential homogenisation with respect to the damage types and locations depends on the complexity in structure and properties [25, 26].

'More heterogeneous' materials

For 'more heterogeneous' materials such as non-crimped fabrics, Gagel and Schulte [27] suggested a non-scalar approach to relate microscopic damage events with a change of integral macroscopic properties. The remaining life could exemplary be predicted from the degradation of an integral damage metric. Hobbiebrunken et al. [28, 29] directly related processing induced thermal residual stresses on the heterogeneous constituent level with crack initiation and failure.

'More homogeneous' materials

Matrix dominated ±45°-laminates may be considered as 'more homogeneous'. There are no preferred locations for damage events e.g. from binding yarns, resin rich zones, or fibre undulation from the weave. The types of damage occurring depend on the loading. Due to the absence of 0°-plies, the laminate can respond to the applied load with viscoelastic and viscous deformation and cracking whereas the lower laminate stiffness reduces stress singularities. Matrix cracking along the fibres occurs at higher loads preferentially under tension and shear [30]. The crack initiation occurs locally and statistically

WITHOUT CRACKS

| Fibre properties $= f(\sigma, t)$ | Matrix properties $= f(\sigma, T, t)$ |

Processing (Structure, temperature, residual stresses)

CLT

Fibre reinforced polymer (FRP)

Description of (visco)elastic properties

WITH CRACKS

FRP modelling & characterisation

Decision on homogenisation with respect to damage types and damage location e.g. by user's experience, structure, or NDT

Durability as a function of
• load,
• time,
• strength,
• etc.

'heterogeneous' e.g. NCF

Microscopic damage at preferred locations

Microscopic damage metric, e.g. delaminated area

Macroscopic Properties e.g. modulus

Failure, Life time

'homogeneous' **e.g. ±45° layers**

Microscopic damage, statistically distributed

Macroscopic damage metric, e.g. modulus degradation

Failure, Life time

Mechanical & environmental service loads

Figure 1.2: Flowchart of the structure dependent material modelling and characterisation [24].

distributed [31]. The damage evolution in terms of deformation progression is continuous and distributed over the material volume. Therefore, analytical and homogenised approaches based on macroscopic properties such as the strain response outline promising attempts to characterise and model the mechanical behaviour of ±45°-laminates and to predict durability and life time.

1.5   Aims of the work

Section 1.3 circumstantiated the significance of $\pm 45°$ layers for structural applications from FRPs. The previous discussion of the homogenisation approaches highlighted a principle way with good prospects to successfully model and characterise $\pm 45°$-laminates. Within the scope of this work the mechanical behaviour of $\pm 45°$-laminates from HTA/6376 carbon/epoxide prepregs will be investigated. The material is commercially available and certified and used for structural applications in aircrafts (Figure 1.1).

The present work targets to a deeper understanding of the laminate behaviour under simple and complex load histories including the effects of preloads and load sequences. To accomplish this goal, materials fundamentals will be reviewed followed by a comprehensive literature survey about the state of the art of $\pm 45°$-laminates. This theoretical background is to be amended and completed by an extensive experimental programme. The experiments to be undertaken include rate dependent quasi-static tests, as well as (mixed) creep and fatigue tests.

The tolerance of the fatigue properties to load uncertainties and unexpected overloads plays a vital role for structural applications. The sensitivity of the fatigue behaviour shall therefore be proved for different load scenarios. The influence and the interaction of load sequences on the fatigue behaviour will be investigated by combinations of different fatigue and creep-recovery-fatigue loadings. Another focus deals with the effects of the creep-fatigue interaction on the material durability. The creep and fatigue loads may act alternately or simultaneously. The mechanisms of the deformation and damage processes shall be assessed by different experimental techniques such as hysteresis measurements, microscopy, and thermography. The observed results are to be described, discussed for a better material comprehension, and wherever applicable modelled by analytical and homogenised approaches based on macroscopic properties aiming to a more reliable life time prediction.

2

Fundamentals - Materials and Characterisation

This chapter describes in brief materials', theoretical, and metrological fundamentals which are presumed for the comprehension of the later chapters. After an introduction to FRPs in section 2.1 and the derivation of their constitutive equations in section 2.2, the sections 2.3 to 2.5 give an overview on the material behaviour of polymers and FRPs under quasi-static, constant, and repeated loads which is completed in section 2.6 by the microscopic damage characterisation. The material description of sections 2.3 to 2.5 is phenomenologically focussed to homogenisation approaches.

2.1 Fibre reinforced polymers

The entire characteristics of FRPs, e.g. the mechanical, thermal, and electrical behaviour, the resistance to environmental effects, and the fabrication are strongly influenced by the proportions and properties of the reinforcement fibre and the matrix. The interface between fibres and matrix is particularly important for the load to be transferred from the matrix to the fibres by shear stresses [32, 33, 34]. The mechanical profile of the composite is significantly affected by the orientation, shape, size, and distribution of the reinforcement fibres [19] and various features of the matrix, such as the cross-link density in case of thermosets. These properties, together with the fibre volume fraction[1] constitute the microstructure of the composite.

---

[1] The fibre volume fraction V_f is the ratio of fibre and total volume of the material. The matrix volume fraction V_m is the complementary value to unity, i.e. $V_f + V_m = 1$.

2.1.1   Fibres

Carbon, glass and aramid fibres are today extensively used in FRPs. Other fibres such as ceramic or natural fibres are of subordinated importance with regard to their market shares [17]. The fibre materials can be processed as unidirectional (UD) rovings, two-dimensional (2D) or three-dimensional (3D) preforms.

Carbon fibres

Carbon fibres come in many types with a range of stiffness and strength values, depending on the processing [35]. There are three main routes for producing carbon fibres, namely from polyacrylonitrile (PAN), from mesophase pitch, and by pyrolytic deposition [36].

As far as fibre technology is concerned, graphite is the most important crystalline form of carbon[2]. Figure 2.1 shows that in a graphite single crystal, the carbon atoms are arranged in hexagonal arrays, stacked in a regular ABAB... sequence. The atoms in these basal planes are held together by strong covalent bonds ($E = 1060\,GPa$), with only weak van der Waals bonds ($E = 36.5\,GPa$) between them. To obtain high axial modulus and strength, good alignment of the basal planes parallel to the fibre axis is required [37].
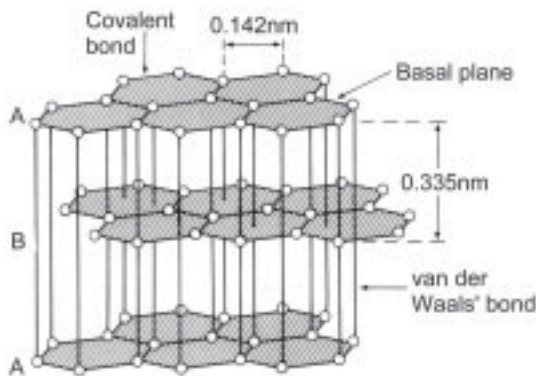
Figure 2.1: Crystal structure of graphite.
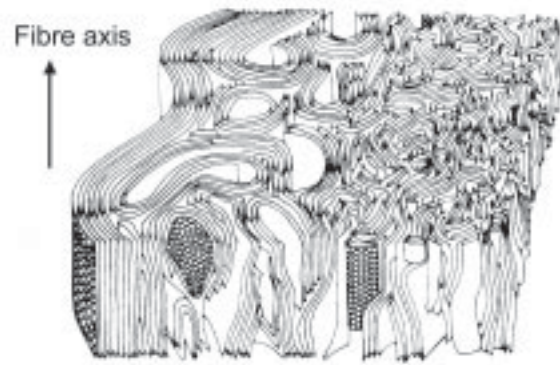
Figure 2.2: 3D model of skin-core organisation in carbon fibres. (Bennett and Johnson [38])

The basal planes are not regularly packed as Figure 2.2 schematically shows. Since the outer sheath has a better alignment of the crystallites, thin fibres exhibit a higher modulus than thick fibres [39]. The manufacturing of carbon fibres from PAN - a three-stage process - is shortly described in the next paragraph. The detailed review can be found by Thorne [40], condensed reviews in references [19] and [36].

---

[2] Carbon has three well known crystalline forms: diamond, C_{60}, and graphite.

Processing carbon fibres from PAN In the first stage, the *spinning*, bulk PAN is drawn to a fibre and stretched 500-1300% to produce alignment of the molecular chains. In the second stage, the *low-temperature stabilisation*, the stretched fibre is heated in air at 200-280°C; the active nitrile groups react to produce a ladder-like polymer. Chemical cross-links between the oriented chains are formed in three dimensions, so that the chains can no longer bend or distort on heating. This is followed by oxidation whereby some two-thirds of the oxygen sites are filled slowly with the release of water. In the third stage, the *graphitisation*, the oxidised PAN is finally reduced at 900-2800°C in nitrogen or argon to give the carbon ring structure. The fibres usually have a thin skin of circumferential basal planes and a core with randomly oriented crystallites, as seen in Figure 2.2. The final heat treatment controls the Young's modulus and the tensile strength [39].

2.1.2 Thermosets

Thermosets differ from other polymeric materials classes[3] in their chemical composition as well as their processing technology. The cured thermoset is an amorphous single cross-linked 3D-network, which after curing cannot be remelt. Rather than to melt, thermosets decompose [41]. Thermosets consist of low molecular monomers. After addition of a hardener a typically thermally initiated, exothermic curing reaction takes place. Because diffusion processes and the reactivity of the reactants benefit from higher temperatures, the cross-link density is favoured as well [42]. A post-cure treatment is often given to minimise any further cure and change in properties during service. A characteristic property determined by the cross-link density is the glass transition temperature T_g. Because thermosets start to soften above T_g, measurement of T_g can inversely be used to determine the cross-link density or the degree of curing [43].

Epoxide resins

Because of their good mechanical and environmental properties, epoxide (EP) resins are the most widely used thermoset for high performance FRPs. The term epoxide is applied to both, the monomer and to the cured resin; the former contains reactive epoxide groups [44]. Cross-linking of the monomer is achieved using amines or acid anhydrides which variously make use of the epoxide end groups or the hydroxy groups along the chains (Figure 2.4) [45].

 With some 80% of the market share [46] the commercial scene of epoxide monomers is dominated by the bi-functional diglycidyl ether of bisphenol A

---

 [3] Thermoplastics, thermosets or duromeric materials, and elastomers represent the three major classes of polymeric materials.

(DGEBA) which is the reaction product of bisphenol A and epichlorohydrin. However, the majority of qualified materials available today for prepreg formulations make up from the tetra-functional tetraglycidyl ether of methylene dianiline (TGMDA) monomer and the aromatic 4,4'-diamino diphenyl sulfone (4,4'-DDS) curing agent [47]. The chemical structures of TGMDA and 4,4'-DDS are shown in Figure 2.3.
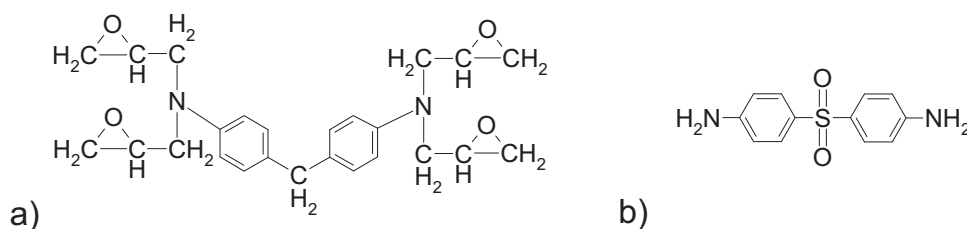
Figure 2.3: Chemical structure of a) tetraglycidyl ether of methylene dianiline (TGMDA) and b) 4,4'-diamino diphenyl sulfone (4,4'-DDS).

Aromatic amines react only slowly with the epoxide monomer, exhibit long pot lives, and require long periods at elevated temperature to attain optimum properties. 4,4'-DDS has the principle advantage over other aromatic amines in providing the highest heat resistance and has become the standard curing agent with TGMDA [48]. The schematic curing reaction of four epoxide groups with two amine groups of the hardener is shown in Figure 2.4.
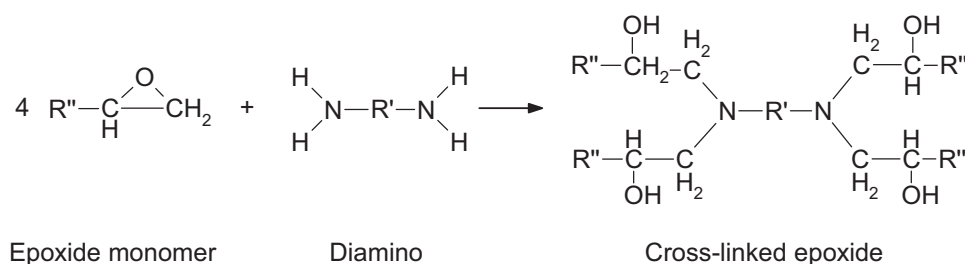
Figure 2.4: Schematic curing reaction of epoxide monomers with amine groups to a cross-linked epoxide.

2.1.3   Laminates

Increasing use is being made today of FRPs in numerous fields and applications. The profile of properties can be adjusted in wide ranges by material matching of the constituents, the processing technique, and the composite architecture. This expression encompasses intrinsic features as well as the volume fraction of fibres and their alignment and packing arrangement. Certain tasks are thereby assigned to the constituents. The fibres mainly provide

stiffness and strength. The purpose of the matrix is to encapsulate and protect the fibres, to transfer the load among them, to prevent micro buckling of the fibres under compression loads, to give resistance against media and abrasion, and to provide adapted deformability [36].

Continuous fibre reinforced thermosets put trough for high performance structural applications from FRPs. More expensive anisotropic and electrically conductive carbon fibres are preferred to isotropic and electrically insulating glass fibres because of better specific properties. Once the constituents with known mechanical properties are defined, the properties of the FRP can be justified by the fibre volume fraction V_f and weighting of the fibre orientations. The *Rule of Mixtures* (ROM) indicates that the stiffness in fibre direction is the weighted mean of the moduli of fibres and matrix depending only on the volume fraction of fibres. Eq. (2.1) assumes equal strain conditions, provided that there is no interfacial sliding. The transverse stiffness can be roughly estimated from the equal stress assumption of the constituents and is given in Eq. (2.2).

$$E_\parallel \quad = \quad V_f E_f + (1 - V_f) E_m \qquad (2.1)$$

$$\frac{1}{E_\perp} \quad = \quad \frac{V_f}{E_f} + \frac{1 - V_f}{E_m} \qquad (2.2)$$

According to the manufacturing process, the fibres are impregnated prior to stacking and consolidation of the laminae (prepreg technology), or for wet technologies like resin transfer moulding (RTM) or resin infusion (RI) imbued with the resin after stacking and consolidation. Wet technologies mainly use woven, braided, knitted or non-crimped fabrics. Figure 2.5 shows
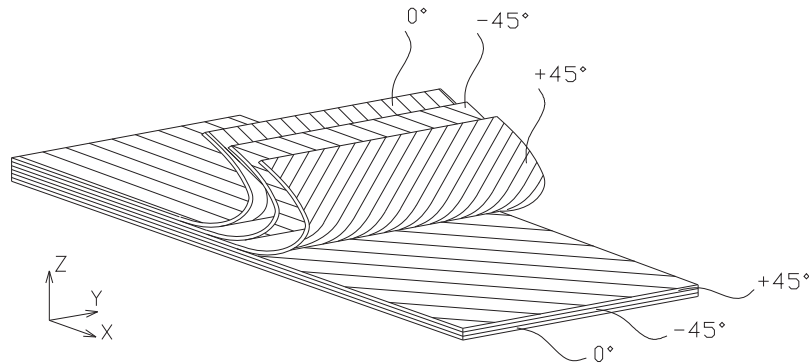

Figure 2.5: Sketch of stacked and partly consolidated layers showing a $[0, \mp45]_S$ lay-up in global coordinates. The subscripted S symbolises the plane of symmetry of the laminate.

a plane laminate consisting of UD layers, which is typical for the prepreg

technology. The semi-finished prepreg product can be produced by three different manufacturing techniques, namely the solution route, the two step process via matrix film production, and the bath route [49].

Especially, when the loads are known, the stacking sequence of the laminate can be chosen to match stiffness and strength requirements in different directions. Whereas tensile and compressive loads are carried by 0° and 90°-layers, the reinforcement to withstand shear loads is achieved by ±45°-layers. Referring to the global coordinates in Figure 2.5, the overall laminate behaviour can be given in so called carpet plots depending on the $0°/\pm45°/90°$ shares [21].

The next section describes in brief the procedure to calculate the elastic properties of multidirectional laminates consisting of UD layers.

2.2 Linear elastic constitutive equations

2.2.1 Stress-strain relations of unidirectional laminae

In the most general case of an anisotropic material, the stress and strain components are expressed by the generalised Hooke's law [50].

$$\varepsilon_{ij} = S_{ijkl}\,\sigma_{kl} \quad ; \quad \sigma_{ij} = C_{ijkl}\,\varepsilon_{kl} \qquad i,j,k,l = 1,2,3 \qquad (2.3)$$

S_{ijkl} and C_{ijkl} are components of the 81 terms containing fourth order compliance and stiffness tensor, respectively. The derivation of the constitutive equations for the individual transversely isotropic[4] lamina assumes plane stress conditions, i.e. $\sigma_{33} = \tau_{13} = \tau_{23} = 0$. With $\varepsilon_{12} = 1/2\,\gamma_{12}$, the strain-stress relations for a lamina then reduce to Eq. (2.4).

$$\left\{ \begin{array}{c} \varepsilon_1 \\ \varepsilon_2 \\ \gamma_{12} \end{array} \right\} = \left[\begin{array}{ccc} S_{11} & S_{12} & 0 \\ S_{21} & S_{22} & 0 \\ 0 & 0 & S_{66} \end{array} \right] \left\{ \begin{array}{c} \sigma_1 \\ \sigma_2 \\ \tau_{12} \end{array} \right\} \qquad (2.4)$$

The components of the reduced compliance matrix S can be given in terms of engineering constants as follows:

---

[4] An orthotropic material has three mutually perpendicular planes of material symmetry. The number of elastic constants is thus reduced to nine, as various terms are interrelated. An orthotropic material is called transversely isotropic when one of its principal planes is a plane of isotropy. Here, the indices 2 and 3 are interchangeable, and the number of elastic constants further reduces to five [51].

$$S_{11} = 1/E_{11} \tag{2.5}$$
$$S_{22} = 1/E_{22} \tag{2.6}$$
$$S_{12} = S_{21} = -\nu_{12}/E_{11} = -\nu_{21}/E_{22} \tag{2.7}$$
$$S_{66} = 1/G_{12} \tag{2.8}$$

In inverse form, Eq. (2.4) may be expressed as

$$\left\{ \begin{array}{c} \sigma_1 \\ \sigma_2 \\ \tau_{12} \end{array} \right\} = \left[\begin{array}{ccc} Q_{11} & Q_{12} & 0 \\ Q_{21} & Q_{22} & 0 \\ 0 & 0 & Q_{66} \end{array} \right] \left\{ \begin{array}{c} \varepsilon_1 \\ \varepsilon_2 \\ \gamma_{12} \end{array} \right\} \tag{2.9}$$

with the components of the reduced lamina stiffness matrix C given as follows:

$$Q_{11} = E_{11}/(1 - \nu_{12}\,\nu_{21}) \tag{2.10}$$
$$Q_{22} = E_{22}/(1 - \nu_{12}\,\nu_{21}) \tag{2.11}$$
$$Q_{12} = Q_{21}\nu_{21}\,E_{11}/(1 - \nu_{12}\,\nu_{21}) = \nu_{12}\,E_{22}/(1 - \nu_{12}\,\nu_{21}) \tag{2.12}$$
$$Q_{66} = G_{12} \tag{2.13}$$

It can be seen that $[Q] = [S]^{-1}$, hence $[Q][S] = [1]$. As far as the plane stress constitutive equations are concerned, the lamina is fully characterised by only four independent constants. Normally, the lamina local (principal) axes (1,2) are aligned under an angle θ to the global (reference) axes (x,y). The transformation of the stresses and strains referred to the principal material axes to those referred to the reference axes is accomplished as shown below [36].

$$\{\varepsilon\}_{12} = [T']\{\varepsilon\}_{xy} \quad ; \quad \{\sigma\}_{12} = [T]\{\sigma\}_{xy} \tag{2.14}$$

With the substitutions $m = \cos\theta$ and $n = \sin\theta$, the transformation matrices $[T']$ and $[T]$ can be expressed in a simplified form.

$$[T'] = \left[\begin{array}{ccc} m^2 & n^2 & mn \\ n^2 & m^2 & -mn \\ -2mn & 2mn & m^2 - n^2 \end{array} \right] \quad ; \quad [T] = \left[\begin{array}{ccc} m^2 & n^2 & 2mn \\ n^2 & m^2 & -2mn \\ -mn & mn & m^2 - n^2 \end{array} \right] \tag{2.15}$$

The transformation of the constitutive Eqs. (2.4) and (2.9) from local to global coordinates leads to Eq. (2.16).

$$[\bar{S}] = [T']^{-1}[S][T] \quad ; \quad [\bar{Q}] = [T]^{-1}[Q][T'] \tag{2.16}$$

Here, $[\bar{S}]$ and $[\bar{Q}]$ denote the transformed global compliance and stiffness matrices respectively. The general stress-strain equations for an arbitrarily oriented lamina under plane stress conditions is expressed in Eq. (2.17).

$$\{\varepsilon\}_{xy} = [\bar{S}] \{\sigma\}_{xy} \quad ; \quad \{\sigma\}_{xy} = [\bar{Q}] \{\varepsilon\}_{xy} \tag{2.17}$$

2.2.2   Classical lamination theory (CLT)

It is apparent that the overall behaviour of a multidirectional laminate, e.g. Figure 2.5, is a function of the properties and the stacking sequence of the individual layers. By use of the classical lamination theory, one can consistently proceed from the lamina behaviour and predict the linear-elastic properties of the laminate. The analysis is based on the assumption that the laminate is thin when compared with its lateral dimensions and is loaded in its plane only. Furthermore, all displacements are continuous throughout the laminate and small compared with the constant thickness. It is further assumed that the normal strain ε_{zz} and the transverse shear strains ε_{xz} and ε_{yz} are negligible, and that the transverse shear stresses σ_{xz} and σ_{yz} vanish on the surfaces normal to the z-direction. A line originally straight and perpendicular to the laminate mid-plane remains so after deformation [50, 51]. Assuming that the stresses are uniform through the thickness of each lamina, the resultant forces $\{N\}$ in global coordinates can be expressed as

$$\{N\}_{xy} = \sum_{k=1}^{K} \int_{h_{k-1}}^{h_k} \{\sigma\}_{xy,k} \, dz \tag{2.18}$$

where h_k and h_{k-1} denote the z-coordinates of the upper and lower surfaces of the layer k out of K layers in total [52]. With the layer thickness $t_k = h_k - h_{k-1}$ and Eq. (2.17) the resultant forces can be written as:

$$\{N\}_{xy} = \sum_{k=1}^{K} t_k \, [\bar{Q}]_k \, \{\varepsilon\}_{xy,k} \tag{2.19}$$

For a thin symmetric laminate[5], it can be assumed that the strains of the individual plies in global coordinates are identical and equal to the total laminate strain $\{\varepsilon\}^0$, i.e. no curvatures are present and $\{\varepsilon\}_{xy,k} = \{\varepsilon\}^0$. Using the relation between the stiffness matrices of the k-th ply and the laminate

---

[5] A laminate is called symmetric in both, geometry and material properties, when for each layer on one side of a mid-plane there is a corresponding layer at an equal distance from the mid-plane on the other side with identical thickness, orientation, and properties. For symmetric laminates in-plane loads cause only in-plane deformations, and vice versa [17, 50].

$$[A] = \sum_{k=1}^{K} t_k \, [\bar{Q}]_k \tag{2.20}$$

the laminate constitutive equation can be expressed in an alternative form.

$$\left\{ \begin{array}{c} N_x \\ N_y \\ N_{xy} \end{array} \right\} = \left[\begin{array}{ccc} A_{xx} & A_{xy} & A_{xz} \\ A_{xy} & A_{yy} & A_{yz} \\ A_{xz} & A_{yz} & A_{zz} \end{array} \right] \left\{ \begin{array}{c} \varepsilon_x^0 \\ \varepsilon_y^0 \\ \gamma_{xy}^0 \end{array} \right\} \tag{2.21}$$

Since multidirectional laminates are characterised by stress discontinuities from ply to ply, it is preferable to work with strains, which are continuous through the thickness. For this reason it is necessary to invert the load-deformation relation from Eq. (2.21).

$$\left\{ \begin{array}{c} \varepsilon_x^0 \\ \varepsilon_y^0 \\ \gamma_{xy}^0 \end{array} \right\} = \left[\begin{array}{ccc} a_{xx} & a_{xy} & a_{xz} \\ a_{xy} & a_{yy} & a_{yz} \\ a_{xz} & a_{yz} & a_{zz} \end{array} \right] \left\{ \begin{array}{c} N_x \\ N_y \\ N_{xy} \end{array} \right\} \tag{2.22}$$

A laminate is balanced when it consists of pairs of layers with identical thickness and elastic properties but $+\theta$ and $-\theta$ directions of their principal axes with respect to the laminate reference axes[6]. For such a laminate, the in-plane shear coupling terms A_{xz} and A_{yz} can be determined from Eq. (2.20) with the transformed global stiffness $[\bar{Q}]$ from Eq. (2.16). One concludes that $A_{xz} = A_{yz} = 0$. The fact that the in-plane shear coupling terms are zero is a defining characteristic trait of a balanced laminate [17].

2.3 Material behaviour under quasi-static loading

In a quasi-static test a specimen is loaded at constant load[7] rate[8] until it fractures or until the stress (force) or strain (positive or negative elongation, displacement) reaches some predetermined value.

The uniaxial tensile test is the most common test method to determine material properties [53]. The description of the stress-strain behaviour differentiates between true and nominal values. While true values refer to the

---

[6] A balanced laminate can be symmetric (e.g. $[+45, -45]_{2S}$) but does not need to be symmetric (e.g. $[+45, -45]_4$).

[7] The term load can refer to as force, displacement, stress, or strain.

[8] rate = differential with respect to time.

actual geometry, nominal and all characteristic material variables are normalised by the initial geometry.

$$\sigma = \frac{F}{A_0} \tag{2.23}$$

$$\varepsilon = \frac{\Delta l}{l_0} \tag{2.24}$$

$$\nu_{xy} = -\frac{\varepsilon_y}{\varepsilon_x} \tag{2.25}$$

The nominal stress given in Eq. (2.23) results from the ratio of the applied force F to the initial cross-section A_0; the nominal strain given in Eq. (2.24) is calculated by dividing the elongation Δl by the initial length l_0. The reduction of the cross-section for elastic deformations under uniaxial loading is considered by the Poisson's ratio ν, the negative ratio of transverse and longitudinal strain (Eq. (2.25)).

Figure 2.6 shows schematically typical stress-strain curves for polymers and characteristic variables according to ISO 527-1[9]. The yield stress σ_y is defined as the first stress at which an increase in strain occurs without an increase in stress. The tensile strength $\sigma_{ut\,t}$ denotes the ultimate (highest) tensile stress (UTS) sustained by the specimen, and σ_B denotes the tensile stress at rupture. The characteristic strains are defined by the corresponding stresses. Hooke's law (Eq. (2.26)) applies within the range of linear increase of the stress-strain curve with the Young's modulus E as the constant of proportionality. For polymers[9] and FRPs[10], the Young's modulus is determined as the slope of the stress-strain curve between 0.5 and $2.5 \cdot 10^{-3}$ strain for a constant actuator velocity of $2mm/min$.

$$\sigma = E\,\varepsilon \tag{2.26}$$

If the load is released rom above the linear-elastic region, the deformation partly recovers elastically, as Figure 2.7 schematically shows. During unloading, the curve ideally (solid line) traces a straight line from the point of unloading (A), and its slope is parallel to the initial elastic load curve. The magnitude of the elastic strain which is regained during unloading represents the elastic strain recovery. If the load is reapplied, the curve essentially passes back through the same linear part. Yielding exactly occurs at the stress where the previous unloading began. This phenomenon of *strain strengthening* in

---

[9] ISO 527-1:1993 *Plastics - Determination of tensile properties; Part 1: General principles*

[10] ISO 527-4:1997 *Plastics - Determination of tensile properties; Part 4: Test conditions for isotropic and orthotropic fibre-reinforced plastic composites*
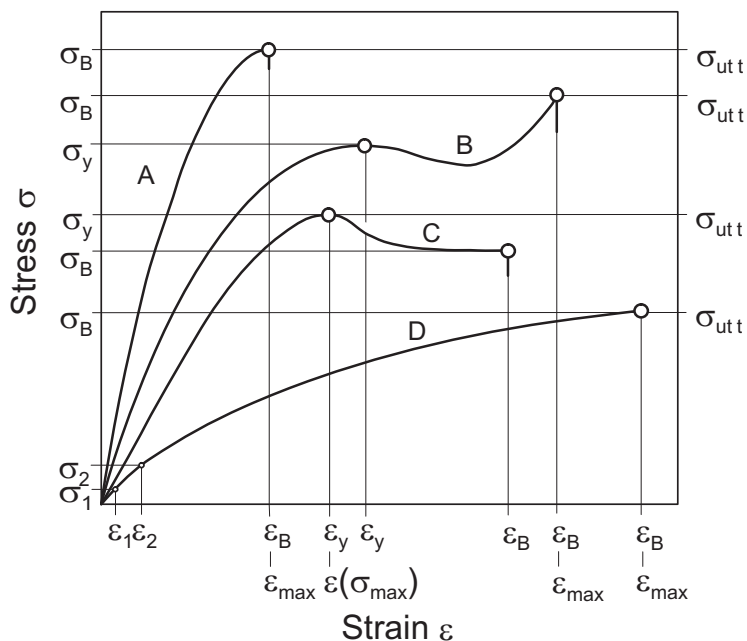
Figure 2.6: Typical stress-strain curves for polymers. Brittle materials (A), tough materials with yield point (B and C), and tough materials without yield point (D). (ISO 527-1)
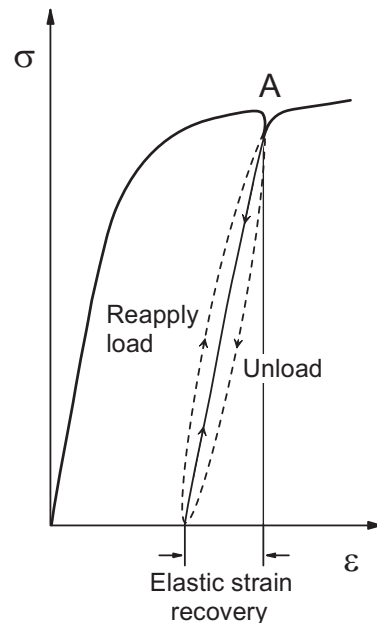
Figure 2.7: Unloading cycle within a stress-strain plot and schematically resultant elastic strain recovery.

polymers has its analogy in the *work hardening* of metals [54]. Due to internal energy dissipation and time dependent deformation, the real unloading and loading curves of polymers and many FRPs follow the dashed lines in Figure 2.7.

The scientific literature does typically not distinguish between the terms *modulus* and *stiffness*. Within the scope of this work, the *stiffness* may be interpreted as the stress, strain, time, temperature, cycle, and damage dependent slope of the stress-strain curve. The *modulus* refers to as an exclusively temperature dependent material inherent stiffness.

Polymers exhibit an elastic material behaviour only for small loads, which is normally nonlinear. As the load increases additional creep and yielding occurs, ascribed to the rearrangement of molecular chains. Its velocity depends on the load level, the time under load, the temperature, and the polymeric structure [41]. Such a material behaviour is called viscoelastic. The tensile test is usually insufficient to describe the mechanical behaviour of polymers due to their pronounced time and temperature dependence. Hence, retardation (creep) tests under constant load as well as stress relaxation tests under constant strain have to be additionally performed.

Figures 2.8 and 2.9 show the effect of temperature and strain rate on the uniaxial tensile stress-strain behaviour of polymers. Brittle behaviour results in high strengths at low temperatures and high strain rates, whereas a ductile
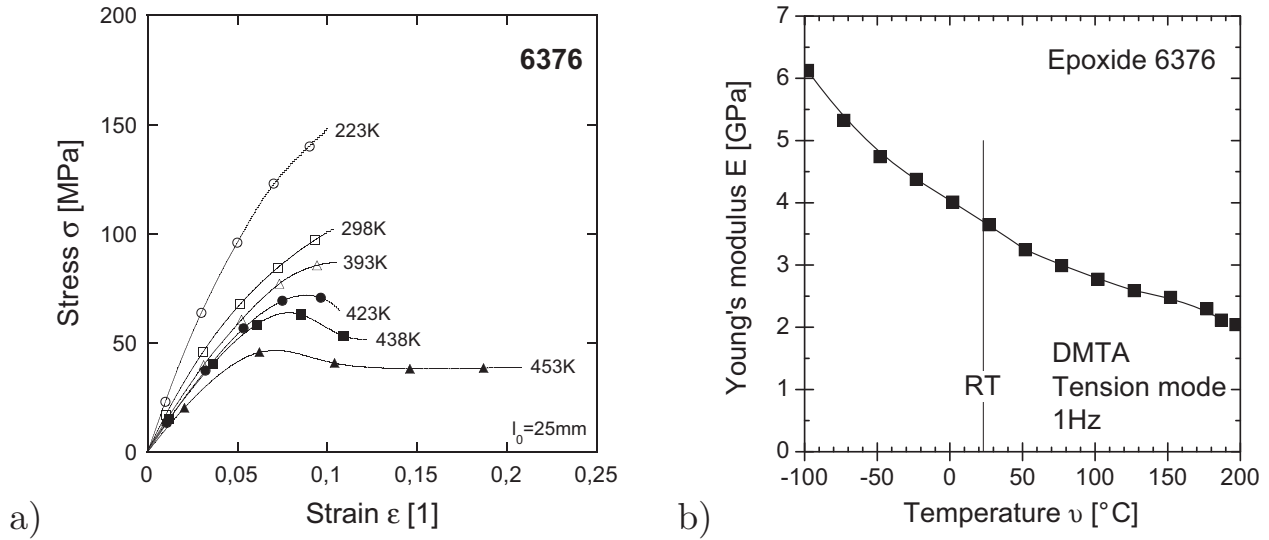
Figure 2.8: Effect of temperature on the a) stress-strain behaviour and b) the Young's modulus of the neat epoxide resin 6376. (Hobbiebrunken [55])

behaviour and low strengths are observed for high temperatures and low strain rates. The strain rate effect of most polymers can be described by Eyring's theory of viscosity [56], which assumes that the deformation of a polymer involves the motion of a molecule over potential energy barriers. The Eyring model suggests that the yield stress varies linearly with the logarithm of strain rate. However, the Poisson's ratio neither of a polymer in the glassy regime [57] nor of a laminate [58] is expected to change with strain rate.
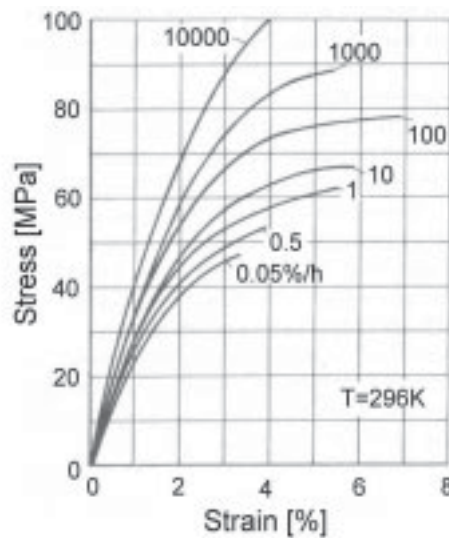
Figure 2.9: Effect of strain rate on the tensile stress-strain behaviour of polymethylmethacrylate (PMMA). (Knausenberger [59])

2.4 Material behaviour under constant loading

2.4.1 Phenomenological creep

Creep is the time-dependent strain that occurs when a material is suddenly subjected to a constant load or stress for a prolonged period of time. Although the mechanisms by which metals, polymers and ceramics deform in creep are different, the phenomena which are observed in these materials are similar [60].

Figure 2.10 shows a graphical representation of the time dependence of strain and strain rate. Three stages can be distinguished for most materials. After the instantaneous strain on initial loading, which can be of elastic, viscoelastic, or elastic-plastic nature, the strain rate decays during the primary stage until an ostensibly constant strain rate is reached during the secondary stage. After the secondary stage, the creep rate increases again during the tertiary stage which leads to failure, typically related to geometrical instabilities [61, 62]. For polymeric materials primary creep is sometimes referred to as transient creep and secondary creep is usually referred to as steady-state creep [60].
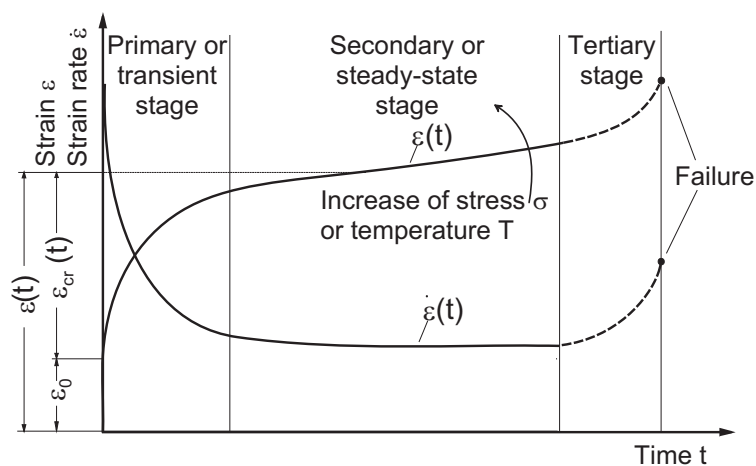
Figure 2.10: Characteristic course of strain $\varepsilon(t)$ (ε_0: instantaneous strain, $\varepsilon_{cr}(t)$: creep strain) and strain rate $\dot{\varepsilon}(t)$ during creep. (Ehrenstein and Sarabi [63])

The influence of the load level on the creep behaviour of unreinforced and short fibre reinforced polymers emerges from Figure 2.11. The difference between the successive load levels is constant. A disproportionate increase of strain is observed for stresses in the range between 0.3 to 0.4 of the tensile strength. These high strain differences already exist during the transient creep stage and persist to long periods of time. Rather than related to damage
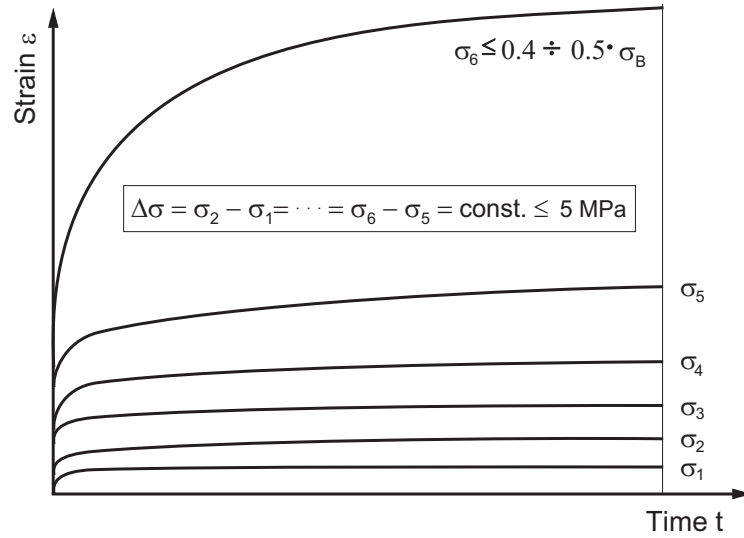
Figure 2.11: Influence of load level on the creep behaviour of (short fibre reinforced) polymers. (Sarabi [64])

evolution in the material, the disproportionality represents a pronounced nonlinearity [64].

The evaluation of creep tests normally takes place in single logarithmic charts with the logarithm of time as the abscissa [65]. According to Figure 2.12, either the strain is plotted versus time for individual stresses (creep curves), or the stress is plotted versus time for different strains (stress vs. time curves). Upon redrawing for constant times one obtains isochronous stress-strain curves.

Normalising the time dependent strain with the constant applied stress σ_0 leads to the creep compliance $J_{cr}(t)$ or the creep stiffness $E_{cr}(t)$ respectively[11], both given in Eq. (2.27).

2.4.2   Viscoelasticity

Bodies are called viscoelastic if they respond to a load simultaneously time independent elastic and time dependent viscous. A viscoelastic behaviour can be described by a combination of Hookean and Newtonian behaviour. The elastic behaviour of Hookean bodies can be modelled by a spring which contracts on application of a load but expands spontaneously to its original position after the load is removed. The model of Newtonian liquid is a dashpot with a viscous liquid through which a perforated plug is moved [53]. The constitutive equation of the spring and the dashpot are given in Eqs. (2.26) and (2.28) where η is the dynamic viscosity.

---

[11] ISO 899-4:1996 *Plastics - Determination of creep behaviour; Part 1: Tensile creep*
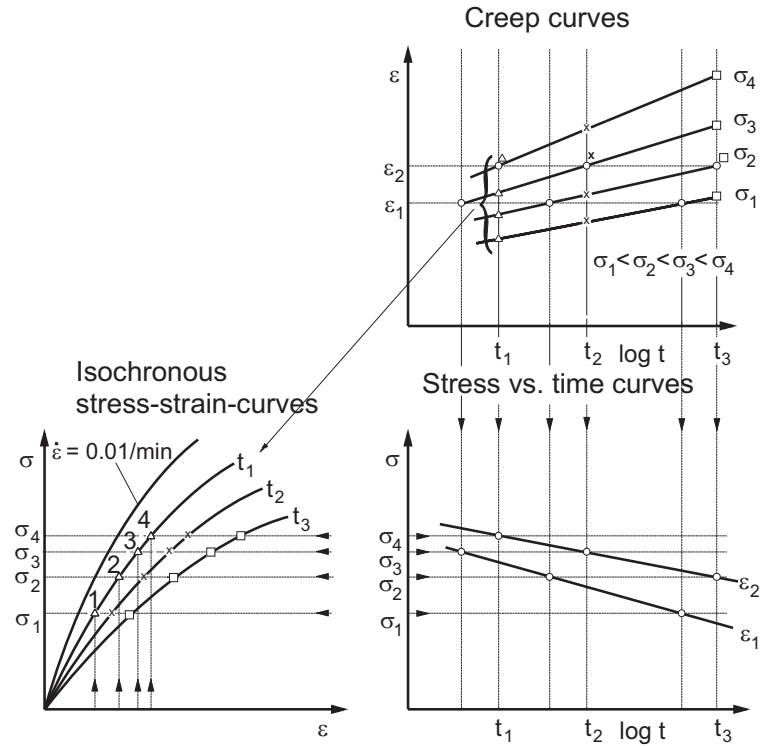
Figure 2.12: Graphical methods to evaluate creep tests. (Menges [65])

$$J_{cr}(t) \;=\; \frac{1}{E_{cr}(t)} \;=\; \frac{\varepsilon(t)}{\sigma_0} \tag{2.27}$$

$$\dot{\varepsilon} \;=\; \frac{\sigma}{\eta} \tag{2.28}$$

Linear viscoelasticity

The linear viscoelastic behaviour can be modelled by combinations of spring and dashpot where each element possesses a linear characteristic curve. Thus, stresses, strains, and strain rates are related linearly. The connection of Hookean body and Newtonian liquid in series leads to the Maxwell element and in parallel to the Kelvin-Voigt element. A Maxwell and a Kelvin-Voigt element in series leads to the Burgers or 4-parameter element [65] (Figure 2.13). These models do not essentially contribute to the comprehension of the underlying molecular processes, but clarify the macroscopic mechanical behaviour of materials under different load cases. The validity range of the linear viscoelastic characterisation of solid polymers is limited to a few per thousand [66].

In experiments one cannot distinguish between contributions of the various elements to the observed behaviour. The constitutive equations can be
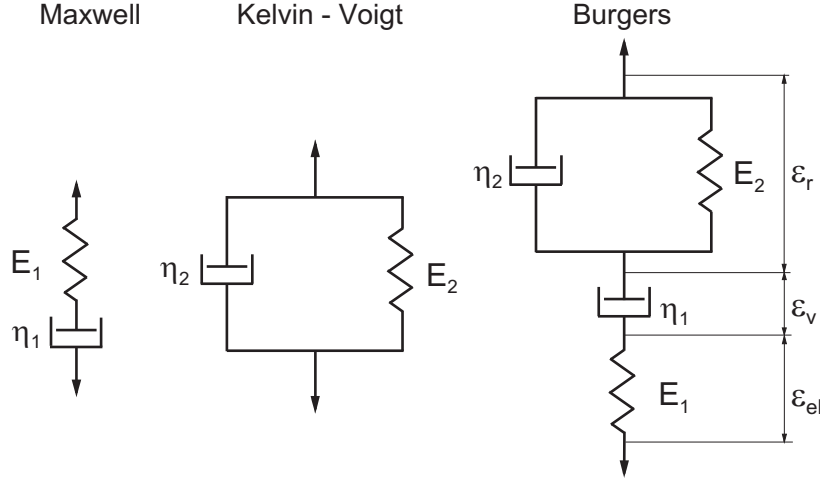
Figure 2.13: Rheological models of linear viscoelastic bodies. (Menges [65])

solved only for the special cases of constant strain(stress relaxation), constant stress(creep), constant strain rate, and constant stress rate [53]. The time dependent total strain $\varepsilon(t)$ consists of an elastic portion ε_{el}, a viscous portion ε_v and a time dependent reversible portion ε_r (Figure 2.14). Since both
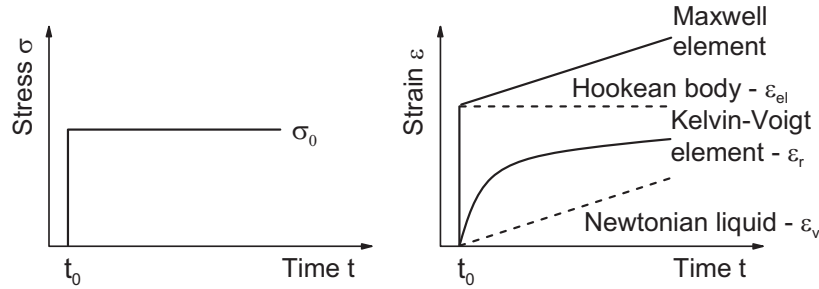
Figure 2.14: Strain response of simple rheological models to a stress σ_0 applied at time t_0. (Harris [60])

ε_v and ε_r increase as a function of time, the corresponding creep stiffness from Eq. (2.27) decreases. Though, the interpretation of the elastic modulus should always remain as a material inherent characteristic unlike the time dependent stiffness, which must be considered for design calculations [41].

$$\varepsilon(t) \quad = \quad \varepsilon_{el} + \varepsilon_v(t) + \varepsilon_r(t) \tag{2.29}$$

$$= \quad \sigma_0 \left[\frac{1}{E_1} + \frac{1}{\eta_1} t + \frac{1}{E_2} \left(1 - e^{-t/\tau} \right) \right] \tag{2.30}$$

$$\tau \quad = \quad \frac{\eta_2}{E_2} \tag{2.31}$$

For a constant stress σ_0 the total strain of the Burgers element can be cal-

culated from Eq. (2.29) or (2.30) where the retardation time τ is defined in Eq. (2.31). In polymers, small chain segments move a little at a time through the remaining network. Obstacles to the displacement of the molecules give the polymer a memory of its before deformation shape. In particular, after removal of the stress, the stretched and distorted chain segments between the entanglement of cross linking points tend to cause the creep deformation to recover with time. The exact approximation of the mechanical properties of polymers for other loads and times is thus limited due to the non-linear mechanical behaviour and the existence of a spectrum of retardation times [53, 61]. More realistic predictions of the mechanical behaviour can be obtained by an extension of the linear viscoelastic elements. This can be achieved by expressing the coefficients of the Burgers element as functions of stress and time or by more complex models with a higher number of Maxwell and Kelvin-Voigt elements. The time dependent creep strain of a serial connection of K Kelvin-Voigt elements can be expressed by the series in Eq. (2.32) which contains an arbitrary set of K retardation times τ_k [61].

$$\varepsilon(t) \;=\; \sigma_0 \sum_{k=1}^{K} J_n \left(1 - e^{-t/\tau_k}\right) \tag{2.32}$$

Nonlinear viscoelasticity

A fundamentally different approach combines the time dependent viscous and viscoelastic parts to the creep strain $\varepsilon_{cr}(\sigma, t)$. For isothermal creep Eq. (2.29) thus simplifies to Eq. (2.33), where the instantaneous strain $\varepsilon_0(\sigma_0)$ may contain non-elastic parts. To model the stress and time dependent creep strain ε_{cr}, Nutting [67] introduced a separation approach in product form (Eq. (2.34)) and suggested power law functions to describe both, the stress function $g(\sigma_0)$ and the time function $h(t)$. In literature, the power law time function is often attributed to Findley.

$$\varepsilon(\sigma_0, t) \;=\; \varepsilon_0(\sigma_0) + \varepsilon_{cr}(\sigma_0, t) \tag{2.33}$$

$$\varepsilon_{cr}(\sigma_0, t) \;=\; g(\sigma_0) \cdot h(t) \tag{2.34}$$

The stress dependence is often expressed by power law, exponential or hyperbolic sine functions [68, 69]. The power law stress function with the stress exponent m, e.g. Eq. (2.35), proves favourably with the handling of proportional loads $a = \sigma_2/\sigma_1$. The resulting strain ratio is independent of the stress level (Eq. (2.36)).

$$g(\sigma_0) \;\sim\; \sigma_0^m \tag{2.35}$$

$$\varepsilon_2/\varepsilon_1 \;\sim\; a^m = (\sigma_2/\sigma_1)^m \tag{2.36}$$

Regardless of their tendency to form singularities if applied in numerical methods, power law functions are suitable for nonlinear stress analysis because of their simple handling and their approximation capabilities being within the range of accuracy of measurements [70]. The useability of the power law time function was experimentally proven for numerous polymers and found to be applicable to long times and the time exponent n to be almost temperature independent [71].

The use of the power law approach for stress and time directs to Eq. (2.37), the stress and time dependent total strain according to Nutting [67] with the parameters K, m and n.

$$\varepsilon(\sigma_0, t) = \varepsilon_0(\sigma_0) + K\,\sigma_0^m\,t^n \tag{2.37}$$

2.4.3 Temperature dependent viscoelastic behaviour

Except for temperatures greater than $T_g - 15K$, polymers will not reach the thermodynamic equilibrium in a practical time frame [72]. Below the glass transition, volume and entropy generally change with time at an ever decreasing rate. This process of slow evolution towards an equilibrium state has been termed physical ageing [73] and found to influence the viscoelastic behaviour in a comparable magnitude to that of the temperature [72, 74]. The retardation and relaxation times can be ascribed to molecular movements, and thus shorten the more the higher the temperature of the material rises [75]. This temperature dependence follows as most thermally activated processes, approximately the Arrhenius equation

$$\tau = f(\sigma_0, H) \exp\left(-\frac{Q}{RT}\right) \tag{2.38}$$

where τ is the retardation time, Q the activation energy, R the gas constant, T the absolute temperature, and f a function depending on the applied stress and the material history H. In consequence of Eq. (2.38) the retardation time spectrum of higher temperatures is shifted to shorter times. As shown in Figure 2.15 on the example of polypropylene, the spectrum further changes its shape, because the individual maxima respond to different molecular movements and activation energies. The global maximum which is little affected from secondary retardation mechanisms, corresponds to the glass transition [57, 75].

One interpretation of the glass transition temperature T_g is that at and above T_g there is sufficient energy for molecular movement [46]. The vacant sites within the bulk of material are the free volume [41]. The increase in the temperature dependence of the free volume naturally causes an increase in
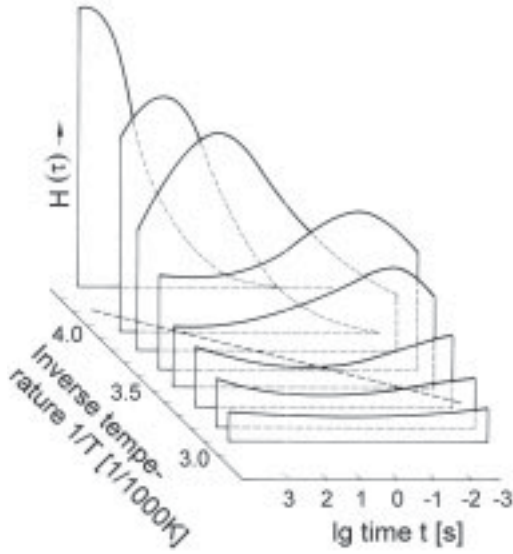
Figure 2.15: Spectrum of relaxation times of polypropylene (PP). (Retting [76])
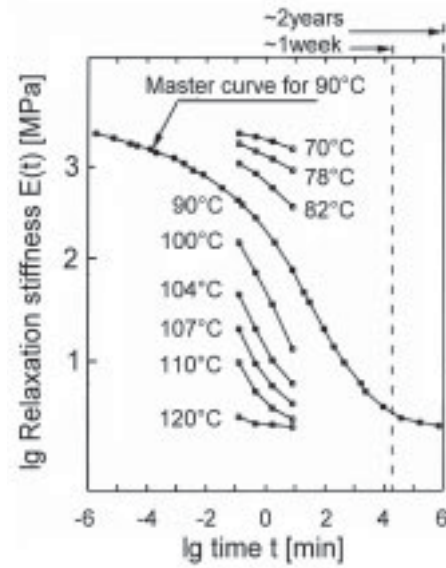
Figure 2.16: Time temperature superposition principle master curve for an EP resin. (Brinson [77])

the coefficient of thermal expansion, given for the neat epoxide resin 6376 in Table 4.1.

From the temperature dependence of the free volume Williams et al. [78] developed a semi-empirical relation known as the universal Williams, Landel and Ferry (WLF) equation (2.39). The WLF equation describes the time temperature superposition principle (TTSP), the shift of the global maximum of the spectrum of retardation times along a logarithmic time scale as a function of the temperature difference to T_g. The WLF equation was found to hold in the temperature range of $T_g < T < T_g + 100K$, but is sometimes used beyond these limits as long as time-temperature superposition still occurs. This would indicate that the same rate-controlling processes were still operative [46, 53]. The values of t_T and t_{T_0} in Eq. (2.39) are the times required to reach a specific creep stiffness E_{cr} at temperatures T and T_0 respectively. The test temperature is given by T and the time shift factor by a_T. Two reference temperatures T_0 are often used to normalise experimental data for which the constants C_1 and C_2 are given in Table 2.1.

$$\lg a_T = \lg \frac{t_T}{t_{T_0}} = \frac{C_1 (T - T_0)}{C_2 + T - T_0} \tag{2.39}$$

A graphical way to obtain long term stiffness or compliance properties from short term test data is through the use of a master curve produced with the TTSP. To obtain the master curve in this manner requires short term creep or relaxation tests be performed and the stiffness or compliance obtained

Table 2.1: Constants for the WLF equation [46, 53].

T_0	C_1 [1]	C_2 [K]
T_g	-17.44	51.6
$T_g + 50K$	-8.86	101.6

therefrom be shifted horizontally to obtain the stiffness or compliance over a time scale which may contain several decades [77]. An example is given in Figure 2.16.

Activation energy

The technological and scientific interest in creep usually concentrates to the steady-state behaviour which is characterised by a constant strain rate. Due to the relation between retardation time, viscosity and strain rate (Eq. (2.28)), the Arrhenius equation (2.38) is also applicable to viscosities and strain rates [46, 65].

$$\dot{\varepsilon} = f(\sigma_0, H) \exp\left(-\frac{Q}{RT}\right) \qquad (2.40)$$

For high temperature creep of ceramics Cannon and Langdon [79] suggested that the function f may contain an additional $G(\sigma_0/G)^m$ term where G is the shear modulus, and m the stress exponent. From Eq. (2.40) follows that the relation between $\ln \dot{\varepsilon}$ and $1/T$ is linear when the material history H does not contain an essential time dependence and Q is not dependent on T. For polymers the latter assumption is obviously valid at T_g, where one primary mechanism dominates and thus controls the creep rate. For numerous metals the validity of this linear relation was proven for homologous temperatures[12] above 0.4 [80, 81].

The knowledge of an array of creep curves offers different methods to determine the activation energy Q based on temperature compensated times or creep rates [80]. For steady state strain rate data from isothermal creep tests Eq. (2.41) can be solved by numerical or graphical means [81].

$$Q \sim -R \frac{\partial \ln \dot{\varepsilon}}{\partial (1/T)} = R T^2 \frac{\partial \ln \dot{\varepsilon}}{\partial T} \qquad (2.41)$$

Another method is based on the assumption that a sudden small temperature change during creep is not connected with a change in structure. If the indices 1 and 2 refer to variables before and after the temperature change,

---

[12] normalised to the melting temperature

one obtains Eq. (2.42) from Eq. (2.40) [81]. The value of Q is approximately constant below T_g and becomes a function of temperature and strain rate once the glass transition range is exceeded [65].

$$Q = R \frac{T_1 \, T_2}{T_1 - T_2} \, \ln \frac{\dot{\varepsilon}_1}{\dot{\varepsilon}_2} \qquad (2.42)$$

2.5 Material behaviour and fatigue life prediction under repeated loading

According to Sendeckyj [82], the development of rational life prediction methods for materials involves :

1. experimental observation of the damage accumulation process and the formulation of an appropriate damage metric;

2. formulation of a damage accumulation model in terms of the damage metric (and experimental characterisation of the model parameters using simple experiments);

3. development of a damage summation procedure based on the damage metric to predict life under general fatigue loading;

4. experimental verification of the life predictions.

Available methods to characterise the degradation characteristics under repeated loading and to predict fatigue lives include a) empirical, b) residual strength degradation, c) stiffness degradation, and d) damage and actual damage state based theories. The observed material degradation depends on the test conditions, i.e. load level, temperature, frequency, and environment as well as structural and processing parameters.

This section is organised in a way that after repeated loads are introduced, the enumerated methods a), b), and c) are presented. On that basis various cumulative fatigue theories are discussed, in particular, it is shown that the fatigue theories based on homogenised damage metrics can be used to predict fatigue life under multi-stage loading. Detailed descriptions of damage mechanics theories can be found by Talreja [83, 84], those of actual damage state based theories by Reifsnider et al. [85, 86, 87].

2.5.1   Definitions

Stress controlled cyclic loading

Cyclic loading is a special case of random loading, where the load history is in some fashion repetitive. Under these circumstances failure can occur at a stress level considerably lower than the yield or tensile strength for a quasi-static load [12]. The term fatigue is used because this type of failure normally occurs after a lengthy period of repeated stress or strain cycling [54]. This cyclic load may be axial, flexural, or torsional in nature and uniaxial or multiaxial. In the following, the focus is on cyclic uniaxial loading with a sinusoidal time dependence in sections.
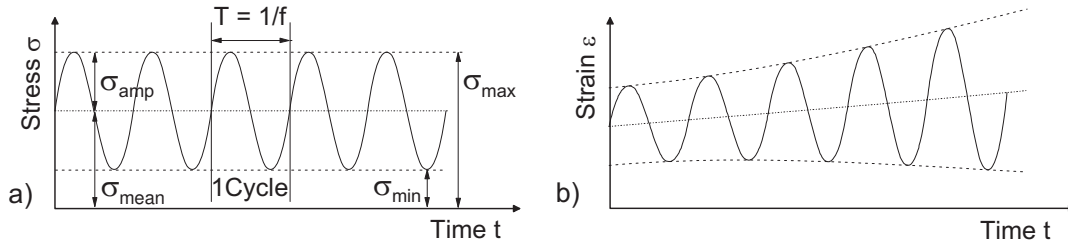
Figure 2.17: Stress controlled cyclic loading: a) constant maximum and minimum stress; b) Cyclic strain increase under repeated loading.

In a stress controlled constant amplitude fatigue (CAF) test, constant stress minima and maxima are set, as shown in Figure 2.17a. Also indicated and given in Eqs. (2.43), (2.44), and (2.45) are parameters used to characterise the stress cycles. The stress amplitude σ_{amp} oscillates about the mean stress σ_{mean} which defined as the mean value of the maximum and minimum stress in the cycle. The stress range $\Delta\sigma$ is twice the stress amplitude. The stress ratio R is the ratio of minimum and maximum stress. By convention, tensile stresses are positive and compressive stresses are negative. The test frequency f is equivalent to the inverse duration time of one cycle T.

$$\sigma_{mean} = \frac{\sigma_{max} + \sigma_{min}}{2} \tag{2.43}$$

$$\sigma_{amp} = \frac{\sigma_{max} - \sigma_{min}}{2} = \frac{\Delta\sigma}{2} \tag{2.44}$$

$$R = \frac{\sigma_{min}}{\sigma_{max}} \tag{2.45}$$

The corresponding values of strain change as the number of cycles n increases(Figure 2.17b). The load, time and cycle dependent change in the state of material and in the global and local state of stress is called damage

evolution. In the following it is described, how the damage process during cyclic loading affects the macroscopic long-term cyclic response, i.e. stiffness, strength, and fatigue life. For the impact of cyclic loading on microscopic damage events it is referred to section 2.6.

In strain controlled testing, similarly to stress controlled testing, maximum and minimum strain limits are maintained at constant values. A major difference between the two control modes is that the stress amplitudes reduce during strain controlled cycling, whereas larger strain amplitudes are experienced during stress controlled cycling [88].

Rate of stress application in fatigue

From Figure 2.17 can be seen that the rate of stress application (RSA) during stress controlled sinusoidal cyclic loading is not constant and the time dependent stress may be described by Eqs. (2.46) or (2.47).

$$\sigma(t) = \sigma_{mean} + \sigma_{amp}(t) \tag{2.46}$$
$$= \sigma_{mean} + \sigma_{amp} \cdot \sin(2\pi ft). \tag{2.47}$$

Equating the total differentials of Hooke's law (Eq. (2.26)) and Eq. (2.47) with respect to time leads to Eq. (2.48).

$$\frac{d\sigma}{dt} = \frac{\partial E}{\partial t}\varepsilon + \frac{\partial \varepsilon}{\partial t}E = 2\pi f \cdot \sigma_{amp} \cdot \cos(2\pi ft) \tag{2.48}$$

From the definition of the true strain

$$\varepsilon = \ln\left(\frac{l}{l_0}\right) \tag{2.49}$$

one obtains by differentiation with respect to time:

$$\frac{d\varepsilon}{dt} = \frac{1}{l}\frac{dl}{dt} \tag{2.50}$$

The boundary condition for the maximum RSA is $\cos(2\pi ft) = 1$. Assuming that the stiffness is currently constant, i.e. $dE/dt = 0$, the maximum RSA is given by

$$\left(\frac{d\sigma}{dt}\right)_{max} = \frac{1}{l}\frac{dl}{dt} \cdot E = 2\pi f \cdot \sigma_{amp} \tag{2.51}$$

which can in simplified form be expressed by Eq. (2.52). The values of l and E are a geometry parameter and a material property respectively, and f and σ_{amp} are load parameters.

$$\frac{dl}{dt} = \frac{l}{E} 2\pi f \cdot \sigma_{amp}. \tag{2.52}$$

Eq. (2.53) can be derived from Eq. (2.52) and the two scenarios of constant cross-head velocity $v = dl/dt$ and constant strain rate $\dot{\varepsilon} = d\varepsilon/dt$. From Eq. (2.53) can be concluded that with regard to quasi-static tests the requirement of a constant strain rate causes a linear increase of the cross-head velocity with the momentary length.

$$v = l\,\dot{\varepsilon} \tag{2.53}$$

A technical strain rate $\dot{\varepsilon}_0$ may be defined by Eq. (2.54), relating v to the initial length l_0.

$$\dot{\varepsilon}_0 = \frac{v}{l_0} \tag{2.54}$$

Hysteresis loops

Real oscillating systems dissipate shares of the input energy into lower energies which is called damping. Material damping appears in any volume element and is called internal damping Λ. It can be calculated from Eq. (2.55) as the ratio of loss work W_L to store work W_S which are defined as [89]:

Loss work: volume related energy consumption by irreversible energy dissipation during one cycle, e.g. by frictional heat, deformation, cracking, chemical reactions, or fracture.

Store work: volume related work, stored during the deformation of the material at the maximum strain within one cycle.

$$\Lambda = \frac{W_L}{W_S} \tag{2.55}$$

Plotting of the stress versus strain during cyclic loading results in hysteresis loops as schematically given in Figure 2.18. The enclosed area of the hysteresis loop can be determined by numerical integration and corresponds to the loss work of one cycle. Since the loss work is always dependent on the load level, the actual meaning of the store work lies in the normalisation of the loss work to receive a dimensionless characteristic value for comparison reasons. A mean curve which is defined as the mean value of the respective two stresses of each strain value is added to the hysteresis loop to determine the stored work of the deformation as the area between the mean curve and the abscissa.

Figure 2.19 shows possible variations of the hysteresis loops in stress controlled fatigue. The effects may govern the macroscopic degradation process
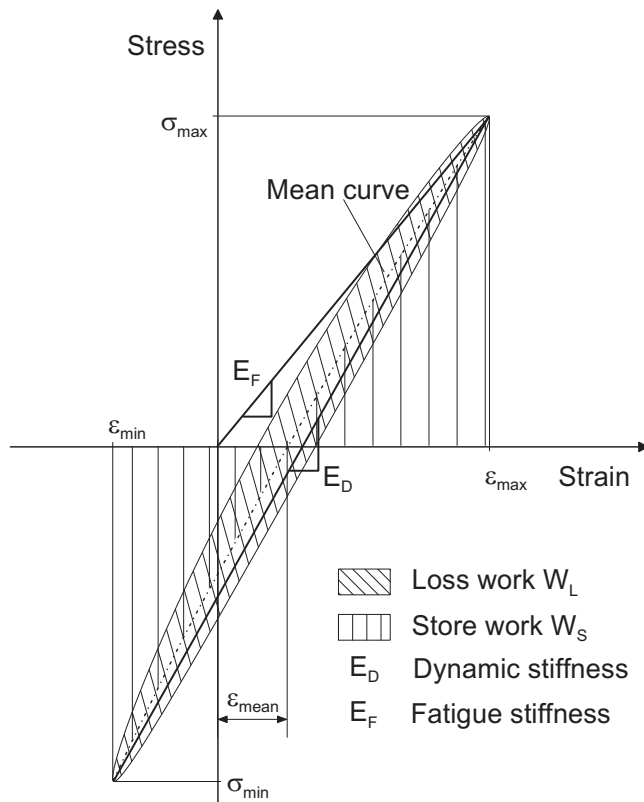
Figure 2.18: Identification of characteristic values from the hysteresis loop (Altstädt [89] and Hwang and Han [90]).
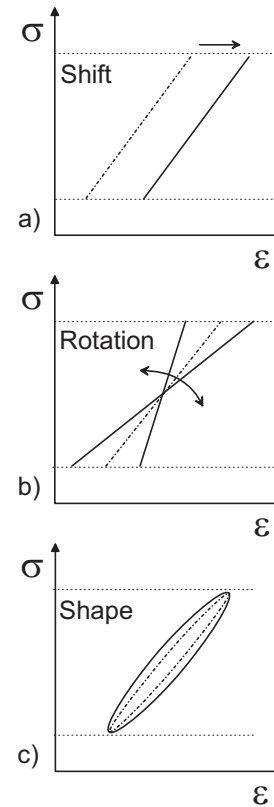
Figure 2.19: Possible variations of the hysteresis loops. (Petermann and Schulte [91])

alone or interact and affect each other. One alternative to minimise the test duration is to increase the test frequency where Eq. (2.56) is valid.

$$n = f \cdot t \tag{2.56}$$

The fatigue life is ideally independent of the test frequency. However, high frequencies may cause accelerated fatigue degradation due to increased internal damping. The related temperature rise may affect the material properties.

2.5.2 Macroscopic degradation characteristics

S-N curve

According to ASTM D 3479[13] and DIN 65586[14] a series of tests are commenced by subjecting a specimen to stress cycling at relatively large maximum stresses compared to the tensile strength whereas the number of cycles

---

[13] ASTM D 3479:1996 Standard test method for tension-tension fatigue of polymer matrix composite materials

[14] EN DIN 65586:1994 Luft- und Raumfahrt - Faserverstärkte Kunststoffe - Schwingfestigkeitsverhalten von Faserverbundwerkstoffen im Einstufenversuch

to failure is counted. This procedure is repeated on other specimens at progressively decreasing maximum stresses. To obtain an S-N curve, the data are plotted as amplitude or (relative) maximum stresses versus the logarithm of the number of cycles to failure or fatigue life N for each of the specimens. As Figure 2.20 indicates, the higher the magnitude of the stress, the smaller the number of cycles the material is capable to sustain before failure. If the
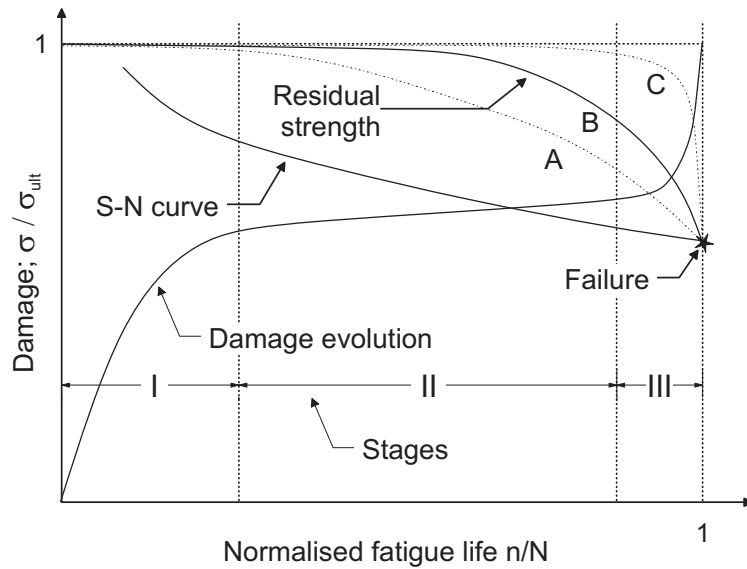
Figure 2.20: Schematic diagram of strength and damage variations during fatigue life. (Reifsnider et al. [92, 93])

S-N curve becomes horizontal at higher N values, the stress below which fatigue failure will not occur is called the fatigue or endurance limit. Many materials do not show an endurance limit [94, 95]. For these materials, the fatigue response is specified as fatigue strength, which is defined as the stress level at which failure will occur for some specified cycle number [54]. DIN 65586 defines the fatigue strength for FRPs at $2 \cdot 10^6$ cycles as the endurance limit, Schmiedel [95] suggests $7 \cdot 10^7$ cycles for polymers, however more fatigue failures are expected for higher cycle numbers.

Residual strength degradation

In the early 1970s, the first residual strength degradation theory was proposed by Halpin et al. [96], who used life prediction methods for metals as guidance. Failure was assumed to occur when the residual strength decreased to the maximum applied cyclic stress. Figure 2.20 displays three different kinds (A, B, and C) of residual strength degradation. The fatigue theory was completed by assuming that the static strength could be represented by a two-parameter Weibull distribution [97]. Because of objections to the dominant

crack assumption, this fatigue theory was recast by a number of authors [98, 99, 100] to account for the process of residual strength degradation. Detailed overviews are given in references [82] and [101]. Hahn and Kim introduced [102] and proved with co-authors [103, 104] an assumption on the relation between static strength and fatigue life; that a sample with a higher static strength has a longer fatigue life. The assumption was named *strength-life equal rank assumption* (SLERA) by Chou and Crowman [105]. As a result, the scatter in the fatigue data is attributed to scatter in the initial static strength of the material.

Residual strength degradation theories suffer from two major weaknesses. The first weakness is that they require extensive experimental characterisation of each laminate and material system. The second weakness is that the remaining life cannot be assessed by non-destructive testing (NDT) [82]. Moreover, the residual strength degradation is often not a sensitive measure of damage accumulation but changes rapidly close to fatigue failure (Trend C in Figure 2.20). This phenomenon of uncontrolled rupture [106] has been termed by Chou and Crowman [107] as *sudden death* behaviour. To overcome the weaknesses of residual strength degradation theories, attempts were made, involving the formulation of damage metrics that can be measured by NDT and exhibit greater changes throughout the fatigue life. One such damage metric is the stiffness change.

Longitudinal stiffness degradation

Two obvious definitions of stiffness are included in Figure 2.18, namely the dynamic stiffness E_{dyn} and the fatigue stiffness E_{fat}. The dynamic stiffness of the n-th cycle is the secant slope of the hysteresis loop between the minimum and maximum stress (Eq. (2.57)). The concept of fatigue stiffness was introduced by Hwang and Han [90, 108] as the slope between the the point of maximum stress on the hysteresis loop and the coordinate origin (Eq. (2.58)). For stress controlled CAF tests, the definitions of dynamic and fatigue stiffness can be ascribed to strain definitions without loss of information.

$$E_{dyn}(n) = \frac{\sigma_{max}(n) - \sigma_{min}(n)}{\varepsilon_{max}(n) - \varepsilon_{min}(n)} = \frac{\sigma_{max}(n) - \sigma_{min}(n)}{1/2 \cdot \varepsilon_{amp}(n)} \tag{2.57}$$

$$E_{fat}(n) = \frac{\sigma_{max}(n)}{\varepsilon_{max}(n)} = \frac{\sigma_{max}(n)}{\varepsilon_{mean}(n) + \varepsilon_{amp}(n)} \tag{2.58}$$

From Figure 2.19 and Eqs. (2.57) and (2.58) can be seen that if in stress controlled fatigue the hysteresis loops are only shifted (Figure 2.19a), the dynamic stiffness and the strain amplitude do not change, although a mean

strain increase occurs. Variations of the dynamic stiffness may cause a stiffening or complying of the laminate (Figure 2.19b), expressed by a change of strain amplitude but a constant mean strain. Due to internal damping, the hysteresis loops may modify in size and shape (Figure 2.19c).

The fatigue stiffness concept covers shift and rotation effects of the hysteresis loops. However, both effects are superimposed and cannot be distinguished. Hence, a separate study of mean strain and strain amplitude or dynamic stiffness is more reasonable [91].

To predict fatigue life by stiffness degradation methods, different macroscopic failure criteria can be established by comparison of the introduced cyclic stiffness values with quasi-static data. Figure 2.21 shows failure criteria via a) secant stiffness, b) resultant strain, and c) elastic modulus.
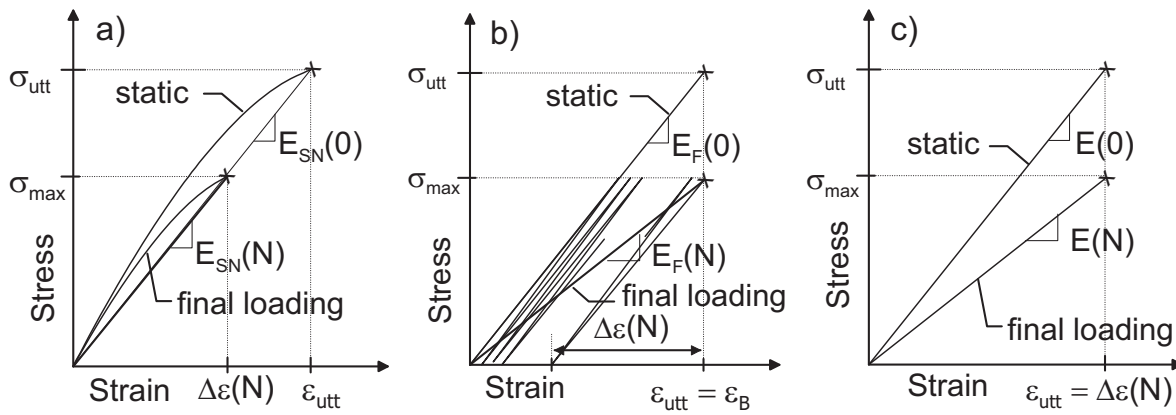
Figure 2.21: Schematic presentation of the a) secant stiffness, b) fatigue stiffness, and c) elastic modulus failure criterion. In a) and c) the lower tip of the stress-strain loops of final loading is translated to the origin. (Hwang and Han [90, 108])

The secant stiffness failure criterion states that failure occurs when the fatigue secant stiffness degrades to the static secant modulus, as proposed by Hahn and Kim [102] and schematically shown in Figure 2.21a.

The fatigue stiffness criterion defines failure when the fatigue resultant strain reaches the static ultimate strain, as suggested by Hwang and Han [90, 108] and schematically shown in Figure 2.21b.

The elastic stiffness failure criterion is another strain failure condition. It was introduced by Reifsnider et al. [93], experimentally verified by Poursartip et al. [109], and is shown in Figure 2.21c. Failure occurs when the fatigue strain under the final cycle equals the static ultimate strain.

2.5.3 Cumulative damage theories (CDTs)

Two basic approaches have been used to predict the life of materials subjected to two-stage and spectrum fatigue loading. The first approach consists of the formulation of a damage summation rule without recourse to experimental observation of the damage accumulation process and the use of a damage summation rule to predict life under general fatigue loading. The other approach consists of the formulation of damage metric that in some manner reflects the observed damage accumulation process and the subsequent cycle by cycle summation of the damage metric to predict fatigue life [82].

CDTs without experimental recourse

Fatigue damage of a material depends on the applied stress level σ_a, the number of fatigue cycles n, frequency f, temperature T, moisture content, geometry of the specimen, et cetera. The damage can be written as a functional form [110].

$$D = F(n, \sigma_a, f, T...) \tag{2.59}$$

As a first approach, constant frequency and environmental conditions are assumed. In addition, the effect of temperature rise during the fatigue test is ignored. Then, Eq. (2.59) is reduced to Eq. (2.60).

$$D = F(n, \sigma_a) \tag{2.60}$$

It is also assumed that the function $F(n, \sigma_a)$ could be expressed as either of Eqs. (2.61) or (2.62).

$$D = F(n, \sigma_a) = f(n/N) \tag{2.61}$$
$$D = F(n, \sigma_a) = f(n)\, g(\sigma_a) \tag{2.62}$$

Eq. (2.61) seems a function of n alone explicitly but the equation has a stress effect because of N which is related to the applied stress. The damage models which do not have stress dependent constants are classified as stress independent damage models. For CAF loading, the damage function should satisfy the following initial and final boundary conditions.

$$D = 0 \quad \text{when} \quad n = 0 \tag{2.63}$$
$$D = 1 \quad \text{when} \quad n = N \tag{2.64}$$

The damage function is also assumed to be a monotonically increasing function with the number of cycles. With this assumption and Eq. (2.61), the damage function has a trend A, B, or C in Figure 2.22. The trend can be determined by the first derivative of D, dD/dn (damage rate), or the second

derivative, d^2D/dn^2. The remaining life of two-stage fatigue loading can be predicted as described below and is illustrated in Figure 2.23.

1. Find n_{12}, the cycle at the stress σ_2, which has an equivalent damage under the stress σ_1 and cycle n_1, by equating

$$\Delta D_1 \;=\; \Delta D_{12} \qquad\qquad \text{or} \qquad\qquad (2.65)$$
$$f(n_1/N_1) \;=\; f(n_{12}/N_2). \qquad\qquad\qquad (2.66)$$

2. Then, the residual fatigue life becomes

$$n_{res} \;=\; N_2 - n_{12}. \qquad\qquad\qquad (2.67)$$
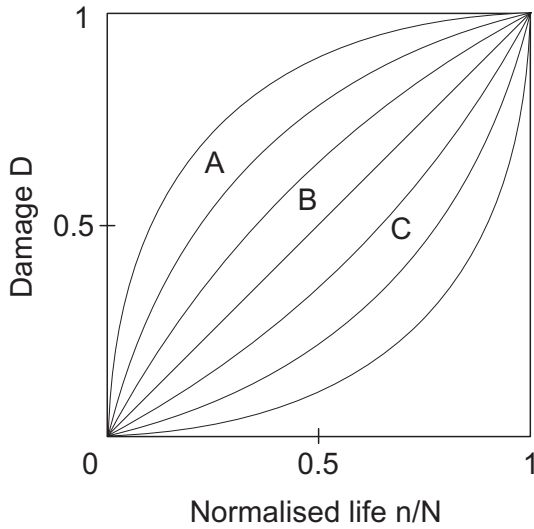
Figure 2.22: Damage as a function of cycle ratio and damage trends. (Hwang and Han [110])
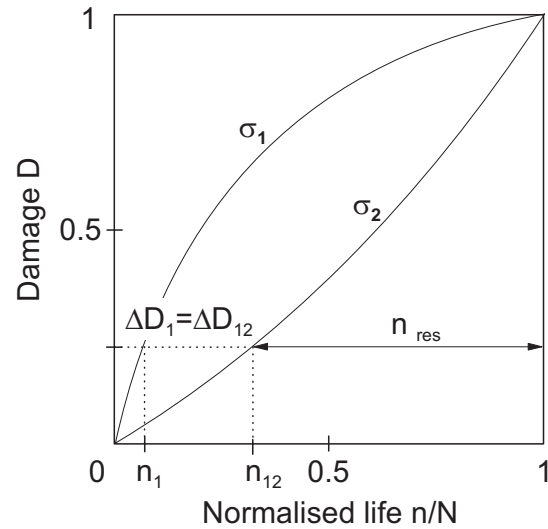
Figure 2.23: Fatigue life prediction for two-stage fatigue loading by stress independent damage models

In an analogous manner, multi-stage fatigue life prediction is performed. Finally, Eq. (2.68) can be written, where m is the number of load stages.

$$D = \sum_{i=1}^{m} \Delta D_i \;=\; f(n_1/N_1 + n_2/N_2 + ... + n_m/N_m) = 1 \qquad (2.68)$$

From the final condition of CAF loading in Eq. (2.64) one obtains Eq. (2.69).

$$D = \; f(N/N) = f(1) = 1 \qquad\qquad\qquad (2.69)$$

Palmgren-Miner rule The function f in Eqs. (2.68) and (2.69) is identical. Therefore, the arguments of f must be equal.

$$\sum_{i=1}^{m} n_i/N_i = 1 \tag{2.70}$$

Eq. (2.70) represents a stress independent, linear cumulative theory known as Palmgren-Miner rule (PM-rule) [13, 14], in which the work done per load stage is assumed to be proportional to the fractional life at the different cyclic stress levels and fatigue failure is assumed to occur when the sum reaches the critical value of unity. To obtain a linear cumulative damage theory, Eq. (2.70) may be modified by $D = n/N$.

$$D = \sum_{i=1}^{m} D_i = \sum_{i=1}^{m} n_i/N_i = 1 \tag{2.71}$$

Eq. (2.71) , also referred to as PM-rule, predicts the linear damage trend B in Figure 2.22. Because of its simplicity, the PM-rule is still widely used but fails to predict the effect of load history.

Marko-Starkey model To account for nonlinear damage accumulation, i.e. trends A and C in Figure 2.22, the PM-rule was later modified by introducing exponents to the fractional life terms. The modifications of Leve [111] and Owen and Howe [112] kept the critical damage sum of unity and the stress independence unchanged. Marco and Starkey [113] suggested a nonlinear, stress dependent cumulative damage model by the exponential relationship of Eq. (2.72) where the $C_i > 1$. They argued that the higher the applied stress, the smaller the exponent C_i. However, because C_i is by definition larger than unity, only the trend C in Figure 2.22 is represented.

$$D = \sum_{i=1}^{m} (n_i/N_i)^{C_i} \tag{2.72}$$

For a more exhaustive analysis of the available CDTs without experimental recourse it is referred to reviews of Sendeckyj [82] and Hwang and Han [108, 110].

CDTs with experimental recourse

Broutman and Sahu [98] proposed one of the earliest CDTs based on residual strength degradation for FRPs. They assumed that the instantaneous strength decreases linearly with the fractional life. More recent residual

strength models use more complex (e.g. damage state) strength functions [114, 115, 116, 117, 118] and statistically interpret the results of fatigue experiments [119, 120, 121, 122, 123]. Because the residual strength degradation rate cannot be experimentally determined in-situ during fatigue (see section 2.5.2), residual strength based CDTs are of implicit form. Via continuous monitoring of the stiffness change and relating it to the damage accumulation, CDTs based on stiffness degradation admit explicit formulations in terms of a well defined engineering property.

Schulte et al. A first approach to describe the damage accumulation in FRPs based on stiffness degradation was proposed by Wang and Chim [124] for random short fibre composites. They introduced a damage parameter

$$D = 1 - \frac{E_{dyn}(n)}{E_{dyn}(1)} \tag{2.73}$$

with $E_{dyn}(n)$ as the dynamic stiffness of the n-th cycle and $E_{dyn}(1)$ as the initial stiffness at the onset of fatigue cycling. To overcome the the fact that failure does not occur at $D = 1$ in Eq. (2.73), Schulte et al. [125] suggested a more appropriate expression for D which satisfies Eqs. (2.63) and (2.64).

$$D = \frac{E_{dyn}(1) - E_{dyn}(n)}{E_{dyn}(1) - E_{dyn}(n_C)} \tag{2.74}$$

The authors argued that in Eq. (2.74), $E_{dyn}(n_C)$ is the final ($C =$ critical) value of the dynamic stiffness at the end of the linear part of the stiffness reduction curve, rather than the value after the sudden drop of stiffness at the end of fatigue life.

  The definition of damage based on dynamic stiffness data is reasonable when the rotation of the hysteresis loops during fatigue (Figure 2.19b) dominates. In the case of dominant or additional ratcheting of the hysteresis loops (Figure 2.19a), damage definitions based on fatigue stiffness data are to prefer.

Hwang and Han Based on their concept of fatigue stiffness [90] given in Eq. (2.58) and Figures 2.18 and 2.21b, Hwang and Han proposed three different fatigue damage models [108, 110]. Eq. (2.75) gives the first model which uses an analogous definition to that of Schulte el al. [125].

$$D = \frac{E_{fat}(1) - E_{fat}(n)}{E_{fat}(1) - E_{fat}(N)} \tag{2.75}$$

For constant maximum stresses, Eq. (2.75) can be completely or in sections expressed by strains as done in Eq. (2.76) which represents the third model of Hwang and Han.

$$D = \frac{\varepsilon_{max}(n) - \varepsilon_{max}(1)}{\varepsilon_{max}(N) - \varepsilon_{max}(1)} \qquad (2.76)$$

The second model of Hwang and Han defines fatigue damage by the ratio of the resultant maximum strain at the n-th cycle and the maximum strain at failure.

$$D = \frac{\varepsilon_{max}(n)}{\varepsilon_{max}(N)} \qquad (2.77)$$

Eq. (2.77) predicts a damage value unequal to zero at $n = 1$, thus the initial condition of Eq. (2.63) is not met. With an increasing number of cycles the model follows the damage trend A in Figure 2.22 and satisfies the final condition of Eq. (2.64) at fatigue failure.

2.5.4 Effect of load sequences

Engineering structures are rarely subjected to a uniform constant load level in service. The load could fluctuate randomly according to a distribution, creating a load spectrum, or the load could vary in sequential steps, meaning a block amplitude loading, or a combination of both. Thus, the effect of load sequences on the fatigue behaviour of structural materials is of practical importance and has received considerable attention, for example in references [15, 126, 127]. In order to predict the load sequence effect on the fatigue life of composite materials, deterministic models [98] as well as statistical models [119, 120, 122, 128] have been proposed. The effect of load sequences was found to be contributed by two different physical phenomena:

the boundary effect, referred to as the difference in the residual strength level when fatigue fracture occurs, and

the memory effect of the material with respect to previously experienced load histories.

Possible types of memory effects may be due to a single cycle of proof load or successive accumulation of previously experienced loading histories, where the first type is negligible for fibre dominated FRPs [102, 103, 104].

When a specimen is subjected to low-high (L-H) and high-low (H-L) sequences, fatigue failure will take place at different levels of residual strength. Such a boundary effect is illustrated in Figure 2.24. Consequently, if the material memory effect is negligible, the L-H sequence is more damaging than the H-L sequence as far as fatigue life is concerned. This is because the fatigue process is terminated at a higher residual strength level under the L-H load sequence. Yang and Jones [120, 128] derived that

1. the Palmgren-Miner damage sum at fatigue failure is always smaller than or equal to unity for H-L load sequences, whereas it is always greater than or equal to unity for H-L load sequences,

2. the deviation of the Palmgren-Miner sum from unity increases as the difference in the stress level increases or as the degradation of the residual strength becomes stronger. Vice versa, the linear damage rule turns out to be effective for constant amplitude fatigue.
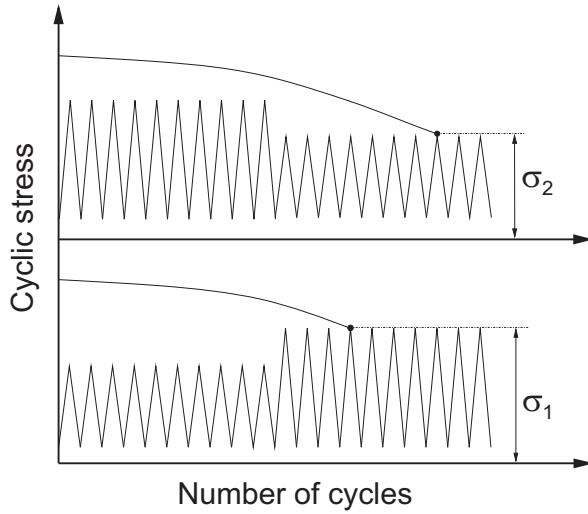
Figure 2.24: Illustration of the boundary effect. (Yang and Jones [128])
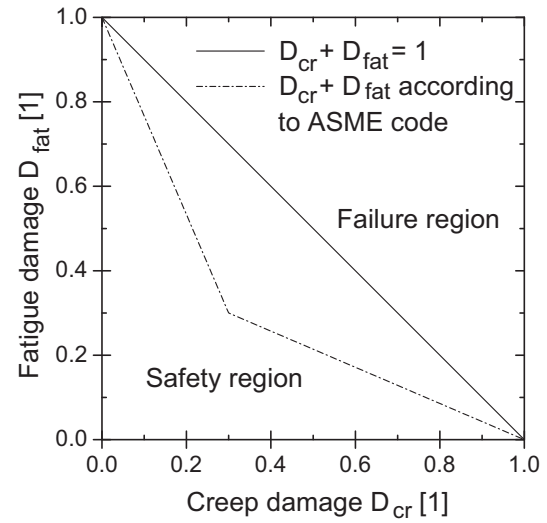
Figure 2.25: Creep-fatigue failure function in ASME code.

Both statements where experimentally proven, a respective literature survey can be found by Found and Quaresimin [127]. However, a more detrimental effect of the H-L sequence was reported by Lee and Jen [129] and Gamstedt and Sjögren [130].

2.5.5   Creep-fatigue interaction

The interaction of creep and fatigue comprises the concerted action of creep and fatigue mechanisms under repeated loading. Robinson [131] proposed a method that is similar the Palmgren-Miner rule to predict the life under creep loading. Eq. (2.78) describes the Robinson rule where t_i is the hold time at the i-th stress level, T_i the creep rupture time for the i-th stress level alone, and m the number of applied stress levels.

$$D_{cr} = \sum_{i=1}^{m} D_{cr,i} = \sum_{i=1}^{m} t_i/T_i = 1 \tag{2.78}$$

A popular creep-fatigue damage evaluation method [132] combines the rules of Palmgren-Miner and Robinson, i.e. Eqs. (2.71) and (2.78)

$$D = D_{cr} + D_{fat} = \sum_{i=1}^{m_{cr}} D_{cr,i} + \sum_{i=1}^{m_{fat}} D_{fat,i} = \sum_{i=1}^{m} t_i/T_i + \sum_{i=1}^{m} n_i/N_i \quad (2.79)$$

where creep-fatigue failure occurs when

$$D = D_{cr} + D_{fat} = 1. \tag{2.80}$$

This criterion ignores the interaction of creep and fatigue and assumes that the critical damage is equal to unity. The ASME Boiler and Pressure Vessel Code[15] suggests a bilinear symmetric function $D = f(D_{cr}, D_{fat})$ as shown in Figure 2.25.

2.6 Microscopic damage characterisation

The previous sections related the mechanical degradation of the material under quasi-static, constant and repeated loads to macroscopic properties such as strength and stiffness. This macroscopic degradation can be understood as an integral damage metric of microscopic damage events.

In contrast to metals, where fracture is known to result from the nucleation or initiation and subsequent growth of a single dominant crack, the failure process in fibre reinforced composite laminates is characterised by the initiation and progression of multiple failures of different modes such as *matrix cracks*, *interfacial debonding*, *fibre breaks*, and *delamination* between adjacent plies of a laminate. The types of failure occurring, their distribution, their onset of initiation as a result of the actual load level, and their possible interactions are dependent on many parameters, such as the properties of the constituents, the curing process, the fibre volume fraction, the stacking sequence, and the influence of temperature and environment under which the material is used. Consequently, there are many more potential failure modes for FRPs than for metallic materials [133, 134].

The application of an arbitrary stress state to a UD lamina may lead to failure by one or more basic failure types. Important types of failure are illustrated in Figure 2.26. Large tensile σ_{11t} and compressive σ_{11c} stresses parallel to the fibres lead to fibre and matrix failure, with the fracture path normal to the fibre direction.

---

[15]ASME Boiler and Pressure Vessel Code, Section III, Division 1, Subsection NH, Class 1: *Components in Elevated Temperature Service*
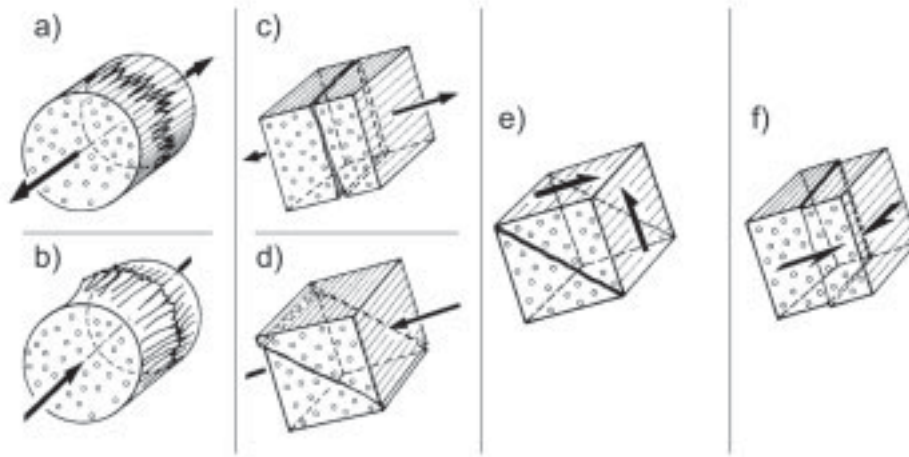
Figure 2.26: Schematic illustration of different types of failure as the result of exceeding strength values of a) axial tension, b) axial compression, c) transverse tension, d) transverse compression, e) transverse shear, and f) longitudinal shear. (Puck [135])

Figure 2.27 shows that in axial compression additional geometrical instabilities may occur by fibre micro-buckling and the formation of kink bands [136, 137, 138], followed by separation of specimen regions and subsequent global buckling [134, 139], as schematically shown in Figure 2.28. The strength is much lower in the transverse tension and the shear modes and the FRP fractures on surfaces parallel to the fibre direction when appropriate stresses σ_{22t}, σ_{22c}, τ_{12}, τ_{13}, and τ_{23} are applied (Figure 2.26c - f). In these cases, fracture may occur entirely within the matrix, at the fibre/matrix interface or within the fibre [36]. In-plane off-axis tensile loaded UD laminates exhibit a combination of the failure types to c) and f) from Figure 2.26 [106, 140]. The ratio of transverse normal stresses σ_{22} to in-plane shear stresses τ_{12} depends on the off-axis angle and the examined location on the fibre circumference [141, 142].

Real multidirectional laminates show a more complex microscopic damage behaviour which is exemplary shown for a cross-ply laminate in Figure 2.29. The distinctive types of failure from Figure 2.26 occur alone and in interaction with each other, e.g. the initiation of the longitudinal cracks in Figure 2.29 can be regarded as transverse tensile failure in the 0°-layer due stress concentrations and related Poisson constraints in front of the transverse crack front in the neighbouring 90°-layer. Similarly, the tensile fibre failure can be explained.

At the specimen edges and between the plies, preferably at the intersections of transverse and longitudinal cracks, additional delamination may appear, as schematically shown in Figure 2.30. Due to imperfections and the mis-
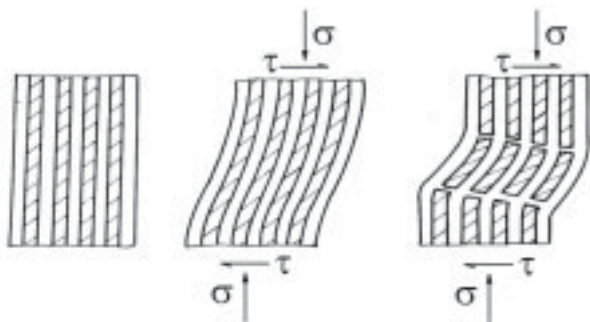
Figure 2.27: Schematic diagrams of shear rippling by in-phase fibre micro-buckling and formation of kink band. (Schulte et al. [134, 139])
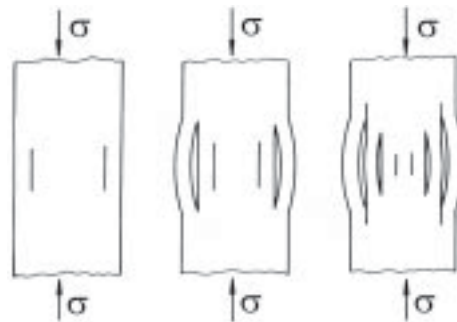
Figure 2.28: Schematic of separation of specimen regions during compressive loading. (Schulte et al. [134, 139])
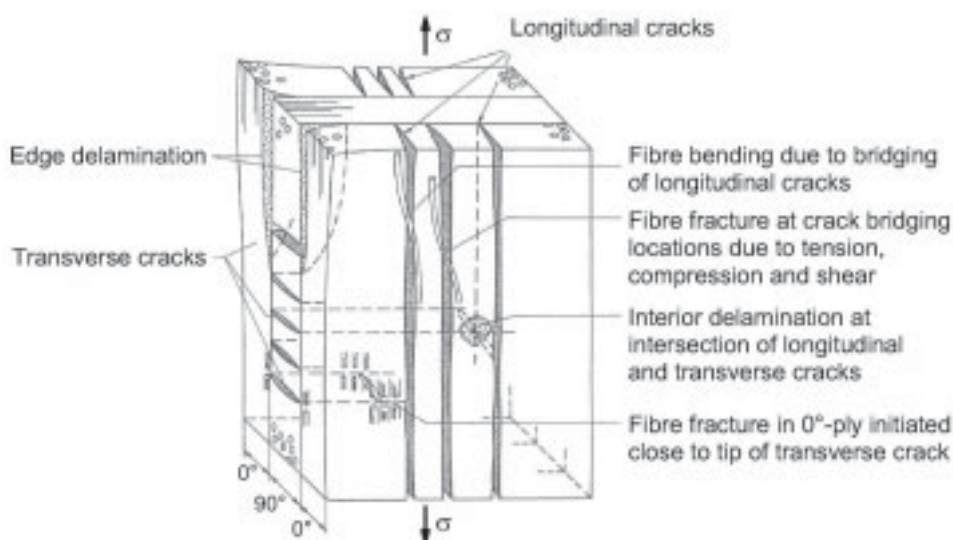
Figure 2.29: Summation of damage mechanisms observed in a cross-ply laminate. (Schulte [133])

alignment of fibres, further damage mechanisms like fibre bending and crack bridging are likely to occur [133].

The occurrence and the interaction of the different damage mechanisms during fracture of continuous FRPs are widely dependent on a variety of factors, which can be categorised according to Schulte and Stinchcomb [134] as:

The damage evolution under quasi-static and cyclic loading has distinctive differences. As the load under quasi-static loading conditions increases, the different damage mechanisms often alternate [17, 36, 134, 143].

Under cyclic loading, the types of damage mechanisms may occur simultaneously. Observations by Owen [144], Dharan [145], and Jessen and Plumtree [146] indicate that the predominant mechanism leading to failure would be

1. Geometrical factors:

   - stacking sequence,
   - sample size,
   - presence of notches.

3. Environmental factors:

   - temperature,
   - humidity,
   - influence of media.

2. Influence of constituents:

   - type of fibre,
   - type of matrix,
   - fibre volume fraction.

4. Type of loading:

   - in-plane/out of plane loading,
   - tensile/compressive loading,
   - quasi-static/cyclic loading.

effective in a limited range of the applied maximum stress or strain. Based on this assumption Talreja [147] suggested that the S-N curve would consist of different regions, each corresponding to the underlying damage mechanism. As shown in Figure 2.31, the horizontal band centred about the fibre failure strain corresponds to fibre rupture and the resulting interfacial debonding. The next region is shown as a sloping band between the lower bound of the fibre rupture scatter band and the horizontal line representing the endurance limit of the matrix. This region corresponds to matrix cracking and interfacial shear failure. These two mechanisms are taken together in one band as they may occur simultaneously, particularly towards the end of fatigue life.
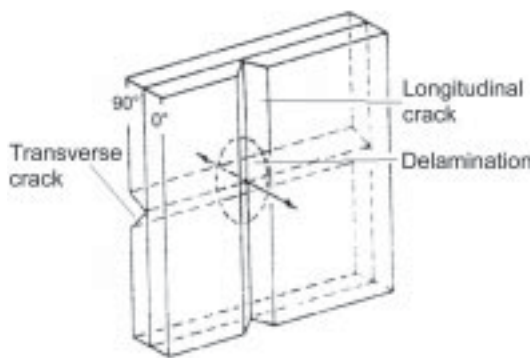
Figure 2.30: Influence of transverse and longitudinal cracks on interior delamination. (Jamison et al. [148])
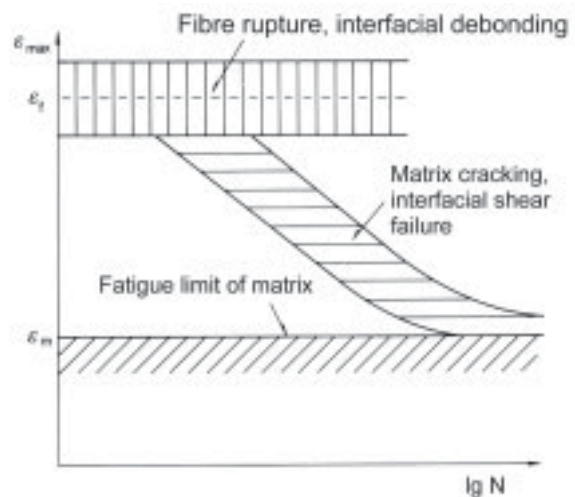
Figure 2.31: Fatigue life diagram for unidirectional laminates under cyclic tensile loading parallel to the fibres. (Talreja [147])

3

State of the Art - ±45°-Laminates

3.1 Geometry effects

3.1.1 Elastic properties from the classical lamination theory

For a symmetric and balanced laminate simple relations can be derived for the engineering properties as a function of laminate stiffness values. The general set of equations from the CLT (subsection 2.2.2) is given in reference [17]. For $[\pm 45]_{nS}$ laminates, exact and approximate expressions of the elastic properties are summarised in Table 3.1 as functions of the UD lamina properties.

Table 3.1: Exact and approximate formulas to calculate the engineering properties of $[\pm 45]_{nS}$ laminates. (Daniel and Ishai [17])

Property	Exact formula	Approximate formula
E_x	$\dfrac{4(Q_{11}+Q_{22}+2Q_{12})Q_{66}}{Q_{11}+Q_{22}+2Q_{12}+4Q_{66}}$	$\dfrac{4Q_{11}Q_{66}}{Q_{11}} = 4Q_{66} = 4G_{12}$
G_{xy}	$\dfrac{Q_{11}+Q_{22}-2Q_{12}}{4}$	$\dfrac{Q_{11}}{4} \approx \dfrac{E_{11}}{4}$
ν_{xy}	$\dfrac{Q_{11}+Q_{22}+2Q_{12}-4Q_{66}}{Q_{11}+Q_{22}+2Q_{12}+4Q_{66}}$	$\dfrac{Q_{11}-4Q_{66}}{Q_{11}+4Q_{66}} \approx \dfrac{E_{11}-4G_{12}}{E_{11}+4G_{12}}$

3.1.2 Free-edge effect

Stresses

The CLT is widely accepted for many aspects of the mechanical behaviour of laminates. Because it assumes infinite dimensions, it ignores the so called *free-edge effect*, the occurrence of interlaminar stresses in a boundary region along the free edges of laminated composites [149].
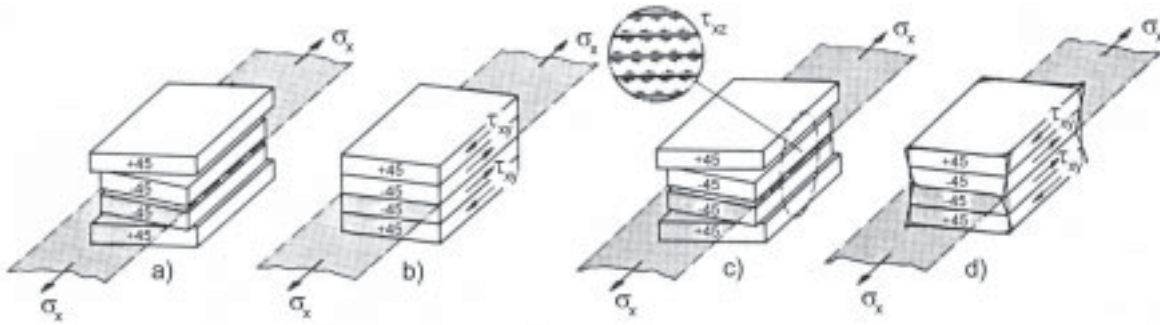
Figure 3.1: Schematic view of shear stresses associated with a tensile load on a $[\pm 45]_S$ laminate. (Prinz [150])

A schematic view of a tensile loaded $[\pm 45]_S$ laminate is shown in Figure 3.1. If an individual $+45°$- or $-45°$-layer is loaded, it shows an additional deformation beside the longitudinal strain, see Figure 3.1a. Despite the discontinuity of the material properties, the bonded adjacent plies have to deform in mutual agreement as shown in Figure 3.1b. Thus, opposite acting shear stresses τ_{xy} appear in the plies, which can be calculated from the CLT. Figure 3.1c shows that these shear stresses are reduced to zero at the edges by additional shear stresses τ_{xz} causing a 3D stress state. Thereby, as shown in Figure 3.1d, a warping of the cross-section appears at the laminate edges [150].

To make the stress distributions mathematically accessible, other analytical or numerical approaches have to be used. Applying finite element analysis (FEA), the distributions of the normal stress and the interlaminar shear stresses along the width and the thickness direction of a $[\pm 45]_S$ laminate have already been calculated by Pipes and Pagano [151], Puppo and Evensen [152], and Trappe et al. [153]. Figure 3.2 shows that significant interlaminar shear stresses τ_{xy} are required to allow shear transfer between the layers of the laminate. In addition, the interlaminar shear stress τ_{xz} was found to be restricted to an edge region approximately equal to the laminate thickness. Finally, Pipes and Pagano concluded that the singularity of τ_{xz} at the intersection of the layer interface and the free edge may be expected to cause delamination.
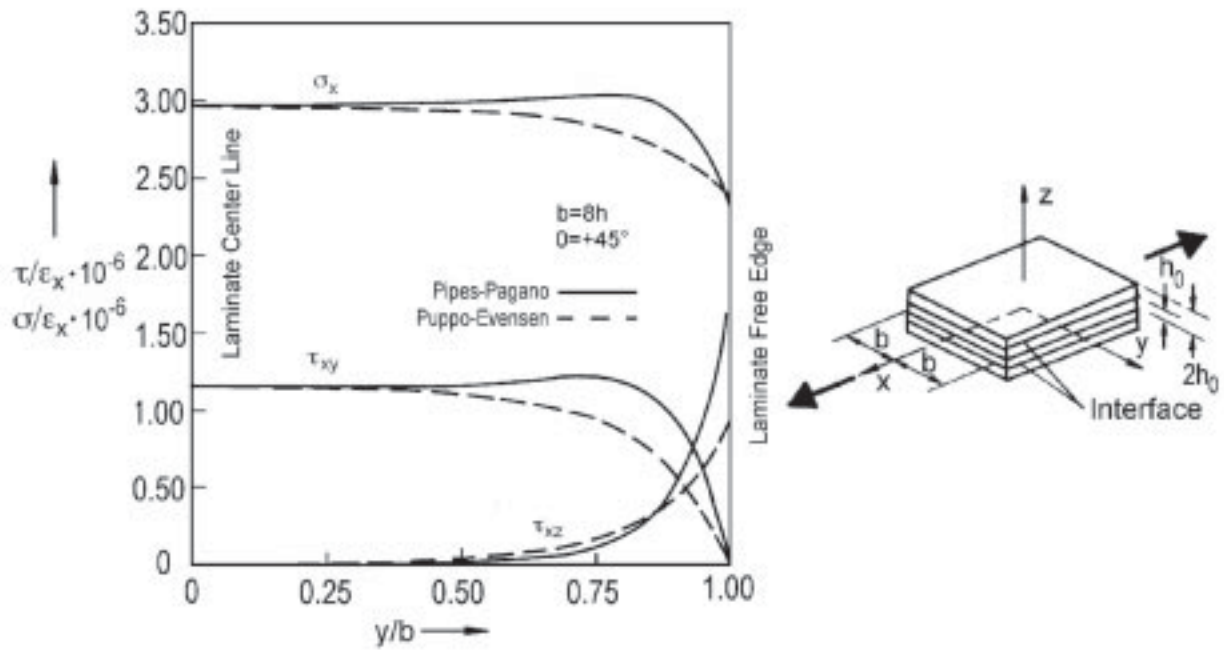
Figure 3.2: Comparison of stresses in the interface of an axially loaded rectangular $[\pm 45]_S$ laminate. (Pipes and Pagano [151])

Stiffness

The free edge effect can also result in a reduced axial stiffness of finite width laminate coupons. For $[\pm \theta]_S$ laminates, an analytical solution of the stiffness as a function of specimen width to thickness ratio w/t was given by Becker and Kress [149]. A comparison of their closed-form analytical and numerical FE-predictions is given in Figure 3.3 for a $[\pm 45]_S$ CFRP laminate. The authors stated very good agreement between analytical and numerical predictions for $w/t > 2$ which will do for practical applications. The reduction of the effective stiffness deceases from 8% at $w/t = 2$ to 2% at $w/t = 5$ and converges to zero as the w/t ratio further increases.

Frame tests

Han and Piggott [155] investigated the strength of $[\pm 45]_{nS}$ carbon/epoxide (HTA/6376) laminates in frame tests to avoid the difficulty of edge effects. The sample sizes were $60mm$ x $60mm$, with $22.5mm$ x $22.5mm$ between the grips. The lay-ups, i.e. $n = 1, 2, 3$, differed by factors of 2 and 3 in thickness. However, no geometry effect on the mean tensile strength of about $230MPa$ for all configurations was found.
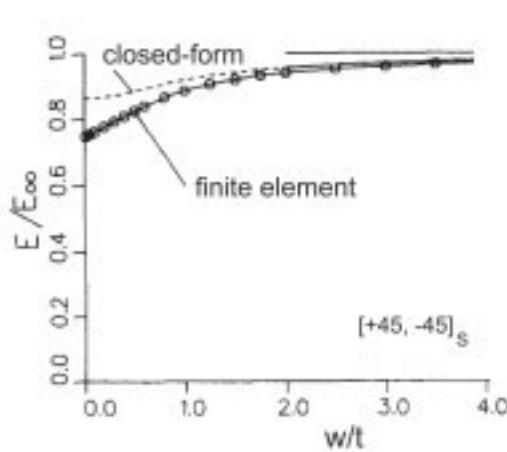
Figure 3.3: Effective stiffness as a function of width to thickness ratio. (Becker and Kress [149])
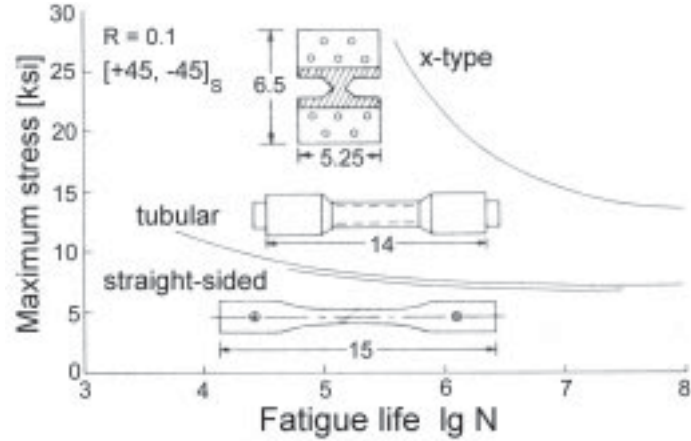
Figure 3.4: Effect of specimen configuration on the axial fatigue behaviour of 1002 E-glass/epoxide. (Salkind [154])

Straight-sided vs. tubular geometry

Comparative studies on straight-sided and tubular specimens allow to assess the free-edge effect experimentally. For CFRP, Trappe et al. [156] compared two rectangular configurations, i.e. A and B ($w/t = 8.3$ and 16.7) with one tubular geometry, i.e. C ($d/t = 16.4$) in quasi-static tension and reverse ($R = -1$) fatigue loading. Stiffness calculations based on the CLT were 5% higher than the measured values for configuration A. The calculated values for configurations B and C were almost identical and in both cases 3% higher than the experimental data. In strain controlled fatigue with $\varepsilon_{max} = 4 \cdot 10^{-3}$, all configurations displayed an identical normalised stiffness degradation to 90% of the initial value during five decades of cycles. For higher cycle numbers, the stiffness degradation of the rectangular configurations A and B was 10% higher than the one of the tubular configuration. The authors explained the behaviour by the strain controlled testing where the material can elude the external load.

Figure 3.4 compares[1] the axial tension-tension fatigue data of GFRP for three different specimen configurations. The straight-sided specimen is flat, and each fibre terminates at the edge, thus creating higher interlaminar shear stresses. The x-type specimen has all fibres continuous from grip to grip, thus precluding interlaminar shear stresses at the edge. The latter type has the disadvantage of having a vanishingly small gauge length, which is not representative of the types of loading experienced in most structures. The resultant

---

[1] The diagram contains dimensions and loads in imperial units. The conversion factors to metric units are $1in = 25.4mm$ and $1ksi = 6.90MPa$.

data are too optimistic to be used for design. The tubular specimen has a uniformly loaded gauge section and no free edges. The difference between the straight-sided and tubular geometry is 5%, but expected to be higher for CFRP because the interlaminar shear stresses are higher for higher modulus materials [154].

Straight-sided geometry

Khatibzadeh and Piggott [157] investigated the effect of specimen width on the tensile mechanical properties of S-glass/epoxy (S2/7376) and carbon/epoxy (T650/6376) $[\pm 45]_S$ prepreg laminates at a constant technical strain rate of $\dot{\varepsilon}_0 = 333 \cdot 10^{-6} s^{-1}$. The specimen widths were 3, 10, 30, and $100mm$, the gauge length $l_0 = 20mm$ for all cases. Thus, the two larger widths were of x-type configuration with an increasing content of continuous fibres between the grips. The tensile strength increased steadily with increasing width. The stiffness was approximately constant up to a width of $30mm$, and then increased.

Kujawski [158] examined the effect of specimen width on the tensile strength and fatigue behaviour of $1.7mm$ thick 1003 E-glass/epoxy coupons. He conducted monotonic ($1.15MPa/s$) and fatigue ($R = 0.05$, $f = 2Hz$) tensile tests on $[\pm\theta]_{2S}$ laminates with six fibre angle orientations (ranging from ± 25 to $\pm 75°$) and five different widths (4.5, 7.6, 10.5, 16.0, and $20.5mm$). For all angles, tensile strength and fatigue life increased and approached a steady value as the specimen width increased. The results for $\pm 45°$ are shown in Figures 3.5 and 3.6.

The stiffness degradation of the above introduced geometry configurations A and B from Trappe et al. [156] was independent of the specimen width. The respective w/t ratios correspond to the region of constant fatigue life in Figure 3.6.

3.2 Material degradation behaviour

3.2.1 Microscopic damage evolution

The literature available on the damage evolution of $\pm 45°$-laminates is limited, mainly due to the fact that the deformation of this type of laminate is matrix dominated and thus subject to high plastic strains and particularly to creep and fatigue interactions. Such a behaviour is undesired for most structural applications, thus $\pm 45°$-layers are often used in combination with $0°$-plies [159].
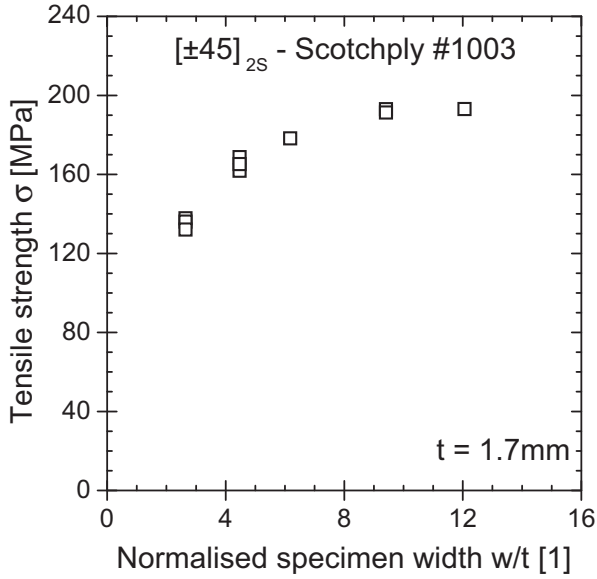
Figure 3.5: Ultimate tensile strength vs. normalised specimen width. (Kujawski [158])
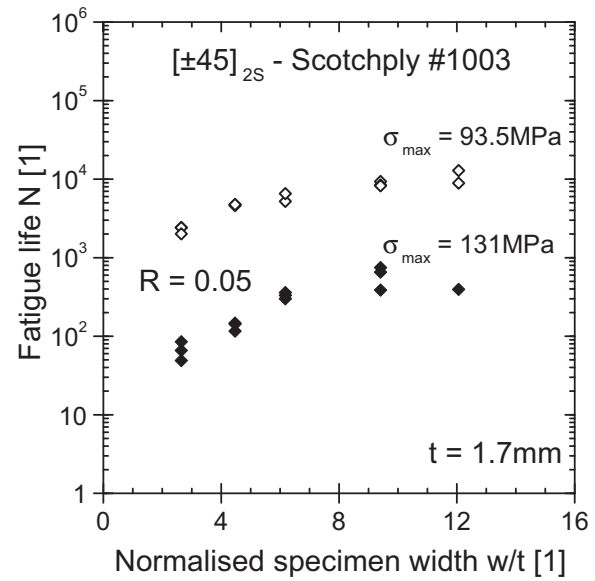
Figure 3.6: Fatigue life vs. norm. specimen width for different cyclic stresses. (Kujawski [158])

Wevers [30] described the damage evolution as firstly, the formation of matrix cracks running parallel with the fibres and secondly, the development of delamination. The formation of matrix cracks is ascribed to interlaminar shear stresses as the result of constraints between plies with different fibre orientation angles. The interlaminar shear stresses encourage the matrix cracks in the plies to propagate to matrix rich regions between the plies and to form delamination. This description of damage evolution in $\pm 45°$-laminates indicates that the static and fatigue tensile damage evolution can be called a matrix mode because the types of damage, i.e. matrix cracking and delamination, are not only governed by the matrix properties but are also located in the matrix.

3.2.2   Stress-strain behaviour

A typical stress-strain curve for a carbon/epoxide (T300/914) $[\pm 45]_{2S}$ laminate and the comparison between a monotonic and a stepwise tensile test is given in Figure 3.7. It can be seen that the unloading cycles do not modify the stress-strain curve. The laminate exhibits large (permanent) strains and a degradation of stiffness prior to complete failure.

Gates [160] investigated the influence of strain rate and its variation during a tensile test on the stress-strain behaviour of $\pm 45_{2S}$ C/BMI (IM7/5260) at elevated temperatures. The experiments at $125°C$ were limited to strains of $10 \cdot 10^{-3}$, such that no yielding occurred. Within this scope, he stated that for
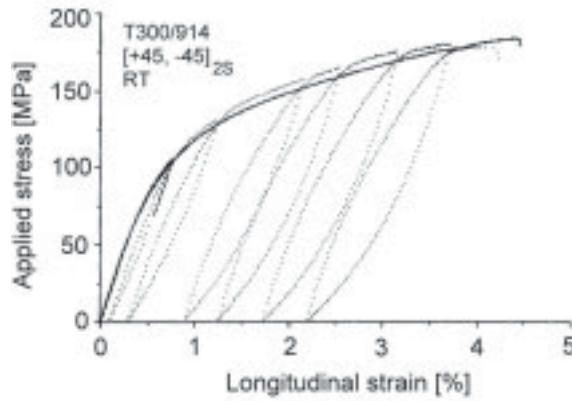
Figure 3.7: Comparison of monotonic and stepwise tensile test. (according Lafarie-Frenot and Touchard [31])
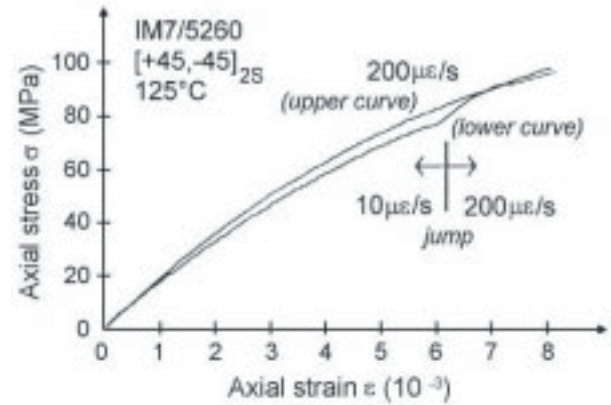
Figure 3.8: Comparison of constant rate and jump rate loading. (Gates [160])

a given strain level, the stress increases as the applied strain rate increases. Figure 3.8 shows a constant rate test ($\varepsilon_0 = 200 \cdot 10^{-6}/s$) and a jump rate test (from 10 to $200 \cdot 10^{-6}/s$). After the jump from 10 to $200 \cdot 10^{-6}/s$ the stress-strain curve coincides with the constant $200 \cdot 10^{-6}/s$ test. Thus, no dependence of stress level on the strain rate history can be seen.

3.2.3 Fibre rotation

Macroscopic expression of the microscopic damage development may be the competing effects of increasing stiffness due to fibre rotation and decreasing stiffness due to the shearing of the matrix without fibre rotation. The effects are schematically shown in Figure 3.9.
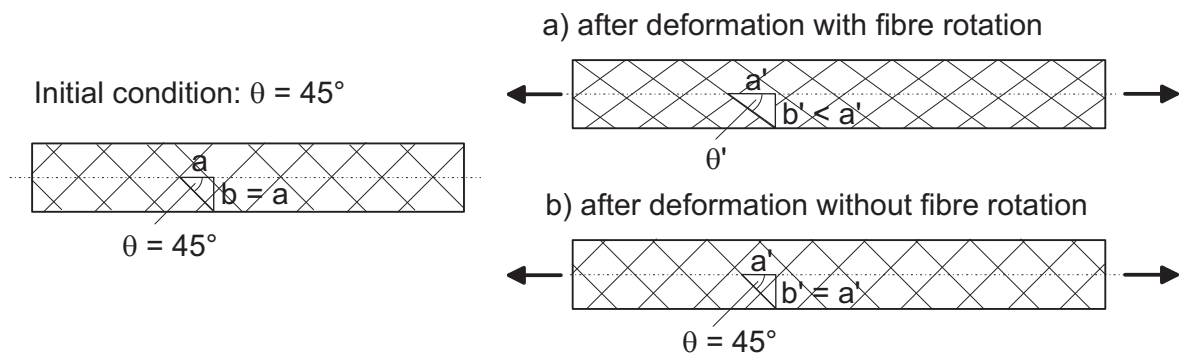
Figure 3.9: Schematic view of competing effects due to deformation.

Herakovich et al. [161] showed that both of these competing effects are less pronounced for small strains but significant for the large strain response. They investigated $[\pm 45]_{3S}$ thermoplastic carbon/polyimide lami-

nates (IM7/K3B) under stepwise tensile tests. As the applied strain increased, large fibre rotations were observed.

For an incremental analysis of $[\pm\theta]_{nS}$ laminates, Sun and Zhu [162] proposed Eq. (3.1) to calculate the fibre orientation change. For $\theta = 45°$ and different Poisson's ratios, the rotated fibre angle is visualised in Figure 3.10. Based on stress-strain calculations and experiments on thermoplastic carbon/PEEK laminates (AS4/PEEK) where θ ranged between 20 and 60°, they concluded that the change in the fibre orientation has a very limited effect for small strain levels.

$$\tan\theta' = \frac{b'}{a'} = \frac{b(1 + \varepsilon_{yy})}{a(1 + \varepsilon_{xx})} = \frac{1 + \varepsilon_{yy}}{1 + \varepsilon_{xx}}\tan\theta \qquad (3.1)$$
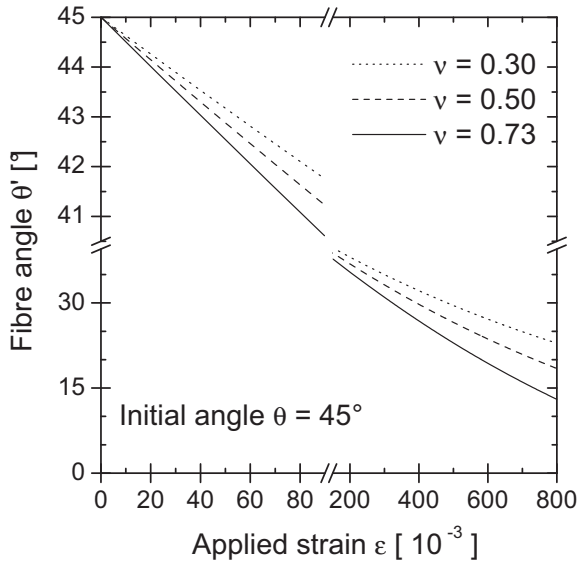
Figure 3.10: From Eq. (3.1) calculated fibre rotations for $\pm 45°$-laminates. (Sun and Zhu [162])
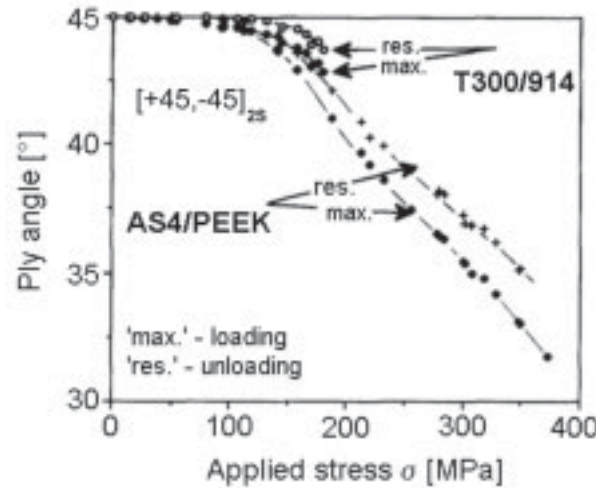
Figure 3.11: Fibre orientation effect a during stepwise tensile test. (Lafarie-Frenot and Touchard [31])

Lafarie-Frenot and Touchard [31] conducted a comparative study of $[\pm 45]_{2S}$ CFRP laminates ($l : l_0 : w = 230mm : 110mm : 20mm$ and $\dot{\varepsilon}_0 = 152 \cdot 10^{-6}s^{-1}$) with thermoset (T300/914) and thermoplastic (AS4/PEEK) matrix. As reported by Herakovich et al. [161], the fibre rotation was particularly marked for the thermoplastic matrix, where the ultimate fibre orientation was about 32°. A slight decrease of θ to 43° was observed in the carbon/epoxy specimens when the applied stress increased (Figure 3.11). As by Herakovich et al. [161], the onset of fibre rotation was approximately $100MPa$ for both materials. A similar fibre rotation behaviour for thermoplastic laminates was reported by Komai et al. [163] for fatigue loadings.

3.2.4   Matrix cracking

Quasi-static tension

On X-radiographs taken during tensile tests, Lafarie-Frenot and Touchard [31], besides the fibre rotation effect, also investigated the development of matrix cracks. For both materials (subsection 3.2.3), only very scarce and short matrix cracks were observed when the applied stress was less than $150 MPa$. The authors observed that cracks were more evenly distributed in the thermoplastic material associated with very large permanent deformations. A relatively localised fracture was observed in the thermoset material which also showed some delamination. The main difference consisted in the crack shape; relatively straight in the thermoset laminate and very curved in the thermoplastic material, which indicates that significant shear deformations are present at the ply interfaces. Figure 3.12 presents the crack density

a)   b)
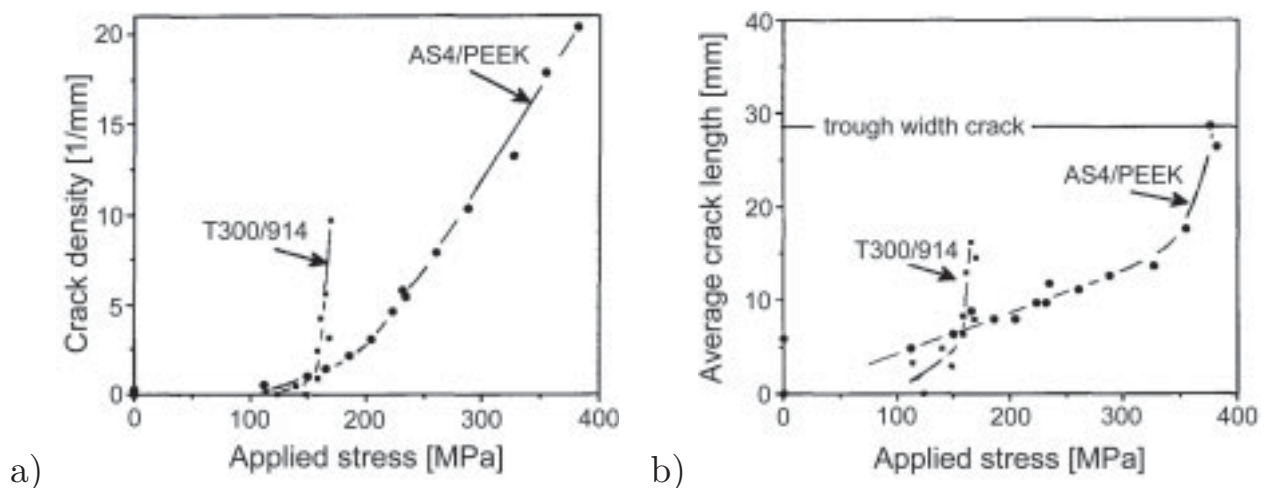
Figure 3.12: Comparison of a) crack density and b) crack length for $[\pm45]_{2S}$ laminates from T300/914 and AS4/PEEK. (Lafarie-Frenot and Touchard [31])

and the average crack length versus the applied stress. No or a few cracks are present for applied stresses below about $150 MPa$. As the stress further increases, the crack density increases until failure. The increase is sudden in the thermoset laminate, whereas the final crack density is higher in the thermoplastic material. The mean crack length increases regularly, but does not reach the opposite side of the specimen in T300/914. In AS4/PEEK laminates, the matrix cracks cross the ply width only close to failure. The authors concluded that in $\pm45°$-laminates tested in tension, matrix cracking is much delayed and becomes important only close to failure.

Tension-tension fatigue

Sturgeon [159] investigated the fatigue cracking of rectangular $[\pm 45]_{2S}$ specimens ($l : l_0 : w : t = 230mm : 140mm : 25mm : 2mm$) of carbon/epoxide (HTS/DX210). After cycling with $R = 0$ for a proportion of the life time, the samples were sectioned, polished and photographed with light microscopy. Those samples taken for $n/N = 5$, 10, and 30% showed no signs of cracking. After 80% of the fatigue life a number of intralaminar cracks appeared, becoming more numerous with further cycling. The section taken close to failure showed extensive delamination in addition to many intralaminar cracks.

The author concluded that once delamination have formed, the plies move relative to one another in a scissoring action allowing correspondingly larger deformations. The combination of increased cracking coupled with scissoring explains the large displacements observed just before separation at failure.

3.3   Creep behaviour

The use of structural components made from FRPs subjected to severe environmental conditions calls for a better knowledge of the long-term properties of this kind of material. Several studies emphasised the ability of $\pm 45°$-laminates to withstand creep loading, especially the effect of hold time during creep and recovery, nonlinearity, and elevated temperature. The experimental results of short-term tests were often combined with time and damage dependent constitutive equations to predict the long-term mechanical behaviour.

Sturgeon [159] conducted one of the earliest but extensive (experiment durations up to 7 months) studies on tensile creep and intermittent creep loading at different temperatures and stresses of 31, 47 and 62% of the UTS of 161MPa. The room temperature data gave evidence to the following statements:

1. creep follows the 'classical' curve (Figure 2.10) with initial rapid primary creep those rate decreases with time followed by secondary creep with almost constant creep rate,

2. proportionately less instantaneous strain is recovered on the first unloading from high stress levels compared with lower stresses,

3. large permanent creep deformations occur after continuous and repeated loading.

An ambient temperature rise of $30K$ produced a significant increase of the overall creep strain but causes no alteration in the general shape of the creep

curve. A plateau of nearly constant creep rate was still established and no evidence of any creep rupture or tertiary creep behaviour was detected for less than $1500h$.

The effect of temperature on the tensile creep behaviour was also investigated by Katouzian and Horoschenkoff [52, 164, 165]. They studied the nonlinear viscoelastic creep response of carbon fibre (T800) reinforced PEEK and epoxide (6376) resin at different temperatures. Series of $10h$ isothermal creep tests were conducted on $[\pm45]_{4S}$ laminates at different stress levels. For comparison the same series of experiments was conducted on the neat resins. Figure 3.13 for the neat epoxide resin and Figure 3.14 for the carbon/epoxide
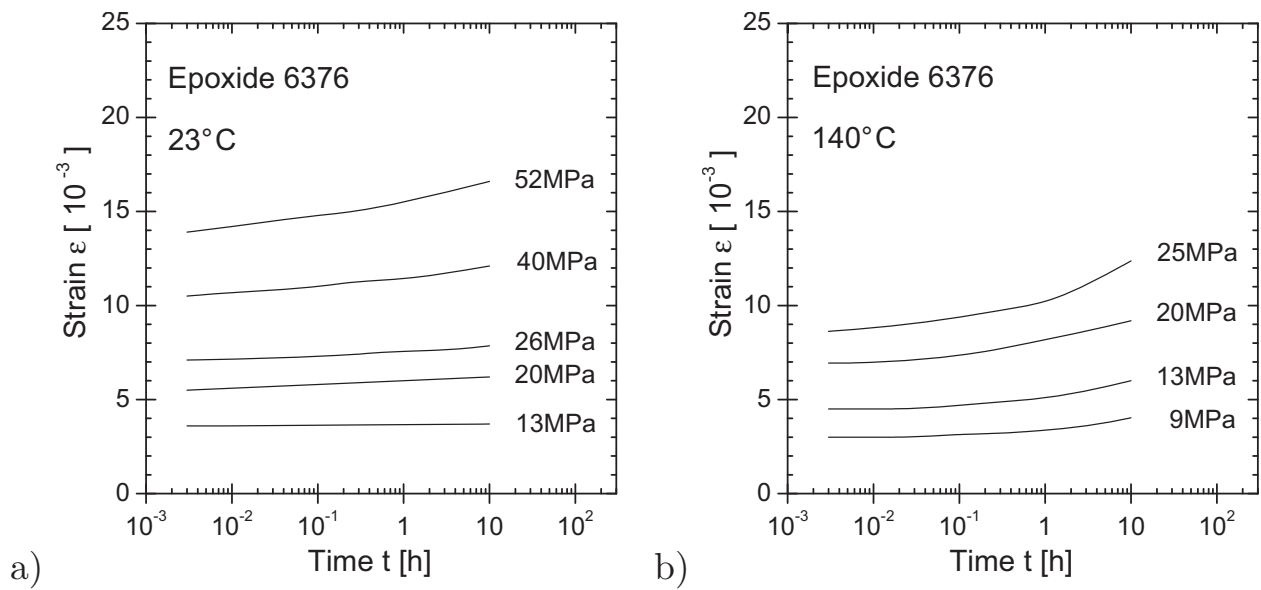
Figure 3.13: Creep curves of the neat epoxide resin 6376 at a) $23°C$ and b) $140°C$. (Katouzian et al. [165])

laminate show that the stress range, in which linear viscoelastic behaviour is observed, is shifted to lower values with increasing temperature.

For all resins and laminates investigated, the influence of temperature on the nonlinear instantaneous response was significantly less than on the nonlinear transient response. For the temperature range investigated, the authors stated that the instantaneous response is linear and temperature independent over the range of stress levels relevant in practical applications. The influence of temperature on the time dependent response was found to be nonlinear.

A similar study on the accelerated characterisation of the creep response due to the effect of temperature and stress was performed by Ma et al. [166] on $[\pm45]_{4S}$ carbon/PEEK (AS-4/PEEK) laminates. The creep strain data for different stresses and times were found to look qualitatively as shown in Figure 2.11. Using a power law time function and a truth table for the stresses, good agreement between prediction and experiment was achieved.
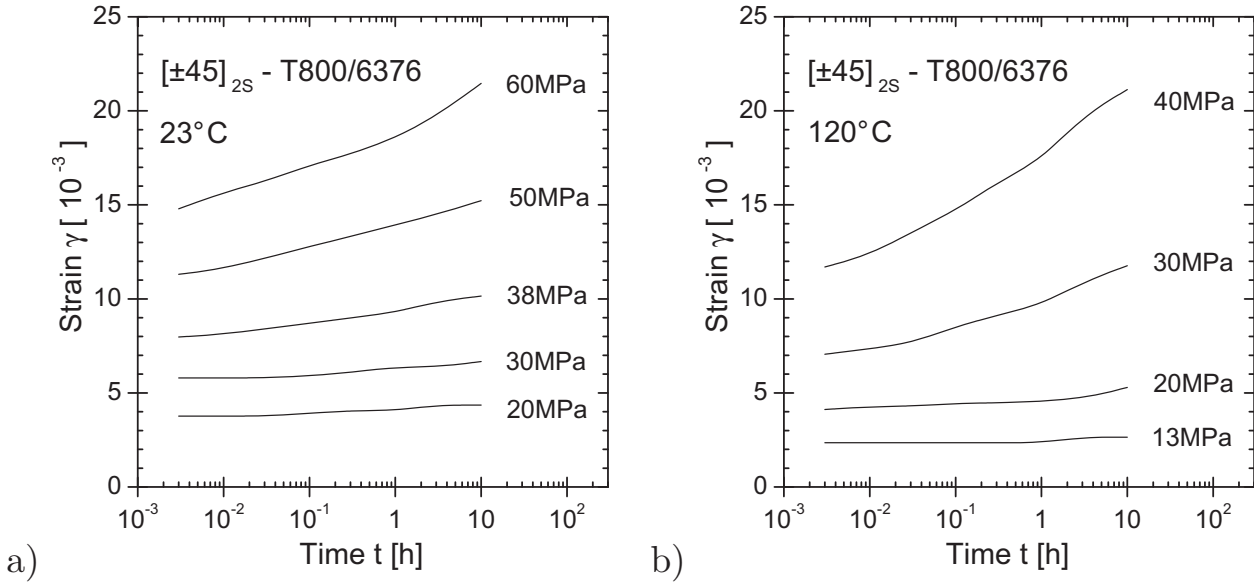
Figure 3.14: Creep curves of $[\pm 45]_{4S}$ carbon/epoxide (T800/6376) laminates at a) $23°C$ and b) $120°C$. (Katouzian et al. [165])

The coupling of the Findley equation and the time temperature stress superposition principle was found to generate a valid master curve to predict the long term tensile creep response. Gates et al. [167, 168] observed that although the creep compliance data of $[\pm 45]_{2S}$ carbon/polyimide (IM7/K3B) laminates with respect to creep time and temperature are similar, slight differences exist due to the loading mode of tension or compression.

Recently, several authors [169, 170, 171] used damage modelling and the constitutive equations of the elementary plies to account for differences of the overall viscoelastic and viscous behaviour of different lay-ups. Applied to $\pm 45°$-laminates, good agreement between experiments and predictions were reported.

3.4 Fatigue behaviour

3.4.1 Constant amplitude fatigue

A large amount of CAF data has been obtained in the past on many types of filamentary composite materials. The objectives of the studies were to extend the use of degradation and failure theories to predict fatigue life and to determine a better understanding of the fatigue characteristics. To accomplish these goals, several parameter studies on the effects of constituents, structure, geometry, load level, stress ratio, test frequency, and wave form were conducted. A chronological selection of references which dealt with the matrix dominated fatigue behaviour of $\pm 45°$-FRPs is given in Table 3.2.

Table 3.2: Summary of CAF reference works on $\pm45°$ composites

Reference	Material	Stress ratio R [1]	Frequency f [Hz]	Miscellaneous
Sims and Brogdon [172]	C/EP, G/EP	0.1 0.5, 0.3, 0.1	15 15	
Sims and Gladman [173, 174]	G/EP	0.1	0.00247-50	fabric; waisted; unnochted, double edge notch, centre hole
Sturgeon [159]	C/EP	0	1, 10	
Sun and Chan [175]	C/EP	0.07	1, 3, 10, 30	centre hole
Jones et al. [176]	C/EP G/EP A/EP	0	$25kN/s$	dried, 65% RH, boiled
Saff [177]	C/EP	0.07	0.1, 1, 10	centre hole
Curtis et al. [178]	C/PEEK	0	0.5, 5	waisted; square, sinusoidal waves
Dan-Jumbo et al. [179]	C/BMI, C/PEEK	0.07 0.07	0.4, 2, 10 0.4, 2, 10	centre hole centre hole
Rotem et al. [180, 181, 182, 183]	C/EP	10, 0.1, -1	1-2.8	
Ma et al. [184]	C/EP	0.1, -1	10	
Jen and Lee [185, 186, 187]	C/PEEK	0, 0.2	5, 25	
Komai et al. [188]	C/PEEK	0.1	1	sinusoidal, triangular waves
Xiao [189]	C/PEEK	0.13	1, 5, 10	
Komai et al. [163]	A/EP	0.1	1	sinusoidal, triangular waves
Quaresimin [190]	C/EP	0.05, -1	1-10	fabric

Effect of test frequency

To evaluate fatigue data from variable amplitude loading conditions or loading with varying frequencies, or to compare fatigue data obtained for different test frequencies, the dependence of the fatigue strength on the test frequency must be known. Figure 3.15a compares fatigue mean lives and standard deviations of several duromeric $[\pm45]_{2S}$ laminates depending on the load frequency. All results were obtained from centre hole ($d = 6.35mm$) specimens. Figure 3.15b summarises the specimen geometries.
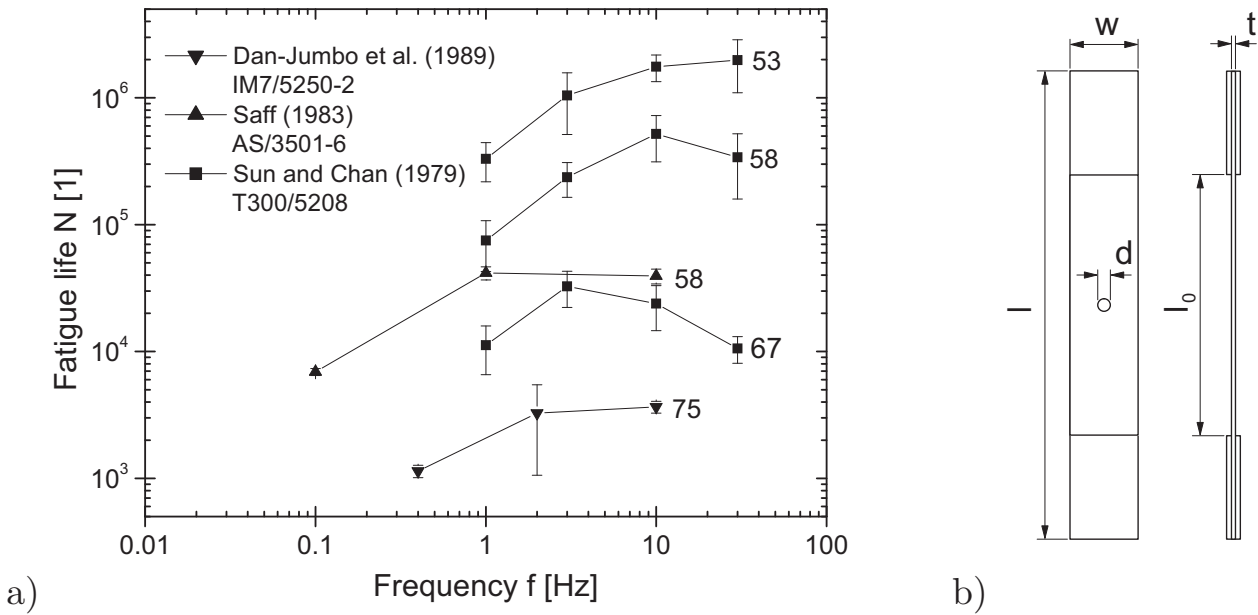
Figure 3.15: Effect of load frequency on the fatigue life of different duromeric $[\pm45]_{2S}$ laminates with a centre hole ($d = 6.35mm$): a) Numbers shown with each line indicate loading level as percentage of UTS ($R = 1/15$ for all references) b) Specimen geometry

The investigations of Sun and Chan [175] on T300/5208 ($l : l_0 : w : t = 254mm : 178mm : 38mm : 1.19mm$) and Saff [177] on AS/3501-6 ($l : l_0 : w : t = 178mm : 51mm : 38mm : 1.27mm$), each on $[\pm45]_{2S}$ carbon/epoxide laminates with a stress ratio of $R = 1/15$ did not show a consistent trend. At a frequency of $1Hz$, the AS/3501-6 material appeared to follow the data from T300/5208. At $10Hz$ however, the fatigue life for AS/3501-6 were an order of magnitude shorter than those for T300/5208. Sun and Chan noted no obvious differences in the failure mode for different frequencies.

Dan-Jumbo et al. [179] compared the frequency dependence of $[\pm45]_{2S}$ specimens ($l : l_0 : w : t = 254mm : 178mm : 38mm : 1.1mm$) of carbon/bismaleimide (IM7/5250-2) and carbon/PEEK (IM6/APC-2) at $R = 1/15$. It was evident that the IM7/5250-2 followed the trend of the carbon/epoxide systems, such as in references [175] and [177]. The fatigue

behaviour of the thermoplastic IM6/APC-2 system was far better than that of IM7/5250-2 at low frequencies. However, at higher frequencies the fatigue life of the thermoplastic system was drastically reduced. The same observation was reported by Lee and Jen [187] and Xiao [189] for unnotched $[\pm45]_{4S}$ AS-4/PEEK laminates. At each frequency of 1, 5 and $10Hz$, Xiao conducted fatigue tests with $R = 0.13$ at stress levels of 60, 70 and 80% of the UTS. The authors [179, 189] attributed the decrease of fatigue strength to the recorded, partly considerable increase of specimen temperature (up to $50K$) with frequency and load level and the temperature induced degradation of material properties (Figure 2.8). Above test frequencies of $2Hz$, no temperature equilibrium appeared in the thermoplastic laminates during the secondary stage. The duromeric laminates however attained a temperature equilibrium at load levels and frequencies as high as 67% of the UTS or $30Hz$ respectively [159, 175, 179]. In these cases, the exhibited temperature rise was less than $10K$.

Stiffness degradation

Rotem et al. [180, 181] investigated the degradation of longitudinal and shear stiffness of $[\pm45]_{4S}$ T300/934 laminates ($l : l_0 : w : t = 130mm : 15mm : 12.7mm : 2mm$) under reverse fatigue loading. The short gauge length was chosen to prevent Euler buckling without the use of an anti-buckling device. It was found that the development of mean and amplitude shear strain was very similar to the corresponding longitudinal strain components. The same result occurred with the normalised shear modulus except that in the primary stage the reduction of stiffness was more pronounced. The axial stiffness degraded in three stages as exemplary shown in Figure 3.16a. The first stage occurred immediately after loading and lasted for a relatively short duration. The degradation was a few percent and decayed exponentially. During the second stage, there was very small degradation at a constant rate. This stage lasted for most of the fatigue life and then, at 70% of the fatigue life, the third stage started by accelerated degradation and continued to accelerate until final failure. The characteristic course of the curves E/E_0 vs. n/N was independent of the applied stress. Figure 3.16b shows the development of longitudinal mean strain and strain amplitude while imposing a constant alternating stress amplitude. The mean strain remained zero, from which the author concluded that the specimen did not creep either way, tension or compression.
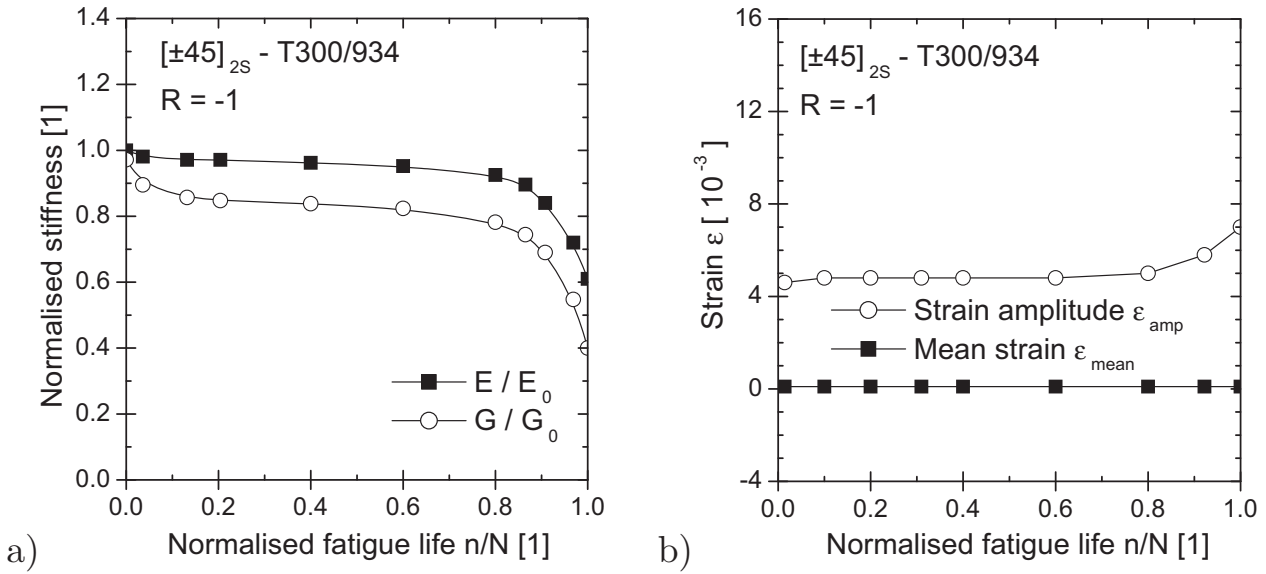
Figure 3.16: Variation of a) axial and shear stiffness and b) mean strain and strain amplitude for $R = -1$ fatigue loading. (Rotem [180])

Effect of waveform and amplitude

Fatigue tests conducted at a constant frequency for different stress amplitudes result in a variation of the rate of stress application (RSA) which falls with decreasing stress amplitude. The ultimate properties of polymers and many composites are rate dependent (section 2.3) and this may be expected to be reflected in the fatigue properties. Additionally, most tests are conducted with a sinusoidal waveform for which the RSA is not constant throughout the cycle. Ideal square waves reach the constant signal level by infinite edge velocities. Triangular waves are characterised by constant absolute values of edge velocity and both waveforms are not continuously differentiable, as is the sinusoidal waveform. Komai et al. [188, 163] and Curtis et al. [178] investigated the effect of these waveforms on the fatigue life and stated that the sinusoidal waveform is the easiest to control and the least damaging.

Sims and Gladman [173, 174] have shown for a glass/epoxy fabric under triangular wave CAF that the dependence of the UTS on the RSA transposes directly to the fatigue strength. Tests at different rates could be normalised with respect to the UTS obtained at the same RSA to give a single fatigue behaviour, thus to avoid the frequently displayed knee and the unexpected region of near zero slope at low cyclic lives in S-N presentation. They concluded that S-N curves obtained at constant RSA rather than constant frequency, can be extrapolated to their individual UTS and allow increased test frequencies, i.e. reduced test duration at low stresses, provided that self-heating is absent.

Intermediary summary on the CAF behaviour of $\pm 45°$-laminates

The material behaviour of $\pm 45°$-laminates under constant amplitude loading conditions exhibits the following characteristics which may be valid for other lay-ups as well:

1. The fatigue life strongly depends on the constituents, the specimen geometry, the test frequency, the stress ratio, and the applied stress. Universal recommendations of test conditions for a minimum but valid test duration cannot be given.

2. Sinusoidal fatigue loading and the absence of edges, holes and notches result in the longest fatigue life.

3. Thermoplastic laminates are more sensitive to frequency induced temperature rises and a reduction of fatigue strength than duromeric laminates.

4. The shear stiffness does not exhibit superior behaviour sensitivity to loading when compared to simple uniaxial longitudinal stiffness.

5. The fatigue life under tension-compression loading is shorter than under tension-tension loading. In tension-tension fatigue with constant maximum stress, the life increases with increasing stress ratio.

3.4.2   Effect of load sequences

Although the CAF behaviour of $\pm 45°$-laminates has been subject to several studies, the knowledge of the effect of load sequences is very limited. A literature survey revealed only three studies which are summarised in Table 3.3. Each of the studies investigates block load fatigue with tension-tension loading in either block.

Yang and Jones [119] and Kam et al. [191] conducted experiments on duromeric carbon/epoxide laminates. The Palmgren-Miner damage sums D_{PM} were greater than unity for the H-L load sequences and smaller than unity for the L-H load sequences. This observation is in line with the expectation according to subsection 2.5.4. Furthermore, the deviation of D_{PM} from unity decreases as the difference in stress level decreases. The results for the thermoplastic carbon/PEEK laminates observed by Lee and Jen [129, 187] do not agree with the expectation from subsection 2.5.4[2]

---

[2] Because the authors did not provide the associated S-N curve, the reasons are spec-

Table 3.3: Summary of block load fatigue reference works on ±45°-laminates

Reference Material l:l_0:w:t all in [mm] R[1]:f[Hz]:σ_{utt}[MPa]	σ_{max} [MPa] H/L (% σ_{utt})	N[1] H/L	n_1/N_1 [1]	n_2/N_2 [1]	$D_{PM}{}^a$ [1]
Yang and Jones [119]	121(61)/	11095	H-L		
[±45]$_{2S}$ - C/EP			0.54	0.71	1.25
254:n.a.:38.1:1.01	103(52)	136860	L-H		
0.1:10:197			0.54	0.43	0.97
Kam et al. [191]	(95)/	249	H-L		
[45, −45$_2$, 45]$_S$ - C/EP			0.32	0.74	1.06
220:140:25.4:1.24	(90)	662	L-H		
T-T^b:2:n.a.			0.30	0.64	0.94
Lee and Jen [129, 187]	154(40)/	468000	H-L		
[±45]$_{4S}$ - C/PEEK			0.20	0.51	0.71
240:140:25.4:1.5			0.50	0.24	0.74
0.2:5:386			0.80	0.28	1.08
	131(34)	833000	L-H		
			0.20	1.12	1.32
			0.50	0.77	1.27
			0.80	0.34	1.14

^{a} mean value, i.e. 50% probability of failure
^{b} tension-tension, stress ratio n.a.

3.5   Creep-fatigue interaction

The earliest discussion of fatigue induced creep of ±45°-laminates can be found by Sturgeon [159]. Comparing displacement vs. time curves from creep tests with displacement vs. cycle curves from fatigue tests, he observed that the small changes in the dynamic stiffness are secondary compared with the fatigue induced permanent strain. To investigate the nature of fatigue induced creep, interrupted tension-tension fatigue tests were conducted. The displacements consisted of increasing recoverable and permanent deformation upon unloading, like the constant load creep tests.

Sun and Chim [192] performed a series of experiments to investigate the

---

ulative. The test frequency of $5Hz$ may lead to self-heating without approaching a temperature equilibrium. Due to the low applied stresses, overlapping of the S-N data and a variation of the S-N characteristics, as the endurance limit is approached, may occur.

effect of creep strain on the fatigue life of $[\pm 45]_{2S}$ carbon/epoxide laminates. In general, each specimen underwent a number of fatigue cycles under constant amplitude sinusoidal loading ($R = 1/15, f = 10Hz$) at intermittent intervals separated by periods during which the specimen was held statically under the peak load of the cyclic loading (67% UTS). The fatigue life increased as the time under static load increased. The authors concluded that the crack growth rate under cyclic loading following each static loading period slowed down significantly. Such an effect was viewed as the development of plastic zones at the crack tips. The permanent strain was explained to be the result of creep in the matrix. A longer hold time then would produce a larger permanent strain that reduces the stress intensities at the crack tips during the subsequent cyclic loading. The authors then expected lower loading frequencies to produce larger creep strains than higher frequencies at the same stress level. Thus, a cyclic loading with a lower frequency preceding one with a higher frequency should have a delaying effect on the subsequent fatigue degradation rate. The effect should not exist if the order of loading is reversed. Conducted experiments involving a switching of frequency ($10Hz \rightarrow 1Hz$ and $1Hz \rightarrow 10Hz$) supported the argumentation.

3.6 Scientific motivation of the work

Increasing use is being made today from FRPs. They partly serve their engineering purposes within the conflicting field of the fundamental material understanding following up performance requirements. The comprehension of the mechanisms of deformation and failure and their dominance under service conditions is essential in engineering design. For a particular application, the mechanisms determine design allowables and the damage accumulation rate which affects damage tolerance, residual strength, durability and life time of the component [20]. A vital role is thereby taken over by the $\pm 45°$-layers, as their inherent characteristics decisively contribute to the strength behaviour of many multidirectional laminates [22].

Despite the anisotropic and heterogeneous material character, $\pm 45°$-laminates may be classified as rather 'homogeneous' materials with respect to the statistically distributed damage evolution. Homogenised and - for a more convenient use - analytical approaches should thus be applied to relate the damage evolution with the variation of macroscopic properties, to characterise and model the mechanical material behaviour of $\pm 45°$-laminates, and to predict durability and life time.

The preceding literature survey of the state of the art revealed that the

mechanical material behaviour of ±45°-laminates is - using the classification of Schulte et al. [134] - among other terms dependent on

1. geometrical factors, e.g. shape and dimensions,

2. the constituents, e.g. fibres and matrix,

3. environmental factors, e.g. temperature, and

4. the type of loading.

Whereas substantial data bases and routinely applied calculation procedures exist for all four categories[3], especially the latter category suffers from a lack of knowledge with regard to integrated load-property interactions such as

- the dependence of the material response on the load rate,

- the interactions of creep and fatigue, and

- the influence of pre-loads and load sequences in fatigue.

The present work is in particular directed towards the improvement of the material understanding of the itemised cases. The integrated consideration plays thereby a significant role to understand the load and material interactions in order to *evaluate and predict the strength and life time of angle-ply laminates under static and cyclic loads*.

---

[3] The results of the case scenarios may have general validity such as for geometrical factors (e.g. as universal recommendations in international standards) or the effect of temperature (e.g. when the material behaviour follows the Arrhenius equation or the time-temperature superposition is valid).

4

Experimental Procedure

4.1 Materials

Unidirectional carbon fibres pre-impregnated with epoxide resin were chosen for this research. The commercially available prepreg Fibredux 6376C-HTA(12k)-5-35% with a nominal mass per unit area of $208g/m^2$ [193] was supplied by Hexcel[1]. The prepreg's name is can be decoded as:

Fibredux 6376	:	product base,
C	:	carbon fibre,
HTA(12k)	:	fibre specification,
5	:	nominal cured thickness in $10^{-3}in\,(\approx 0.125mm)$,
35%	:	resin content of the prepreg by weight.

The prepreg material contains Tenax[2] HTA(12k) high tenacity carbon fibres produced from the PAN precursor under license of Toho Rayon (Japan). The epoxide resin known under the commercial name Fibredux 6376 is produced by Ciba[3]. The resin belongs to the class of TGMDA/DDS epoxides [194] with a curing temperature of $180°C$ and contains thermoplastic particles as additives to improve toughness and impact resistance. Tensile stress-strain curves for the neat resin at different temperatures are given in Figure 2.8a. The material properties of fibres and matrix are summarised in Table 4.1.

---

[1] Hexcel Composites, Duxford, CB2 4QD, United Kingdom
[2] Tenax Fibers GmbH & Co. KG, 42097 Wuppertal, Germany
[3] Ciba Specialty Chemicals, 4002 Basel, Switzerland

Table 4.1: Properties of HTA carbon fibres [195, 196] and 6376 epoxide matrix at RT [55, 197].

Property	Symbol [Unit]	Carbon fibre HTA	Epoxide resin 6376
Young's modulus	$E_{11}\,[GPa]$	235.0	3.6
	$E_{22}\,[GPa]$	19.1	3.6
	$E_{33}\,[GPa]$	19.1	3.6
Shear modulus	$G_{12}\,[GPa]$	24.0	-
	$G_{13}\,[GPa]$	24.0	-
	$G_{23}\,[GPa]$	7.2	-
Poisson's ratio	$\nu_{12}\,[1]$	0.28	-
	$\nu_{31}\,[1]$	0.02	-
	$\nu_{23}\,[1]$	0.33	-
Tensile strength	$\sigma_{utt}\,[MPa]$	3400	103
Tensile strain at failure	$\varepsilon_{utt}\,[\%]$	1.4	5.8
Density	$\varrho\,[kg/m^3]$	1780	1310
Specific heat capacity	$c_p\,[J/(kg\,K)]$	710	$1000^{\,a}$
Thermal conductivity	$\lambda\,[W/(m\,K)]$	17	$0.2^{\,a}$
Coefficient of thermal expansion	$\alpha\,[10^{-6}/K]$	-0.11	$47\,/\,60^{\,b}$
Specific electrical resistance	$\rho\,[10^{-6}\,\Omega\,m]$	15	-
Diameter	$d\,[\mu m]$	7	n.a.
Linear density $^{\,c}$		$800\,tex^{\,d}$	n.a.
Twist		0	n.a.
Energy release rate	$G_{IC}\,[J/m^2]$	n.a.	432

[a] Source: www.matweb.com; standard epoxide resin
[b] for $T \leq 414K\,/\,T > 414K$
[c] for 12k(=12000 filaments) fibres
[d] $1tex = 1g/km$

4.2   Material preparation

This section describes in brief the procedure to manufacture the laminate plates, different techniques to characterise the laminates and to ensure consistent quality, and the further processing to the individual samples.

4.2.1   Manufacturing of the laminate plates

The manufacturing of the laminate plates took place in multiple steps. Prior to manufacturing, the prepreg material, was stored at $-18°C$ to delay curing. The prepreg material was administered wound on a $300mm$ wide roll and was protected by a polymer foil at the inner and siliconised paper at the outer perimeter. After removal from the refrigerator storage, the prepreg was allowed to reach room temperature before opening the protection bag, thus preventing condensation.

For the research programme, three different 8-layered laminate types were fabricated, namely $[0]_8$, $[\pm45]_{2S}$, and $[90]_8$. For that purpose, sheets with dimensions of up to $424mm \times 300mm$ were cut from the prepreg roll. After removal of the polymer foil two different prepreg sheets were laid one over the other. Special care was taken that eventually entrapped air was squeezed out by a squeegee roll and to ensure the correct orientation of the layers. Next, the siliconised paper at the upper side of the prepreg package was removed to continue further stacking. Once the desired lay-up was stacked and the siliconised papers were removed, a peel ply and a protection foil were added on each side of the prepreg stack. The whole stack was placed between two $5mm$ thick brass plates and underwent strictly adhered the recommended curing schedule of the prepreg manufacturer [197] and Airbus [198] in a computer controlled press. The courses of temperature and pressure during the cure cycle are shown in Figure 4.1. After cooling, the peel ply was removed from the cured laminate plates.
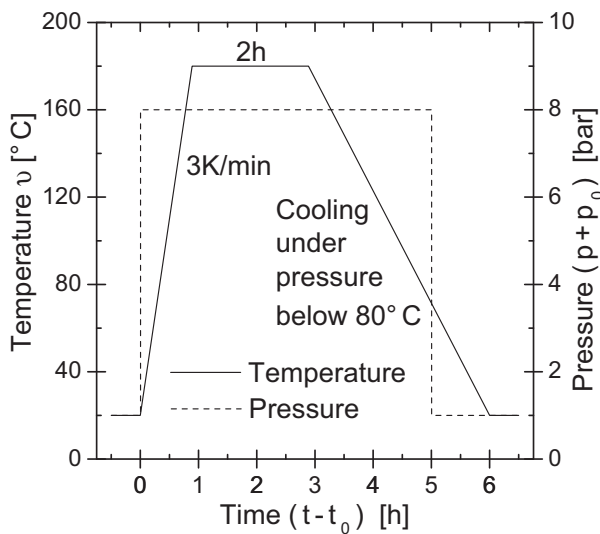
Figure 4.1: Cure cycle for Fibredux 6376C-HTA(12k)-5-35% prepreg [197, 198].
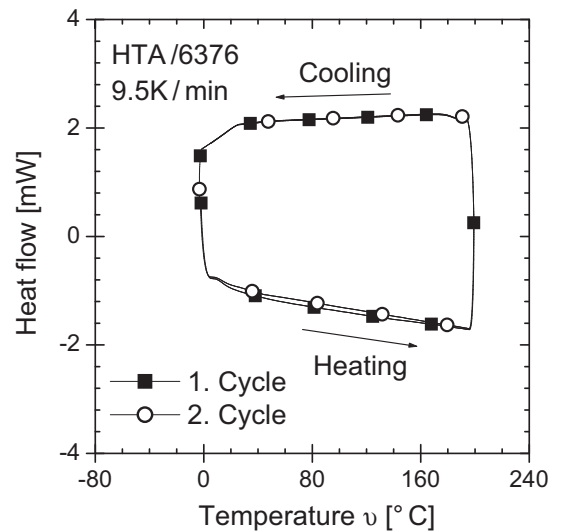
Figure 4.2: DSC analysis of the cured laminate.

4.2.2 Characterisation of the laminates

Degree of cure

To verify that the manufactured laminate plates are cured, so that no chemical or thermal post-curing is expected on storage or loading, plate samples were characterised by the differential scanning calorimetry (DSC).

The samples were first cooled to 0°C. With $9.5 K/min$, the samples were subsequently heated to $200°C$ and afterwards cooled to $0°C$. The temperature cycle was applied two times. Figure 4.2 shows the results of the DSC analysis as a heat flow vs. temperature plot. During both temperature cycles no post-curing reaction was found and the heat flow vs. temperature curves are practically identical during heating and cooling. Therefore, the laminate plates can be regarded as fully cured.

Fibre volume fraction

The fibre volume fraction of selected laminate plates was experimentally determined by the buoyancy-flotation method and by pyrolysis in accordance to ASTM D792[4]. For this purpose, $20mm \times 20mm \times 1mm$ large samples were cut out of the plates. Because buoyancy-flotation method is non-destructive, the same sample could be examined by both methods.

$$\text{Buoyancy-flotation method} \quad : \quad V_f = \frac{(m_c\, \varrho_w)/(m_c - m_w) - \varrho_m}{\varrho_f - \varrho_m} \quad (4.1)$$

$$\text{Pyrolysis method} \quad : \quad V_f = \frac{m_f\, \varrho_m}{m_f\, \varrho_m + (m_c - m_f)\, \varrho_f} \quad (4.2)$$

For the pyrolysis, the samples were exposed to $500°C$ for $80min$. Eqs. (4.1) and (4.2) were applied to calculate the fibre volume fractions where the variables m and ϱ refer to as mass and density and the subscripts f, m, and c to as fibre, matrix, and composite. The density of water ($0.9981 g/cm^3$ at RT) is denoted as ϱ_w and the virtual mass of the sample in water is given by m_w. The determined results are $V_f = 61.2\% \pm 1.7\%$ for the buoyancy floatation and $V_f = 60.5\% \pm 1.9\%$ for the pyrolysis method. Both methods agree well in mean value and standard deviation and the results are in accordance with the required fibre volume fraction of 60% from the material data sheet [193].

---

[4] ASTM D792-00: *Standard test methods for density and specific gravity (relative density) of plastics by displacement*

Microscopic inspection

Polished microsections were prepared to inspect the quality of the consolidation between the layers and to investigate the local distribution of the fibres. Figure 4.3a shows neither pores and inclusions, nor pronounced resin rich regions. A micrograph of a $[\pm45]_{2S}$ laminate is shown in Figure 4.3b. Good consolidation during manufacturing can be concluded from the almost undisturbed transitions between the individual layers. The partly merging of the layers along the symmetry plane indicates parallel alignment of the middle layers.

a)

b)
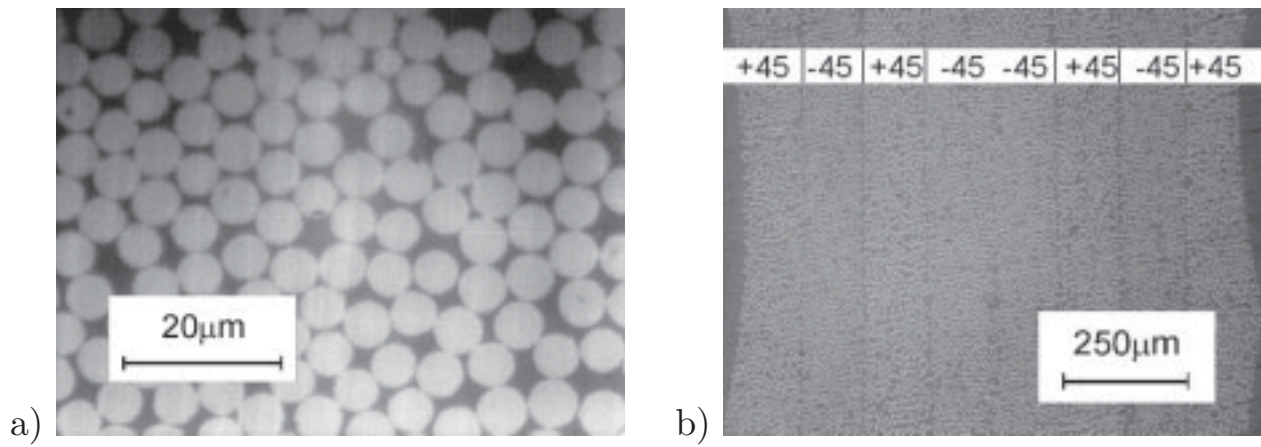
Figure 4.3: Micrographs of the manufactured laminates, a) magnification of a single layer, b) magnification of a $[\pm45]_{2S}$ laminate.

4.2.3   Specimen preparation

The laminate plates were cut into sub-plates using a diamond blade table saw. Extreme care was taken to accurately cut the sub-plates at the desired angle of orientation. All sub-plates were rectangular and $180mm$ long. To prevent damage from the grips of the test rig, thus to ensure that failure occurred in the gauge section away from the grips, glass fibre fabric/epoxide tabs (Duraver® Hgw 2372.4 [199]) were fastened to the ends on both sides of the sub-plates using the two-part epoxide adhesive (UHU plus endfest 300 [200]). The tab material of $1mm$ thickness was glued with the warp and weft direction aligned at 45° to the loading direction. After curing at room temperature for one day the adhesive was post-cured at $100°C$ for $30min$ to assure that the curing was completed and to reach the optimum strength of the adhesive[5]. The sub-plates with the attached tabs were finally cut into

---

[5] The strength of the adhesive can be adjusted by cure time and temperature. Obtainable strength values are: $12MPa$ for $12h$@$20°C$, $18MPa$ for $3h$@$40°C$, $20MPa$ for $45min$@$70°C$, $25MPa$ for $10min$@$100°C$, or $30MPa$ for $5min$@$180°C$.

rectangular specimens with dimensions of $l : l_0 : w : t = 180mm : 100mm : 16mm : 1mm$ as schematically drawn in Figure 4.4. The dimensions were chosen according to the results of the literature survey of subsection 3.1.2 and ISO 527. All specimens were numbered to identify the location on the original laminate plate and to be able to trace back possible uncertainties in the data. The specimen edges were finally polished with wet silicon carbide papers in steps from 240 to 1200 grit to avoid notch effects. The exact dimensions of every specimen were measured and noted prior to testing.
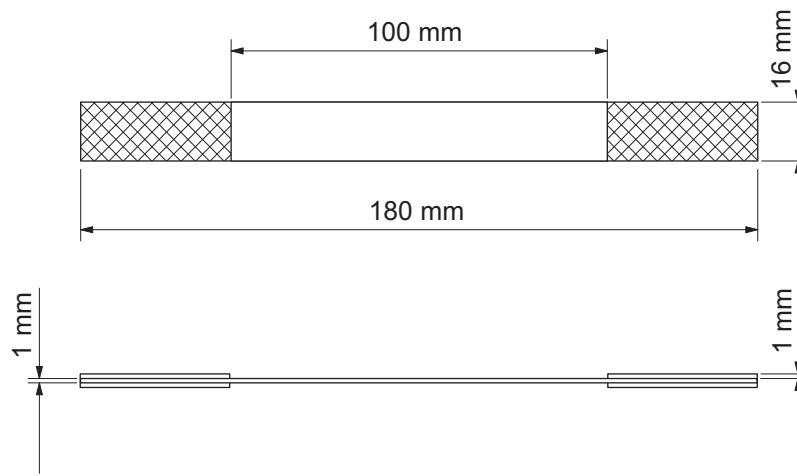
Figure 4.4: Specimen geometry.

4.3   Testing apparatus and procedures

Different mechanical test facilities and testing procedures were applied to characterise the investigated laminates. All experiments were conducted under laboratory environment conditions. The tests were performed on different machines depending on the fracture loads of the different specimens, the type of testing, and the requirements in data acquisition. For all investigated laminates tensile tests were carried out under quasi-static conditions. Further tests were performed with the angle-ply laminate including tests to investigate the strain rate dependence as well as the compression, tensile creep and fatigue behaviour and their interactions. The influence of constant amplitude cyclic loading was investigated under tension-tension and reverse fatigue loading. Block load fatigue and combined creep-recovery-fatigue tests were conducted under different load conditions.

4.3.1   Quasi-static tests

Tensile tests

Uniaxial data acquisition   The stress-strain behaviour of the different laminates was determined under uniaxial tension according to ISO 527 with a constant actuator velocity of $2mm/min$. The specimens were tested with universal testing machines equipped with a $10kN$(Zwick Type 1445) or $100kN$ load cell(Zwick Type 1474). The machines ran computer controlled by the software code (Zwick Z 7005) with automatic data acquisition. The elongation Δl of the specimens was measured using a clip-on extensometer (MTS Type 632.12C-20) with a gauge length of $20mm$ or alternatively with a macro extensometer (Zwick Type 066511-00).

The effect of strain rate on the stress-strain behaviour of the AP laminate was determined with a servohydraulic testing machine running in displacement control with actuator velocities in the range of $0.003 - 333 \cdot 10^{-3}m/s$ ($0.2 - 20000mm/min$). The machine (Instron-Schenck PC100N with a 8800 digital control unit) was operated via a personal computer and the software interface RS Console. For programming and data acquisition, the software codes StaComp and RS Scope were used. The capacity of the load cell was $100kN$. The hydraulic actuator had an integrated inductive displacement transducer and a maximum displacement of $\pm50mm$.

Biaxial data acquisition   All tensile tests with biaxial data acquisition were run with the machines described above. However, measurement of the longitudinal and lateral strains was conducted by strain gauges (HBM Type LY 11-3 or Showa Type N22-FA-2-120-11) or clip-on extensometers (Sandner Type A25-1.25x and A10-0.5o) with gauge lengths of 25 and $10mm$ respectively. The data were recorded with a HBM MGC amplifier and the associated MGC Panel software.

Compressive tests

Compressive tests were only conducted on AP specimens with servohydraulic machines. The actuator velocity was $2mm/min$. The material properties were determined in analogy to the tensile tests. Due to the specimen geometry, the use of an anti-buckling device was necessary to prevent Euler buckling. An anti-buckling device similar to that suggested and proved by Schulte [139] was designed. It consisted of two bolted aluminium plates each with a recess to guide the specimen. The centre of the anti-buckling device contained an unsupported length of $12.5mm$. Teflon layers were bonded to the contact surfaces in the anti-buckling guide to reduce friction. The max-

imum strain applicable to the samples was limited by the geometry of the anti-buckling device.

Stepwise tests

Using the PC100N machine, stepwise quasi-static tests were conducted in tension and compression on the AP laminates. The restrictions of the standard compressive tests apply to the stepwise compressive tests as well. All tests were run in displacement control. The actuator velocity was $2mm/min$. For every load stage, an upper (in tension) or lower (in compression) strain value was applied. Upon load release a force target value of zero was set. Table 4.2 contains the target strain data of the different load stages.

Table 4.2: Applied strains $\varepsilon[10^{-3}]$ during stepwise quasi-static tests.

Stage	1	2	3	4	5	6	7	8	9	10	11	12
Tension	1	2	3	5	7.5	10	15	20	30	50	70	110
Compression	-1	-2	-3	-4	-5	-7.5	-10	-15	-20	-30	-	-

4.3.2 Creep tests

Universal testing machines equipped with $10kN$ (Zwick Type 1445) and $5kN$ (Zwick Type 1474) load cells were used to perform creep tests on the AP laminate according to ISO 899. Both machines were programmed appropriately. The creep strains were recorded with the MTS clip-on extensometer and the HBM MGC amplifier/software package (Zwick Type 1445) or the macro extensometer (Zwick Type 1474). The creep stresses were in the range of 50 to $142MPa$, the creep times went up to $120h$, the subsequent recovery times up to $48h$.

4.3.3 Fatigue tests

Constant amplitude fatigue

The constant amplitude fatigue data were generated on four different servohydraulic machines. The majority of CAF tests were conducted with the Instron-Schenck PC100N machine and the 8800 digital control unit and a Schenck PSA PC10N machine equipped with a $10kN$ load cell and controlled by a S31 analog control unit. Both machines were operated via a personal

computer. For programming and data acquisition, the software code Dyn-Mat was used. The special feature of the software code is, that besides the basic input data only time, force and displacement data are saved in a binary format. For further data analysis the software code Measure Vision was used to calculate and visualise stresses and strains, and further properties such as stiffness, damping, or loss and store works.

Further CAF tests were conducted on two hydraulic test rigs at the Department of Mechanical Engineering of the University of Waterloo, Canada within the scope of a scientific cooperation. The first test rig had a $156kN$ load cell and tapered grips and was controlled by an Instron Model 8500 unit. Data were taken continuously using a Sciemetric series 7000 data acquisition system and customised software SCI2, written in Quick Basic. The second test rig, an Instron Model 1350 mounted with a $22kN$ load cell, had a load capacity of $98kN$ with a maximum displacement of $\pm50mm$. The output voltages of force and displacement were automatically saved in ASCII format by the data logging software Gen200. The data were later converted by calibration curves for further analysis.

All CAF tests were carried out under load control with sinusoidal waves. Unless otherwise indicated, a standard test frequency of $10Hz$ was used to test the specimens to failure or a cycle limit of $N \geq 2{\cdot}10^6$. Stress ratios of 0.5, 0.3, and 0.1 were applied for tension-tension fatigue. Tension-compression fatigue tests were conducted with the anti-buckling device and $R = -1$.

Effect of test frequency   In case of the AP specimens, the dependence of fatigue life on the test frequency was investigated for stress ratios of 0.1 and -1. This was systematically performed for $R = 0.1$ on the PC100N machine by a test matrix consisting of three frequencies (2, 5, and $10Hz$) and two maximum stresses (110 and $140MPa$). The reverse loading tests on the were conducted at test frequencies of 1, 2, 3, 5, and $10Hz$.

Block load fatigue

The effect of load sequences on the fatigue behaviour was only investigated for AP specimens whereas three different cases were considered which are summarised in Table 4.3. In all cases, two load blocks were applied.

The cases A1 and A2 investigated high-low and low-high sequences at a constant stress ratio, i.e. $R = 0.1$ and $R = -1$. The load levels were chosen such that expected mean fatigue lives had more than 1.5 decades difference and that no overlapping in fatigue life due to scatter occurred. In case A3, the stress ratio and the applied stress changed. The applied stresses for both stress ratios were selected to correspond to a fatigue life of approximately

Table 4.3: Cases of block load fatigue.

Case	Characteristics	Sequences ($R[1], \sigma_{max}[MPa]$)
A1	constant $R = 0.1$ different stresses	$(0.1, 140) \longleftrightarrow (0.1, 110)$ $\equiv$ to H(high) $\longleftrightarrow$ L(low)
A2	constant $R = -1$ different stresses	$(-1, 110) \longleftrightarrow (-1, 65)$ $\equiv$ to H(high) $\longleftrightarrow$ L(low)
A3	different R-ratios different stresses	$(-1, 75) \longleftrightarrow (0.1, 127)$

$50 \cdot 10^3$ cycles in CAF loading. The case A1 was carried out at a test frequency of $10 Hz$ on the PC100N machine, cases A2 and A3 were carried out at $2 Hz$ using the anti-buckling device and the Instron Model 1350.

4.3.4   Initial loads in fatigue

Two different initial load scenarios were applied prior to CAF loading to investigate their effects on the fatigue behaviour of the AP laminate. All tests were performed with the PC 100N servohydraulic machine. Both load scenarios are schematically drawn in Figure 4.5.
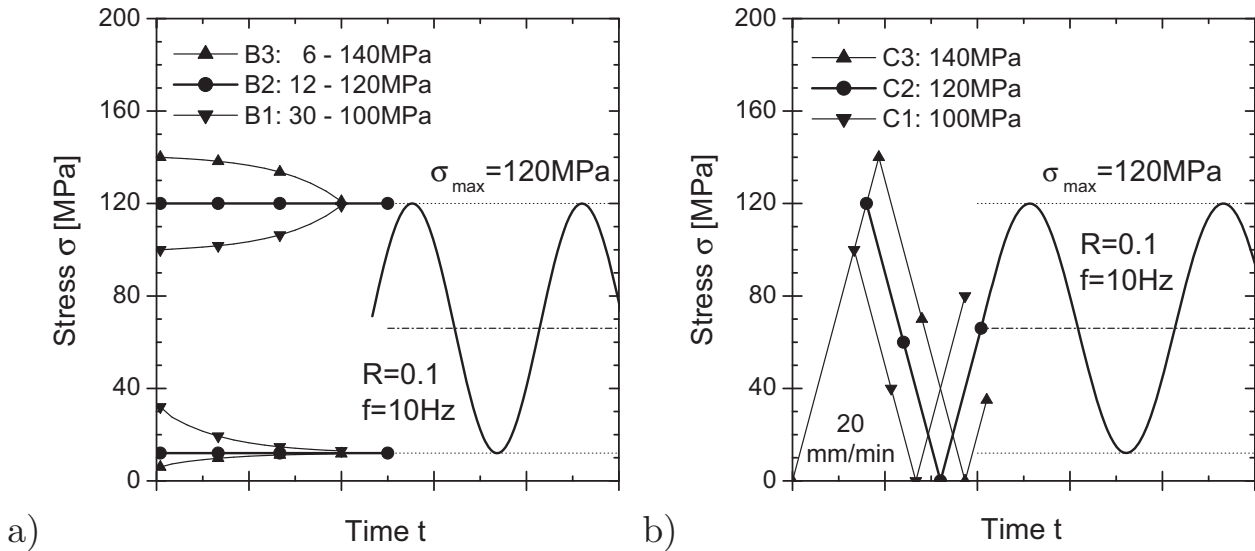

Figure 4.5: Sketches of initial load cases prior to the CAF loading. a) cyclic initial load (load scenario B) and b) triangular pulse load (load scenario C).

The initial maximum and minimum stresses of the first load scenario differed from the nominal values. Three different cases (B1-B3) of approaching the nominal values were investigated at a constant test frequency of $10 Hz$.

In case B1, the maximum stress increased from 100 to $120MPa$ and the minimum stress decreased from 30 to $12MPa$. In case B3, the maximum stress decreased from 140 to $120MPa$ and the minimum stress increased from 6 to $12MPa$. The case B2 aimed to approach the reference CAF loading of $R = 0.1$ and $\sigma_{max} = 120MPa$ after the very first cycles. Once for the cases B1 and B3 the nominal values were reached after approximately 200 cycles, the reference CAF loading was continued until fatigue failure occurred.

The second load scenario consisted of one positive triangular stress pulse. Three different cases of the pulse were investigated, namely 100, 120, and 140MPa, referred to as C1, C2, and C3. The pulse was applied in stroke control by the software code StaComp. The actuator velocity for loading and unloading to $F = 0$ was $20mm/min$. Without unclamping the samples (thus keeping any viscoelastic strain), a reference CAF loading was subsequently applied until failure. The loading of $R = 0.1$, $\sigma_{max} = 120MPa$ and $f = 10Hz$ was controlled by the software code DynMat.

4.3.5 Creep-recovery-fatigue (CRF) tests

The CRF tests comprise those experiments where creep and (recovery) loading is followed by subsequent fatigue loading. With two different load cases only AP specimens were investigated. During the first case D1, the creep specimens which were loaded for $120h$ with stresses between $70 - 145MPa$ were allowed to recover for about $2000h$ without load. Afterwards, the samples were tested on the PC100N machine with $R = 0.1$, $f = 10Hz$ and $\sigma_{max} = 120MPa$ until fatigue failure occurred.

The second case D2 was conducted on the Instron Model 1350. Figure 4.6 shows the scheme of the CRF tests. The CRF tests were carried out starting with the creep part for a duration of t_{cr} at the stress level of $91MPa$ followed by a recovery part for a duration of t_{rec} during which the stress was zero. Finally, a reference fatigue loading of $R = 0.3$, $\sigma_{max} = 140MPa$, and $f = 10Hz$ was applied until failure. The stresses were chosen such that the mean stress in fatigue was identical to the creep stress. The D2 case was subdivided into two groups depending on the creep time t_{cr}. The first group ($t_{cr} = 2h$) was further subdivided by three different recovery times t_{rec}, namely 0, $2h$ and $24h$. The second group had a creep time of $t_{cr} = 24h$ and was further subdivided as the first group. Altogether, six combinations of creep and recovery times were investigated.

To simplify the identification of the different tests, the following notation will be used. **CxRyF** means that a sample experienced **x**h **C**reep followed by **y**h stress-free **R**ecovery and the compulsory reference **F**atigue loading until failure.

Load case D1	t_{cr} = 120h	t_{rec} = 2000h	R = 0.1
	σ_{cr} = 70 - 145MPa	σ_{rec} = 0	σ_{mean} = 66MPa
Load case D2	t_{cr} = 2h, 24h	t_{rec} = 0, 2h, 24h	R = 0.3
	σ_{cr} = 91MPa	σ_{rec} = 0	σ_{mean} = 91MPa
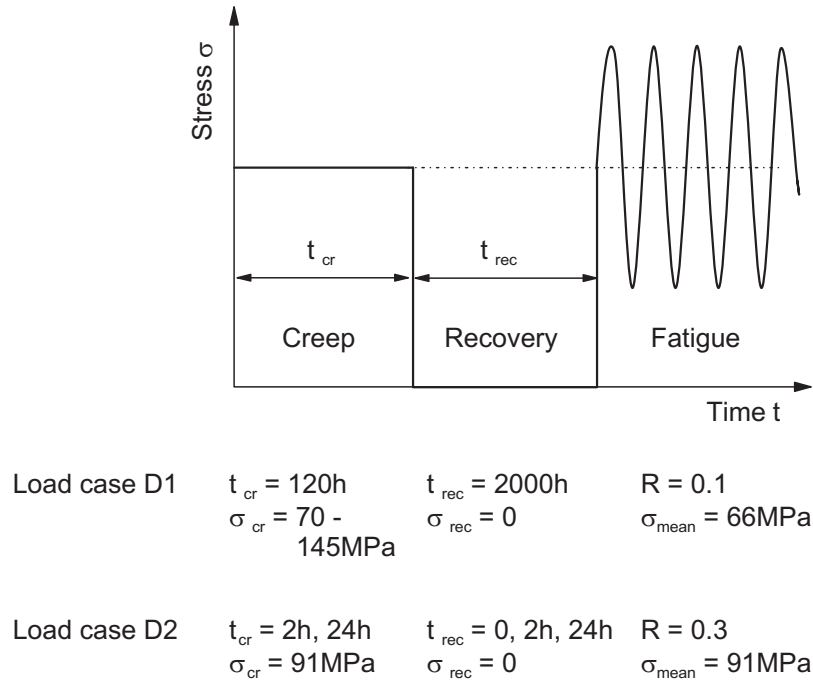
Figure 4.6: Scheme of creep-recovery-fatigue tests.

4.3.6 Microscopy

The microscopic analysis of different morphological details and damage mechanisms were performed by light microscopy (LM) and scanning electron microscopy (SEM).

For LM, the specimens were sectioned and embedded in cold curing epoxide resin. The microsections were ground with SiC grit in steps from 320 to 4000 and following polished with diamond suspensions of 9, 3, and $1\mu m$. Micrographs of different magnifications were taken with analog and digital cameras using a Pabisch Polyvar light microscope with a lens revolver.

The SEM investigations of the fracture surfaces were carried out with a Gemini GSMIC-848 microscope. Acceleration voltages of 5 to $15kV$ were used. Depending on the acceleration voltage, the fracture surfaces were gold coated to prevent electrostatic charging.

4.3.7 Infrared thermography

The strain rate dependent tensile tests and selected fatigue tests were accompanied by infrared (IR) thermography[6], a non-contact quantitative method

---

[6] The sequences of thermographic pictures were evaluated by the overall appearance of the surface temperature distribution and the temperature development at four different positions. The positions P01 and P02 refer to fixed locations on the specimen surface termed as 'top' and 'bottom'. The distance of P01 and P02 to the upper and lower gripping jaw is $20mm$ respectively. No shorter distance could be chosen due to the configuration of

to determine surface temperature distributions. Thus, a heat flow through the volume to the surface is necessary to detect internal sources of increased energy dissipation. Eqs. (4.3) and (4.4) give the fundamental relations of the stored heat and all heat conductivity processes [95]. It can be seen that the surface temperature distribution depends on the time t, the specific heat capacity c_p and thermal conductivity λ of the constituents.

$$Q = m\,c_p\,\Delta T \qquad (4.3)$$

$$Q = -\lambda\,t\,A_0\,\frac{dT}{dl} \qquad (4.4)$$

The method was applied to monitor the general heat development during the test duration and the localised heating due to damage evolution. The applied InfraTec VarioTHERM camera had the following technical specifications:

resolution	:	$256 pixel \times 256 pixel$,
IR spectrum	:	$3.4 - 5\mu m$,
shutter speed	:	$0.02s$,
temperature resolution	:	$0.1K$ at $30°C$,
lens	:	$1.3/50mm$,
flare angle	:	$7° \times 7°$.

The thermographic data were saved on a personal computer. The software package IRBIS professional was used for further image analysis and evaluation. The combination of camera resolution and working distance resulted in a geometric resolution of each pixel of about $200\mu m$.

The bottom region of the specimen during the experiment was typically warmer than the top region which is due to the heat conduction from the servohydraulic actuator via the gripping jaws to the samples. The temperature gradient was less than $3K$ over the gauge length and did not cause preferred failure in one or the other region.

---

the gripping jaws. The screw heads to tighten the samples have a height of approximately $20mm$ and hide this length from the upper and lower zone of the gauge length. The fixed position P03 marks the ambient temperature. The highest temperature of the selected detail view is pointed by the variable position 'Max'. The different positions of the lower screw head on some of the thermographic pictures results from the actuator movement.

5

Results

5.1 Quasi-static loading

5.1.1 Unidirectional laminates

Representative tensile stress-strain curves for the UD laminates loaded in and transverse to the fibre direction are shown in Figure 5.1. The MVs
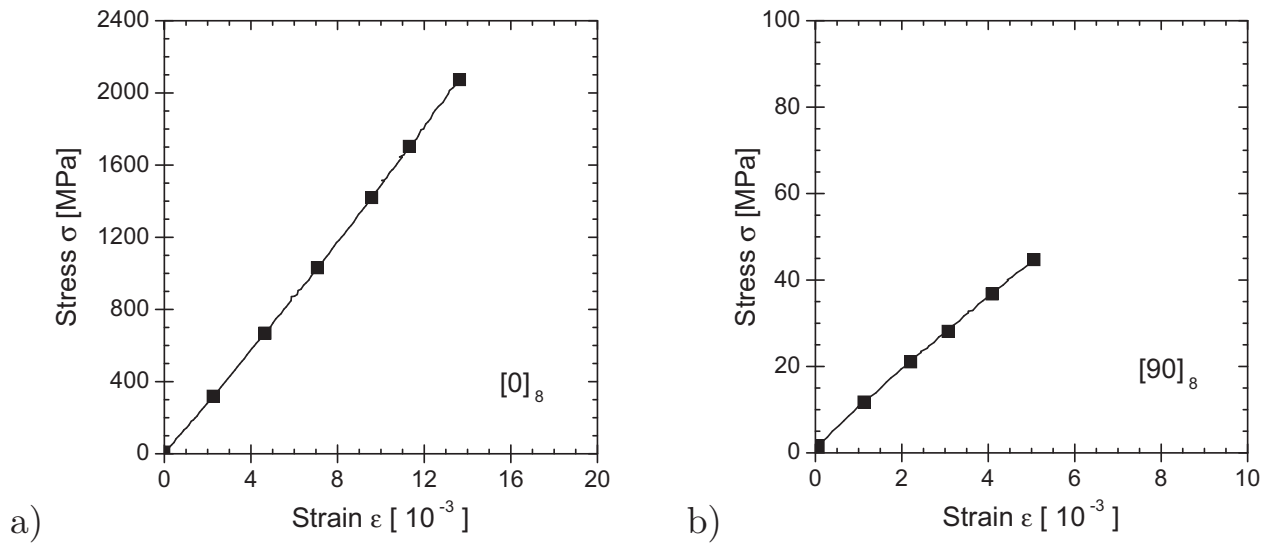
Figure 5.1: Stress-strain curves for the unidirectional laminates loaded in a) fibre and b) transverse direction

and SDs of the ultimate tensile stresses and strains and the elastic moduli are summarised in Table 5.1. The complete sets of experimental data are given in Table A.1. The Young's moduli and Poisson's ratios of the $[0]_8$ and $[90]_8$ laminate can be regarded as E_{11} and E_{22}, and ν_{12} and ν_{21} of the UD lamina respectively. The courses of axial stiffness and Poisson's ratio with

the applied strain are shown in Figure 5.2. Due to scatter of the of the strain gauge readings, the curves are not plotted for very low strains.

a)   b)
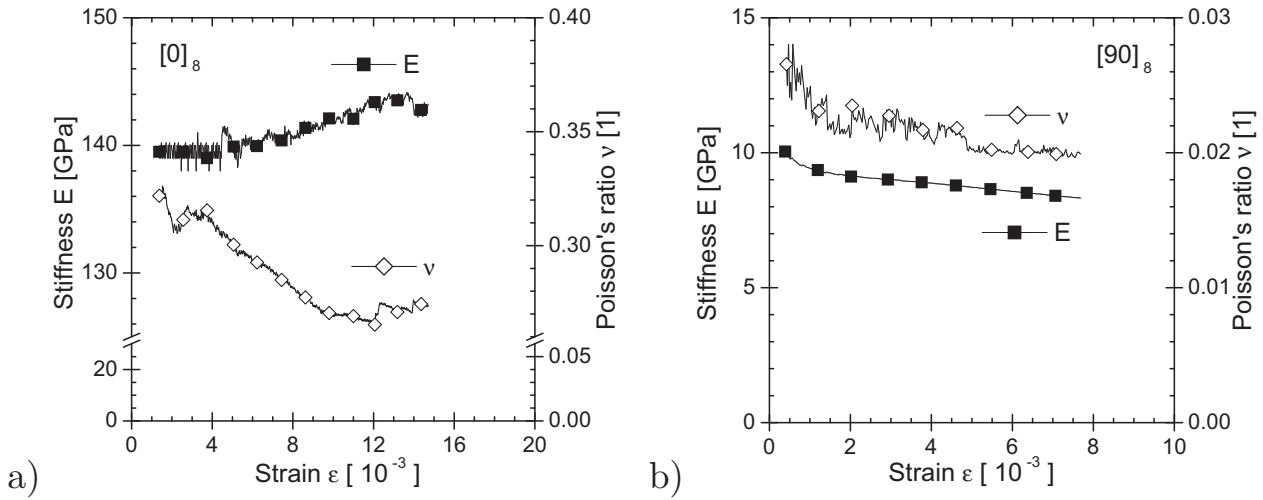
Figure 5.2: Courses of stiffness and Poisson's ratio for the unidirectional laminates loaded in a) fibre and b) transverse direction

Table 5.1: Tensile properties of the unidirectional laminates (MV±SD)

Property	$[0]_8$	$[90]_8$
$\sigma_{utt}[MPa]$	2088 ± 90	48 ± 15
$\varepsilon_{utt}[10^{-3}]$	14.1 ± 0.8	5.3 ± 1.9
Young's modulus	$E_{11} = (140.9 \pm 4.9)GPa$	$E_{22} = (8.9 \pm 0.6)GPa$
Poisson's ratio	$\nu_{12} = 0.32$	$\nu_{12} = 0.022$

Loaded in fibre direction, the stress increases linearly until $\varepsilon = 3 \cdot 10^{-3}$. Between the strains of 3 and $10 \cdot 10^{-3}$, the stress increases progressively, visible at the increasing course of stiffness. From $\varepsilon = 12 \cdot 10^{-3}$ to brittle failure at $\varepsilon = 14 \cdot 10^{-3}$, the stress increase is linear. The relative decrease of Poisson's ratio between the strains of 2 and $10 \cdot 10^{-3}$ is more pronounced than the increase of stiffness. The Poisson's ratio decreases from 0.33, approaches the ν_{12}-value of the fibres at $\varepsilon = 10 \cdot 10^{-3}$ and keeps approximately constant on further loading. Above $\varepsilon = 10 \cdot 10^{-3}$ crackling was observed. The crackling increased in audibility and frequency until failure. The failure process comprised the whole specimen volume and was related with the loss of any structural integrity. The fracture type was brush-like.

A declining increase of stress over the full range of strain is observed when the laminate is loaded in the transverse direction. Axial stiffness and Poisson's ratio approximately decrease at the same rate. Failure occurred suddenly without prior notice by one dominant crack perpendicular to the loading direction.

5.1.2   Angle-ply laminate

Tension

A typical stress-strain curve of the AP laminate until failure is shown in Figure 5.3a. The linear region is followed by a declining increase of stress until yielding occurs at $\varepsilon = 32 \cdot 10^{-3}$. As the strain further increases, the stress slightly decreases until necking causes a renewed stress increase which is terminated by separation of the specimen due to final failure. Rather than by
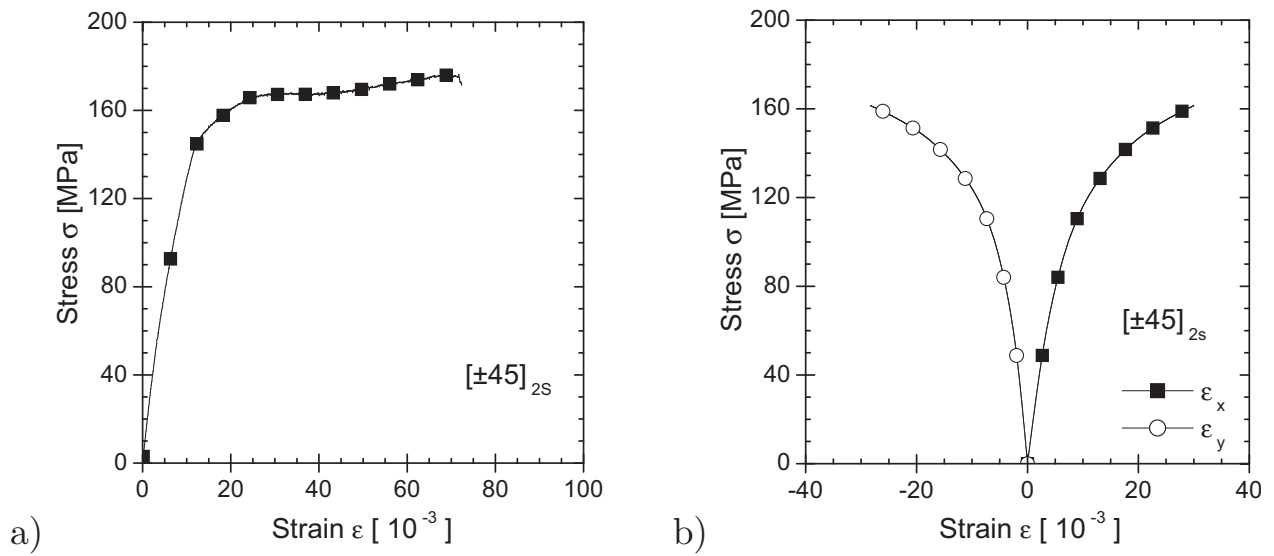
Figure 5.3: Tensile behaviour of the angle-ply laminate. a) stress vs. strain until failure and b) stress vs. axial and lateral strain until $30 \cdot 10^{-3}$

the ultimate properties which are subject to considerable scatter (Table A.2), the stress and strain at yielding are characteristic for the AP laminate. The mean values (MVs) and standard deviations (SDs) of yield stress and yield strain, and the elastic modulus are summarised in Table 5.2. The complete sets of experimental data are given in Table A.2.

Table 5.2: Properties determined from tensile tests on the angle-ply laminate

Property	MV±SD
Yield stress $\sigma_y[MPa]$	172±5
Yield strain $\varepsilon_y[10^{-3}]$	32±1
Young's modulus $E_x[GPa]$	19.6±0.7
Poisson's ratio $\nu_{xy}[1]$	0.73[a]
Shear modulus $G_{12}[GPa]$	5.2[a]

[a] too small data base for reasonable SD

Figure 5.3b shows the characteristic curves of axial strain ε_x and lateral strain ε_y vs. the applied stress until $30 \cdot 10^{-3}$ strain[1]. The axial strain runs as described before. The absolute value of the lateral strain runs in the same way at a lower level for the same stress.

Calculating Eq. (2.25) as secant value between 0.5 and $2.5 \cdot 10^{-3}$ applied strain provides the Poisson's ratio ν_{xy} of the laminate. The result is included in Table 5.2. The in-plane shear stress τ_{xy} and strain γ_{xy} due to loading in x-direction can be calculated according to Eqs. (5.1) and (5.2) where Eq. (5.3) is valid.

$$\tau_{xy} = 0.5 \cdot \sigma_x \tag{5.1}$$

$$\gamma_{xy} = \varepsilon_x - \varepsilon_y \tag{5.2}$$

$$\tau_{xy} = G_{12} \cdot \gamma_{xy} \tag{5.3}$$

$$G_{12} = \frac{\Delta F}{2 A_0 \left(\Delta \varepsilon_x - \Delta \varepsilon_y \right)} \tag{5.4}$$

According to DIN 29971[2], the in-plane shear modulus of the UD lamina can be determined from Eq. (5.4). Following ISO 527, the secant value of G_{12} is evaluated between 0.5 and $2.5 \cdot 10^{-3}$ applied strain. The resultant value is given in Table 5.2.
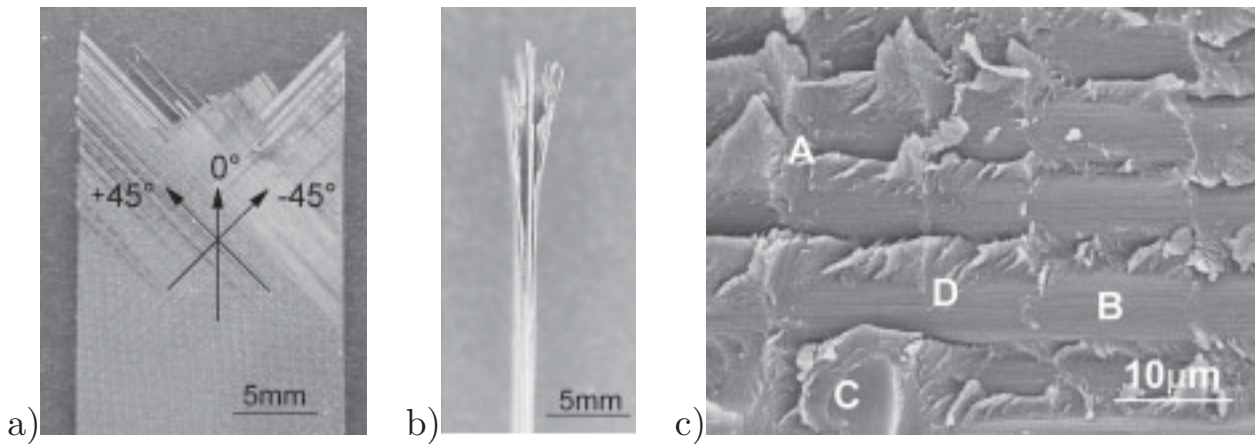
Figure 5.4: Angle-ply laminate after tensile failure. Lateral view of a) sample width, b) sample thickness, and c) SEM micrograph of the fracture surface.

Figure 5.4 shows photographic images (a, b) and a SEM micrograph (c) of the fracture surface of a failed coupon under tensile load. From the markings in the lateral view of the width (a) can be clearly seen, that the fibre orientation after failure remains under $\pm 45°$. The individual plies are visible at the lateral view of the thickness (b). Intra-ply failure has occurred in each ply

---

[1] not until fracture due to the limited application range of the strain gauge

[2] DIN 29971:1986 *Unidirektionalgelege-Prepreg aus Kohlenstofffasern und Epoxidharz*

transverse to the fibre direction. The centre layers of the same orientation remain bonded. Delamination is only observed in the immediate neighbourhood of the failed region between layers of opposite orientation. Both failure modes coalesce and develop a V-shaped fracture surface on both sides of the specimen. Characteristic microscopic features in the SEM micrograph, Figure 5.4c, are fibre imprints (A), partly bare fibre surfaces, highly deformed matrix regions (C), and the creation of new surfaces (D) forming *cusps* (or *hackles* as they are alternatively known).

Compression

Figure 5.5 shows the axial stress and the secant stiffness during compressive loading. In absolute values, the courses follow the trend of the tensile test results. Due to the test configuration the applicable strain was limited to

a) b)
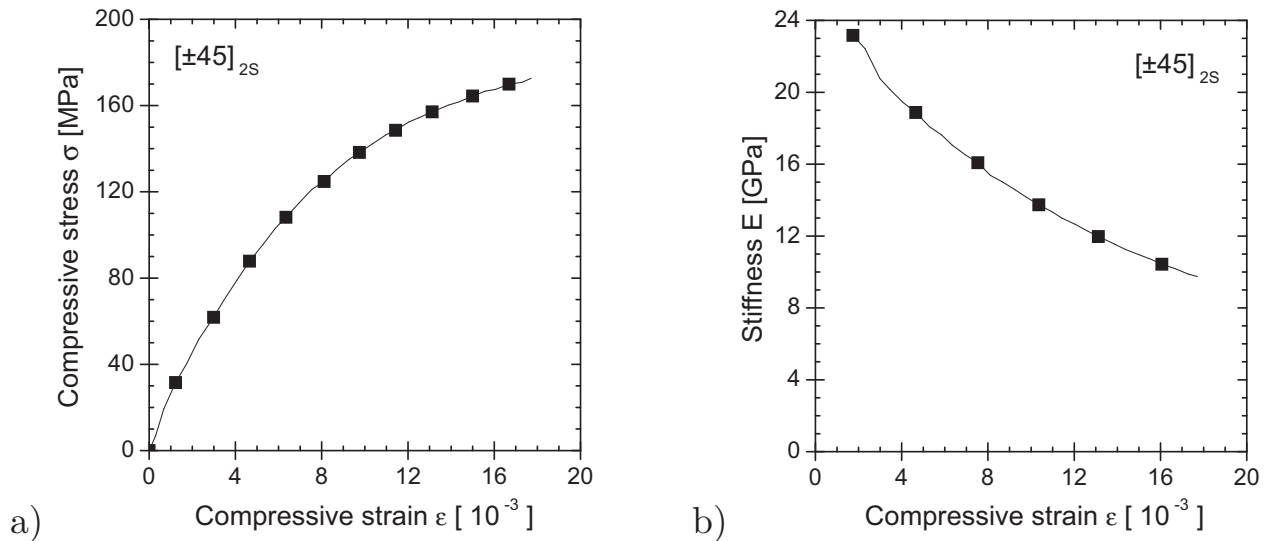
Figure 5.5: Compressive behaviour of the angle-ply laminate. a) stress vs. strain and b) secant stiffness vs. compressive strain

$\varepsilon \approx 30 \cdot 10^{-3}$ to avoid contact between the anti-buckling device and the grips. However, failure normally occurred at lower strains. In some cases failure occurred outside the supported length by buckling close to the grips. The Young's modulus in compression was determined from five tests to $20.6 GPa \pm 0.2 GPa$.

Stepwise tests

The stepwise tests on the AP laminate were carried out under identical test conditions for tension and compression. The only difference were the applied target strains for the load stages four and higher (Table 4.2). Figure 5.6 shows the development of stresses and strains in tension and compression.

According to the applied stroke control the courses of strain are in sections linear vs. time. For either loading, tension and compression, the course of

a)   b)
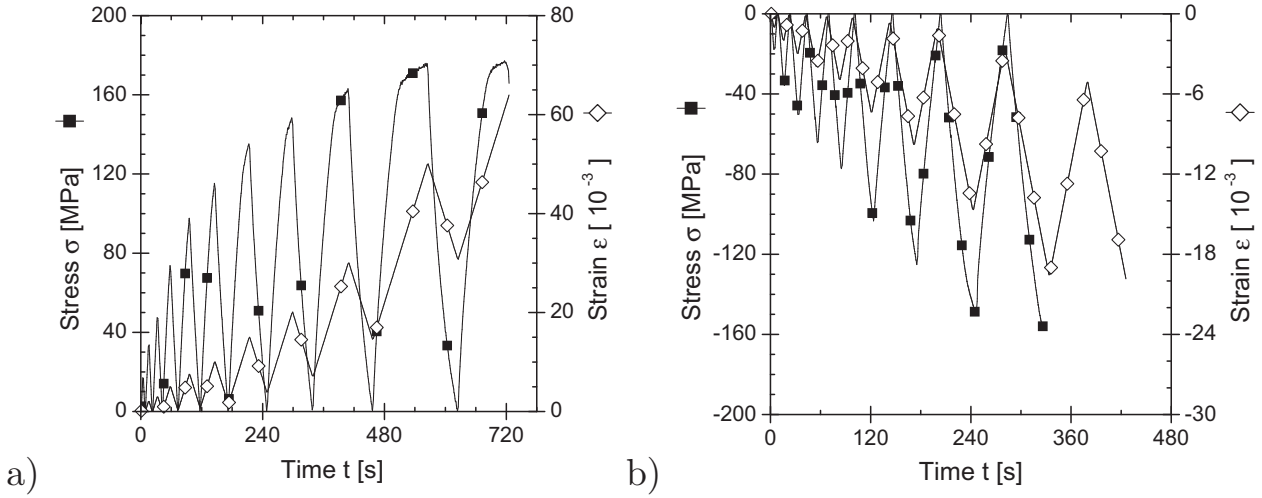
Figure 5.6: Stress and strain vs. time during stepwise loading in a) tension and b) compression.

stress becomes nonlinear with time at about $4 \cdot 10^{-3}$ applied strain. Above $3 \cdot 10^{-3}$ applied absolute strain the strain does not instantaneously decrease to zero after unloading to $F = 0$. The absolute value of viscoelastic strain after unloading increases as the load stages progress.

5.2 Strain rate dependent tensile loading

5.2.1 Stress-strain behaviour

The applied actuator velocities of $v = 0.2$, 2, 20, 200, 2000, and $20000 mm/min$ cover five decades of RSA. The chosen actuator velocities correspond according to Eq. (2.54) and $l_0 = 100mm$ to technical strain rates of $\dot{\varepsilon}_0 = 0.0\overline{3}$, $0.\overline{3}$, $3.\overline{3}$, $33.\overline{3}$, $333.\overline{3}$ and $3333.\overline{3} \cdot 10^{-3}\,s^{-1}$. Figure 5.7a compares the stress-strain behaviour for the different applied strain rates. The curve marked with the closed squares ($\dot{\varepsilon}_0 = 0.\overline{3}$) conforms to the standardised tensile test conditions according to ISO 527-1.

Figure 5.7a shows that the yield stress increases with increasing strain rate. More details with all results are shown in Figure A.1. The stress-strain curves for $\dot{\varepsilon}_0 = 0.0\overline{3} \cdot 10^{-3}\,s^{-1}$ and $3.\overline{3} \cdot 10^{-3}\,s^{-1}$ exhibit the same characteristics as the curve from the standardised tensile test. For the higher applied strain rates of $\dot{\varepsilon}_0 = 333.\overline{3} \cdot 10^{-3}\,s^{-1}$ and $3333.\overline{3} \cdot 10^{-3}\,s^{-1}$ no renewed stress increase is observed after the decrease from the the yield stress. Both kinds of the stress-strain behaviour are observed for the medium strain rate of $\dot{\varepsilon}_0 = 33.\overline{3} \cdot 10^{-3}\,s^{-1}$.
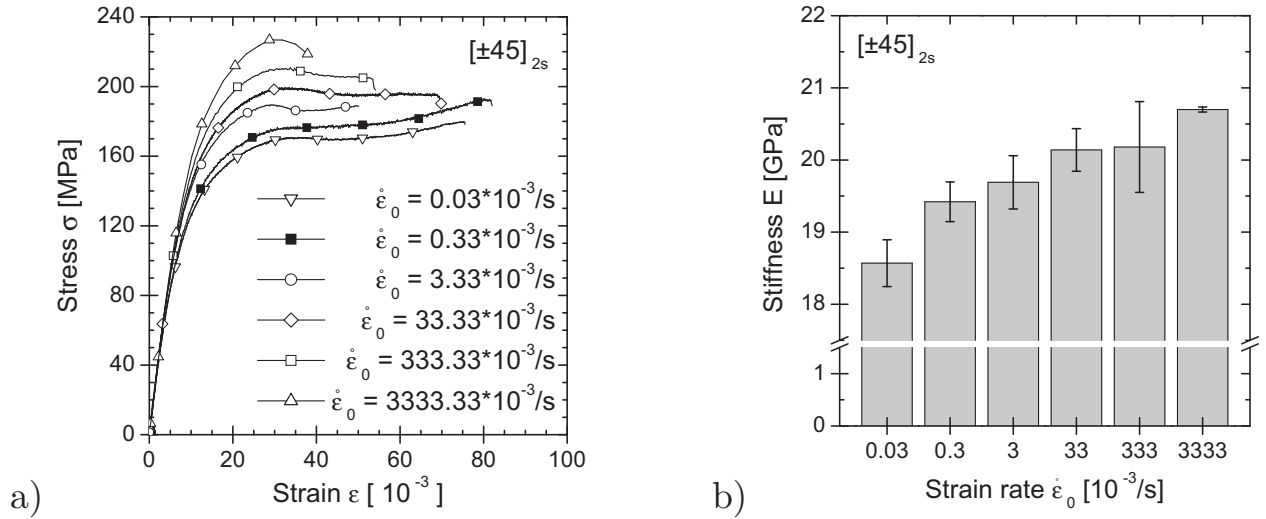
Figure 5.7: Effect of strain rate on the a) stress-strain behaviour and b) the Young's modulus.
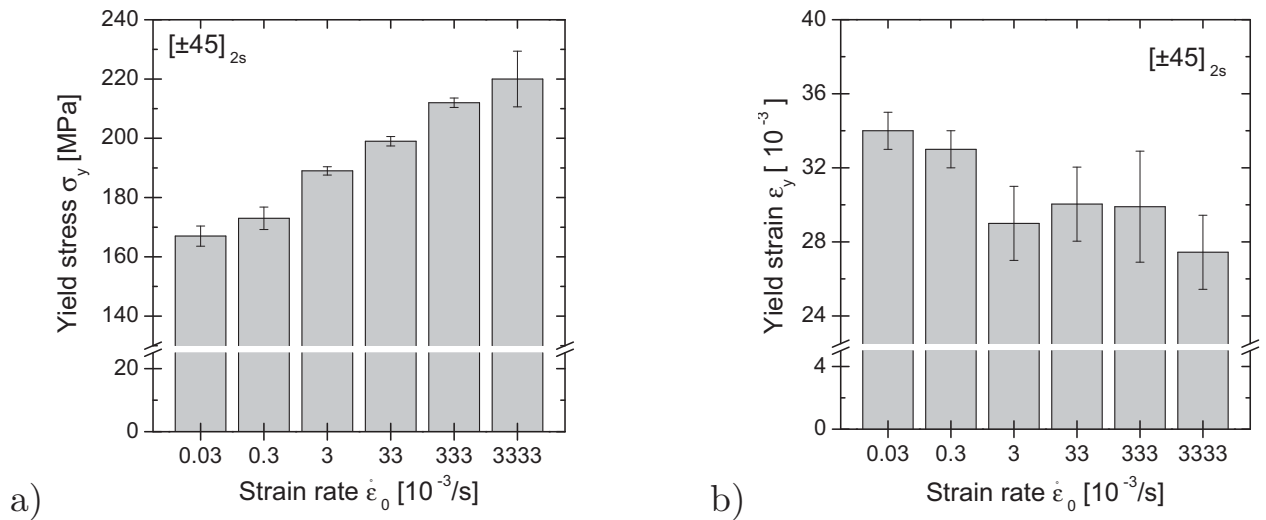
Figure 5.8: Effect of strain rate on the a) yield stress and b) the yield strain.

Figure 5.7b visualises mean values and SDs of the laminate stiffness. The stiffness increases with increasing strain rate. The dependence of the yield stress and the yield strain on the strain rate is shown in Figure 5.8. Whereas the yield stress increases with increasing strain rate, the yield strain tends to decrease. The higher the strain rate, the lower is the amount of plastic strain after yielding. For all applied strain rates, the yield properties are more characteristic than the ultimate properties.

MVs and SDs of stiffness, yield stress and yield strain are summarised in Table 5.3, all data are given in Table A.3. Aiming to exclude any effects from the specimen preparation and conducting the experiment, only those samples were chosen as reference data for $\dot{\varepsilon}_0 = 0.\overline{3}$ which came from the same charge as the samples for the other strain rates. Based on these data, Eqs. (5.5) to

(5.7) give linear approximations determined by least square method. The quality of the fit is excellent for the yield stress and moderate for the yield strain and the stiffness.

Table 5.3: Rate dependent properties (MV±SD) [201].

Strain rate $\dot{\varepsilon}_0 \, [10^{-3} \, s^{-1}]$	Stiffness E [GPa]	Yield stress $\sigma_y[MPa]$	Yield strain $\varepsilon_y[10 \cdot 10^{-3}]$
$0.0\overline{3}$	18.3 ± 0.4	167 ± 4	34 ± 1
$0.3\overline{3}$	19.4 ± 0.3	173 ± 4	33 ± 1
$3.3\overline{3}$	19.6 ± 0.5	188 ± 3	30 ± 3
$33.3\overline{3}$	19.8 ± 0.7	199 ± 1	29 ± 2
$333.3\overline{3}$	19.9 ± 0.4	212 ± 2	30 ± 2
$3333.3\overline{3}$	20.6 ± 0.3	220 ± 9	28 ± 2

$$
\begin{aligned}
E(\dot{\varepsilon}_0) &= 19.2 GPa + 0.38 GPa \cdot \lg(\varepsilon_0 \, [10^{-3} \, s^{-1}]), \ R^2 = 0.76 \quad (5.5) \\
\sigma_y(\dot{\varepsilon}_0) &= 182 MPa + 11.2 MPa \cdot \lg(\varepsilon_0 \, [10^{-3} \, s^{-1}]), \ R^2 = 0.98 \quad (5.6) \\
\varepsilon_y(\dot{\varepsilon}_0) &= 32 \cdot 10^{-3} - 1.2 \cdot 10^{-3} \cdot \lg(\varepsilon_0 \, [10^{-3} \, s^{-1}]), \ R^2 = 0.74 \quad (5.7)
\end{aligned}
$$

5.2.2 Thermographic results

Figures 5.9, 5.10, and 5.13 show sequences of thermographic pictures taken during quasi-static tensile tests. The applied strain rates were $\dot{\varepsilon}_0 = 3.\overline{3} \cdot 10^{-3}/s$ for Figures 5.9 and 5.10, and $\dot{\varepsilon}_0 = 3333.\overline{3} \cdot 10^{-3}/s$ for Figure 5.13. Each picture contains temperature values in units of $[°C]$ from four different positions (subsection 4.3.7). All pictures show a surface temperatures rise from the top to the bottom of the specimen. This effect is due to the conducted heat input from the actuator via the lower clamping fixture into the samples. The Figures 5.9a, 5.10a, and 5.13a represent reference pictures of clamped yet unloaded specimens. The temperature gradients over the gauge length are in the range of 1 to $3K$.

Figure 5.9b shows an almost uniform temperature distribution for $20 \cdot 10^{-3}$ applied strain. A localised surface temperature increase of $3K$ around the position P02 is visible at $30 \cdot 10^{-3}$ applied strain (Figure 5.9c). This zone of increased temperature is oriented in one of the fibre directions. Failure occurs shortly after[3] along this line of increased temperature at $32 \cdot 10^{-3}$ applied strain (Figure 5.9d).

---

[3] As described in detail in subsection 4.3.7, the distance of P02 to the lower gripping jaw is $20mm$. Failure occurred therefore away from the grips.

Figure 5.9: Development of the surface temperature during a tensile tests with $\dot{\varepsilon}_0 = 3.\overline{3}\cdot 10^{-3}/s$. a) $\varepsilon = 0$, b) $\varepsilon = 20\cdot 10^{-3}$, c) $\varepsilon = 30\cdot 10^{-3}$, and d) $\varepsilon_{utt} = 32\cdot 10^{-3}$.
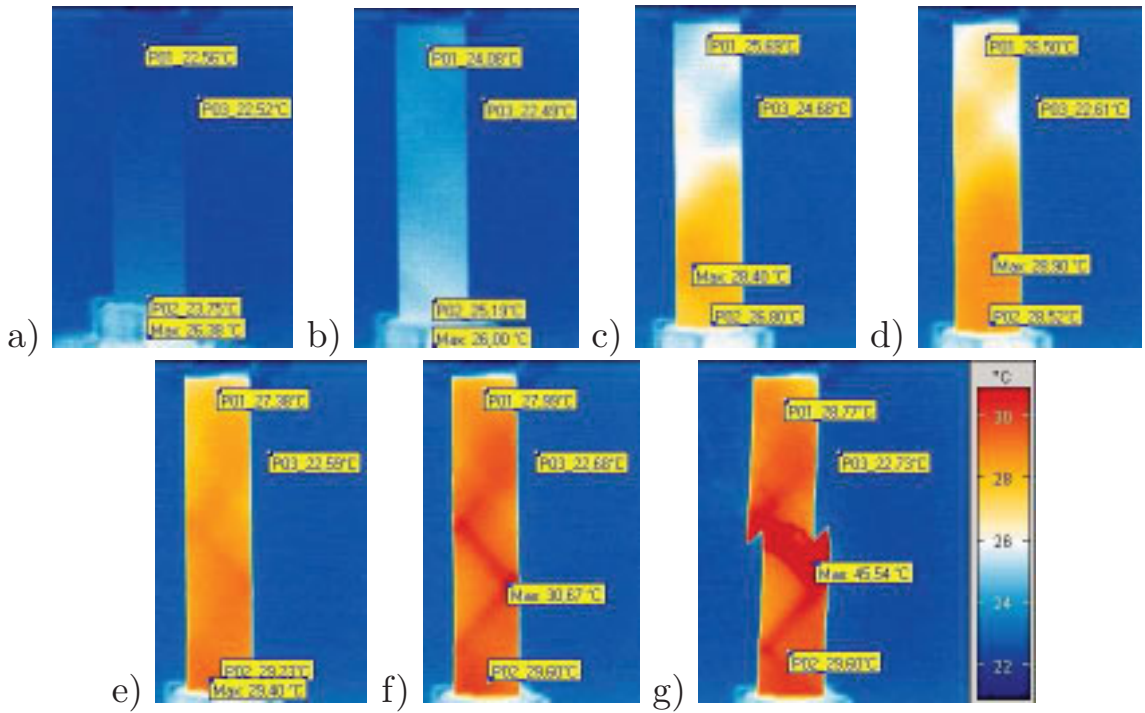
Figure 5.10: Development of the surface temperature during a tensile tests with $\dot{\varepsilon}_0 = 3.\overline{3} \cdot 10^{-3}/s$. a) $\varepsilon = 0$, b) $\varepsilon = 30 \cdot 10^{-3}$, c) $\varepsilon = 50 \cdot 10^{-3}$, d) $\varepsilon = 60 \cdot 10^{-3}$, e) $\varepsilon = 70 \cdot 10^{-3}$, f) $\varepsilon = 80 \cdot 10^{-3}$, and g) $\varepsilon_{utt} = 82 \cdot 10^{-3}$.

Figure 5.10 shows an example of surface temperature development of another specimen but the same applied strain rate as in Figure 5.9. The temperature gradient over the gauge length of approximately $2K$ remains constant during loading. The surface temperature increase shows no characteristic pattern until $60 \cdot 10^{-3}$ applied strain (Figures 5.10b-d). A zigzag temperature pattern with blurry borders running at $\pm45°$ to the load direction and parallel to the fibres from one edge to the other begins to form at $70 \cdot 10^{-3}$ applied strain (Figure 5.10e). The further temperature increase is more pronounced along the zigzag pattern which becomes more distinct (Figure 5.10f). Rupture of the sample occurs in the middle of the gauge length along the

hottest central zigzag line at $82 \cdot 10^{-3}$ applied strain (Figure 5.10g).

Figures 5.11 and 5.12 represent continuous temperature vs. time courses of the selected thermographic pictures in Figures 5.9 and 5.10. For better comparison, the abscissas and ordinates use the same scaling. The strain values from thermographic pictures are marked by numbers and the vertical dash-dotted lines. It can be seen that a higher strain to failure corresponds to
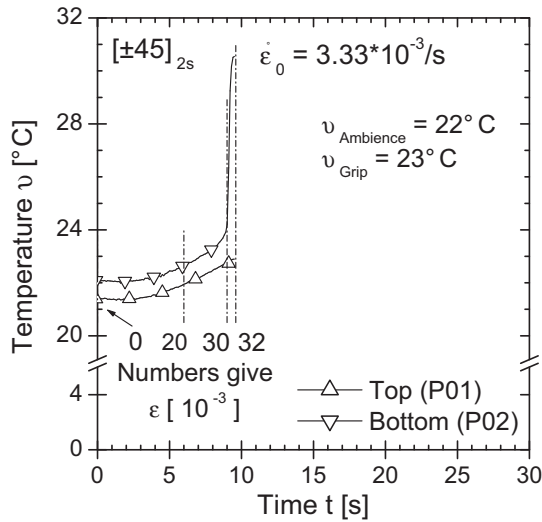
Figure 5.11: Temperature vs. time plot of Figure 5.9.
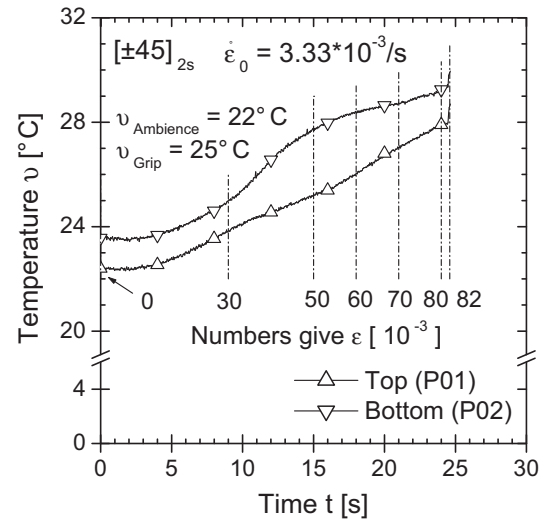
Figure 5.12: Temperature vs. time plot of Figure 5.10.

a longer test duration at the same strain rate. Ambient and grip temperatures remain constant in both tests. The initial bottom surface temperatures are about $1K$ higher than the top surface temperatures. The surface temperature increase is very similar until $30 \cdot 10^{-3}$ applied strain[4].

The intense increase of only the bottom temperature in Figure 5.11 above $30 \cdot 10^{-3}$ strain signalises immanent rupture and is in good agreement with the observed localised temperature distribution of Figures 5.9c and d. In Figure 5.10, an entire warming is seen opposed to the localised heating in Figure 5.9. The top and bottom temperatures increase approximately linear with time until $80 \cdot 10^{-3}$ applied strain (Figure 5.12). Failure occurs shortly after, without a further intense temperature rise.

Figure 5.13 shows a tensile test with a higher strain rate of $\dot{\varepsilon}_0 = 333.\overline{3} \cdot 10^{-3}/s$. In contrast to Figure 5.10 lines of increased temperature start to form at $20 \cdot 10^{-3}$ applied strain (Figure 5.13b) and become more frequently with further loading. The distinct differences in colour characterise a higher temperature gradient. The orientation of the lines coincides with the fibre directions.

---

[4] An applied strain of $30 \cdot 10^{-3}$ corresponds to the onset of yielding.
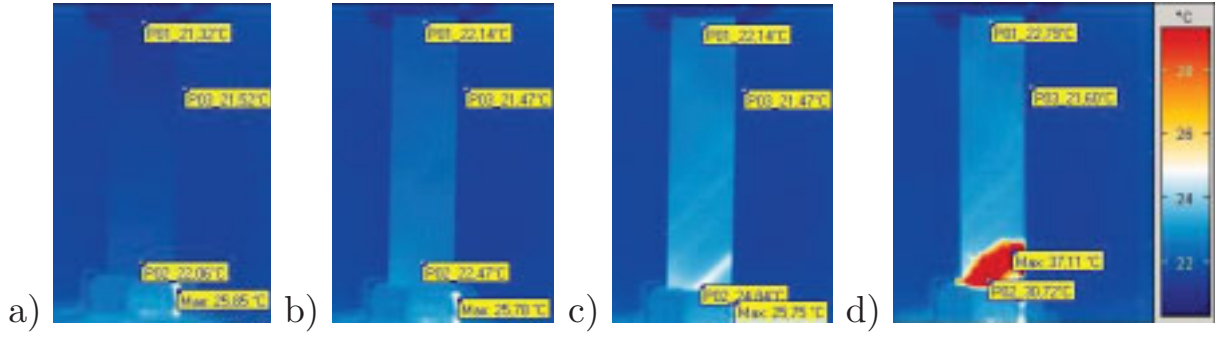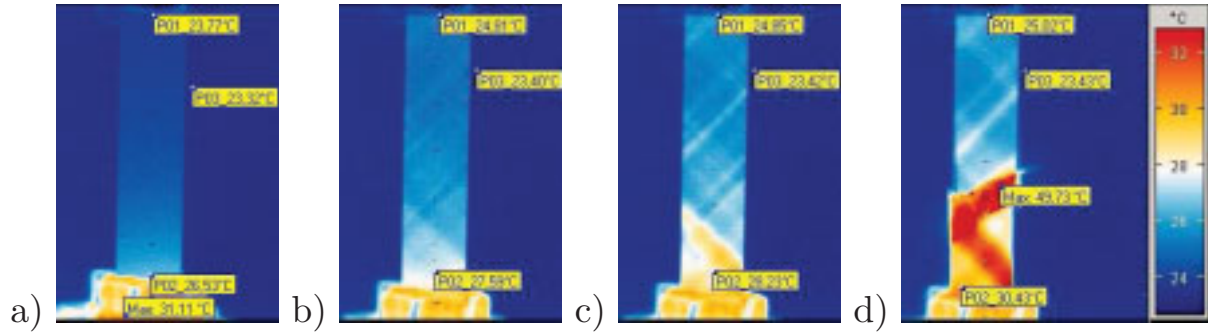
Figure 5.13: Development of the surface temperature during a tensile tests with $\dot{\varepsilon}_0 = 333.\overline{3}{\cdot}10^{-3}/s$. a) $\varepsilon = 0$, b) $\varepsilon = 20{\cdot}10^{-3}$, c) $\varepsilon = 30{\cdot}10^{-3}$, and d) $\varepsilon_{utt} = 42{\cdot}10^{-3}$.

5.2.3   Light microscopy

Figure 5.14 shows a photographic picture of a specimen edge after tensile failure at a technical strain rate of $\dot{\varepsilon}_0 = 333.\overline{3} \cdot 10^{-3}\,s^{-1}$. The symmetric lay-up can clearly be distinguished. The layers 1, 3, 6, and 8 have a $+45°$ orientation, the layers 2, 4, 5, and 7 have a $-45°$ orientation. No layer interface is visible in the symmetry plane. The layers 4 and 5 can thus be
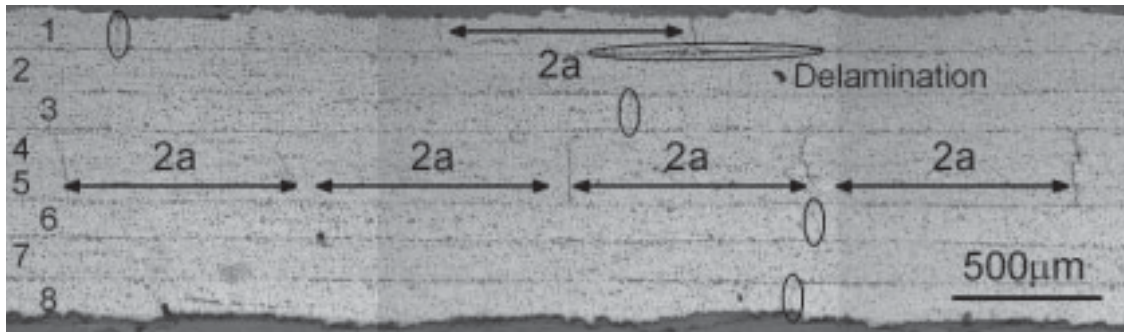
Figure 5.14: Micrograph of a specimen edge after tensile failure ($\dot{\varepsilon}_0 = 333 \cdot 10^{-3}s^{-1}$).

regarded as one centre layer of doubled thickness. The centre layer shows a crack pattern with a characteristic crack spacing $2a$ of about $0.8mm$ which corresponds to a crack density of $2500/m$. No cracks are observed in the layers 2 and 7 of the same orientation. Further cracks are found in layers with the opposite direction, i.e. plies 1, 3, 6, and 8. The cracks seem to be scattered and irregular and are pointed out in Figure 5.14 by vertical ellipses. The shortest crack spacing remains also in these plies $2a \approx 0.8mm$. A delaminated region is seen at the intersection between the layers 1 and 2 and a crack in layer 1.

5.3 Constant loading

5.3.1 Creep results

Nine stress levels ranging between 29 and 83% times the yield stress were chosen for creep testing. The creep curves in linear time scale are given in Figure 5.15a. The curves exhibit the characteristics of the 'classical creep' curve during the first and secondary stage. For the investigated stresses and times, no evidence of a tertiary creep stage or creep rupture was found. Dependent on the applied stress and with increasing time a strain increase
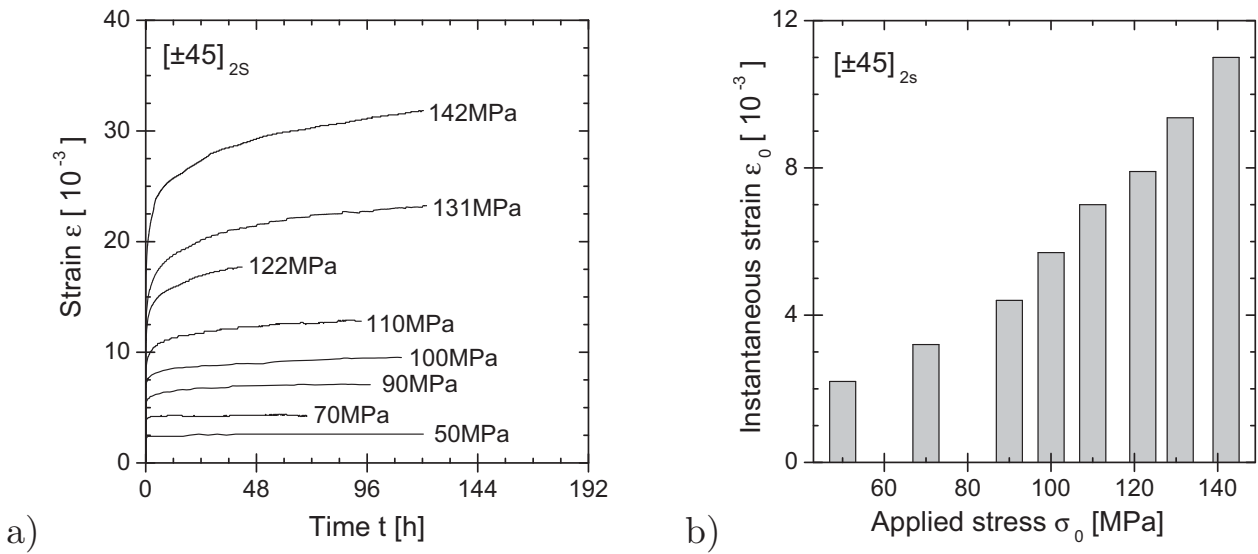
Figure 5.15: Creep results. a) creep strain vs. time and b) instantaneous strain vs. applied stress.

is observed. The creep strain nearly converges to a constant value for applied creep stresses up to $90MPa$. A disproportional strain enhancement is observed at approximately half of the yield stress. Below this applied stress, the time dependent strain is secondary when compared to the instantaneous strain which is plotted in Figure 5.15b. The instantaneous strain increases as the applied stress increases [202].

5.3.2 Recovery results

The acquisition of the strain data was continued after unloading for selected creep samples. The decay of the strain with time is shown in Figure 5.16a together with the duration and the level of the preceding creep load. The curves are plotted that unloading starts at $t = 0.1h$. The scatter of the $70MPa$ curve corresponds to the resolution of the data acquisition system of $10\mu m$.
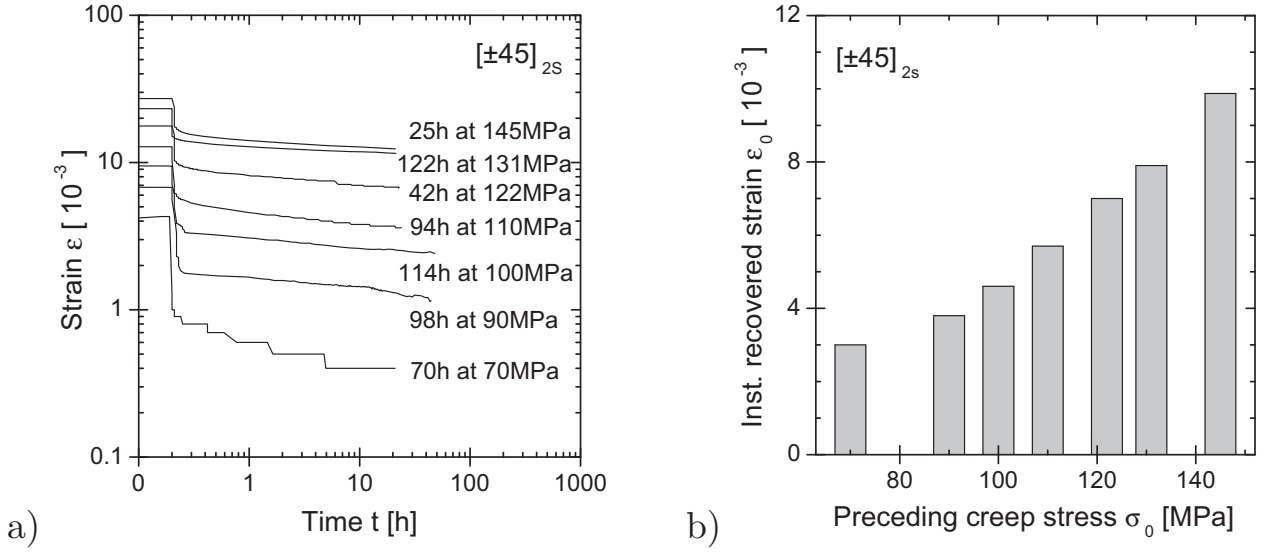
Figure 5.16: Recovery results. a) recovery strain vs. time and b) instantaneously recovered strain vs. applied stress.

After the instantaneous strain relaxation, the recovery strain decreases as the time increases. The shape of the strain decay $d\varepsilon/dt$ is similar for all curves in the double-logarithmic plot. The recovery strain is higher, the higher the preceding creep stress was for the same creep and recovery times. The lower the creep stress, the higher the portion of recovered strain for identical times. The instantaneously recovered strain is plotted in Figure 5.16b. It increases with increasing creep stress.

5.4   Constant amplitude fatigue (CAF) loading

5.4.1   Effect of test frequency

The fatigue life vs. frequency dependence of the AP laminate on the applied stress and the stress ratio is shown in Figure 5.17. The complete data sets are given in Table A.4. No obvious dependence of the S-N data on the test frequency is seen for reverse fatigue loading. Across all frequencies the fatigue life decreases almost linearly in semi-logarithmic presentation as the maximum stress increases.

Figure 5.17b shows the variation of the fatigue life for $R = 0.1$ loading and six combinations of frequency and maximum stress. The disparate positive and negative SDs result from the logarithmic presentation. MVs and SDs are summarised in Table 5.4. Included in the double-logarithmic plot are linear isochronous curves according to Eq. (2.56). As the frequency increases, the fatigue lives decrease for both stress levels. However, the intervals of the SDs overlap for all frequencies.
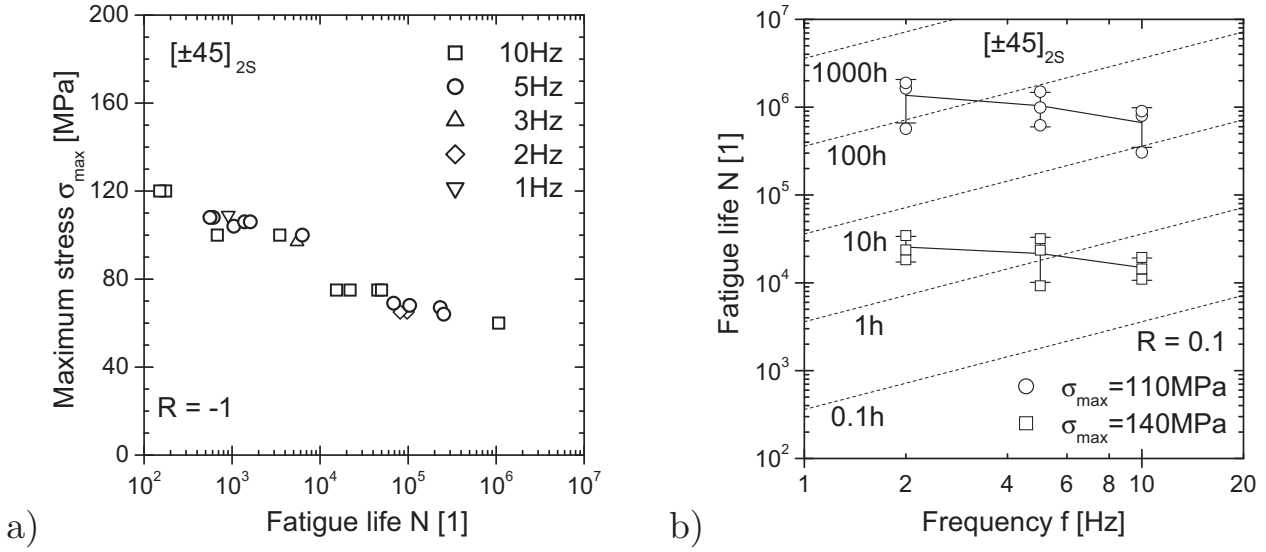
Figure 5.17: Effect of load frequency on the fatigue life for a) $R = -1$ and b) $R = 0.1$.

Table 5.4: Stress and frequency dependent fatigue lives for $R = 0.1$

Maximum stress σ_{max}	$110MPa$			$140MPa$		
Frequency f	$2Hz$	$5Hz$	$10Hz$	$2Hz$	$5Hz$	$10Hz$
Mean fatigue life N $[10^3]$	1363	1037	669	25.5	21.5	14.9
SD of N $[10^3]$	±701	±440	±319	±8.2	±11.4	±4.2

Figure 5.18 shows the evolution of mean strain and strain amplitude with the number of cycles for each of the investigated combinations of maximum stress and frequency. The higher the stress, the higher are the levels of mean strain and strain amplitude. All curves show a linear course for several decades of cycles in the semi-logarithmic presentation. Towards the end of the fatigue life, mean strain and strain amplitude evolution increase progressively. For the linear region can be stated that for both stress levels the mean strain increases linearly, e.g. from $8 \cdot 10^{-3}$ at 100 cycles to $12 \cdot 10^{-3}$ at 20000 cycles for $140MPa$ maximum stress. The strain amplitude remains almost unchanged for $140MPa$ and decreases slightly for $110MPa$.

As presented in Figure 5.18, the mean strain and the strain amplitude correlate independent from the test frequency with the number of cycles. The strain evolution for $R = 0.1$ loading and mean stresses between 60 and $77MPa$ is thus primarily a function of the cycle number and the applied stress whereas the effect of frequency (between 2 and $10Hz$) is secondary.
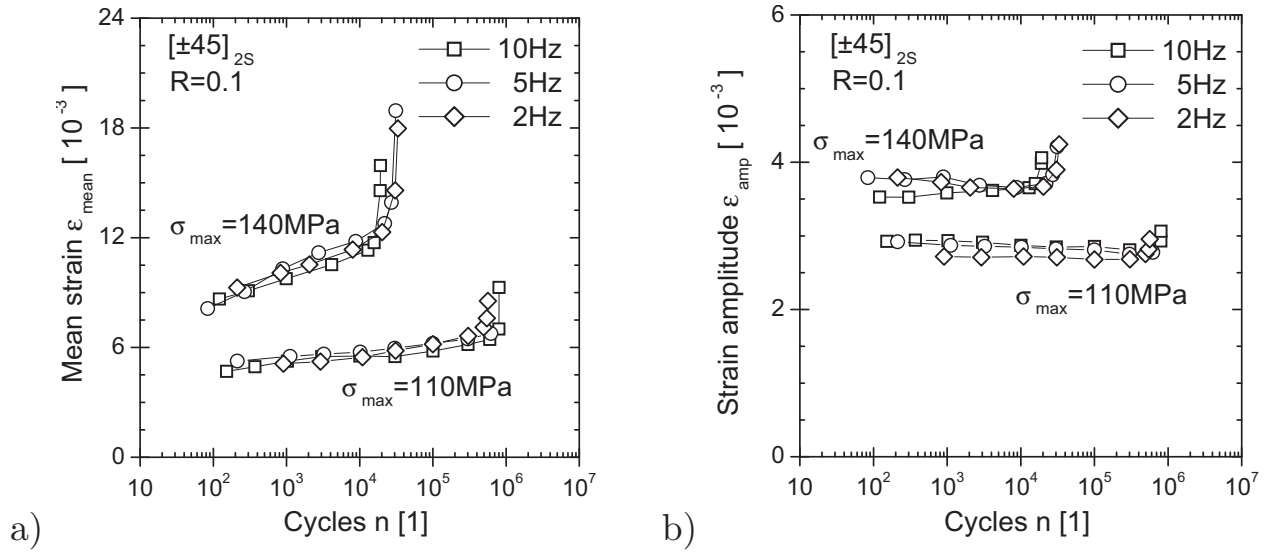
Figure 5.18: Effect of load frequency on strain evolution for $R = 0.1$ CAF loading and different maximum stresses. a) mean strain and b) strain amplitude.

Surface temperature

A representative temperature development vs. the normalised fatigue life on a semi-logarithmic scale is plotted in Figure 5.19. The ambient temperature of $25°C$ and the grip temperature of $29°C$ are constant throughout the test duration. The top and bottom surface temperatures run parallel for most
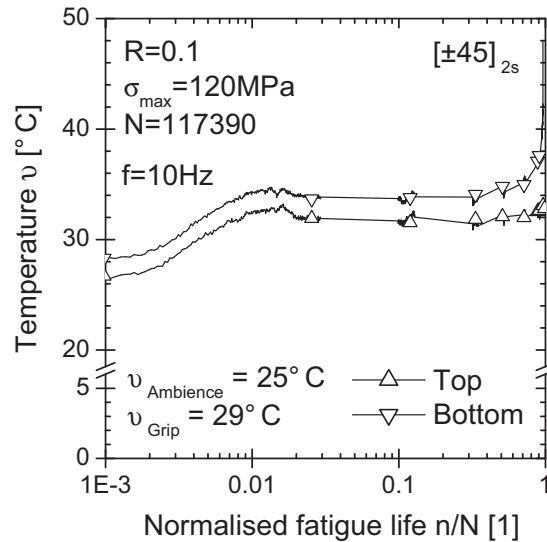
Figure 5.19: Temperature development during CAF.

of the fatigue life. The bottom temperature remains permanently about $2K$ higher which is due to the heat input from the hydraulic actuator. The surface temperature increases as the fatigue cycling starts and approaches a $6K$ higher plateau value after about 1500 cycles ($t = 150s$) or approximately

1.3% of the fatigue life). Following, this temperature plateau value is kept for more than 75% of the fatigue life.

A localised accelerated temperature increase is observed towards the end of the fatigue life (Figure 5.20) whereas the remaining material keeps the plateau temperature. The local temperatures of the hottest regions rise up to values of about $50°C$ close to failure which occurs in the region of highest temperature.
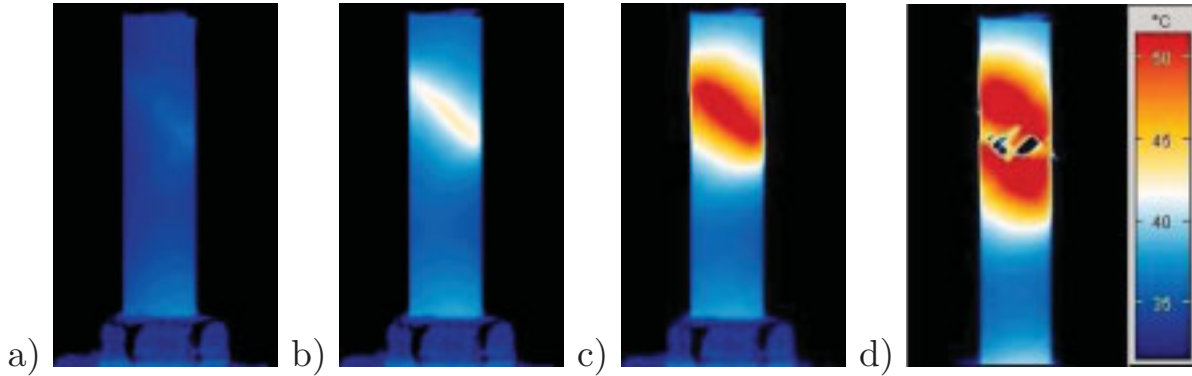
Figure 5.20: Development of the surface temperature during a fatigue test with failure at $N = 258060$. a) $n/N = 0$, b) $n/N = 0.81$, c) $n/N = 0.98$, and d) $n/N = 1$.

5.4.2   Effect of stress ratio

Three S-N curves for tension-tension loading and the S-N curve for reverse loading are shown in Figure 5.21. The half filled symbols represent samples surviving the indicated number of more than 10^6 cycles. All individual S-N data are collected in Tables A.4 and A.5.

The S-N data can be well approximated by a straight line in semi-logarithmic presentation. Linear approximations of the S-N data are marked by the solid lines, the confidence bands for $P = 68\%$ by the dotted lines, and those for $P = 95\%$ by the dashed lines. With a probability of P, the S-N data points are within the respective confidence interval[5]. The best fit equations which are given in Eqs. (5.8) to (5.11) were determined by the least square method. The run out data were not used for the statistical analysis. The data bases for $R = 0.5$ and $R = 0.3$ are limited each to two decades of cycles whereas the approximations for $R = 0.1$ and $R = -1$ are based on data from four decades of cycles. All curves should not be applied to fatigue lives outside the underlying S-N data base. This is due to the increasing uncertainty of the prediction visible at the larger confidence intervals.

---

[5] The confidence intervals are calculated from the logarithms of the fatigue lives. They are symmetric to the mean curve in logarithmic presentation.
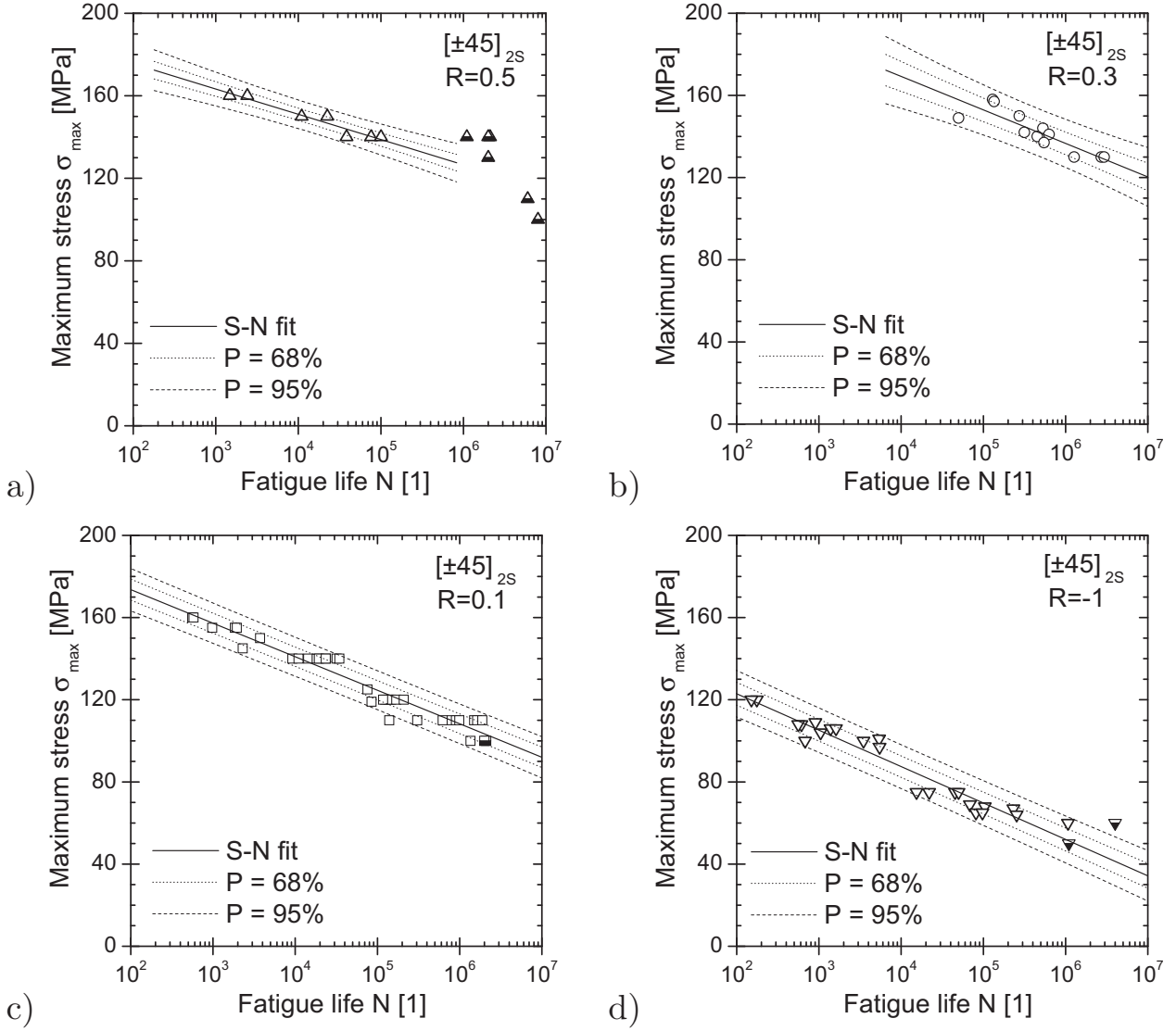
Figure 5.21: S-N curves for different stress ratios. a) $R = 0.5$, b) $R = 0.3$, c) $R = 0.1$, and d) $R = -1$.

$$R = 0.5 \; : \; \sigma_{max}(N) = 200.0 MPa - 12.24 MPa \cdot \lg(N), R^2 = 0.94 \quad (5.8)$$

$$R = 0.3 \; : \; \sigma_{max}(N) = 234.5 MPa - 16.30 MPa \cdot \lg(N), R^2 = 0.77 \quad (5.9)$$

$$R = 0.1 \; : \; \sigma_{max}(N) = 206.2 MPa - 16.32 MPa \cdot \lg(N), R^2 = 0.94 \quad (5.10)$$

$$R = -1 \; : \; \sigma_{max}(N) = 158.4 MPa - 17.72 MPa \cdot \lg(N), R^2 = 0.94 \quad (5.11)$$

From the experimental results can be stated that the intercept with $N = 1$ and the slope of the S-N curve tend to decrease as the stress ratio decreases. The alleviated trend for $R = 0.5$ and $R = 0.3$ results from the limited underlying S-N data base. For a constant maximum stress, a decrease of the stress ratio (for $R < 1$) is related to an increase of the stress amplitude.

Definite endurance limits cannot be identified from Figure 5.21. For $R = 0.1$ and $R = -1$ one obtains from Eqs. (5.10) and (5.11) for $N = 2 \cdot 10^6$ maximum stresses of 103 and $46 MPa$ respectively. From Tables A.4 and A.5 can be seen that a survival of the samples may be expected for applied maximum stresses of 100 and $50 MPa$ respectively. The results are in good agreement but not statistically secured.

The variations of the hysteresis loops and the courses of mean strain and strain amplitude with the normalised fatigue life are shown in Figures 5.22 to 5.27. For each of the stress ratios $R = 0.5$, 0.1 and -1 one example for a high load (low fatigue life) and one for a low load (long fatigue life) is given.

$\mathbf{R = 0.5}$

Figures 5.22 and 5.23 follow the same general trend. In a first stage up to 20% of the fatigue life the mean strain increases in a declining fashion. In a second stage from $n/N = 20\%$ to final failure the mean strain increases further on linearly, being in value (ε_{mean}) and slope ($d\varepsilon_{mean}/dn$) larger for the higher applied stress. The strain amplitude and thus the dynamic stiffness is almost the same for both applied stresses and remains constant throughout the fatigue life. Final failure occurs suddenly without the typical third stage of disproportional loss of stiffness, i.e. increase of strain amplitude or a progressive mean strain increase.

Figure 5.22: $R = 0.5$: Variation of a) mean strain and strain amplitude and b) the hysteresis loops for a high cyclic stress.

As indicated by the constant strain amplitudes and increasing mean strains, the hysteresis loops shift to higher strains as the cycle number increases. The rotation of the loops is negligible. A difference between Figures 5.22b and 5.23b is the level of damping, visible at the area of the hysteresis loops.
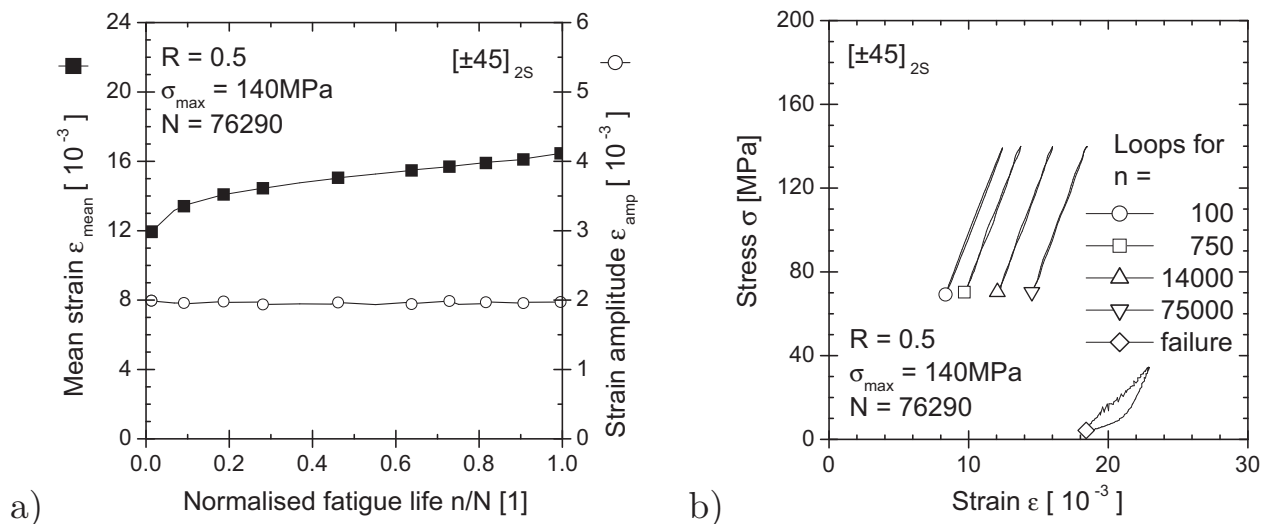
Figure 5.23: $R = 0.5$: Variation of a) mean strain and strain amplitude and b) the hysteresis loops for a low cyclic stress.

Although the loops are narrow for both stress levels, their area is larger for the higher applied stress.

$R = 0.1$

Three characteristic stages (Figures 2.10 and 2.20) can be distinguished for the course of mean strain (Figures 5.24a and 5.25a). The stages are more pronounced for the higher maximum stress. The mean strain increase during the primary stage occurs disproportional to the applied stress, it doubles from 6 to $12 \cdot 10^{-3}$ mean strain at $140MPa$ maximum stress and increases by 20% from 5 to $6 \cdot 10^{-3}$ mean strain at $110MPa$ maximum stress.

The steady-state stage lasts for 50% (from 30 to 80%) of the fatigue life at $140MPa$ maximum stress and 75% (from 20 to 95%) of the fatigue life at at $110MPa$ maximum stress. The slope $d\varepsilon_{mean}/dn$ is higher for the higher load.

The strain amplitude for $110MPa$ maximum stress remains about constant at $3 \cdot 10^{-3}$ throughout the fatigue life. For $140MPa$ maximum stress the strain amplitude increases from its initial value by one twentieth during the first 10% of the fatigue life. For the next 60% of the fatigue life the strain amplitude decreases continuously but remains above the initial value. The last 30% of the fatigue life are accompanied by another increase of the strain amplitude by about 10%. The onset of this final increase of the strain amplitude coincides with the transition from the secondary to the tertiary stage of the mean strain evolution.

The hysteresis loops (Figures 5.24b and 5.25b) have the same characteristics as for $R = 0.5$. Regarding the enclosed area, the loops are larger for $R = 0.1$

a)
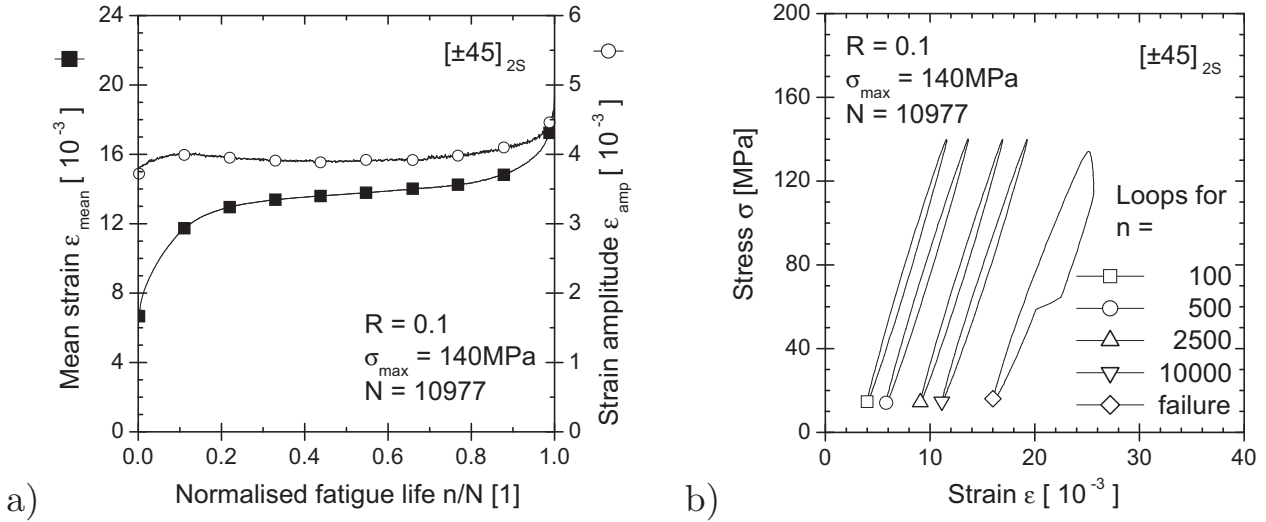
Figure 5.24: $R = 0.1$: Variation of a) mean strain and strain amplitude and b) the hysteresis loops for a high cyclic stress.

a)
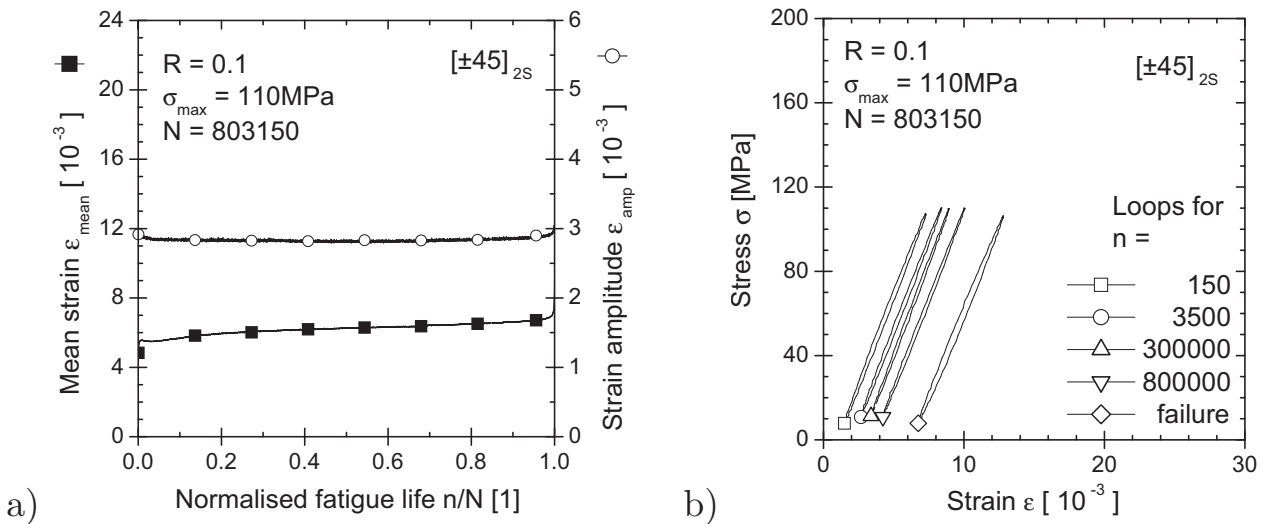
Figure 5.25: $R = 0.1$: Variation of a) mean strain and strain amplitude and b) the hysteresis loops for a low cyclic stress.

which means that more energy is dissipated per load cycle.

R = -1

The applied mean stress for $R = -1$ is zero. The maximum stress is equal to the stress amplitude. Figures 5.26 and 5.27 show that the mean strain for reverse fatigue loading is zero as well. Zero mean strain denotes that the maximum strain is equal to the strain amplitude.

The courses of strain amplitude follow the above described curves with three stages. The strain level and the extent of each of the stages depend on the applied stress. The secondary stage for $75MPa$ maximum stress lasts for
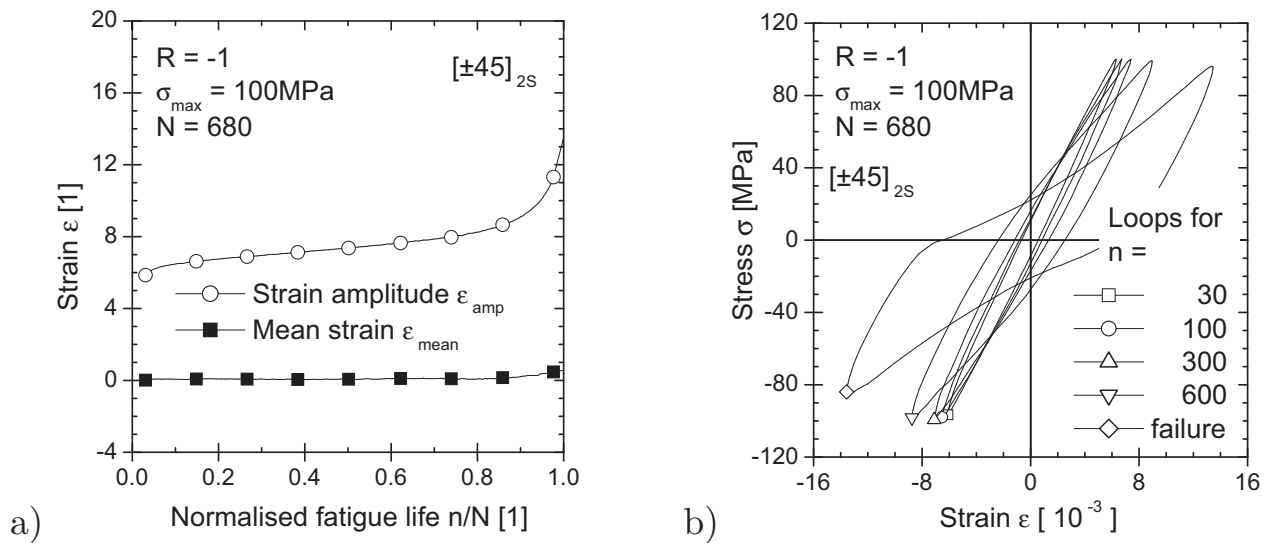
Figure 5.26: $R = -1$: Variation of a) mean strain and strain amplitude and b) the hysteresis loops for a high cyclic stress.

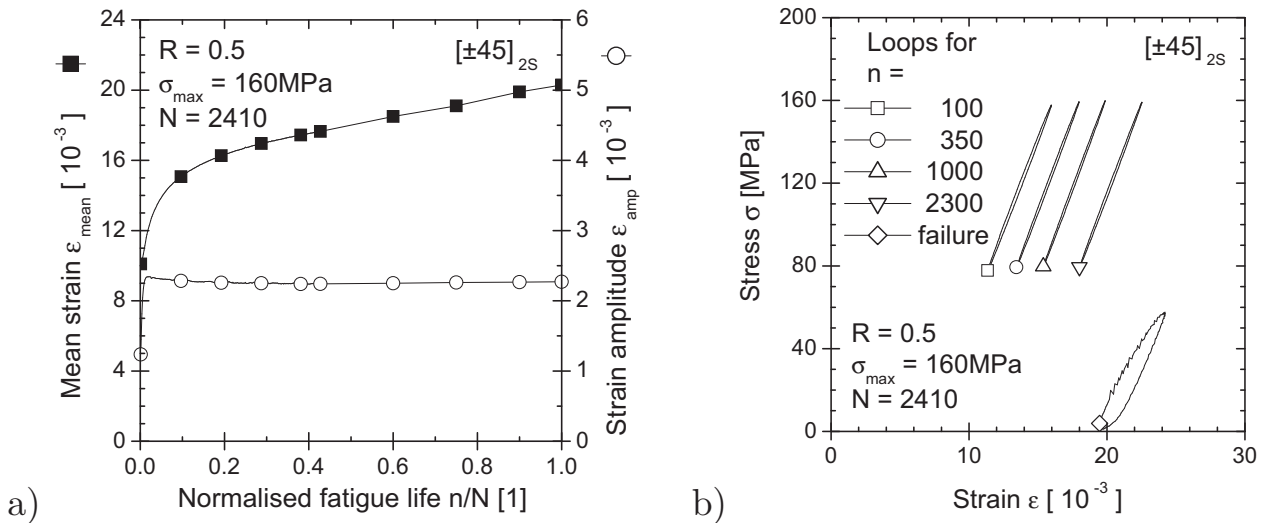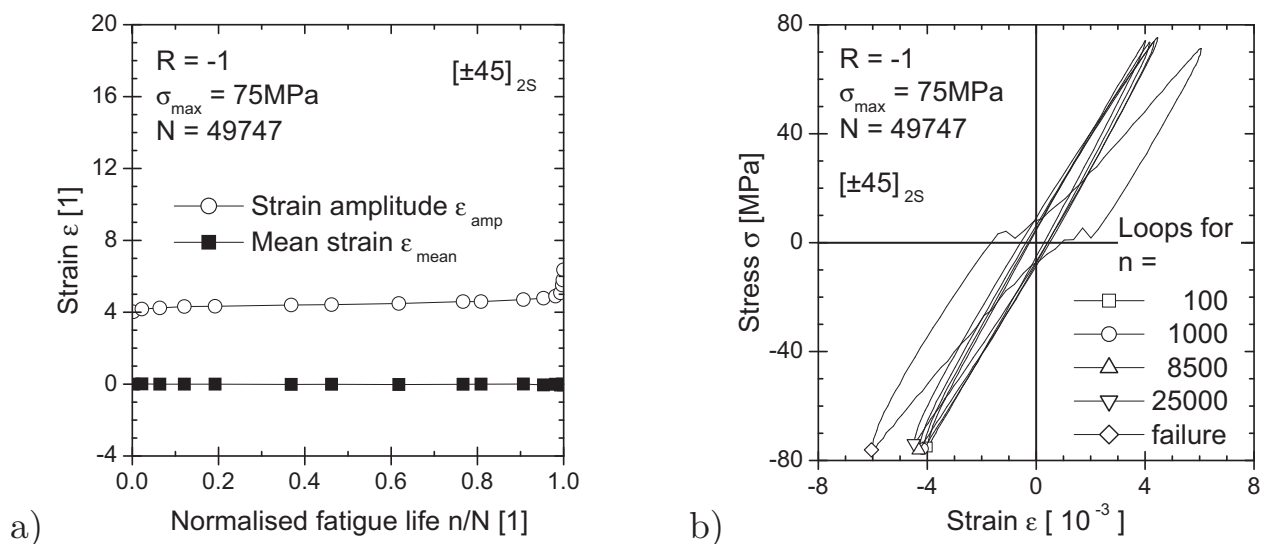**Figure 5.27:** $R = -1$: Variation of a) mean strain and strain amplitude and b) the hysteresis loops for a low cyclic stress.

more than 90% (from 5 to 95%) of the fatigue life. The strain amplitude increases during that stage by 20% from 4 to $5 \cdot 10^{-3}$ which corresponds to a loss in stiffness by 20%. The relative increase of the strain amplitude for $100 MPa$ maximum stress during the secondary stage is similar. However, the secondary stage lasts for about 50% (from 20 to 70%) of the fatigue life. During the tertiary stage, the strain amplitude increases disproportional from $8 \cdot 10^{-3}$ strain amplitude at 70% of the fatigue life to $12 \cdot 10^{-3}$ strain amplitude just before final failure. This increase in strain amplitude by 50% corresponds to a loss of 50% stiffness during that stage.

5.4.3 Microscopic results

Optical analysis of the specimen edges

Figure 5.28 shows a light micrograph of a specimen edge after fatigue failure. The layer characteristics is as described in subsection 5.2.3, the layers 1, 3, 6, and 8 have a $+45°$ orientation, the layers 2, 4, 5, and 7 have a $-45°$ orientation. The layers 4 and 5 can be regarded as one centre layer of doubled thickness because no layer interface is visible in the symmetry plane.

Representative for all other fatigue loadings, no signs of cracking or delamination are observed away from the immediate neighbourhood of the ruptured region, which looks apparently like that of a tensile test shown in Figures 5.4a and b.
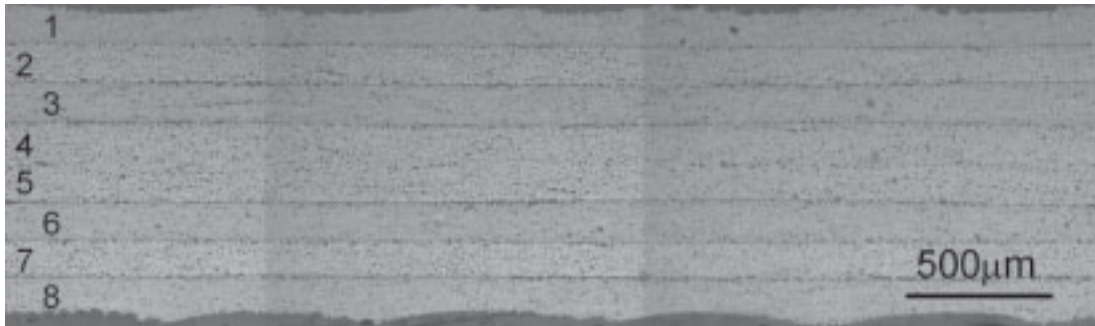
Figure 5.28: Micrograph of a specimen edge after CAF with $R = 0.1$, $\sigma_{max} = 120 MPa$ and failure at $N = 209130$.

Fractographic analysis with SEM

SEM pictures of typical fracture morphologies for tension-tension and tension-compression fatigue are shown in Figures 5.29 and 5.30 respectively. The figures to a) show highly loaded samples and those to b) lowly loaded samples. A more complete selection can be found by Stange [203].

Figure 5.29a shows for $R = 0.1$ and a short fatigue life regions on the fibres (A) and on the fibre imprints (B) where the fibre/matrix interface is still intact as well as regions without fibre/matrix bonding (C). The intralaminar crack (K-K) propagating in the matrix parallel to the fibres indicates a strong fibre/matrix interface when compared to the matrix strength. Sharp and large cusps (D) inclined to the interlaminar 1-2 plane and aligned with the fibre direction are found in the volume between the tightly packed fibres. The surface topography is about one fibre diameter deep. The interface to the adjacent layer of opposite direction is not visible.

For a long fatigue life, Figure 5.29b shows that there is almost no more fibre/matrix bonding on those fibre surface areas (E) that are directed to the fracture plane. The fracture surface has a low roughness and the matrix

cusps look abraded. The volume between the tightly packed fibres (F) keeps filled with resin. Imprints of fibres from the adjacent layer with opposite direction (G) can be observed.
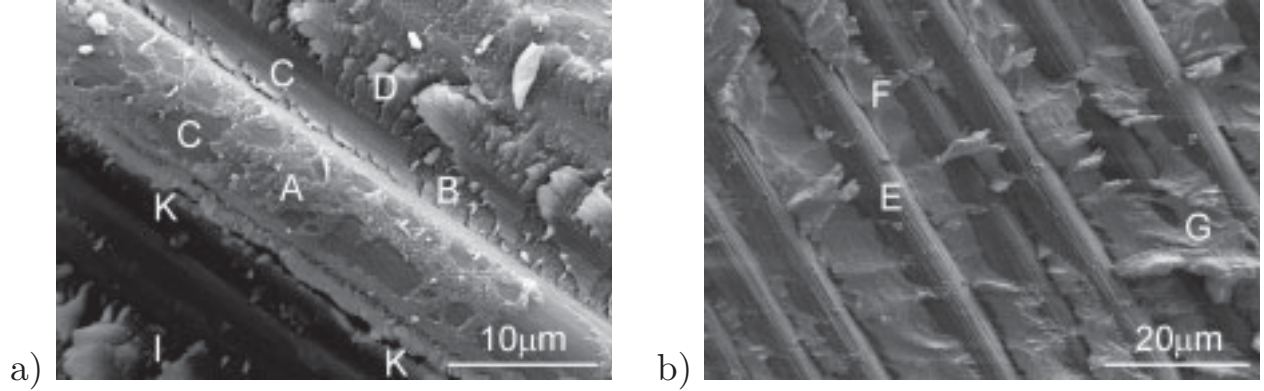
Figure 5.29: SEM pictures of fracture morphologies for $R = 0.1$ fatigue loading.
a) $\sigma_{max} = 160MPa$ and $N = 560$,
b) $\sigma_{max} = 120MPa$ and $N = 146630$.
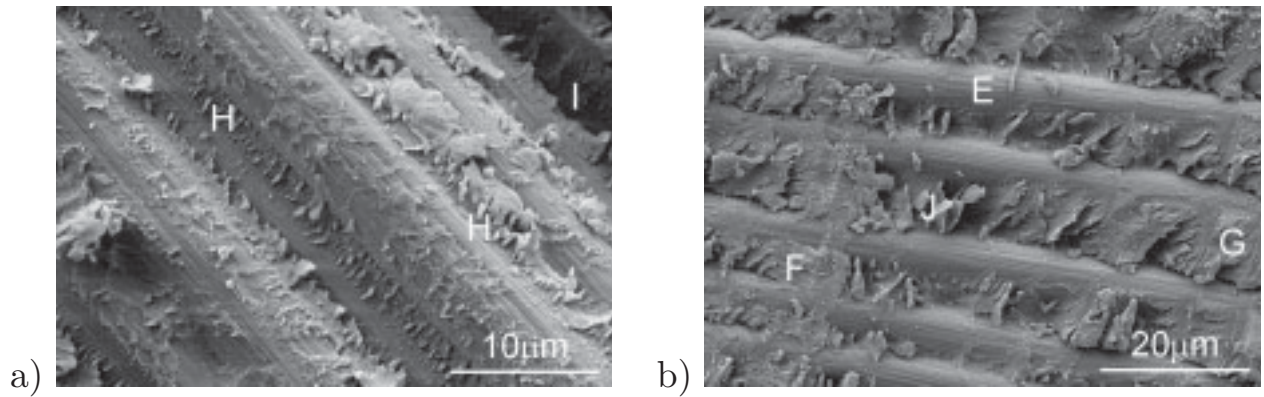
Figure 5.30: SEM pictures of fracture morphologies for $R = -1$ fatigue loading.
a) $\sigma_{max} = 120MPa$ and $N = 151$,
b) $\sigma_{max} = 60MPa$ and $N = 1.07 \cdot 10^6$.

A strong fibre/matrix interface is observed in Figure 5.30a for tension-compression fatigue and a high load. The fibre surfaces and the tightly packed regions between them contain many tiny cusps (H) perpendicular to the fibre direction and the interlaminar plane. Indications of the adjacent layer cannot be distinguished. The fracture surface can be described similarly to Figure 5.29a as rough and deep (I). The fracture surface for low loads in reverse fatigue loading (Figure 5.30b) can by characterised in similar terms as the one for tension-tension loading regarding the microscopic features E, F and G. Opposed to Figure 5.29b, the fracture surface is rougher and contains cusps (J). The orientation of the cusps is identical to the one in Figure 5.30a, however, the size of the cusps is larger.

5.5 Block load fatigue

The effect of load sequences on the fatigue life was investigated for three different load cases (subsection 4.3.3). At a first stress level sinusoidal CAF was applied to a predetermined number of cycles. At the second stress level cycling was continued until failure. Palmgren-Miner's linear cumulative damage law according to Eq. (2.71) was applied to calculate the fractional fatigue lives by normalising the respective (applied and survived) numbers of cycles to the expected fatigue lives from the S-N relations of the same stress ratio.

5.5.1 R = 0.1

Nominal maximum stresses of 140 and $110 MPa$, here referred to as H (high) and L (low) were chosen for the two load stages in tension-tension block load fatigue with $R = 0.1$. The expected fatigue lives were calculated from Eq. (5.12) which uses the $10 Hz$ CAF results as data base.

$$\sigma_{max}(N) \ = \ 208 MPa - 17.1 MPa \lg(N), \ R^2 = 0.98 \qquad (5.12)$$

For maximum stresses of 140 and $110 MPa$ one obtains expected fatigue lives of 9476 and 538263 cycles respectively. For both load sequences, i.e. H-L and L-H, the load stages were changed between 23 and 69% of the expected fatigue life. For both load sequences the stress and fractional fatigue life data are collected in Table A.6 and plotted in Figure 5.31. The abscissa shows the fractional fatigue life of the first load block, the ordinate that of the second load block. The diagonal line predicts failure according to the Palmgren-Miner rule. The cumulative damage sums for failure, i.e. the sum of both fractional fatigue lives, are found to be dependent on the load sequence. The linear damage law gives a conservative fatigue life estimation for the high-low load sequence but overestimates the fatigue life for the low-high sequence.

Typical courses of mean strain and strain amplitude for both load sequences are shown in Figure 5.32. The load level was changed at about 50% fractional life for both load sequences. The evolution of mean strain and strain amplitude during the first load block follows the courses from Figures 5.24a and 5.25a. After the change from H to L at 4800 cycles, mean strain and strain amplitude immediately approach new stable values which are higher than those from CAF loading. Both strain values remain nearly constant during further cycling until failure occurs suddenly at 645607 cycles. The change from L to H at 253800 cycles leads to an immediate progressive increase of mean strain and strain amplitude. Final failure occurs at 255154 cycles, before stable strain values are approached.
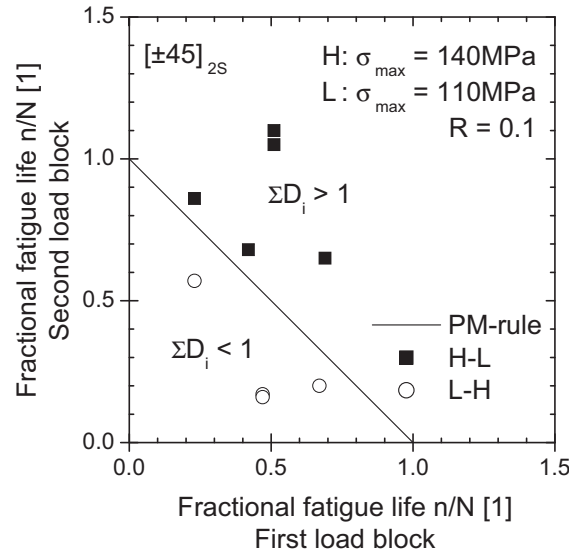
Figure 5.31: Load sequence dependence of fatigue lives for $R = 0.1$ block load fatigue.
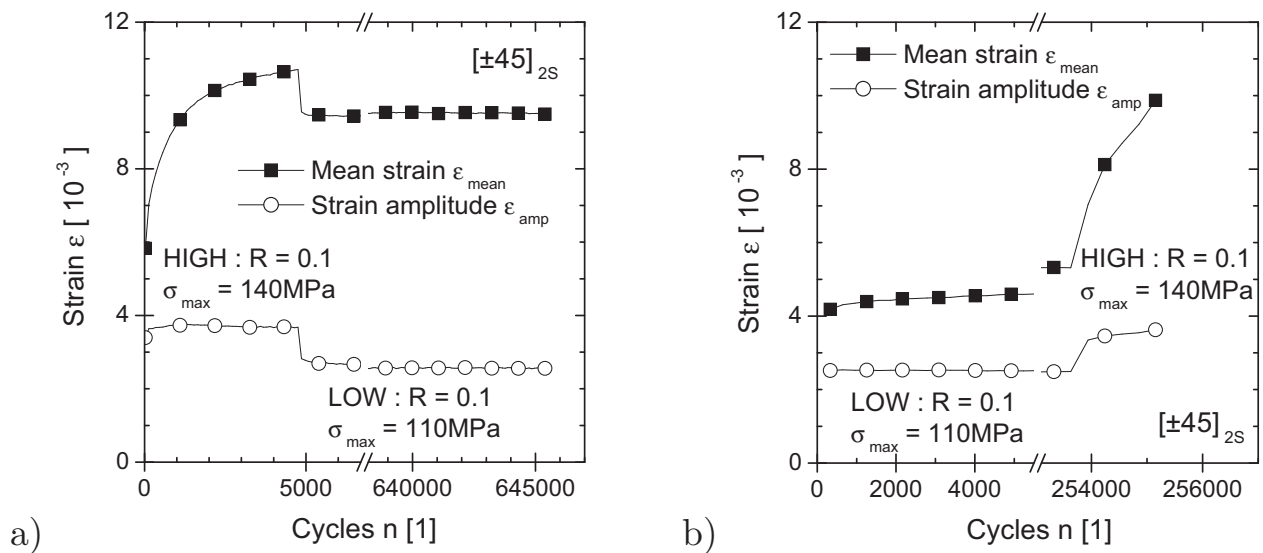
Figure 5.32: Development of mean strain and strain amplitude during block load fatigue with $R = 0.1$. a) high-low load sequence and b) low-high load sequence.

5.5.2 R = -1

Nominal maximum stresses of 105 and $65 MPa$, here referred to as H (high) and L (low) were chosen for the two load stages in reverse tension-compression block load fatigue. The expected fatigue lives were calculated from Eq. (5.11). For maximum stresses of 105 and $65 MPa$ one obtains expected fatigue lives of $N = 987$ and $N = 179571$ respectively. For both load sequences, i.e. H-L and L-H, the load stages were changed between 16 and 87% of the expected fractional fatigue life. All result data are summarised in Table A.7.

The fractional fatigue lives of both load sequences and the prediction according to the Palmgren-Miner rule are compared in Figure 5.33. The linear cumulative damage law gives conservative fatigue life predictions for both load sequences. A dependence of the damage sums for failure on the load sequence cannot be observed.
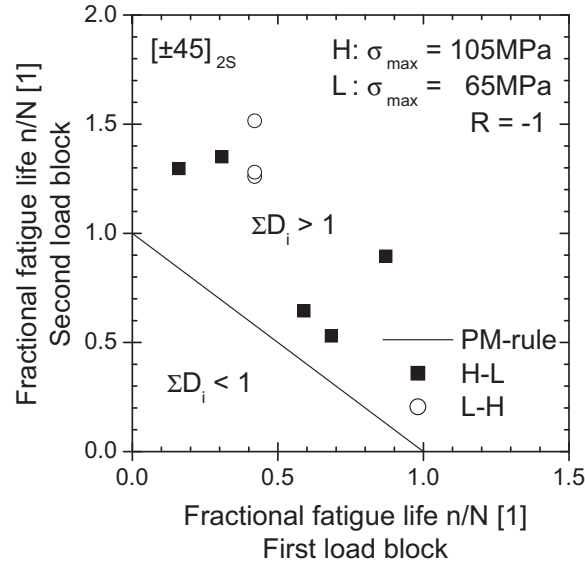
Figure 5.33: Load sequence dependence of fatigue lives for $R = -1$ block load fatigue.
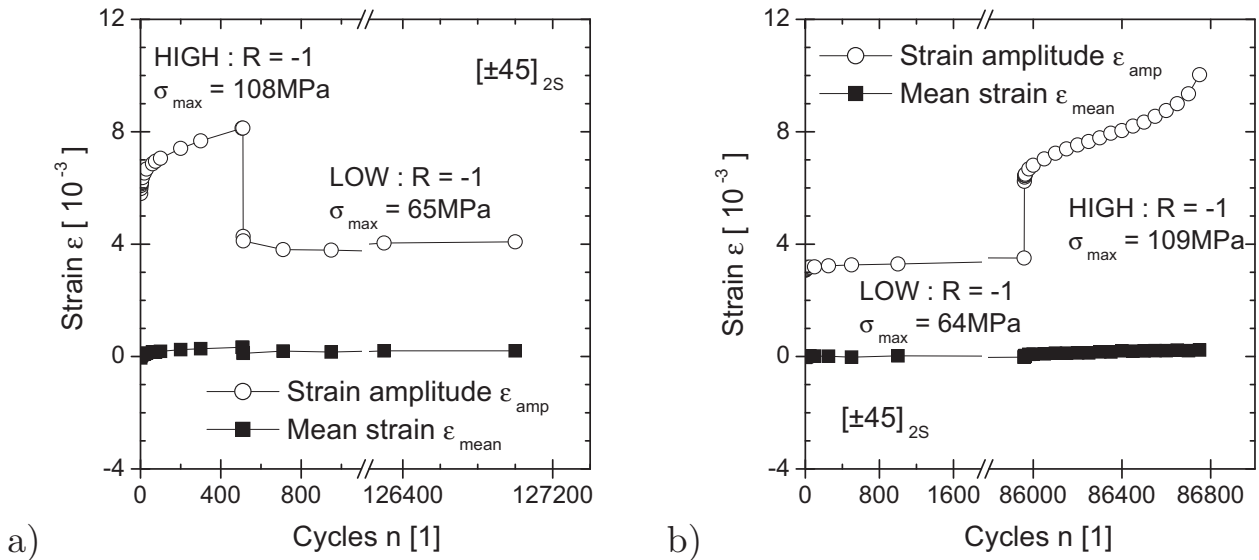
Figure 5.34: Development of mean strain and strain amplitude during block load fatigue with $R = -1$. a) high-low load sequence and b) low-high load sequence.

Figure 5.34 shows that the mean strain remains nearly zero ($0 \leq \varepsilon_{mean} \leq 0.5 \cdot 10^{-3}$) during both load stages for both load sequences. The constant mean strain and the course of the strain amplitude during the first load block

are in good agreement with the results from the CAF tests, see Figures 5.26a and 5.27a.

The strain amplitude immediately approaches a new stable value after the change from H to L at 510 cycles. This new value of $\varepsilon_{amp} = 4 \cdot 10^{-3}$ remains unchanged during further cycling until sudden failure occurs after 127000 cycles. The change from L to H at 85960 cycles causes an instantaneous increase of about $3 \cdot 10^{-3}$ strain amplitude from 3.5 to $6.5 \cdot 10^{-3}$. The further course of the strain amplitude until final failure after 86750 cycles at $10 \cdot 10^{-3}$ strain amplitude exhibits the characteristic three-stage curve.

5.5.3   Variation of the stress ratio

Target maximum stresses in the range of 125 to $131 MPa$ were applied during the $R = 0.1$ load block. The other load block consisted of reverse fatigue loading and maximum stresses between 73 and $80 MPa$. Here, an assignment of H and L to the load blocks would be random, because the maximum stress is higher during the $R = 0.1$ load block whereas the stress amplitude is larger during the $R = -1$ load block. The expected fatigue lives can be calculated from Eqs. (5.10) and (5.11). For loads of $R = 0.1$ and $\sigma_{max} = 127 MPa$ and $R = -1$ and $\sigma_{max} = 75 MPa$ one obtains expected fatigue lives of 70247 and 48895 cycles respectively.
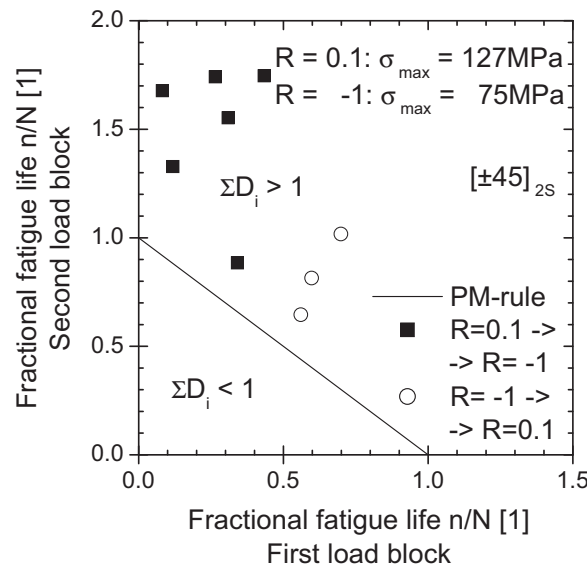
Figure 5.35: Load sequence dependence of fatigue lives for block load fatigue with variation of the stress ratio.

Figure 5.35 compares the fractional fatigue lives of both load sequences with the prediction according to the Palmgren-Miner rule. No clear dependence of the damage sums for failure on the load sequence is observed. The linear

cumulative damage law gives conservative fatigue life predictions for both load sequences. All stress and fatigue life data are given in Table A.8.

Figure 5.36 shows that mean strain and strain amplitude progress during the first load stage as already seen and described for the CAF tests. The mean strain drops from 8.3 to $0.6 \cdot 10^{-3}$ after the change from $R = 0.1$ and $\sigma_{max} = 126MPa$ to $R = -1$ and $\sigma_{max} = 74MPa$ at 25000 cycles, approximately 22% of the fatigue life. The mean strain further decreases to $0.3 \cdot 10^{-3}$ until final failure occurs after 111452 cycles. As the stress ratio changes, the strain amplitude increases slightly from 3.5 to $3.8 \cdot 10^{-3}$ and remains constant at that level during further cycling.
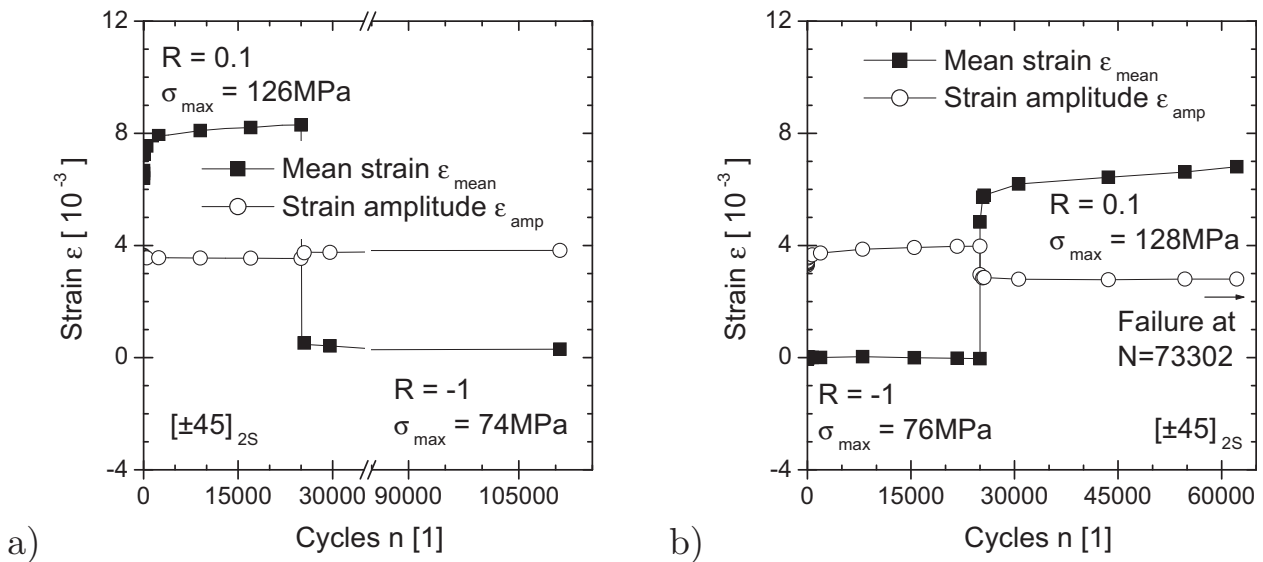
Figure 5.36: Development of mean strain and strain amplitude during block load fatigue with variation of the stress ratio. a) $R = 0.1 \longrightarrow R = -1$ load sequence and b) $R = -1 \longrightarrow R = 0.1$ load sequence.

The change from $R = -1$ and $\sigma_{max} = 76MPa$ to $R = 0.1$ and $\sigma_{max} = 128MPa$ at 25000 cycles (34% of the fatigue life) causes the strain amplitude to drop from 4 to $2.8 \cdot 10^{-3}$. The strain amplitude remains unchanged during further cycling until the data acquisition stops at about 85% of the fatigue life. The mean strain, being zero during the first ($R = -1$) load block, progresses during second ($R = 0.1$) load block, as seen for CAF loading in Figures 5.24a and 5.25a.

5.6 Initial loads in constant amplitude fatigue loading

5.6.1 Cyclic initial stresses

Figure 5.37a shows for the load scenario B that the actual stresses approach the reference fatigue loading conditions of $R = 0.1$, $\sigma_{max} = 120MPa$, and $f = 10Hz$ after 300 cycles.
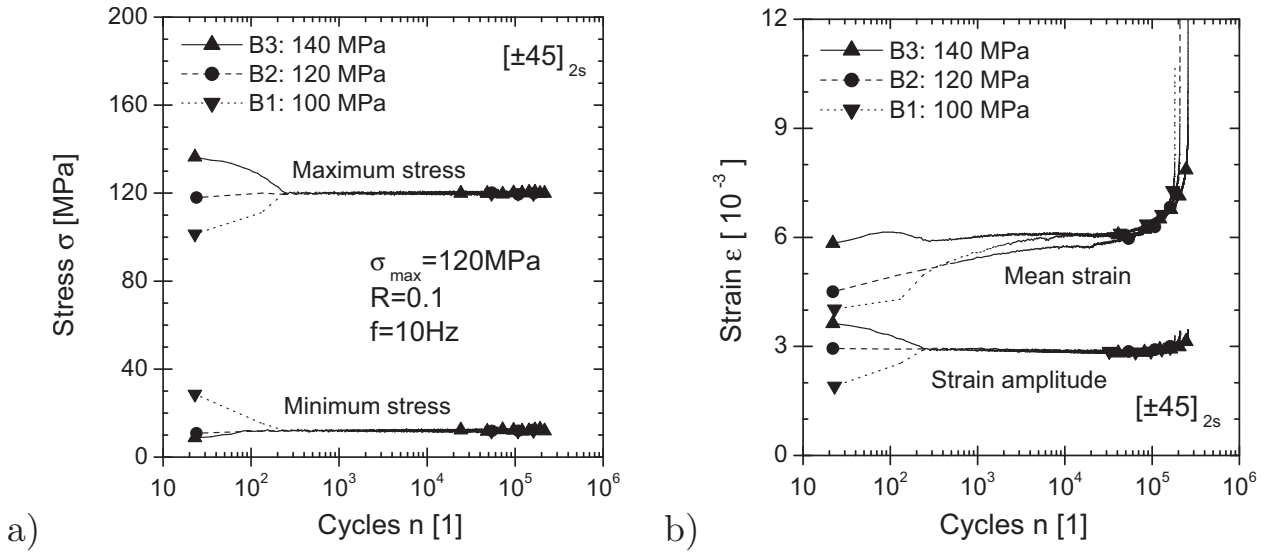
Figure 5.37: Effect of cyclic initial stresses (load scenario B) on subsequent fatigue. a) provided stress signal and b) strain response.

The realised stress signals agree well with the target signal (Figure 4.5a). The response of mean strain and strain amplitude is plotted in Figure 5.37b. The higher the stress amplitude, the higher is the respective strain amplitude. Once the stress amplitude has reached the constant value of $\sigma_{amp} = 54MPa$ for $n \geq 300$, the strain amplitudes for the load cases B1, B2, and B3 coincide. They follow one curve for the remaining fatigue life which has been already described for the CAF loading.

The mean strain for B3 increases for $n \leq 100$ from 5.8 to $6.1 \cdot 10^{-3}$ while the mean stress decreases in that cycle range. This is followed by a decrease of the mean strain back to $5.9 \cdot 10^{-3}$ for $100 < n < 300$ while the mean stress approaches its nominal value of $\sigma_{mean} = 66MPa$. The further mean strain evolution is marked by approaching a plateau value of $6.1 \cdot 10^{-3}$ which is kept until a disproportional increase is observed above 10^{5} cycles. The mean strain courses for B1 and B2 follow the CAF results from subsection 5.4.2.

MVs and SDs of the resulting fatigue lives are compared in Figure 5.38 whereas the data base for each load case is three. All experimental S-N data are collected in Table A.9. The 'virgin' reference value of $N = 140022$ can

be calculated from Eq. (5.12). No dependence of the fatigue life on the cyclic initial stress is observed for the load cases B1 and naturally B2. However, the fatigue life is extended for the load case B3, where the mean fatigue life is outside the upper 68% confidence band of the reference loading.
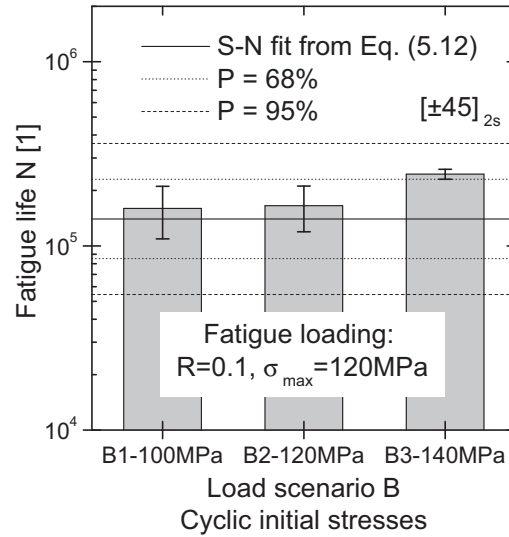
Figure 5.38: Fatigue lives for $R = 0.1$ and $\sigma_{max} = 120MPa$ CAF with preceding cyclic initial stresses.

5.6.2   Positive triangular pulse

Figure 5.39a shows, that the actual stress signal for load scenario C, a positive triangular pulse with $20mm/s$ ramp velocity to different stress levels followed by CAF, is in good agreement with the target signal (Figure 4.5b). The strain response on the applied load is plotted in Figure 5.39b. The abscissa contains the time and the number of cycles on a semi-logarithmic scale. Different strain values for the pulse and subsequent fatigue loading are plotted on the ordinate.

  The duration of the pulse increased from $5.5s$ for the load case C1 via $6.5s$ for C2 to $7.5s$ for C3. The viscoelastic strain after stress-free unloading increases as the pulse stress increases. The mean strain development in subsequent CAF starts consequently on a higher strain level. The slope $d\varepsilon_{mean}/dn$ decreases with increasing cycle number and is lower for higher pulse stresses. The mean strains of all load cases approach a value of approximately $7 \cdot 10^{-3}$ at 50000 cycles. The course of the strain amplitude does not depend on triangular pulse stress. The strain amplitudes of all load cases decrease slightly until the last but one decade of the fatigue life. Towards fatigue failure the strain amplitudes increase.
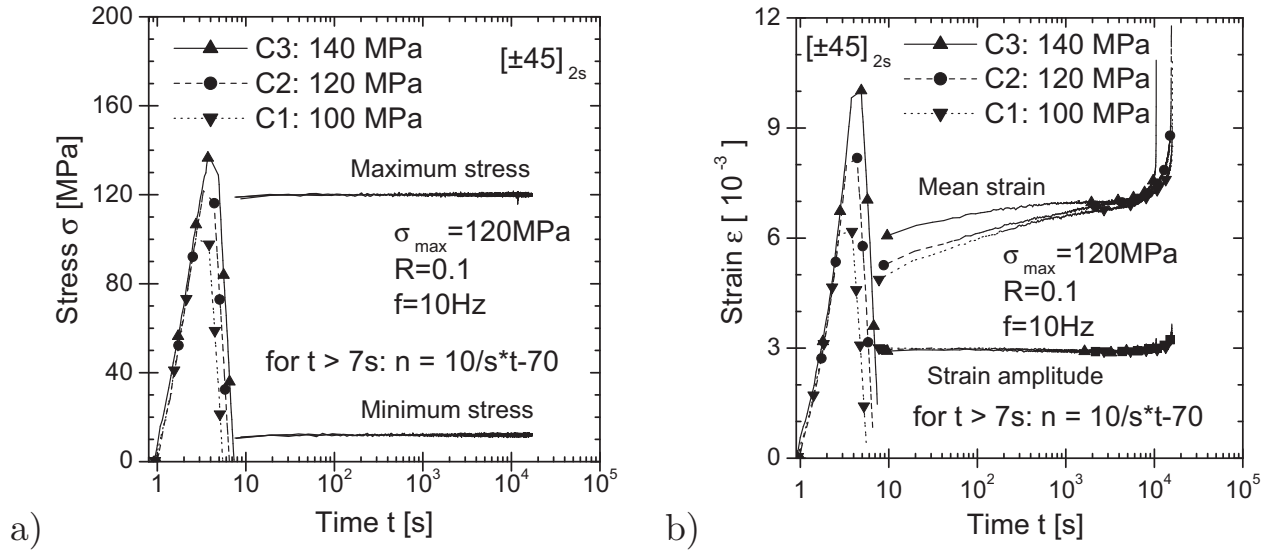
Figure 5.39: Effect of a positive triangular pulse (load scenario C) on subsequent fatigue. a) provided stress signal and b) strain response.
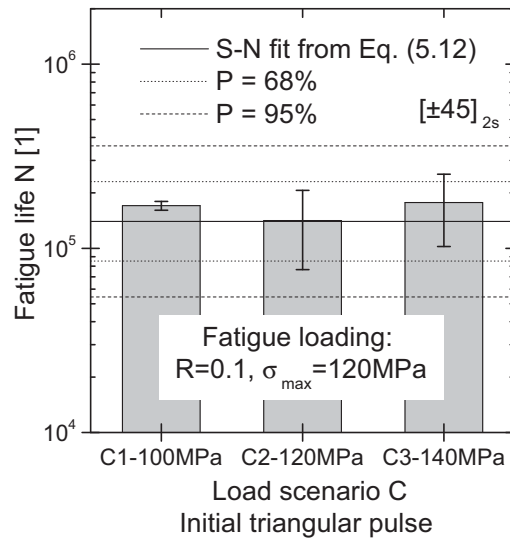
Figure 5.40: Fatigue lives for $R = 0.1$ and $\sigma_{max} = 120MPa$ CAF with preceding triangular pulse stress.

Figure 5.40 compares MVs and SDs of the resulting fatigue lives. The data base of all load cases consists of three samples. All experimental S-N data are collected in Table A.10. The fatigue lives of C1 and C3 tend to be higher than the 'virgin' reference value but the trend is not significant as the SDs overlap.

Taking the confidence intervals of the reference value and the SDs of the load cases into account, triangular pulse stresses in the range of 100 to $140MPa$ prior to fatigue loading do not effect the subsequent fatigue life, neither to longer nor to shorter life times.

5.7   Creep-recovery-fatigue loading

5.7.1   Creep stress dependence

The CRF load case D1 (Figure 4.6) was defined to investigate the stress dependence of preceding creep and recovery on the CAF behaviour. Figure 5.41 includes the resulting fatigue lives plotted on a semi-logarithmic scale vs. the preceding creep stress. All S-N data are summarised in Table A.11. The horizontal solid line is equivalent to $N = 140023$, the expected mean fatigue life of the reference fatigue loading from Eq. (5.12). The dotted and dashed lines represent the upper confidence bands of 68 and 95% failure probability. Compared to the 'virgin' reference fatigue life, a significant increase of the fatigue life in the range of 2.0 to 3.2 is observed regardless of the applied creep stress. All data are outside the $P = 68\%$ interval. Three out of seven data are outside the $P = 95\%$ interval. Moreover, a weak trend of fatigue life extension with increasing creep stress can be seen [204].
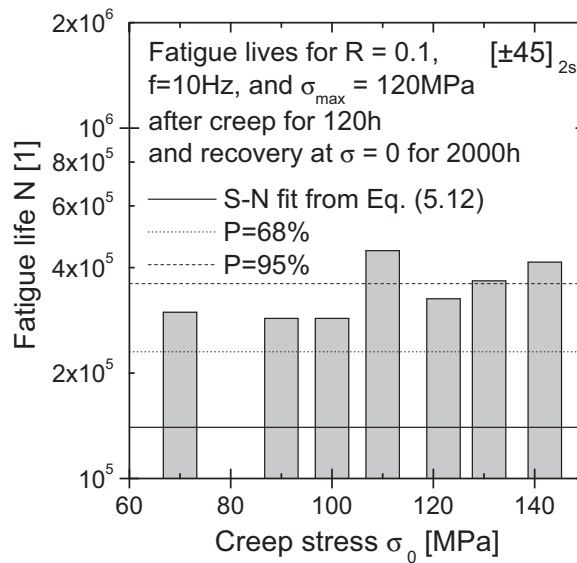
Figure 5.41: Dependence of preceding creep stress level on fatigue life. (load case D1).

A comparison of the evolution of the mean strain and the strain amplitude between a virgin and four creep-recovery (CR) samples is shown in Figure 5.42. The CR specimens were loaded for $120h$ at 70, 90, 110, and $130MPa$ respectively, followed by a stress-free recovery for circa $2000h$. The mean strain and the strain amplitude of the virgin specimen is always higher than that of the CR specimens for the same cycle number. In case of the mean strain, it partly results from some time dependent strain which is lost during clamping and unclamping.

No dependence is visible between the creep stress level and the evolution of mean strain of the CR specimens. The mean strain curves are within a very tight band during the primary and secondary stage. The difference of the mean strain between the virgin and the CR samples increases to $0.7 \cdot 10^{-3}$ at failure of the virgin sample at $N = 124343$. No trend is seen with regard to a more pronounced formation of a tertiary stage which could be recognised at a steeper mean strain and strain amplitude increase at the end of the fatigue life.

Figure 5.42: Comparison of a) mean strain and b) strain amplitude during constant amplitude fatigue with and without preceding creep-recovery loading.

The initial strain amplitude of $2.8 \cdot 10^{-3}$ $(E = 19.3 GPa)$ is the highest for the virgin sample. The CR specimens are initially stiffer; their initial strain amplitudes of 2.73 to $2.63 \cdot 10^{-3}$ correspond to stiffness values of 19.8 to $20.5 GPa$. For a higher creep stress, the strain amplitude tends to be higher as well. However, this trend is weak and superposed by limitations due to actuator resolution[6]. All curves show a constant strain amplitude for the first 1000 cycles which is followed by a linear decrease for approximately two decades of the fatigue life. The slope $d\varepsilon_{amp}/dn$ is the same of the CR specimens. The absolute value of the slope for the CR specimens is about twice as high as for the virgin specimen which corresponds to an increase of the dynamic stiffness during the fatigue loading, which is two times higher.

---

[6]The actuator resolution is $20\mu m$. One obtains for low cycle numbers $(\varepsilon_{amp} : \varepsilon_{mean} \approx 1 : 1.5)$ a resolution of the strain amplitude of approximately $0.08 \cdot 10^{-3}$.

5.7.2 Creep and recovery time dependence

The CRF load case D2 (Figure 4.6) investigated the effect of six combinations of creep and recovery times on the subsequent CAF behaviour. Figure 5.43 shows a typical plot of the strain evolution during a C2R24F test in a linear scale. The creep stress and the fatigue mean stress are equal to 91MPa. The mean strain in fatigue increases more rapidly compared to the development of the strain during creep. The instantaneous creep strain and the courses of creep and recovery strain comply with the results from pure creep loading (section 5.3.1). The course of the fatigue mean strain exhibits the same characteristics as already described for high load CAF tests (subsection 5.4.2).
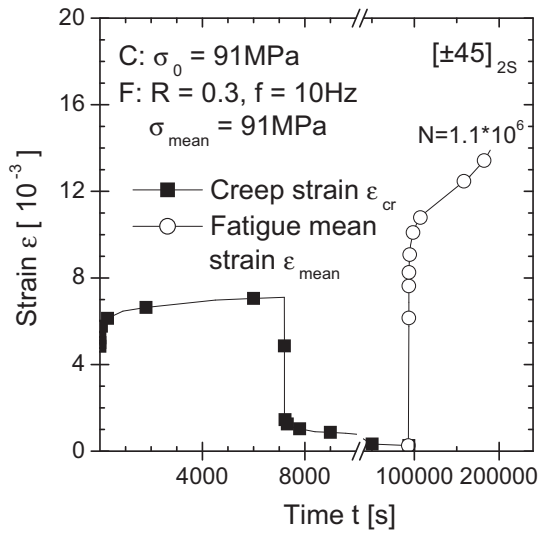
Figure 5.43: Creep, recovery, and fatigue mean strain development during a C2R24F test.
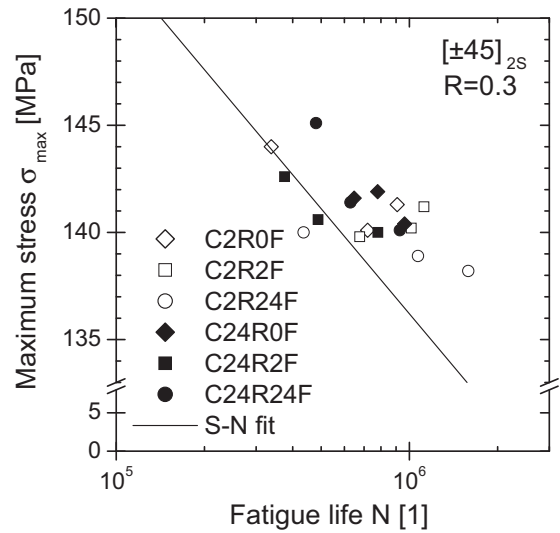
Figure 5.44: Original CRF S-N data for the load case D2.

All experimental S-N results including MVs and SDs are collected in Table A.12. It can be seen that the applied creep and fatigue stresses do not in all cases match their target values exactly. The applied creep stresses are in the range of $90.7MPa \leq \sigma_{cr} \leq 91.8MPa$, the fatigue stresses in the range of $138.1MPa \leq \sigma_{max} \leq 145.1MPa$. Dahl [205] showed by plotting the creep stress vs. the fatigue life that the deviation of the creep stress from the nominal value had no effect on the resulting fatigue lives of the CRF tests. Figure 5.44 shows the maximum cyclic stress in fatigue vs. the fatigue life. It can be seen that the deviation of the applied cyclic stress from the nominal value has an effect on the resulting fatigue life of the CRF test. Higher cyclic stresses lead to shorter fatigue lives. To account for the variations of the applied cyclic stresses during the CRF tests, the fatigue lives are normalised with respect to the nominal maximum stress of $140MPa$:

1. The inverse function of Eq. (5.9), gives $N_{Eq.\,(5.9)}(\sigma_{max} = 140MPa) = 584617$.

2. Calculation of the expected fatigue life $N_{Eq.\,(5.9)}(\sigma_{max})$ for the actual applied stress.

3. According to Eq.(5.13), calculation of the expected fatigue life of the CRF tests such that a maximum stress of $140MPa$ would have been applied.

$$N_{norm}(140MPa) = N_{exp}(\sigma_{max}) \frac{N_{Eq.\,(5.9)}(140MPa)}{N_{Eq.\,(5.9)}(\sigma_{max})}$$

$$= N_{exp}(\sigma_{max}) \frac{584617}{N_{Eq.\,(5.9)}(\sigma_{max})} \tag{5.13}$$

The normalised data including the MVs and SDs are compared with the original data in Table A.12 and displayed in Figure 5.45 divided into groups of equal combinations t_{cr} and t_{rec}. The abscissa indicates the group, the ordinate contains the fatigue life.
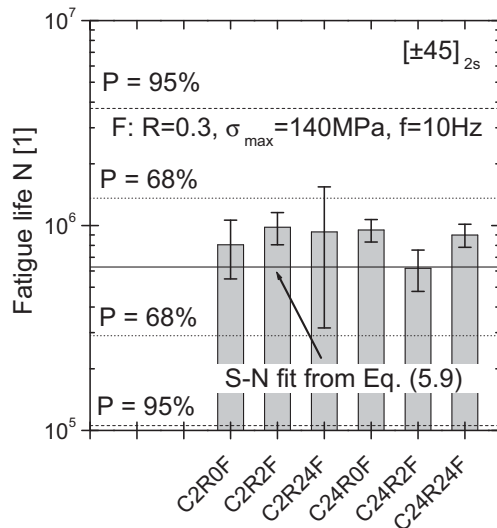
Figure 5.45: Time dependence of preceding creep and recovery on the normalised fatigue life (load case D2).
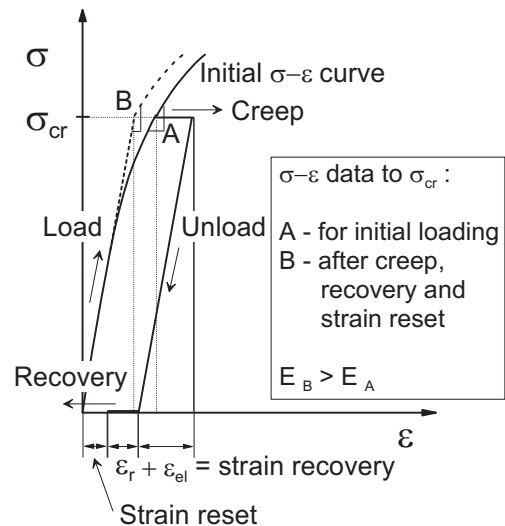
Figure 5.46: Sketch of stress-strain behaviour for CRF tests.

The solid line of $N = 627402$ in Figure 5.45 is calculated from Eq. (5.9) and indicates the expected 'virgin' mean fatigue life of the reference loading. The dotted and dashed lines describe the upper and lower confidence bands for 68

and 95% probability of failure. The normalised mean fatigue lives and SDs are plotted along the abscissa for each CxRyF combination. Compared to the reference data, the mean fatigue life is generally extended with preceding creep and recovery regardless of their combination. However, neither for the creep nor the recovery time a significant trend can be found, as the wide confidence bands of the reference loading do not permit statistically secured statements.

A comparison of the mean strain evolution between a virgin and three CR samples of the same creep time $t_{cr} = 2h$, but recovery times of $t_{rec} = 0, 2h$, and $24h$ is given in Figure 5.47. All curves run nearly parallel in semi-logarithmic presentation. The mean stress level of the virgin sample is higher than that of CRF samples which results from a strain reset due to operation after creep and recovery but prior to the fatigue loading. A schematic drawing is given in Figure 5.46. The constant sum of strain reset and viscoelastic strain recovery further explains, that all mean strain curves are similar.
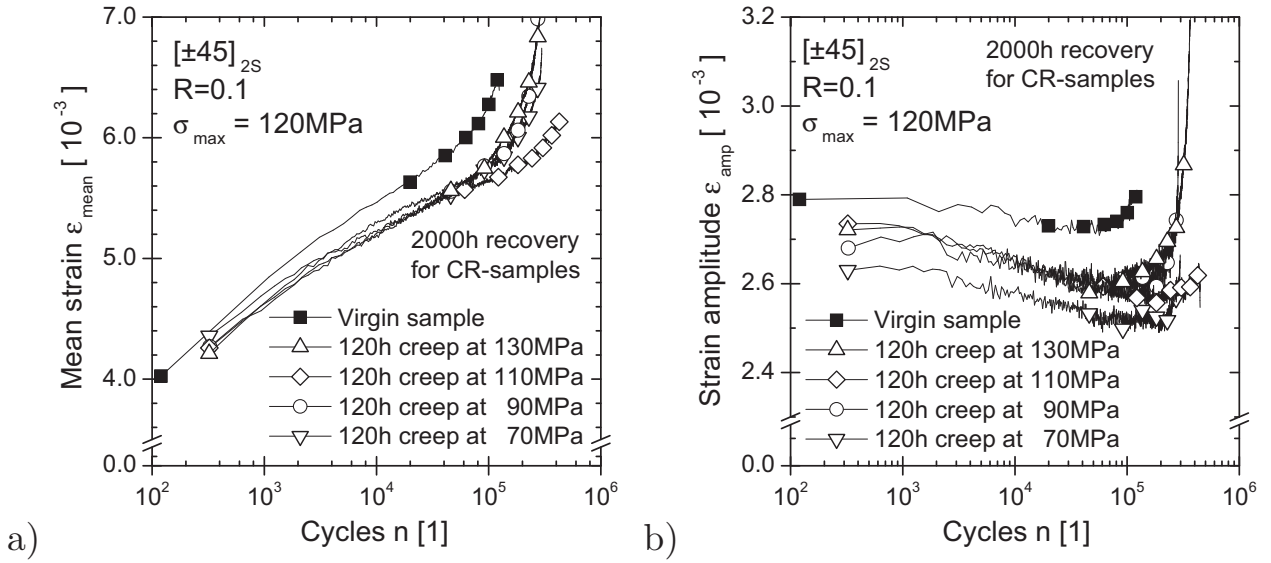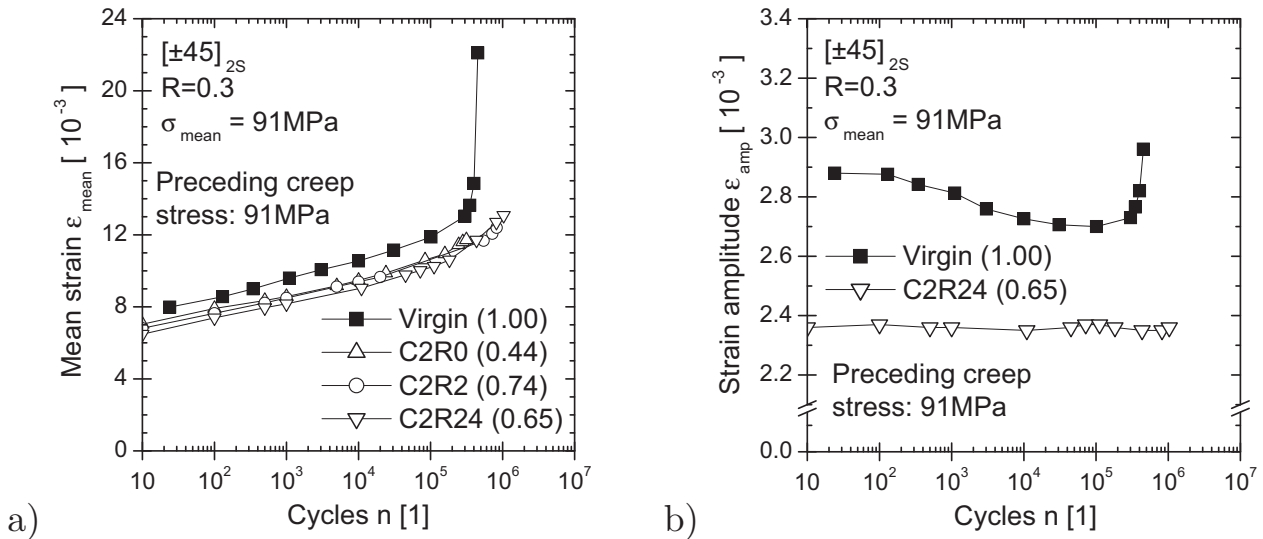

Figure 5.47: Comparison of a) mean strain and b) strain amplitude during constant amplitude fatigue with and without preceding creep-recovery loading. The values in brackets give the last data records in terms of n/N.

The strain amplitude of the virgin sample behaves similar as already described for the CRF load case D1. The strain amplitude of the CRF samples is 0.3 to $0.5 \cdot 10^{-3}$ lower than for the virgin sample (Figure 5.46 where $E_B > E_A$). Figure 5.47b shows for the six investigated combinations of CxRy the course of strain amplitude for C2R24F loading. The strain amplitude remains nearly constant for the first two thirds of the fatigue life.

6

Modelling

6.1 Elastic properties

The elastic engineering properties of the angle-ply laminate can be determined from Table 3.1. The values of Q_{ij} can be calculated from Eqs. (2.10) to (2.13) where the engineering properties of the UD lamina are given in section 5.1. The value of ν_{21} was not used for the calculation because only four out of the five experimentally determined properties are independent. From E_{11}, E_{22}, G_{12} and ν_{12} one obtains for the UD lamina:

$$Q_{11} = 141.81 GPa \qquad (6.1)$$
$$Q_{22} = 8.96 GPa \qquad (6.2)$$
$$Q_{12} = 2.87 GPa \qquad (6.3)$$
$$Q_{66} = 5.20 GPa \qquad (6.4)$$

The exact and approximate solutions of the laminate engineering properties according to the classical lamination theory (CLT) are given in Table 6.1 and compared with the experimental data. It can be seen that the experimental tensile and compressive results are in good agreement with the CLT results. The experimental Poisson's ratio of 0.73 is 4% lower than the predicted value, the experimental axial stiffness values of $19.6 GPa$ in tension and $20.0 GPa$ in compression are within the range of exact $(18.3 GPa)$ and approximate $(20.8 GPa)$ solutions from the CLT.

Substituting Eqs. (6.1) to (6.4) to the transformation expressions of the UD lamina and the CLT allows to calculate the dependence of the engineering constants of the AP laminate from off-axis angle (section 2.2). Figure 6.1 shows the polar diagrams of a) the rotated axial and shear stiffness and b)

Table 6.1: Comparison engineering properties of the HTA/6376 $[\pm45]_{2S}$ laminate according to the CLT vs. the experimental data.

Property	CLT		Experiment	
	Exact value	Appr. value	Tension	Compression
$E_x[GPa]$	18.3	20.8	19.6	20.0
$G_{xy}[GPa]$	37.5	35.2	-	-
$\nu_{xy}[1]$	0.76	0.74	0.73	-

the Poisson's ratio. All curves have a fourfold symmetry. The shear stiffness and the Poisson's ratio attain their maximum values at $n \cdot \pi/2$ $(n \,\epsilon\, \mathbb{N}_0)$ and their minimum values at $(2n-1)\cdot\pi/4$ $(n \,\epsilon\, \mathbb{N}_0)$, vice versa for the axial stiffness.
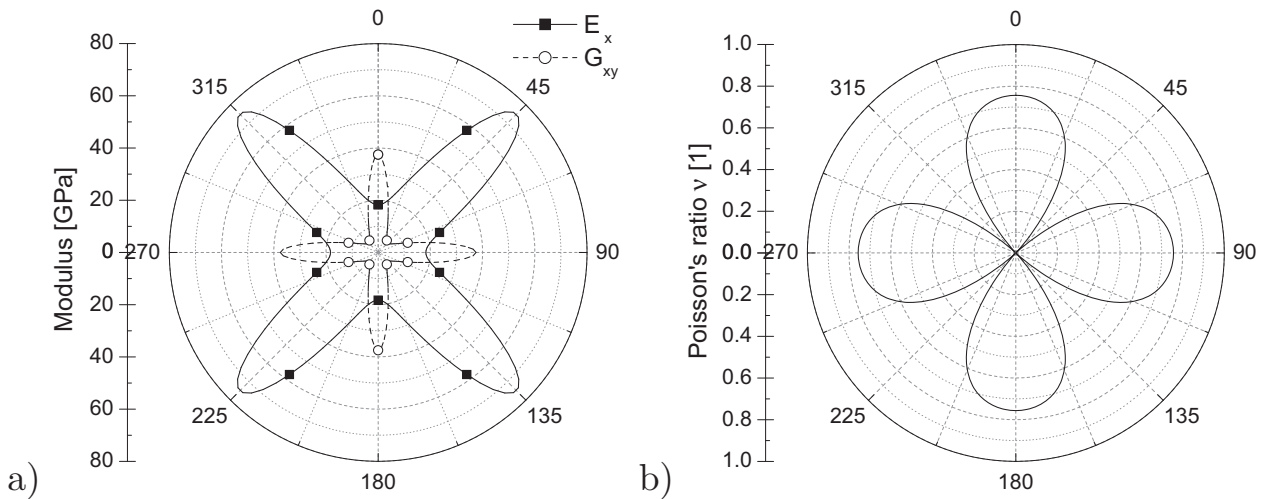
Figure 6.1: Polar diagrams of the rotated engineering properties of the HTA/6376 $[\pm45]_{2S}$ laminate. a) axial and shear moduli and b) Poisson's ratio.

6.2   Tensile behaviour

For the numerical analysis it is more convenient to formulate a functional relationship of the stress-strain data rather than to use pairs of variates. An appropriate function describes the stress-strain curve over a wide application range with a minimum of variables, runs linear for small strains, is multiple continuously differentiable, and applicable to tensile and compressive loading. Eq. (6.5) fulfils all requirements. As the strain increases, the stress converges to the value of a whereas b adopts the strain to the abscissa arguments. The

tangent stiffness, the first derivative of the stress with respect to the strain, is given by Eq. (6.6); the secant stiffness is given in Eq. (6.7).

$$\sigma \quad = \quad a \cdot \tanh\left(b\,\varepsilon\right) \tag{6.5}$$

$$E_{tan,fit} \quad = \quad \frac{d\sigma}{d\varepsilon} = a\,b\left(1 - \tanh^2\left(b\,\varepsilon\right)\right) \tag{6.6}$$

$$E_{sec,fit} \quad = \quad \frac{a}{\varepsilon}\,\tanh\left(b\,\varepsilon\right) \tag{6.7}$$

Figure 6.2a compares an experimental stress-strain curve (Figure 5.3) with the functional relationship of Eq. (6.5) where the choice of $a = 168MPa$ is equal to the yield stress for that sample and $b = 100$. Good agreement is observed for small strains in the linear-elastic region as well as for strains corresponding to the yield stress where both curves run horizontally. The applicability of the analytical approximation function is limited to this strain range.
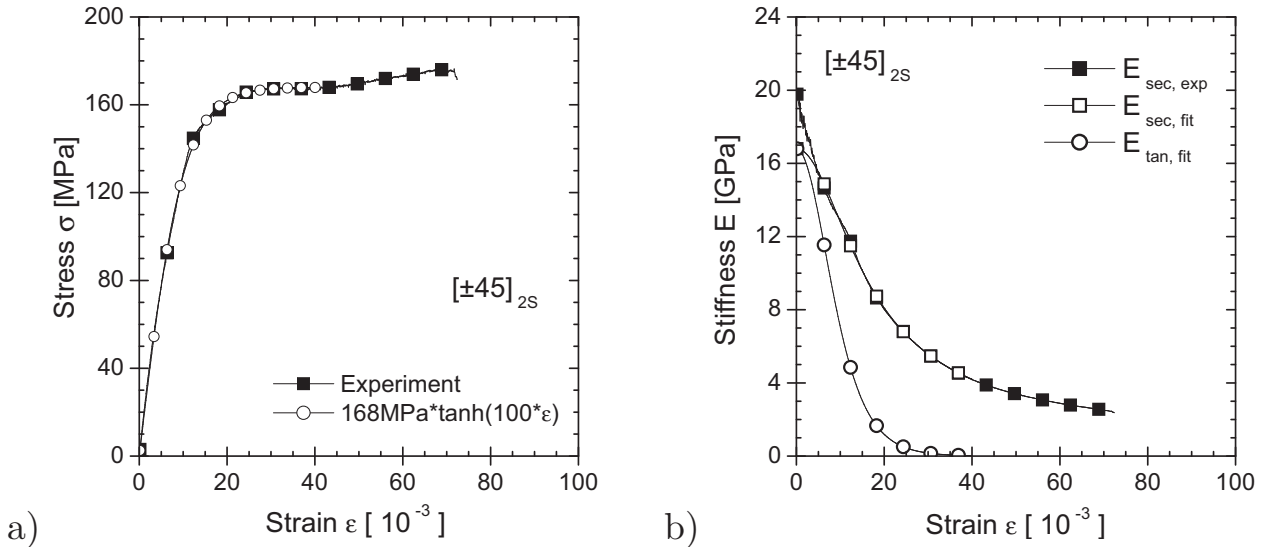
Figure 6.2: Comparison of experimental and approximated tensile properties. a) stress vs. strain and b) stiffness vs. strain.

A comparison of the experimental secant stiffness with the calculated tangent and secant stiffness values from Eqs. (6.6) and (6.7) is shown in Figure 6.2b. All curves decline as the strain increases. The experimental stiffness starts at $19.8GPa$ and exhibits a declining decrease to approximately 20% of the initial stiffness at failure. The calculated curves start at $16.8GPa$. The tangent stiffness decreases more rapidly and approaches zero at the yield strain. The calculated secant stiffness approaches the experimental curve at $4 \cdot 10^{-3}$ strain. Following, both curves show very good agreement.

6.3   Creep behaviour

6.3.1   Activation energy

Methods to determine the activation energy for steady-state creep were introduced in subsection 2.4.3. With the knowledge of the activation energy, direct relations between strain rate and temperature can be established. To determine the activation energy of the neat epoxide resin 6376 and a $[\pm45]_{2S}$ carbon/epoxide (T800/6376) laminate, experimental data from Horoschenkoff [164] have been used. He presented creep curves for both materials at different stresses and temperatures (Figures 3.13 and 3.14). Here, strain vs. time data have been extracted for the different test conditions and converted to steady-state strain rate vs. temperature data. The results are plotted in Figure 6.3 as the logarithm of strain rate vs. the inverse temperature. From Eq. (2.41) can be derived that in this presentation the activation energy is directly proportional to the slope of the curves.
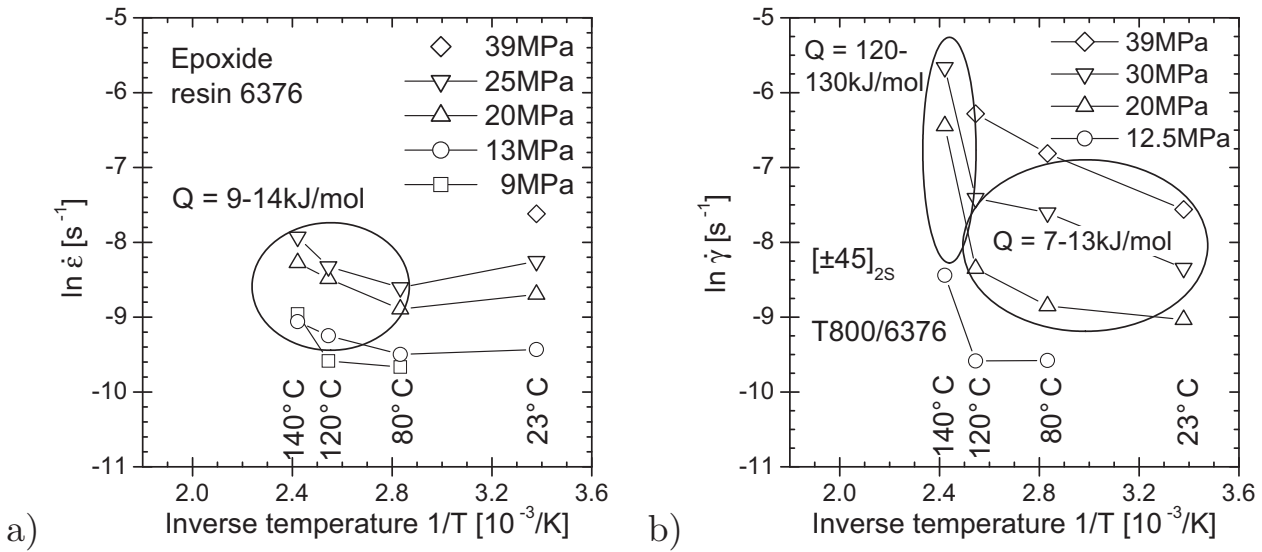
Figure 6.3: Arrhenius plots of the logarithm of creep strain rate vs. inverse temperature to determine the activation energy. a) neat epoxide resin 6376 and b) $[\pm45]_{2S}$ carbon/epoxide (T800/6376) laminate. The original creep data were taken from Horoschenkoff [164].

Depending on the applied stress, the calculated curves in Figure 6.3 run parallel in first approximation. Higher stresses cause higher strain rates. For the neat resin and the laminate, the strain rate and its logarithm tend to increase as the absolute temperature increases. Neither for the neat resin nor for the laminate a single constant slope and thus activation energy for steady-state creep can be determined. The activation energy tends to increase with the absolute temperature. Evaluation of the parallel segments of the creep

curves for the neat resin (Figure 6.3a, $80°C \leq \vartheta \leq 140°C$ and $13MPa \leq \sigma \leq 25MPa$) leads to activation energies of $Q = 9 - 14kJ/mol$.

A value of $Q = 13 - 14kJ/mol$ is obtained from Eq. (2.42) assuming that two different tests at the same stress (13 or $20MPa$) but different temperatures (120 and $140°C$) result in the same steady-state strain rate as one test with a temperature change.

Two arrays of semi-parallel curves are marked in Figure 6.3b for the angle-ply laminate. An activation energy of $Q = 7 - 13kJ/mol$ can be determined for $23°C \leq \vartheta \leq 120°C$ and $20MPa \leq \sigma \leq 39MPa$, a higher value of $Q = 120 - 130kJ/mol$ for temperatures between 120 and 140°C.

6.3.2   Creep curves

In section 5.3.1, the creep behaviour of the investigated AP laminate was found to be stress and time dependent. The Nutting equation (subsection 2.4.2) has been proven to be capable to model such a material behaviour.

Discrete values of the instantaneous strain response versus the applied stress are given in Figure 5.15b. To obtain a continuous description of the isochronous stress-strain curve for zero creep time, the data are fitted in Figure 6.4a. In good approximation the data fall on two straight lines. The bilinear approximation determined by the least square method is given in Eqs. (6.8) and (6.9). The intersection of both equations at $88MPa$ constitutes the transition from linear to nonlinear instantaneous viscoelastic behaviour. Eq. (6.8) contains the coordinate origin and displays the linear elastic material response. The compliance of $0.048/GPa$ corresponds to an initial stiffness of $20.8GPa$ which is in good agreement with the theoretical and quasi-static experimental values (Table 6.1).

$$0 \leq \sigma \leq 88MPa \quad : \quad \varepsilon_0 \quad = \quad \frac{0.048}{GPa}\sigma, \ R^2 = 0.99 \tag{6.8}$$

$$\sigma \geq 88MPa \quad : \quad \varepsilon_0 \quad = \quad \frac{0.127}{GPa}\sigma - 0.0071, \ R^2 = 0.99 \tag{6.9}$$

Figure 6.4b compares the experimental creep data of Figure 5.15a with the predictions according to Eq. (2.37). The instantaneous strain data were taken from Eqs. (6.8) and (6.9). Good correlation between prediction (thick lines) and experiment (symbols+thin lines) is observed.

Table 6.2 includes the best fit Nutting parameters. It should be noted that only one data set of K, m and n is needed to predict the stress and time dependent creep strain evolution. To obtain the total strain ε in units of [1], the values of ε_0, σ_0, and t must be supplied in units of [1], [MPa], and [h] respectively.
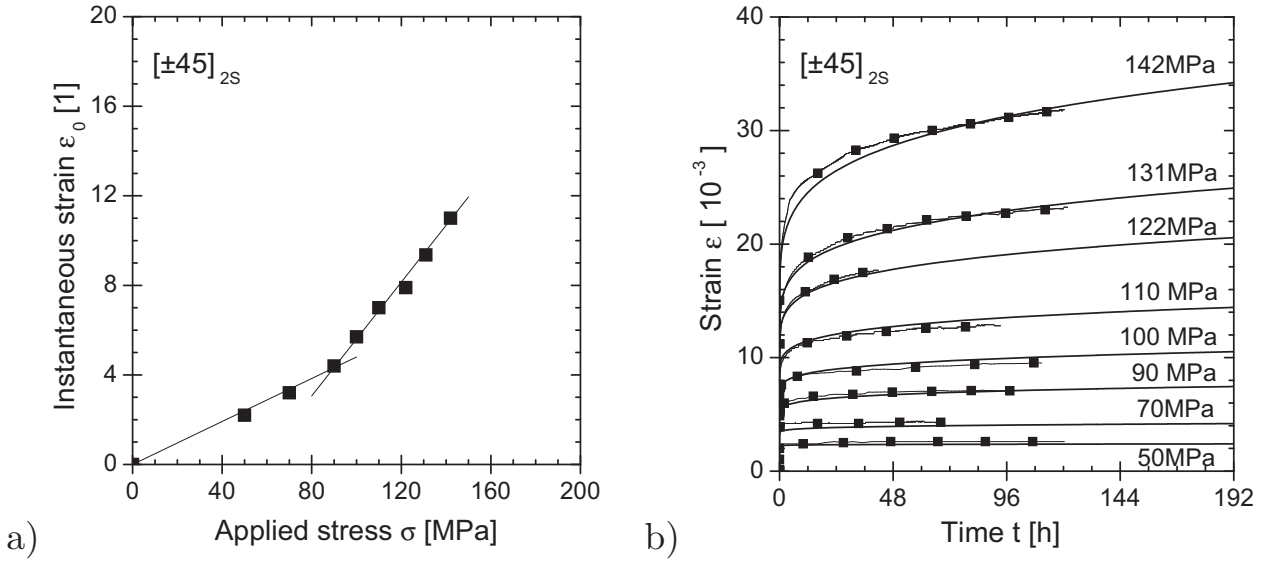
Figure 6.4: Modelling of creep data. a) instantaneous strain response: experiment (symbols) and approximation (lines) and b) creep curves: experiment (symbols+lines) and prediction (lines).

Table 6.2: Nutting parameters.

$K[1]$	$m[1]$	$n[1]$
$1.5 \cdot 10^{-12}$	4.5	0.21

6.4 Block load fatigue with R=0.1

6.4.1 Proposal of a damage accumulation model

The constant amplitude results from section 5.4 and the block load fatigue results from subsection 5.5.1 show that the maximum strain in fatigue steadily increases during cycling. The second model of Hwang and Han [108, 110] which is given in Eq. (2.77) thus represents a potentially suitable metric to model the degradation process of the AP laminate. This choice of degradation parameter is justified and discussed in subsection 7.4.

While the absolute number of cycles during the tertiary stage is approximately constant, their relative amount increases with increasing stress and thus decreasing fatigue life. Furthermore, the characteristic of the tertiary stage is arbitrary and geometry dependent. Opposed to the primary and secondary stage which grasp the entire material, the tertiary stage is occasionally not detected if the region of final failure is outside the gauge length.

To obtain representative reference curves, the maximum strain development during the secondary stage can be extrapolated to the end of the fatigue life

which is schematically shown by the dashed lines in Figure 6.5. Schulte et al. [125] implemented a similar procedure to their CDT in Eq. (2.74) by ignoring the stiffness loss during the tertiary stage. Following, the scalar damage metric D is the ratio of the maximum strain per fatigue cycle $\varepsilon_{max}(n)$ normalised to the extrapolated maximum strain at failure.
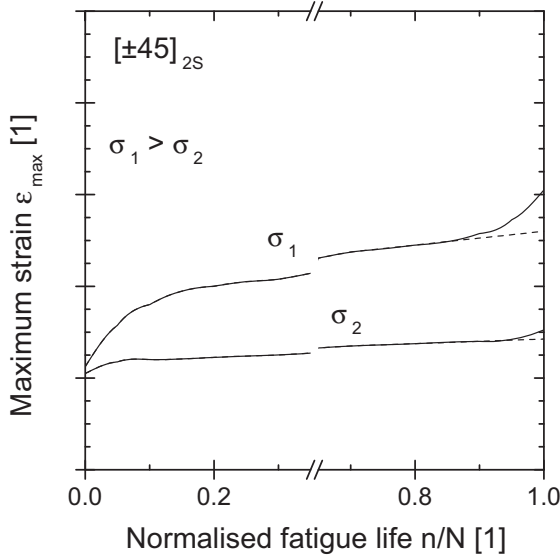
Figure 6.5: Sketch of real (solid lines) and extrapolated (dashed lines) maximum strains during CAF loading.
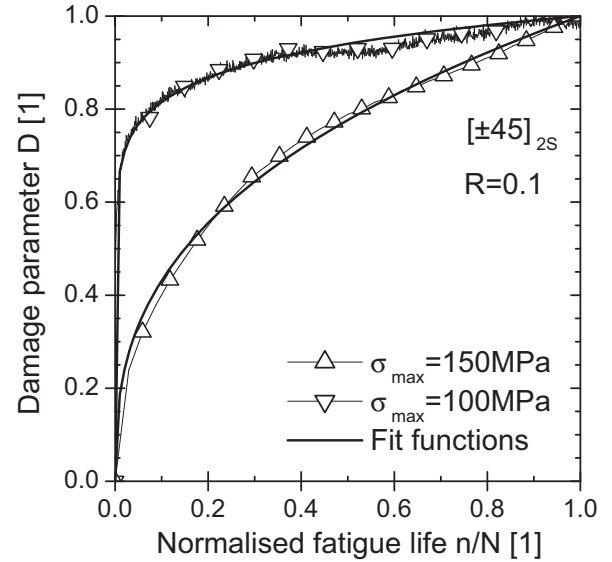
Figure 6.6: Normalised experimental (symbols + thin lines) and approximated (thick lines) damage curves.

Figure 6.6 shows experimental maximum strain curves of two different stress levels normalised to the fatigue life (abscissa) and the extrapolated strain at failure (ordinate). The curves enable a good comparison as they start at (0,0) and finish at (1,1) for failure. It should be noted that compared to Figure 6.5, the shape of the curves has changed and its position interchanged.

For more generality, it is to prefer to approximate the damage curves in Figure 6.6 by analytical functions with a minimum of variables and constant parameters. The power law approach of Eq. (6.10) exhibits a more pronounced nonlinearity as σ_{max} decreases.

$$D = \left(\frac{n}{N}\right) \exp\left(\frac{\sigma_{max}}{a}\right)^{b} \tag{6.10}$$

For a given fractional life, the resulting damage state is the higher, the lower the stress is. The constant parameters a and b can be determined to $a = 200 MPa$ and $b = 3.5$ for CAF loading with $R = 0.1$ [206]. The comparison of experimental and approximated damage curves in Figure 6.6 shows good agreement. Thus, a mathematical description that relates the maximum applied stress and the fractional life to the damage parameter D is established.

For block load fatigue, the residual fractional fatigue life and the actual cycle number until failure during the last (m-th) block are given in Eqs. (6.11) and (6.12). Although the damage parameter D is originally based on strains, Eq. (6.10) supersedes the knowledge of the maximum strain to predict the fatigue life [207].

$$\frac{n_m}{N_m} = D_{m-1} \exp\left(\frac{\sigma_{m,max}}{a}\right)^{-b} \tag{6.11}$$

$$n_{m,residual} = \left(1 - \frac{n_m}{N_m}\right) N_m \tag{6.12}$$

6.4.2 Application of the proposed model

Theoretical damage curves depending on the fractional life can be calculated from Eq. (6.10) for any stress level of interest. The calculated damage curves exhibit a declining increase and follow the trend A in Figure 2.22. The knowledge of constant amplitude S-N data enables to calculate the exhausted as well as the residual fatigue life. Using the above equations, the residual life of two-stage fatigue loading can be predicted from the procedure described in subsection 2.5.3. The fatigue life prediction for the load case A1 (subsection 5.5.1) is for example ($n_1/N_1 = 0.5$) plotted in Figure 6.7 and described in the next paragraphs.
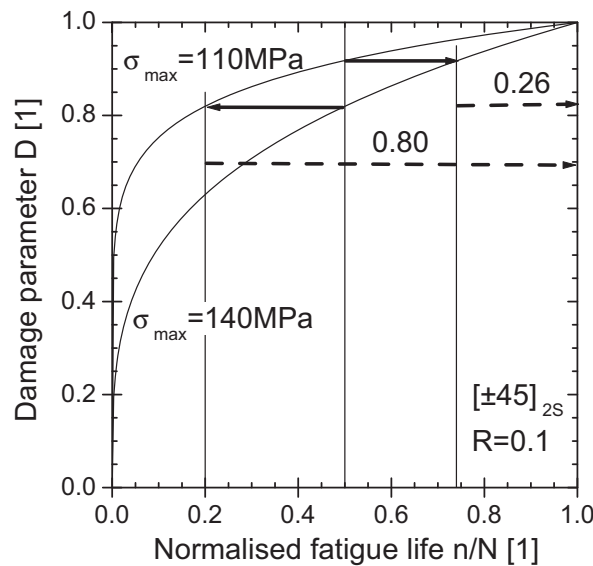
Figure 6.7: Application of the proposed model to predict block load fatigue lives depending on the load sequence.

The damage curves for the maximum stresses of 110 and $140 MPa$ are calculated from Eq. (6.10). The first block load is applied for 50% fractional life,

i.e. $n/N = 0.5$. The second block load is applied until cyclic failure occurs.

The first block load for the L-H load sequence is given by $\sigma_{1max} = 110MPa$. Using Eq. (6.10), a damage value of $D_1 = 0.92$ is obtained. Applying D_1 to Eq. (6.11) for the second block load ($i = m = 2$) with $\sigma_{2max} = 140MPa$, a virtual fractional life of $n_2/N_2 = 0.74$ can be calculated. The residual fractional life is the complementary value to unity, i.e. 0.26. Thus, the model predicts failure at a damage sum of $D = 0.50 + 0.26 = 0.76$ for the L-H load sequence.

In analogy, if a sample is first loaded for 50% fractional life at $140MPa$, a damage value of $D_1 = 0.82$ can be calculated. The corresponding fractional life at $110MPa$ to that damage state is $n_2/N_2 = 0.20$. Again, the residual fractional life is the complementary value to unity, i.e. 0.80. Thus, for the H-L load sequence a damage sum of $D = 0.50 + 0.80 = 1.30$ is obtained for failure.

6.4.3   Verification of the proposed model

Table 6.3 compares mean values of the experimentally observed damage sums (Figure 5.31) with the predictions from the proposed model and the Palmgren-Miner rule. The complete set of predictions is included in Table A.6. The PM-rule gives conservative results for the H-L load sequence but overestimates the fatigue lives for the L-H load sequence [207]. For both load sequences, good agreement is found between the proposed model and the experiment. The proposed model is capable to reflect the observed nonlinear damage evolution behaviour under block load fatigue with $R = 0.1$. The deviations are within the range of fatigue related experimental scatter.

Table 6.3: Damage sums for load case A1 - experiment and prediction

Sequence	High-Low		Low-High	
Damage sum/dev. from exp.	D	dev.	D	dev.
Experiment	1.34	n.a.	0.74	n.a.
Palmgren-Miner $\sum_{i=1}^{m} n_i/N_i = 1$	1.00	-25%	1.00	+35%
Proposed model	1.27	-5%	0.76	+3%

7

Discussion

7.1 Quasi-static loading

7.1.1 Unidirectional laminates

Loaded in fibre direction, the progressive nonlinear course of stress at the intermediate level of tension is due to the reorientation of misaligned fibres into the load direction. The stiffening effect has been similarly reported and already discussed by van Dreumel et al. [208] and Ishikawa et al. [209]. Within experimental scatter, the laminate strain at rupture of $14.1 \cdot 10^{-3}$ coincides with the fibre failure strain of $14 \cdot 10^{-3}$ (Table 4.1) because, once the fibres have failed, the remaining matrix cannot carry the applied load alone. Following, the entire laminate fails. An overload is transferred to the neighbouring intact fibres presumed that the load transfer is not intermitted by longitudinal cracks. With further load increase, even more fibres fail with contemporaneously rising interference of the load transfer.

The declining increase of stress when the laminate is loaded in transverse direction can be attributed to the equal stress assumption (subsection 2.1.3). The nonlinear stress-strain behaviour of the resin (Figure 2.8a) is reflected to the laminate behaviour. Fiedler et al. [210] calculated, that as a consequence of the microscopic triaxial stress state, the matrix fails at a global stress of about one third of that corresponding to the strain to failure from the uniaxial tensile test of the neat resin. The calculations are in good agreement with the experimentally obtained strength of $48 MPa$ at $5.3 \cdot 10^{-3}$ strain. The absence of ductile deformation at failure indicates the dominance of brittle failure.

All experimentally obtained properties achieve the requirements according to the material data sheet [193, 198] in MV and SD. The material data sheet information are based on a nominal fibre volume fraction of $V_f = 0.6$.

This nominal value is within the range of the experimentally determined fibre volume fractions (subsection 4.2.2). The stiffness values calculated by the rule of mixtures (ROM) in both, the longitudinal and the transverse direction show very good agreement with the experimental data. Table 7.1 compares MVs and SDs of the experimental data vs. the material data sheet and ROM data. The ROM stiffness in fibre direction is higher than the experimental Young's modulus. However, the fibre reorientation effect causes the experimental stiffness to increase during loading and to reach the ROM stiffness (Figure 5.2).

Table 7.1: Comparison of tensile properties for the unidirectional laminates.

| Method | $[0]_8$ | | | | $[90]_8$ | |
| | $E_{11}[GPa]$ | | $\sigma_{utt}[MPa]$ | | $E_{22}[GPa]$ | |
	MV	SD	MV	SD	MV	SD
Experiment	140.9	±4.9	2088	±90	8.9	±0.6
Material data sheets [193, 198]	140.0	±8.0	2000	±175	8.8	±1.8
ROM ($V_f = 0.6$)	142.4	-	-	-	8.8	-

From the comparison can be concluded that the material preparation process applied in the laboratory possesses a high quality and reproducibility concerning the fibre and matrix dominated mechanical properties. This quality is supported by the results of the microscopic inspections (subsection 4.2.2).

7.1.2 Angle-ply laminate

Elastic properties

The elastic engineering properties of the AP laminate were determined from the ROM, based on fibre and matrix properties, the fibre volume fraction, and according to the CLT from basic tensile tests. The CLT assumes perfect bonding between the different layers and the absence of edge effects. From the good agreement between experiment and calculation can therefore be concluded that

- the investigated laminate exhibits a high interfacial shear stiffness and strength,

- the specimen preparation is of high and reproducible quality, and that

- the selected specimen geometry guarantees that edge effects have decayed, such that the material rather than the geometry is investigated.

The rotated engineering properties (Figure 6.1) show that the axial stiffness and the Poisson's ratio behave less sensitive to angle variations about the x-direction as does the shear stiffness. Thus, both properties are potentially capable to account for a material degradation with a reduced sensitivity to laminate rotations.

Tensile degradation

Figure 6.2 shows that the tensile stress-strain behaviour and the degradation of axial secant stiffness can be well approximated by a 2-parametric function with the characteristic yield stress as one parameter. To further characterise and model the tensile behaviour, Eq. (6.5) will be applied. The material parameters a and b will be set to the mean yield stress of $172MPa$ and 100 respectively. With this choice, Eqs. (6.6) and (6.7) have to be used carefully when applied to low strains because they predict an initial stiffness of $17.2GPa$ which is 6% below the exact CLT solution and 12% below the experimental mean value.

A comparison of the experimentally determined degradation of the axial secant stiffness and the Poisson's ratio vs. the shear strain is shown in Figure 7.1. Both curves are plotted until $30 \cdot 10^{-3}$ applied strain[1]. Within this strain range, the laminate exhibits a reduction of the axial stiffness to approximately 25% of the initial value. In contrast, the Poisson's ratio increases up to approximately 130% of its initial value. The increase of the Poisson's ratio to absolute values close to unity may be interpreted such that the lateral contraction is strongly dominated by the component in y-direction whereas that in z-direction is secondary. Thus, under quasi-static tensile loading the biaxial Poisson's ratio does not exhibit superior sensitivity to loading when compared to the simple uniaxial longitudinal stiffness. A similar result was reported by Rotem [180] from the comparison of the biaxial shear stiffness with the uniaxial longitudinal stiffness. It can therefore be concluded, that the axial stiffness is an appropriate metric to describe the tensile degradation of the AP laminate.

Stepwise tests

The experimentally determined strain limits of linear elasticity mark the onset of viscoelastic material behaviour approximately at $4 \cdot 10^{-3}$ strain or $75MPa$ stress correspondingly. The laminate behaves time-dependent during loading beyond the range of elasticity. Upon unloading from these or higher loads, the laminate response is time-dependent as well. Figure 7.2 shows the evolution of viscoelastic strain after unloading from tension and compression

---

[1] due to restrictions from the strain gauge measurements
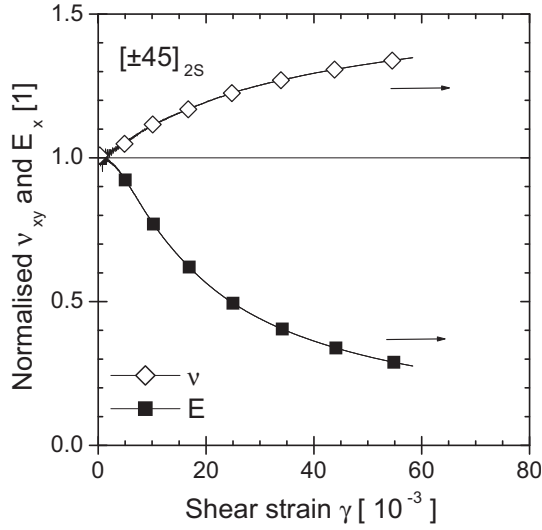
Figure 7.1: Variation of normalised axial secant stiffness and Poisson's ratio vs. shear strain during quasi-static tensile tests.
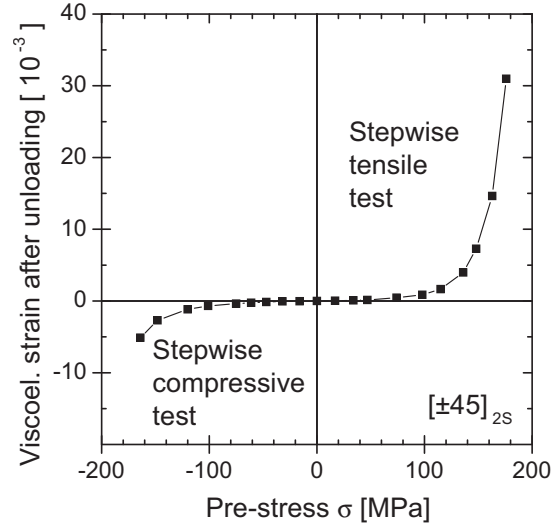
Figure 7.2: Viscoelastic strain after unloading vs. pre-stress for stepwise tests.

whereas each symbol represents one load stage. From Figure 7.3 can be seen that the phenomena of elastic strain recovery and strain strengthening (Figure 2.7) occur during the loading/unloading cycles. The curves in Figures 7.2 and 7.3 shall be interpreted to start at the coordinate origin $(0,0)$ and then to continue to either tensile or compressive loading. An increasing energy dissipation during the higher load stages can be concluded from the increasing area of the unloading/loading loops. After the last tensile load stage, the fraction of the viscous strain (including some additional portion of the reversible strain) to the total strain is about 60% $(31 \cdot 10^{-3}/50 \cdot 10^{-3})$.

Contrary to the stepwise tests, where the load acts for a short duration, the mean stress in constant amplitude fatigue may be interpreted as an enduring constant load. The viscoelastic behaviour will cause larger time-dependent strains for higher cyclic mean stresses. From Figure 7.2 can be concluded that short-term stresses of e.g. $105 MPa$, $91 MPa$, or $77 MPa$ (i.e. $\sigma_{max} = 140 MPa$ and $R = 0.5$, $R = 0.3$, or $R = 0.1$ respectively) correspond to viscoelastic strains immediately after unloading in the range of $\varepsilon = 0.5$ to $\varepsilon = 1.5 \cdot 10^{-3}$. Higher strains are expected for higher stresses and/or longer times.

The degradation of the axial stiffness of the tension-compression stress-strain curve from Figure 7.3 is plotted in Figure 7.4. The stiffness data were calculated as secant values between 0.5 and $2.5 \cdot 10^{-3}$ additional strain during loading after $F = 0$. Each closed square symbol corresponds to one load stage. It can be seen that the stiffness does not increase above the
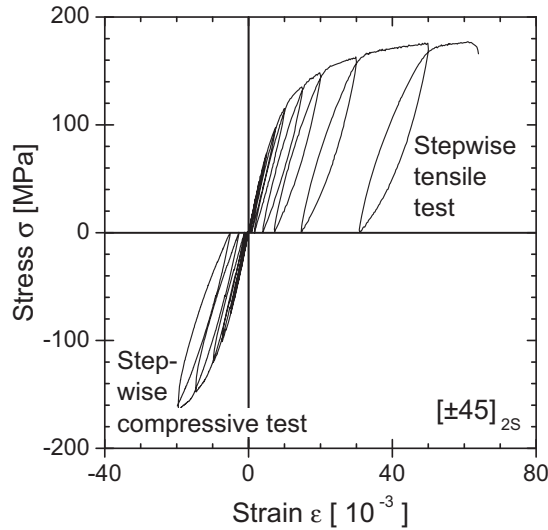
Figure 7.3: Stress-strain during step-wise tests for tension and compression loading.
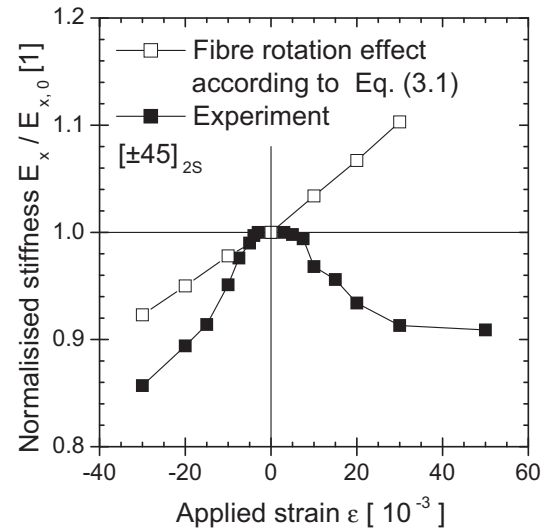
Figure 7.4: Variation of normalised axial stiffness vs. strain during stepwise tensile test. Comparison with fibre rotation effect.

initial value. The stiffness remains unchanged between -5 and $5 \cdot 10^{-3}$ applied strain. As the absolute value of strain increases, the stiffness decreases in a declining manner, however, more pronounced in compression than in tension, where it approaches 91% of the initial value for large strains. The open squares predict the variation of axial stiffness due to the fibre rotation effect according to Eq. (3.1). The discrepancy of both curves suggests that the fibre rotation effect is negligible for the investigated laminate. This conclusion is in accordance with the observation from Figure 5.4a and the inquiries of subsection 3.2.3. Lafarie-Frenot and Touchard [31] reported a fibre rotation of 2° for the investigated carbon/epoxide AP laminate from x-ray experiments, and Sun and Zhu [162] stated a very limited fibre rotation effect for small strain levels (Figure 3.10).

Microscopic failure analysis

Generally, fractographic features represent deformation released internal stresses which arise from the external load. In the elastic region, internal stresses develop in accordance with the applied load and the laminate lay-up. The individual layers of the laminate deform in mutual agreement without cracking or yielding.

Tensile loading of the AP laminate leads to transverse tension and longitudinal shear within the plies (Figure 2.26) and interlaminar stresses at the ply interfaces. Once a stress component exceeds its strength, yielding or local cracking initiates and partly releases the internal stresses. The crack initi-

ation of two different $\pm 45°$-laminates has been reviewed in subsection 3.2.4 to have threshold stresses of approximately $150MPa$ at RT [31]. At elevated temperatures, the deformation may even elapse crack free until fracture [160]. The micrograph in Figure 5.14 shows that cracking occurs preferentially in the centre layer with doubled thickness. The scarce appearance of delamination gives indications for a strong interface.

The presence of cusps (as seen in Figure 5.4c) indicates shear dominated fracture[2] [212]. The shear fracture occurs preferentially along the axis of the fibres rather than across them, since it is the line of least resistance [213]. The relative motions of the two surfaces can be ascertained from the cusps [214]. Here, shear fracture occurred at an angle to both adjacent plies at the interlaminar boundary; the cusps occurring at an angle to the fibre directions but perpendicular to the direction of shear. The angle of approximately $45°$ between the fibre directions and the cusps points to the significance of Mode II shear and the secondary importance of Mode III shear. Because the fibre rotation effect is caused by Mode III shear, its insignificance proves the absence of fibre rotations on a microscopic basis.

The yielding characteristic and the onset of viscoelastic deformations (Figures 5.3a and 7.3) can be attributed to intralaminar yielding of the resin between the tightly packed fibres and even more to the interlaminar, highly shear deformed matrix regions as shown in Figure 5.4c.

7.2   Rate dependent material behaviour

7.2.1   Stress-strain-time relation

Polymers (Figure 2.9) and matrix dominated laminates (Figure 3.8) have been proven to exhibit a strain rate dependent material behaviour [59, 160]. The standard tensile test according to ISO 527 with an actuator velocity of $2mm/min$ therefore constitutes an insufficient reference data base for low and high velocity tests as well as for fatigue tests.

The rate of stress application in fatigue depends on the type of cyclic load and the control mode. The maximum RSA during stress controlled sinusoidal cyclic loading can be calculated from Eq. (2.52). Figure 7.5 shows the effect of the load parameters frequency f and stress amplitude σ_{amp} on the technical strain rate. Figure 7.6 shows the dependence of the required actuator velocity on the geometry and material parameters length l_0 and stiffness E.

---

[2] There are three basic modes of fracture. Mode I is the *tensile opening mode* in which the crack faces separate in a direction normal to the plane of the crack. Mode II is the *in plane sliding mode* in which the crack faces are mutually sheared in a direction normal to the crack front. Mode III is the *tearing shear mode* in which the crack faces are sheared parallel to the crack front. [12, 211]
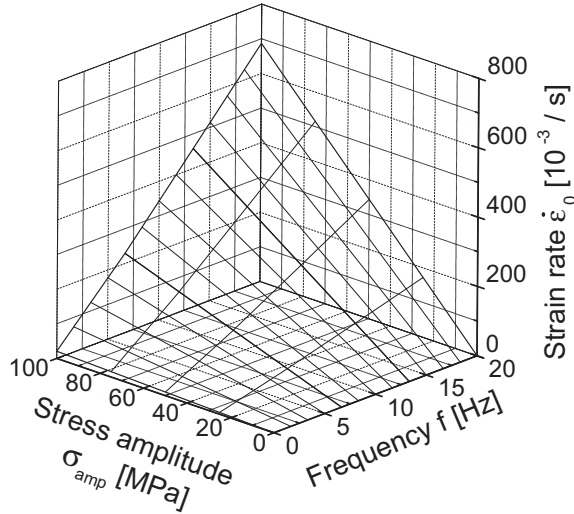
Figure 7.5: Strain rate as a function of stress amplitude and frequency for $E = 19.6 GPa$ and $l_0 = 100 mm$.
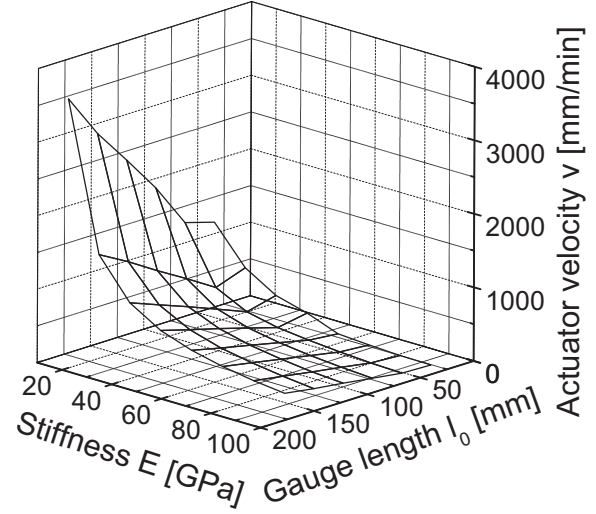
Figure 7.6: Actuator velocity as a function of stiffness and gauge length for $\sigma_{amp} = 54 MPa$ and $f = 10 Hz$.

Equating Eq. (2.52) with Eq. (2.54) leads to an initial maximum strain rate according to Eq. (7.1). One obtains for the AP laminate ($E = 19.6 GPa$) under a fatigue loading of $R = 0.1$, $\sigma_{max} = 120 MPa$, and $f = 10 Hz$ a maximum initial strain rate of $\dot{\varepsilon}_{0\,max} = 173 \cdot 10^{-3}/s$. This value corresponds for a gauge length of $l_0 = 100 mm$ to an actuator velocity of $v_{0\,max} = 1039 mm/min$.

$$\dot{\varepsilon}_{0\,max} = \frac{2\pi f \cdot \sigma_{amp}}{E} \tag{7.1}$$

The rate dependent tensile tests were conducted at technical strain rates between $0.0\bar{3}$ and $3333.\bar{3} \cdot 10^{-3}/s$; the corresponding test durations are approximately 2400 and $0.02 s$. Figures 5.7 and 5.8 show that stiffness E and yield stress σ_y increase with increasing strain rate. The linear increase of σ_y with the logarithm of the strain rate agrees with Eyring's theory of viscosity [56]. The rate dependence of the deformation can by explained with the rheological models discussed in subsection 2.4.2. The time dependent deformation of Maxwell and Kelvin-Voigt elements (Figures 2.13 and 2.14) decreases with a shorter test duration, i.e. a higher strain rate. Upon loading, the polymer network is stretched and distorted. Small chain segments have less time to move over potential energy barriers in the entanglement of the cross linking points. The AP laminate has as a consequence an enlarged range of elasticity and exhibits less plastic deformation. Visible expression of the change in material response depending on the strain rate are, beside the variation of stiffness and yield stress, the onset and the preferred way of yielding which becomes more pronounced below $\dot{\varepsilon} = 33 \cdot 10^{-3}/s$.

7.2.2   Internal energy dissipation

Limitations of the thermographic method

Rate dependent tensile tests are an integral method to characterise the material behaviour in terms of global stresses and strains. The IR thermography enables to investigate the nature of energy dissipation and yielding more localised, yet not at the scale of the constituents (subsection 4.3.7).

Table 4.1 shows that the thermal conductivity of the carbon fibres is approximately two decades higher than that of an epoxide resin while the specific heat capacities of the constituents are similar. Compared to the fibre direction of a single layer, higher temperature gradients are expected transverse to the fibres, where the heat flux crosses alternately fibres and matrix. The overall heat propagation in each layer may be imagined as cigar shaped. The consequences for time dependent tests are that

- events of low heat output (per time) may appear blurry or may not be detected, e.g. for very small strain rates in Figure 7.7,

- a surface temperature distribution may be inhibited by very short test durations, e.g. for internal heat dissipation and very high strain rates in Figure 7.8.

More limitations arise from the experiment conduction and the temperature and time resolution of the equipment. Figure 7.8d shows a superposed picture (detail A) of the specimen width and the warm screw head from the clamping fixture at that position. The red spot (detail B) similarly contains nearly no material but the blurry trace of the moving fractured region.
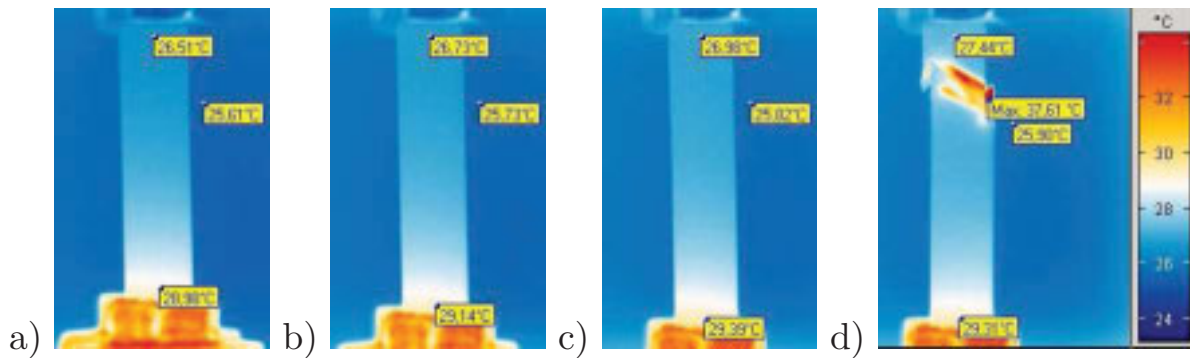
Figure 7.7: Development of the surface temperature during a tensile test with $\dot{\varepsilon}_0 = 0.0\overline{3} \cdot 10^{-3}/s$. a) $\varepsilon = 0$, b) $\varepsilon = 30 \cdot 10^{-3}$, c) $\varepsilon = 60 \cdot 10^{-3}$, d) $\varepsilon_{utt} = 66 \cdot 10^{-3}$.
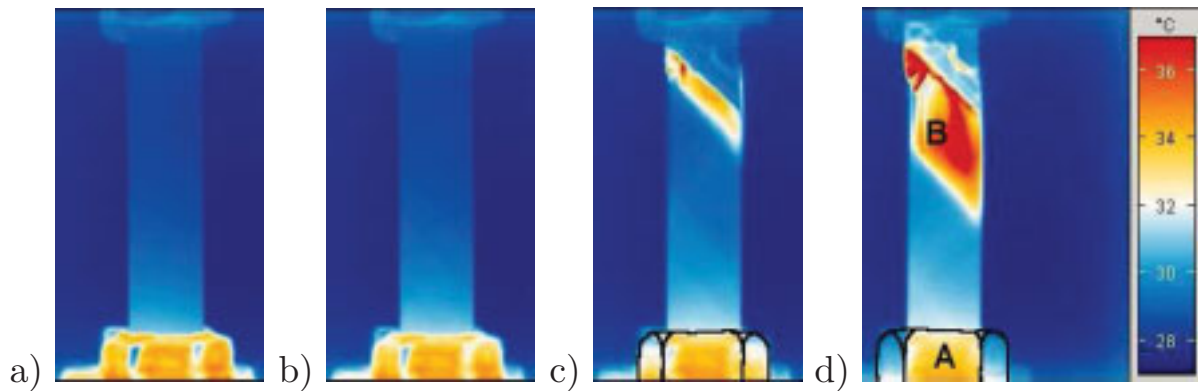
Figure 7.8: Development of the surface temperature during a tensile test with $\dot{\varepsilon}_0 = 3333.\overline{3} \cdot 10^{-3}/s$. a) $\varepsilon = 0$, b) $\varepsilon = 20 \cdot 10^{-3}$, c) $\varepsilon_{utt} = 28 \cdot 10^{-3}$, d) after failure, $\Delta l \approx 16mm$.

Influence of temperature

Figures 5.9 to 5.12 show surface temperature distributions and the respective temperature vs. time plots for $\dot{\varepsilon}_0 = 3.\overline{3} \cdot 10^{-3}/s$. The temperature increase is less than $10K$ during the test duration.

Hobbiebrunken [55] reported from DMTA measurements of the neat epoxide resin 6376 (Figure 2.8b) that a temperature rise of $10K$ from RT reduces the Young's modulus less than 4%. The moduli of the resin and AP laminate at RT are $3.6GPa$ and $19.6GPa$ respectively. The temperature related reduction of the laminate modulus plays thus a secondary role for the evaluation of the rate dependent tensile tests in the elastic region.

Mechanisms

The discussed differences of the yielding response (subsection 7.2.1) can be visualised with the thermographic method. Yielding occurs at about $30 \cdot 10^{-3}$ applied strain according to Table 5.3. Cracking and plastic deformation are related to internal energy dissipation. The local temperature increase in Figure 5.9 indicates that yielding does not comprise the entire gauge length. A strain concentration occurs in initially softer domains. Fracture occurs early after the onset of yielding at the location of the local strain overloads. Yielding within the entire gauge length causes the global temperature increase in Figure 5.10. The material responds with $50 \cdot 10^{-3}$ plastic strain before fracture. The author believes that the arising zigzag pattern above $70 \cdot 10^{-3}$ applied strain results from cracks with large crack opening displacements. Those opposite crack surfaces begin to slide in Mode II and form delamination propagating in the fibre direction (Figure 5.14). The stress concentration at the intersection of the crack or the delamination with the specimen edges

(subsection 3.1.2) causes cracks and/or delamination in opposite orientated layers to start sliding or propagating.

The yield point is always reached, independent of the nominal strain rate. Initial or processing induced defects, weaker domains, and stress intensities in the material do thus not effect the strength and initial stiffness properties. However, their extent and distribution controls the preferred way of localised or global yielding and finally the ultimate properties.

The thermal conductivity of the carbon fibres is approximately two orders of magnitude higher than that of the neat epoxide resin (Table 4.1). From this difference has been previously argued how higher temperature gradients on the surface can be be associated to the fibre directions. All thermographic pictures show the highest temperature gradients aligned under $\pm45°$ to the load direction. The independence of this alignment angle from the applied strain supports the arguments from subsection 7.1.2, that the fibre rotation effect is negligible for the investigated laminate. Otherwise, $80 \cdot 10^{-3}$ applied strain from Figure 5.10f would correspond to a fibre rotation of $4°$ according to Eq. (3.1) and Figure 3.10.

Comparison of microscopic and thermographic results

A characteristic crack spacing of $2a \approx 0.8mm$ was determined from Figure 5.14. The short experiment duration of only $0.2s$ ($\dot{\varepsilon}_0 = 333.\overline{3} \cdot 10^{-3}s^{-1}$) did not allow for significant internal heat dissipation from viscoelastic and viscous deformation. The observed temperature rise in Figure 5.13 is rather believed to originate from the released heat of the cracking along the fibres. This assumption is supported by the sharp lines of increased temperature along the fibre directions.

7.3   Creep loading

7.3.1   Activation energy

The theoretical background outlined in subsection 2.4.3 was applied in subsection 6.3.1 to calculate the activation energies for the epoxide resin 6376 and a $\pm45°$ T800/6376 laminate. The knowledge of the activation energy enables to identify discriminative creep mechanisms for different temperatures and stresses and for this particular case to compare similarities and differences of resin and laminate creep. The experimental creep data were taken from Horoschenkoff [164] and converted to strain rate vs. inverse temperature plots. A single activation energy could neither be determined for the resin

nor for the laminate. However, subdividing the Arrhenius plot in sections of temperatures and stresses allowed to calculate a set of activation energies.

The positive slope between 80 and 23°C in Figure 6.3a eliminates to calculate a reasonable value of Q for the epoxide resin at RT. This phenomenon has to be related to experimental errors, otherwise energy would be released during creep.

Menges [65] described for polymers that the value of Q is approximately constant below the glass transition temperature. Hobbiebrunken [55] determined for the epoxide resin 6376 (Figure 2.8b) a T_g of more than 180°C. It would therefore be permitted to extend the Arrhenius curves (related to $Q = 9 - 14kJ/mol$) as straight lines up to 180°C and down to lower temperatures.

The activation energy of the laminate (Figure 6.3b) between temperatures of RT and 120°C was determined to be in the range of $Q = 7 - 13kJ/mol$ which complies with the value of the neat resin. From the agreement can be concluded, that either mechanisms with comparable values of the activation energy or the same mechanisms act during creep. The equity can be explained by the absence of fibres in the load direction and the matrix dominated behaviour of the AP laminate. The calculated conspicuous increase of Q between 120 and 140°C is doubtful because neither the fibres [195] nor the resin [55, 164, 165] show evidence of characteristic changes in that temperature range.

7.3.2   Creep and recovery

The transition from linear viscoelastic to nonlinear viscoelastic behaviour takes place once the isochronous stress-strain curves, another presentation of creep curves, become nonlinear. Visible expression is the change of the creep compliance $J(t) = \varepsilon(t)/\sigma_0$ which is independent from the applied stress for linear viscoelastic behaviour.

From Figure 7.9a can be seen that the instantaneous response is linear viscoelastic up to approximately $90MPa$. Figures 5.15a and 7.9b show that up to $70MPa$ applied stress, creep strain and compliance increase but approach constant values as the time progresses. Above $70MPa$ applied stress, creep strain and compliance increase with stress and time and do no reach a equilibrium. The overall material behaviour can therefore be characterised as nonlinear viscoelastic.

From Figure 5.16b can be seen that in consequence of the phenomenon of elastic strain recovery (Figure 2.7), the instantaneously recovered strain increases with increasing creep stress. However, no complete strain recovery is observed for the investigated stresses and times. From a decreasing portion
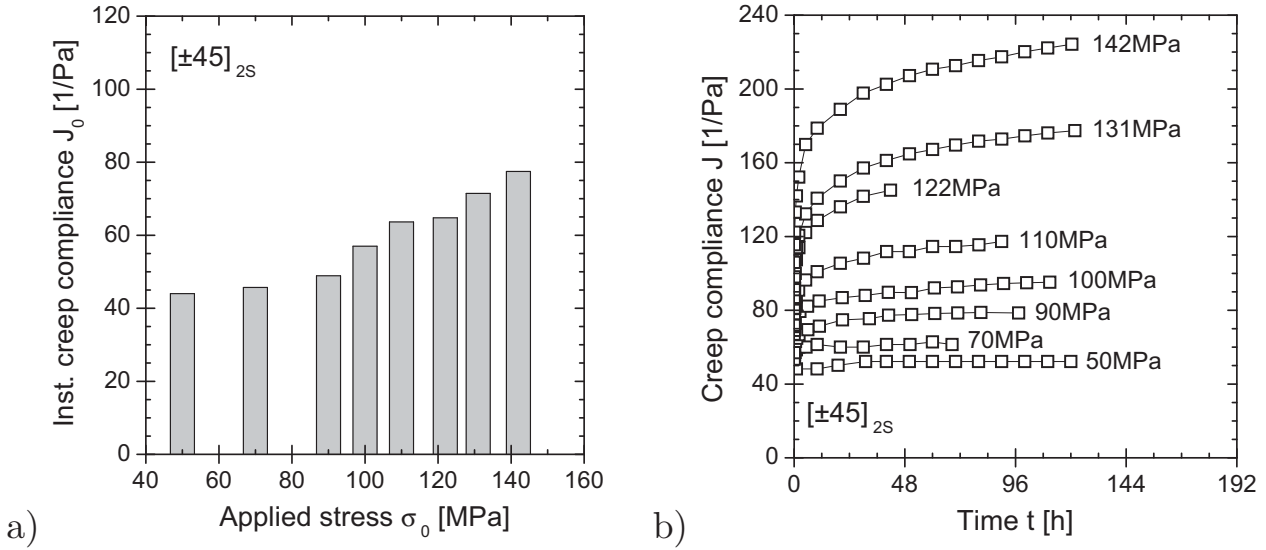
Figure 7.9: Creep results. a) instantaneous creep compliance vs. applied stress and b) creep compliance vs. time.

of recovered strain with increasing creep stress, which was similarly observed by Sturgeon [159], can be concluded that an increasing build-up of viscous strain takes place. The slope at the end of the recovery curves in Figure 5.16a suggests the same effect, that the unrecovered strain is mainly contributed by the viscous rather than the reversible portion.

7.4 Constant amplitude fatigue

7.4.1 Effect of test frequency

Test recommendations

The ambiguous results of the literature survey (Figure 3.15) demanded to an investigation of how the fatigue degradation, i.e. S-N data and strain evolution, is affected by the test frequency. $R = -1$ and $R = 0.1$ fatigue loading were applied. Compared to tension-tension fatigue, reverse loading (highest possible load amplitude) describes a more severe load case. It may additionally include micro-kinking of the fibres and global buckling due to a reduced bending stiffness as a result of delamination propagation. Figure 5.17 shows no significant dependence of the fatigue life on the load frequency because the SDs overlap for all frequencies. Figure 5.19 shows for the highest frequency of $10 Hz$ that a temperature equilibrium only $6K$ above the initial surface temperature is approached during CAF. This temperature rise is expected to be even less for lower frequencies. One can therefore conclude that the unnotched angle-ply laminate does not behave in a strongly frequency de-

pendent manner between 2 and $10Hz$. Test frequencies up to $10Hz$ can thus be recommended for fatigue testing of the investigated laminate.

Time vs. cycle dependence

The testing time is according to Eq. (2.56) inverse proportional to the test frequency for a given cycle number. From Figure 5.18 can be concluded for $R = 0.1$ loading that the hysteresis loops (Figure 2.19) are shifted to higher strains (increase of mean strain) and depending on the maximum stress rotated towards higher stiffness values (decrease of strain amplitude). The strain development clearly correlates with the number of cycles rather than with the test duration. The strain evolution can therefore be attributed as pure cycle dependent fatigue degradation rather than as a time dependent strain in fatigue. A more detailed discussion is given in section 7.5.

7.4.2   Effect of stress ratio

The S-N data and approximation curves of four different stress ratios are given in Figure 5.21 and Eqs. (5.8) to (5.11). From the confidence bands can be seen that the fatigue lives for a given stress scatter less than one decade for $P = 68\%$ and about 1.5 decades for $P = 95\%$ which is comparable to other laminates [215]. Although some restrictions apply to the statistical significance of the data (subsection 5.4.2), the similar slopes for tension-tension fatigue advise analogue mechanisms of failure. This argumentation does not apply for $R = -1$ due to the compression part of the loading. Visible expression is the much lower stress level of the S-N data. The similarity of the S-N slopes is just by chance.

7.4.3   Rate of stress application in fatigue

The Figure 5.21c shows that maximum applied stresses in the range of the the yield stress of $\sigma_y = 172MPa$ correspond to fatigue lives of some hundred cycles. The usual approaching of the S-N data to the yield stress or the UTS (obtained for $2mm/min$) would thus result in a knee of near zero slope at short cyclic lives. A more appropriate choice of the reference value is based on 'quasi-static' stress data which were obtained for rates of stress application which are comparable to the maximum RSA in fatigue. One obtains from Eq. (7.1) maximum strain rates of $\dot{\varepsilon}_0 \approx 200 \cdot 10^{-3}s^{-1}$ in fatigue. Substitution of this value into Eq. (5.6) gives a corresponding yield stress of $\sigma_y = 208MPa$. This value is in good agreement with the numerical intercept of Eq. (5.10) at $N = 1$ which is $206MPa$. Similar results can be obtained for $R = 0.5$ where experimental data for low cyclic lives are, opposed to $R = 0.3$, available.

Therefore, when normalising or extrapolating of the S-N data is required, it is recommended to convert the S-N data with respect to the yield stress obtained for the same RSA to give a single fatigue behaviour. Sims and Gladman [173, 174] stated similar conclusions for other FRPs and fatigue loadings. However, not taking into account the rate dependent material behaviour leads to conservative statements, because the AP laminate becomes stronger and stiffer with increasing strain rates.

7.4.4 Choice of degradation parameters

It was specified in section 2.5 that life prediction methods require the experimental observation of the damage accumulation process and the formulation of an appropriate damage metric [82]. The dependence of the fatigue strength, the mean strain and the strain amplitude, and the variation of the hysteresis loops on the applied loading, i.e. the stress ratio and the stress level, is illustrated and described in subsection 5.4.2. The separate presentation of mean strain and strain amplitude allows to conclude the evolution of the minimum and maximum strain (Eqs. (2.43) and (2.44)) as well as the degradation of the dynamic and fatigue stiffness (Figure 2.18 and Eqs. (2.57) and (2.58)). The degradation of the stiffness and the variation of the damping characteristics (Eq.(2.55)) can be read off the hysteresis loops. Figure 7.10 shows that the amount of damping increases with an increasing stress amplitude. However, due to the different curve characteristics depending on the stress ratio, the damping is not a suitable damage metric to formulate the material degradation.
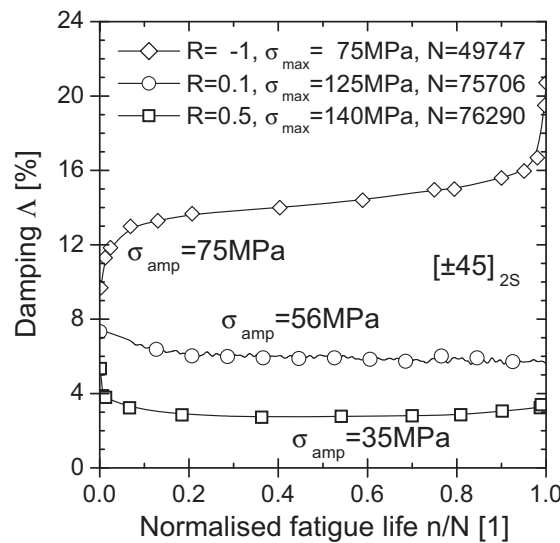
Figure 7.10: Effect of stress ratio on the damping behaviour in constant amplitude fatigue

Similar conclusions can be drawn for the strain amplitude and the mean strain. Whereas the mean strain continuously increases in tension-tension fatigue, it is insensitive to reverse fatigue loading. Almost the opposite behaviour is observed for the strain amplitude, i.e. the dynamic stiffness. Depending on the tension-tension loading, the dynamic stiffness may exhibit a rising, declining, or alternating behaviour [91]. An analogous behaviour was found for the Poisson's ratio [216] and the dynamic shear stiffness (Figure 3.16a).

The maximum strain steadily increases during the fatigue life for a given fatigue stress. The fatigue stiffness concept of Hwang and Han [90, 108] is based on the maximum strain and hence covers the effects of hysteresis loop shift and rotation. For a given maximum stress, the fatigue stiffness can be reduced to the maximum strain and the second model (Eq. (2.77)) of Hwang and Han [108, 110] can moreover be applied to define fatigue damage. The choice of the maximum strain as a damage parameter has obvious benefits [207]:

- direct physical damage metric, availability without extensive mathematical operations,

- suitability for more complex load regimes,

- applicability on various geometric structures, as required for constructive designs,

- possibility of different monitoring techniques, e.g. optical, mechanical, or electrical measurements.

7.4.5   Microscopic failure analysis

From the hysteresis loops of Figures 5.22 to 5.27 can be seen that the maximum strain in fatigue was in the majority of cases below $20 \cdot 10^{-3}$. This strain value corresponds for a wide range of strain rates to the nonlinear part of the stress-strain curve (Figure 5.7a) but remains below the yield strain (Table 5.3). Lafarie-Frenot and Touchard [31] determined the onset of cracking under quasi-static loading above $20 \cdot 10^{-3}$ strain. The discussion of the thermographic results in subsection 7.2.2 gave a similar strain value for the investigated laminate. From this consideration which is supported by the results of Sturgeon [159] (subsection 3.2.4) can be expected that no signs of cracking or delamination are observed for most of the fatigue life. This behaviour is further attracted by

- the chemical composition of the epoxide resin 6376 which, compared to other epoxide resins, exhibits an improved toughness and crack resistance [197] and

- the slightly increased temperature due to the fatigue loading (Figure 5.19) which entails a more ductile material behaviour.

The absence of cracks in Figure 5.28 confirms these thoughts. Solely the immediate neighbourhood of the fractured region shows signs of cracking and delamination. The SEM micrographs of fracture morphologies (Figures 5.29b and 5.30b) show considerable matrix abrasion at the delamination interface, whereas the Figures 5.29a and 5.30a show ruptures with (partly) intact fibre/matrix interfaces.

Sustained internal friction at the ply interfaces is necessary to create the worn out fracture morphologies. An increase of temperature is thus expected in the region of subsequent failure towards the end of the fatigue life. The surrounding material is expected to approach temperature equilibrium. Some energy is dissipated from the hysteresis loops, however, no additional contribution results from cracking and delamination. This argumentation is supported by Figures 5.19 and 5.20.

7.5   Creep-fatigue interaction

7.5.1   Theoretical deliberations

Fatigue loads have a twofold effect. In fatigue, one might suppose that the mean load can be considered as a constant load. Then, the material would creep under its effect. For a given fatigue load under constant amplitude stress control, information about the creep strain evolution would be transferable to the creep induced mean strain development in fatigue [91, 217]. Eqs. (7.2) and (7.3) summarise the strain components, contributing to the maximum strain in fatigue. The creep strain is one portion of the fatigue mean strain, i.e. $\varepsilon_{cr} \in \varepsilon_{mean}$. Depending on the stress ratio and the stress level, either ε_{cr} or ε_{fat} will dominate the maximum strain. The term ε_{fat} is contributed by both, fatigue mean stress and stress amplitude.

$$
\begin{aligned}
\varepsilon_{max} &= \varepsilon_{mean} + \varepsilon_{amp} & (7.2)\\
&= \varepsilon_{cr}(\sigma_{mean}, t) + \varepsilon_{fat}(\sigma_{mean}, \sigma_{amp}, n) & (7.3)
\end{aligned}
$$

The portion $\varepsilon_{cr}(\sigma_{mean}, t)$ of the total strain in fatigue and its components as separated in Eq. (2.29) can be determined from creep tests. Knowledge of an array of creep curves hence enables to predict the influence of creep on the

strain development in fatigue [91, 217]. In subsection 6.3.2 could be shown, that the Nutting equation (2.37) is capable to predict the stress and time dependent strain during creep loading of the AP laminate.

The evaluation of the experimental results in subsection 7.3.2 revealed an approximate threshold stress of $\sigma_{th,cr} = 70 MPa$ for static creep. The fatigue related strain from Eq. (7.3) shall be negligible during fatigue loading below the endurance limit. A variation of the total strain in fatigue during cycling would thus result from cyclic creep. It may then be expected that the suggested modelling technique for static creep can be applied to cyclic creep and that the threshold stresses for static and cyclic creep are identical.

$$\sigma_{mean} = \sigma_{max}\,\frac{1+R}{2} \qquad (7.4)$$

The mean stress in fatigue σ_{mean} can be calculated for any maximum stress σ_{max} and stress ratio R from Eq. (7.4) which was determined from mathematical manipulation of Eqs. (2.43) to (2.45). Eq. (7.4) is visualised by the solid lines in Figure 7.11 for stress ratios of $R = 0.5, 0.1$, and -1. The vertical dashed line represents the tensile strength. The dash-dotted lines describe depending on the stress ratio corresponding pairs of maximum cyclic stress and fatigue mean stress at the endurance limit of $N = 2 \cdot 10^6$.

$$\text{Condition for cyclic creep} : \sigma_{mean} \geq \sigma_{th,cr} \qquad (7.5)$$

According to the theoretical deliberations, cyclic creep is expected to occur for mean stresses higher than the threshold stress for creep, i.e. Eq. (7.5) is true. These loadings are marked by the hatched area in Figure 7.11.

7.5.2 Experimental verification

No creep is expected for $R = -1$ because of zero mean stress, thus $\sigma_{mean} < \sigma_{th,cr}$. This argument is in agreement with the mean strain evolution under CAF and block load fatigue (Figures 5.26a, 5.27a, and 5.34) and the results of Rotem [180].

The higher the stress ratio in tension-tension fatigue ($0 \leq R < 1$), the higher is the mean stress. Thus, the laminate is expected to be more susceptible to creep. Figure 7.11 shows for $R = 0.1$ that a maximum stress σ_{max} equal to the endurance limit of $100 MPa$ corresponds to a mean stress of $\sigma_{mean} = 55 MPa$, which is below the threshold stress for creep. The portion of creep strain on the mean strain evolution in fatigue should be negligible. Unlike this consideration, creep is expected to increasingly contribute to the fatigue mean strain once the mean stress exceeds the threshold stress for

creep. However, the effect may be counterbalanced because higher stresses correspond to shorter fatigue lives, thus less time for creep.

Following the previous explanations, one predicts that the fatigue mean strain evolution during $R = 0.5$ loading is contributed by creep, even for cyclic stresses clearly below the endurance limit.
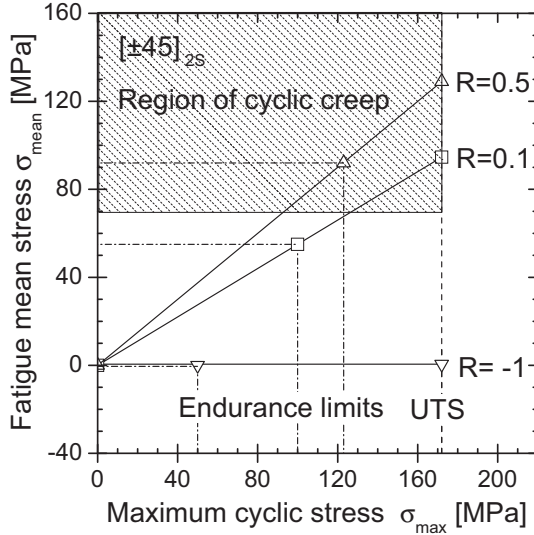
Figure 7.11: Relation of mean and maximum stress in fatigue for different stress ratios. Cyclic creep is expected for loading within the hatched area.
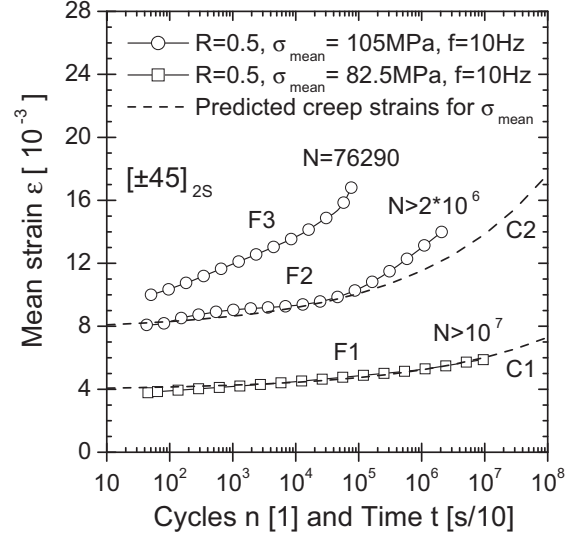
Figure 7.12: Comparison of experimental fatigue mean strains (F1-F3) with creep strains (C1, C2) predicted for the mean stresses in fatigue [217]

The Tables 7.2 and 7.3 estimate the amount of creep strain to be expected from different combinations of stress ratio, cyclic stress, and frequency. The fatigue lives were determined from the mean S-N curves. The creep strain calculation is based on the modelling results from subsection 6.3.2. The assumption of a creep threshold stress $\sigma_{th,cr}$ is not reflected by Nutting's power law approach which contains an inherent stress dependence of the estimated creep strains ε_{cr}. Despite this drawback and the statistical uncertainties from the modelling of the CAF and creep data, the creep strain during $R = 0.1$ loading never exceeds $\varepsilon_{cr} = 0.6 \cdot 10^{-3}$. One can therefore conclude for this type of loading that the fatigue strain development is not affected by creep. This conclusion is in accordance with the experimental observations from Figure 5.18 where the strain evolution in fatigue was independent from the load frequency.

Non-negligible creep strains of $\varepsilon_{cr} = 2 - 4 \cdot 10^{-3}$ must be expected during $R = 0.5$ loading. Both ε_{cr} columns in Table 7.3 show the opposite trends of creep strain increase due to the stress increase and creep strain decrease due to the stress induced fatigue life reduction. These counterbalancing effects cause the highest creep strain to develop for medium stresses and times.

Table 7.2: Estimated creep strains at fatigue failure for $R = 0.1$.

σ_{max} [MPa]	σ_{mean} [MPa]	N [1] [a]	$t\,[h]$ @10Hz [b]	ε_{cr} [10^{-3}] [c]	$t\,[h]$ @2Hz [b]	ε_{cr} [10^{-3}] [c]
80	44	$5.41 \cdot 10^7$	$1.50 \cdot 10^3$	0.17	$7.51 \cdot 10^3$	0.24
100^d	55	$3.22 \cdot 10^6$	$8.93 \cdot 10^1$	0.26	$4.47 \cdot 10^2$	0.37
110	61	$7.85 \cdot 10^5$	$2.18 \cdot 10^1$	0.30	$1.09 \cdot 10^2$	0.42
140	77	$1.14 \cdot 10^4$	$3.16 \cdot 10^{-1}$	0.36	$1.58 \cdot 10^0$	0.51
160	88	$6.77 \cdot 10^2$	$1.88 \cdot 10^{-2}$	0.37	$9.41 \cdot 10^{-2}$	0.51

[a] Fatigue life from Eq. (5.10)
[b] corresponding time to N from Eq. (2.56)
[c] time dependent strain from Eq. (2.37) with parameters taken from Table 6.2
[d] experimental endurance limit

Table 7.3: Estimated creep strains at fatigue failure for $R = 0.5$.

σ_{max} [MPa]	σ_{mean} [MPa]	N [1] [a]	$t\,[h]$ @10Hz [b]	ε_{cr} [10^{-3}] [c]	$t\,[h]$ @2Hz [b]	ε_{cr} [10^{-3}] [c]
80	60	$6.37 \cdot 10^9$	$1.77 \cdot 10^5$	1.90	$8.84 \cdot 10^5$	2.67
100	75	$1.48 \cdot 10^8$	$4.11 \cdot 10^3$	2.36	$2.05 \cdot 10^4$	3.31
130^d	98	$5.24 \cdot 10^5$	$1.45 \cdot 10^1$	2.35	$7.27 \cdot 10^1$	3.29
140	105	$7.98 \cdot 10^4$	$2.22 \cdot 10^0$	2.21	$1.11 \cdot 10^1$	3.10
160	120	$1.85 \cdot 10^3$	$5.15 \cdot 10^{-2}$	1.83	$2.57 \cdot 10^{-1}$	2.56

[a] Fatigue life from Eq. (5.8)
[b] corresponding time to N from Eq. (2.56)
[c] time dependent strain from Eq. (2.37) with parameters taken from Table 6.2
[d] experimental endurance limit

Figure 7.12 compares different experimentally obtained mean strain curves with creep curves predicted for the mean stresses in fatigue. Based on the relation that one cycle at $10Hz$ lasts $0.1s$, the abscissa is used for the cycle number as well as the creep time. Below the endurance limit, the fatigue mean strain evolution (curve F1) coincides with the creep strain prediction for the fatigue mean stress (curve C1). This agreement indicates that the total strain in fatigue is solely dominated by the creep term ε_{cr} in Eq. (7.3).

The two mean strain curves F2 and F3 in Figure 7.12 correspond to fatigue lives of $N > 2 \cdot 10^6$ and $N = 76290$. In the former case, the fatigue mean strain evolution agrees with the creep prediction (curve F2) until 10^5 cycles which indicates the dominance of creep. Fatigue damage develops for $n > 10^5$,

noticeable at the increasing distance between the curves C2 and F2. This distance may be used as a fatigue damage metric. In the latter case of fatigue failure (curve F3), the fatigue mean strain is from the beginning on a higher level. As the cycling continues, the vertical distance between the curves C2 and F3 increases as well. One can therefore conclude that the fatigue term ε_{fat} from Eq. (7.3) dominates the total strain evolution.

7.6   Pre-loads preceding fatigue loading

Pre-loads of quasi-static, constant, cyclic or random character may occur accidentally or on purpose in the laboratory scale and for real structures, e.g. by

- improper handling during processing and preparation,

- accidental loadings during storage and transportation,

- proof loads from strength check-up's,

- unexpected loads, e.g. tool drop, and

- uncertainties of the service loads.

The reviewed literature gave dissatisfactory indications whether and how pre-loads prior to the regular cyclic load influence the fatigue behaviour of FRPs, especially angle-ply laminates. To investigate the influence of pre-loads on the stiffness evolution in stress controlled CAF and on possible variations of the fatigue life, two different initial load scenarios (B and C) and two different creep-recovery cases (D1 and D2) were selected.

7.6.1   Initial loads

A reduction of the fatigue life could neither be determined for cyclic initial stresses nor positive triangular pulse loads (Figures 5.38 and 5.40). In fact, the fatigue lives tend to increase as they are in the majority of cases above the mean value of the 'virgin' reference loading. Tables A.9 and A.10 moreover show that the maximum obtainable fatigue life increases with the level of the applied initial load. This trend is not strong but cannot be neglected as some data points are outside the upper 68% confidence band.

Positive triangular pulse

In Figure 7.2 is shown that tensile stresses of 100 to $140 MPa$ result in viscoelastic strains of 1 to $4 \cdot 10^{-3}$ immediately after unloading. The author

believes that some plastic deformation build-up reduces stress intensities in the matrix, e.g. at defects, micro-voids, or locations of intimate fibre contact.

Figure 5.39b illustrates that the dynamic stiffness of the material is not affected by the residual viscoelastic strain from the initial pulse load. The mean strain on the other hand starts at a higher level but exhibits a declining slope $d\varepsilon_{mean}/dn$ which is mainly due to the release of the viscoelastic strain from the initial load. The cyclic loading passes off without any cracking or delamination (Figure 5.28). The arrays of mean strain and strain amplitude curves approach identical values before the final strain increase. Here, the reduction of stress intensities in the matrix may lead to a retardation of the initiation and progression of cracks and delamination in the failure zone to be and as a consequence to an extension of the fatigue life. This effect cannot be used for design purposes because cracking merely accompanies the last fatigue stage.

The observation of delayed cracking is supported by the observations of Sturgeon [159] for fatigue loads and Lafarie-Frenot and Touchard [31] for tensile loads (for both see subsection 3.2.4). A possible fatigue life extension due to the triangular pulse load should thus be regarded as an 'extra time' of the rupture process.

Cyclic initial stresses

It can be seen from Figure 5.37b that the way of approaching the nominal cyclic stresses has no influence on the dynamic stiffness degradation. From the trait of cyclic initial stresses can be concluded, that the introduced effect of the reduction of stress intensities by a proof stress cannot occur for the load cases B1 and B2. Solely the cyclic overloads during B3 (cycling down from $\sigma_{max} = 140MPa$ to $\sigma_{max} = 120MPa$) may lead to additional viscoelastic strains at the beginning of the regular cycling. This argumentation is supported by the fatigue life results of Figure 5.38. The duration for additional deformation build-up is the time during which the cyclic overload is higher than the maximum stress of the subsequent regular cycling. The mean strain for B3 is consequently the highest with the lowest slope $d\varepsilon_{mean}/dn$. The further argumentation on the relation between cracking and fatigue life extension follows that of the triangular pulse stress.

7.6.2   Creep and recovery prior to fatigue loading

The dependence of the fatigue behaviour on preceding creep and recovery loading was systematically investigated by two different load cases (D1 and D2). The first case addressed the effect of the creep stress level, the second case the effects of the creep and recovery times. Neither one of the load

cases was found to have a negative effect on the subsequent fatigue lives; the fatigue lives tended moreover to increase (Figures 5.41 and 5.45).

The trend of fatigue life extension is not statistically significant for the load case D2 in Figure 5.45. Following the argumentation that a fatigue life extension results from a sustained reduction of localised stress intensities by plastic deformation build-up, two competing effects are possible. The applied creep stress was higher than the creep threshold stress which causes cyclic creep according to section 7.5. Due to the special case that the preceding creep stress was equal to the fatigue mean stress, a reduction of stress intensities due to static creep competed with that due to cyclic creep. The resulting fatigue life extension was not pronounced.

The load case D1 revealed a stronger trend of fatigue life extension. All fatigue life data are above the upper 68% confidence band of the reference loading. In subsection 7.5.2 could be shown that the strain evolution during $R = 0.1$ CAF loading is not contributed by creep. The previously discussed effect of competing static and cyclic creep is therefore absent. The reduction of stress intensities is achieved by the prolonged preceding creep load whereas the effectiveness tends to grow with increasing creep stress. This conclusion is in accordance to the observations of Sun and Chim [192] (section 3.5).

7.7 Block load fatigue

There is very limited information available on the material behaviour of angle-ply laminates under block load fatigue conditions. All surveyed reference works from subsection 3.4.2 deal with a constant stress ratio and tension-tension fatigue. Here, the block load fatigue tests comprised three different load cases, including tension-compression fatigue and the variation of the stress ratio. Prior to conducting the block load fatigue tests, the individual block loads have been studied in CAF (section 5.4). In doing so, the maximum strain has been found to describe the material degradation in an appropriate manner (subsection 7.4.4).

7.7.1 Constant stress ratio

R=0.1

The load case A1 ($R = 0.1$, maximum stresses of 110 and $140 MPa$) revealed a strong dependence of the fatigue life on the load sequence. The damage sums are greater than unity for the H-L load sequence, whereas the damage sums for the L-H sequence are smaller than unity. This dependence follows the boundary effect (Figure 2.24) of Yang and Jones [128].

To predict the fatigue life, the second model of Hwang and Han [108, 110] from Eq. (2.77) was modified. The previously required knowledge of an array of maximum strains was replaced by one stress dependent power law equation and combined with a linear cumulative damage theory. Although the proposed model utilises a linear damage accumulation technique, it has a non-linear character because the strain based damage metric develops nonlinearly with the fractional life.

From Figure 6.7 can be seen how the proposed model is capable to predict stress and load sequence dependent damage sums. The comparison of experiment and model in Table 6.3 shows good agreement for both load sequences. The proposed model accounts for the observed nonlinear damage evolution and gives thus better predictions than the Palmgren-Miner rule. The generic character of the model suggests its universal applicability to other matrix dominated laminates under similar loads.

R=-1

H-L sequence   The fatigue lives for the load case A2 ($R = -1$, maximum stresses of 65 and $105 MPa$) are independent of the load sequence extended when compared to the PM-rule prediction. The data points for the H-L sequence in Figure 5.33 follow the boundary effect and are similarly distributed as those for the load case A1. However, the boundary effect for both load cases, A1 and A2, is superimposed by the memory effect. Tables A.6 and A.7 list samples with fractional lives larger than unity during the second (L) load stage. This observation does not result from fatigue related scatter but can be attributed to a strengthening effect of the first (H) load stage expressed by the strain (damage) development during that stage. This permanent deformation build-up (Figures 5.32a and 5.34a) may reduce stress intensities in the matrix. As a result, the onset of cracking and delamination may be retarded even though the far field stress might remain the same.

L-H sequence   The fatigue life data for the L-H sequence at $R = -1$ do contrarily not agree with the expectation from the boundary effect and are therefore dominated by the memory effect. The laminate experienced previous to the H-stage a reverse fatigue loading with $\sigma_{max} = 65 MPa$. Figures 5.27 and 5.34 show that such a load level does the stiffness properties not cause to change noticeably for up to 99% fractional life. Using the terminology of Chou and Crowman [105], final failure occurs by *sudden death* (trend C in Figure 2.20). Assuming a correlation between stiffness degradation and residual strength, the damage evolution (during the first load stage of A2) is thus retarded to fractional lives very close to unity. These long fractional lives do not appear for the load case A2.

The first load stage has moreover a strengthening effect because all fractional lives of the second load stage are larger than unity. However, this effect is not significant if one takes the confidence bands from Figure 5.21d into account. The 'extension' of life remains within the P=68% band.

7.7.2 Variation of the stress ratio

The load case A3 was chosen to investigate the block load fatigue behaviour for a variation of the stress ratio between $R = 0.1$ and $R = -1$ and vice versa. Whereas the maximum stress is higher during the $R = 0.1$ block ($127MPa$ vs. $76MPa$), the stress amplitude is larger during the $R = -1$ block ($76MPa$ vs. $57MPa$). Thus, the boundary effect cannot explain that the fatigue lives are regardless of the load sequence extended if compared to the PM-rule prediction.

From the CAF results can be seen, that the maximum strain of the A3 stress levels increases steadily and, relatively and absolutely, more for $R = 0.1$ when compared to $R = -1$. Relating the strain development to the damage evolution, i.e. the residual strength degradation, one can conclude that the residual strength of the first stage at $R = 0.1$ follows the trend A in Figure 2.20, whereas that at $R = -1$ follows the trend C.

The apparent life extension of the $R = -1 \rightarrow R = 0.1$ sequence can thus be explained such as that of the L-H sequence for the load case A2. However, due to the higher stresses during the first stage of A3 compared to A2 ($\sigma_{max} = 76MPa$ vs. $\sigma_{max} = 64MPa$), some damage develops during that stage. The fractional lives of the second stage are therefore lower for A3 and on average smaller than unity (Table A.8).

The strengthening mechanism suggested for the H-L sequence for A1 causes the apparently extended fatigue lives of the $R = 0.1 \rightarrow R = -1$ sequence. Here, the memory effect is more pronounced, as the fractional lives of the second load block are on average considerably larger than unity. As for A1 and A2, the strengthening effect remains within the P=68% band and is hence not significant.

8

Summary

Introduction

Fibre reinforced polymers (FRPs) have unique advantages over monolithic materials, such as a high specific stiffness and strength related to a superior structural performance. Furthermore, FRPs afford the ability to design the material and the structure in one unified and concurrent process, and they possess a versatile adaptability to the intended function. Therefore, increasing use is being made today from FRPs such as carbon/epoxide laminates which serve their engineering purposes in many industries.

Motivation

The anisotropic and heterogeneous character of the material provides many degrees of freedom for optimum configuration but requires a high degree of know-how for design, computation, manufacturing, and life prediction. A vital role is thereby taken over by the ±45°-layers. Nearly all multidirectional laminates contain a considerable fraction of these angle-plied reinforcement layers to carry shear loads, to control stress concentrations and the damage behaviour, and to account for load uncertainties. The fundamental understanding of the mechanisms of deformation and failure in ±45°-layers and their dominance and interactions under service conditions is thus essential for engineering design and justifies a scientific engagement.

Scientific relevance and keys to the solution

Chapter 3 reviewed that pure ±45°-laminates are to a great extent subject to a geometry, load and load rate, temperature, time, and cycle dependent material response. To avoid such a complex material behaviour and to account for other loadings, ±45°-layers in structural applications are often used in combination with layers of other fibre orientations. Even though the overall state

of deformation is then changed towards constraints due to the mutual agreement with the other layers, the inherent characteristics of the $\pm45°$-layers are included. Altogether, the investigation and the fundamental knowledge about $\pm45°$-laminates is of scientific relevance, and as it contributes to a better understanding of the $\pm45°$-layers in multidirectional laminates it is as well of engineering interest.

The state of the art has reviewed that the geometry and temperature dependence of $\pm45°$-laminates are well understood and that the creep behaviour can be well predicted by the time temperature superposition principle. Moreover, wide experience is available on the constant amplitude fatigue behaviour with regard to the constituents and the effects of load and frequency on the fatigue life. Insufficient knowledge exists for integrated load-property interactions. Therefore, the present work aimed to improve the material understanding of matrix dominated $\pm45°$-laminates for the following cases:

1. the dependence of the (quasi-static and cyclic) material response and the load rate,

2. the interactions of creep and fatigue, and

3. the influence of pre-loads and load sequences in fatigue.

The integrated consideration of the load and material interactions centres to *evaluate and predict the strength and life time of angle-ply CFRP laminates under static and cyclic loads*. On the basis of the observed statistically distributed microscopic damage evolution, homogenised approaches were thereby preferentially applied. The material choice of HTA/6376 carbon/epoxide prepreg laminates was based on its practical relevance as a certified and used material for structural applications in aircrafts.

Results

The mechanisms of the deformation and the damage process in $[\pm45]_{2S}$ HTA/6376 laminates were assessed by different experimental techniques such as stress-strain hysteresis measurements, microscopy, and thermography. The conducted experiments included (rate dependent) quasi-static tests, creep tests, constant amplitude and block load fatigue tests, tests with initial loads in fatigue, and combined creep-recovery-fatigue tests. The observed experimental results have been discussed, modelled by homogenised approaches, and linked to each other. The main findings are:

(Quasi-)static loading

- The stress-strain behaviour exhibits a *characteristic yielding*. The stiffness and yield properties are independent from the distribution of ma-

terial defects. Above the yield point, the distribution of material defects decides whether the structural performance is dominated by local or global heat dissipation. The heat dissipation during yielding and cracking can be detected by infrared thermography.

- *Cracking and delamination* occur during quasi-static loading. The cracks propagate under $\pm 45°$ to the load direction. A characteristic shortest crack spacing (of about $0.8mm$) is approached.

- The stress-strain behaviour exhibits a *load rate dependence*. Whereas stiffness and yield stress increase linear with the logarithm of the strain rate, the yield strain decreases linearly. The occurrence of a yield point is independent from the strain rate. The amount of yielding decreases with increasing strain rate which results from a retarded reduction of stress intensities by viscoelastic and viscous deformation.

- The linear elasticity is early in loading (at about $3 \cdot 10^{-3}$ strain) displaced by linear viscoelasticity followed by a nonlinear viscoelastic and viscous behaviour. The *threshold stress for static creep* could be determined to approximately 40% of the yield stress.

- Equal *activation energies for static creep* were found for the neat resin and the laminate, which suggests the dominance of the same mechanisms during creep. The equity follows from the absence of fibres in the load direction and supports the matrix dominated characteristics of the laminate.

- Based on experimental data, a bilinear approximation for the instantaneous strain response was combined with parametric power law functions to *predict the stress and time dependent strain evolution* for constant loading. Good agreement between experiment and prediction was observed.

Cyclic loading

- The logarithm of the *fatigue life* increases linearly with decreasing maximum cyclic stress for a given stress ratio in stress controlled fatigue. For a given maximum cyclic stress, the fatigue life decreases with increasing stress amplitude.

- There is a wide frequency and load spectrum where the fatigue life and the strain evolution are *independent from the load frequency*. Self-heating due to internal damping is secondary as a *temperature equilibrium* is approached.

- *No characteristic crack pattern* is formed under cyclic loading. In fact, no cracking or delamination occurs away from the rupture region to-be.

- The *maximum strain in fatigue*, i.e. the sum of mean strain and strain amplitude displays an *integrated damage metric* to account for hysteresis loop shift and rotation, is universally applicable, and offers different monitoring techniques.

- The fatigue life under block load conditions is *load sequence dependent*. The damage accumulation behaviour depends on the load sequence and the load level. Strain based damage evolution concepts and models were developed and verified for different load sequences.

General comments and load interactions

- As confirmed by stiffness measurements, the thermography method, the fracture morphology, and literature predictions, the *fibre rotation effect is negligible* for any loading and neither not observed as an edge effect.

- *Relating tension-tension fatigue data* to quasi-static data obtained for the same rate of load application avoids the frequently displayed knee and the region of near zero slope at low cyclic lives in S-N presentation.

- *Cyclic creep* occurs once the mean stress in fatigue exceeds the threshold stress for static creep. The portions of creep and fatigue strain on the total strain development under cyclic loading depend on the stress ratio and the mean stress and can be well estimated.

- Pre-loads in terms of *initial pulse or cyclic stresses* (of 58 to 81% of the yield stress), or *creep and recovery prior to fatigue loading* do not reduce the expected subsequent fatigue life. The fatigue life tends rather to be prolonged which is believed to result from the reduction of stress intensities in the matrix by plastic deformation. The plastic deformations due to initial loads and due to cyclic creep are thereby competitive. Enduring loads are more beneficial than short-time loads.

Résumé

The material behaviour of matrix dominated $\pm 45°$ carbon/epoxide laminates has been extensively reviewed and studied for simple and complex loading conditions. The fundamental material understanding of the angle-ply layers has been improved by the integrated consideration of load interactions. The common characteristics of neat resin and angle-ply laminate enabled to develop and successfully apply strain based homogenised approaches to predict the strength and life under static and cyclic loads.

Appendix A

Table A.1: Tensile test results of the unidirectional laminates

$[0]_8$				$[90]_8$			
#	σ_{utt} [MPa]	ε_B [10^{-3}]	E_x [GPa]	#	σ_{utt} [MPa]	ε_B [10^{-3}]	E_x [GPa]
0603	2175	14.4	135.0	0216	25	2.7	8.7
0604	2140	15.2	136.0	0217	64	7.3	8.0
0605	2000	14.1	148.9	0218	46	5.2	8.8
0606	2145	15.2	137.6	0219	42	4.8	8.5
0607	2133	14.4	142.5	0221	53	6.2	8.5
0608	2185	14.3	144.0	0222	51	-	-
0609	1894	12.5	141.8	0618	56	6.0	9.9
0610	2089	13.8	136.8	0619	24	2.3	9.3
0611	1993	13.1	136.9	0706	66	7.7	9.4
0612	2129	14.0	148.3	1913	57	6.7	8.7
0613	2082	13.9	142.3				
n	11	11	11	n	10	9	9
MV	2088	14.1	140.9	MV	48	5.3	8.9
SD	±90	±0.8	±4.9	SD	±15	±1.9	±0.6

Table A.2: Tensile test results of the angle-ply laminate ($2mm/min$).

#	σ_y [MPa]	ε_B [10^{-3}]	ε_y [10^{-3}]	E [GPa]	ν [1]
0903	173	48	32	20.1	-
0905	169	67	32	20.4	-
0909	165	53	32	19.7	-
0912	164	56	31	19.2	-
2110	172	-	-	19.5	0.74
2111	170	-	-	18.0	0.72
3300	176	56	32	19.7	-
3304	173	82	34	19.1	-
3307	168	72	32	19.6	-
3316	176	74	34	19.3	-
3321	176	56	32	19.3	-
4605	181	57	32	20.7	-
4610	180	73	33	20.6	-
n	13	11	11	13	2
MV	172	63	32	19.6	0.73
SD	±5	±11	±1	±0.7	-
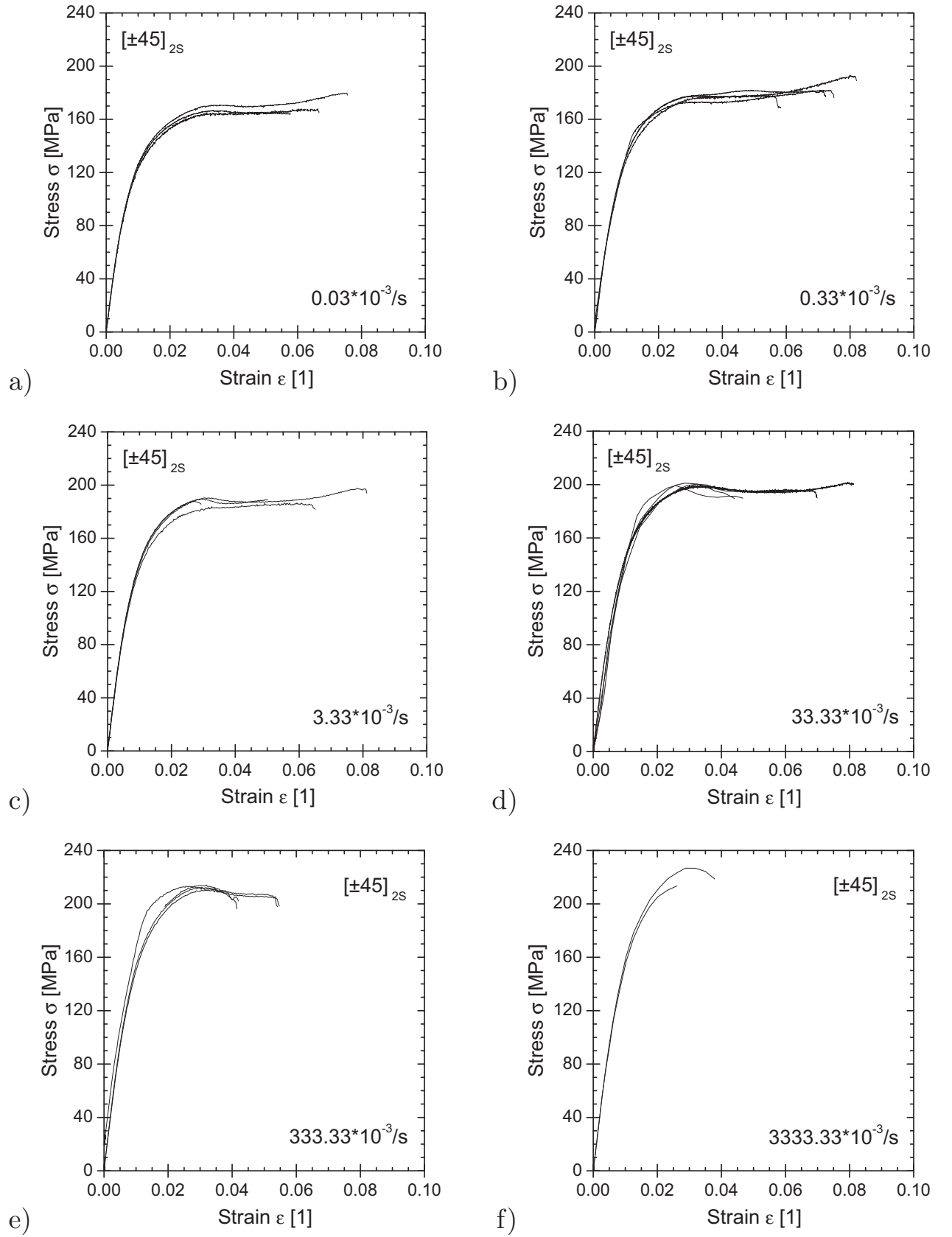
Figure A.1: Effect of strain rate on the stress-strain behaviour. a) $\dot{\varepsilon}_0 = 0.0\overline{3} \cdot 10^{-3}/s$, b) $\dot{\varepsilon}_0 = 0.\overline{3} \cdot 10^{-3}/s$, c) $\dot{\varepsilon}_0 = 3.\overline{3} \cdot 10^{-3}/s$, d) $\dot{\varepsilon}_0 = 33.\overline{3} \cdot 10^{-3}/s$, e) $\dot{\varepsilon}_0 = 333.\overline{3} \cdot 10^{-3}/s$, and f) $\dot{\varepsilon}_0 = 3333.\overline{3} \cdot 10^{-3}/s$ (Mohr [201]).

Table A.3: Rate dependent tensile test results of the angle-ply laminate [201].

$\dot{\varepsilon}_0[10^{-3}\ s^{-1}]$	#	$\sigma_y[MPa]$	$\varepsilon_y[10^{-3}]$	$E_x[GPa]$
$0.0\overline{3}$	3303	167	33	17.8
$0.0\overline{3}$	3308	164	33	18.6
$0.0\overline{3}$	3311	171	35	18.5
$0.3\overline{3}$	3300	176	32	19.7
$0.3\overline{3}$	3304	173	34	19.1
$0.3\overline{3}$	3307	168	32	19.6
$0.3\overline{3}$	3316	176	34	19.3
$3.3\overline{3}$	3301	188	27	20.0
$3.3\overline{3}$	3306	190	30	19.2
$3.3\overline{3}$	3310	190	29	20.0
$3.3\overline{3}$	3315	183	33	19.0
$33.3\overline{3}$	3302	201	29	19.1
$33.3\overline{3}$	3309	199	26	20.8
$33.3\overline{3}$	3312	200	31	-
$33.3\overline{3}$	3409	197	29	19.8
$33.3\overline{3}$	3415	199	31	19.6
$333.3\overline{3}$	3305	214	29	-
$333.3\overline{3}$	3314	213	27	19.6
$333.3\overline{3}$	3408	210	31	19.7
$333.3\overline{3}$	3414	212	32	20.4
$3333.3\overline{3}$	3404	227	29	20.4
$3333.3\overline{3}$	3410	214	26	20.8

Table A.4: S-N data of the AP laminate for different frequencies.

	R = −1				R = 0.1		
#	f	σ_{max}	N	#	f	σ_{max}	N
	[Hz]	[MPa]	[1]		[Hz]	[MPa]	[1]
4510	1	109	907	2516	2	110	566900
4520	2	65	81197	2703	2	110	1633000
4516	2	65	97319	2711	2	110	1890130
4613	3	97	5485	2706	2	140	18278
4619	5	64	254034	2701	2	140	23708
4502	5	67	231890	2704	2	140	34463
4501	5	68	104435	2708	5	110	622180
4620	5	69	68656	2713	5	110	990014
4601	5	100	6280	2710	5	110	1498830
4503	5	104	1048	2707	5	140	9254
4504	5	106	1387	2517	5	140	23560
4505	5	106	1615	2702	5	140	31800
4509	5	108	561	2405	10	110	304800
4507	5	108	613	2204	10	110	803150
1712	10	60	1070000	2505	10	110	900800
1708	10	75	15390	2709	10	140	10977
1709	10	75	21890	1304	10	140	14383
1710	10	75	45350	1303	10	140	19408
1711	10	75	49747				
1703	10	100	680				
1715	10	100	3480				
2102	10	120	151				
1714	10	120	176				
1704	10	50	$> 1.1 \cdot 10^6$				
1713	10	60	$> 4.0 \cdot 10^6$				

Table A.5: S-N data of the AP laminate for stress ratios ($f = 10Hz$).

	$R = 0.5$			$R = 0.3$			$R = 0.1$	
#	σ_{max} [MPa]	N [1]	#	σ_{max} [MPa]	N [1]	#	σ_{max} [MPa]	N [1]
1705	160	1480	3203	158	131717	1307	160	560
1706	160	2410	3204	157	135246	1308	160	580
1603	150	10990	3220	150	273805	2407	155	980
1601	150	22444	4402	149	49974	1305	155	1850
1701	140	38350	5408	144	531089	1306	155	1950
1707	140	76290	5406	142	315186	2108	150	3740
2103	140	100590	5412	141	631042	2408	145	2300
2107	140	$> 1.1\,10^6$	3217	140	452830	2404	125	75706
2112	140	$> 2.1\,10^6$	5405	137	546171	0913	120	124343
1702	140	$> 2.0\,10^6$	3216	130	1273798	0915	120	136680
2205	130	$> 2.0\,10^6$	3218	130	2817100	0911	120	146630
1312	110	$> 6.0\,10^6$	3219	130	2947903	3401	120	169430
1310	100	$> 9.2\,10^6$				3407	120	117390
						3413	120	209130
						2402	119	84860
						2406	100	1354491
						1309	100	$2.0\,10^6$
						1302	100	$2.1\,10^6$

Table A.6: S-N data for the block load fatigue tests - Case A1: $R = 0.1$ [206, 207].

#	σ_{max1} [MPa]	n_1 [1]	N_1 [1] Eq. (5.12)	n_1/N_1 [1]	σ_{max2} [MPa]	n_2 [1]	N_2 [1] Eq. (5.12)	n_2/N_2 [1]	D_{PM} [1]	$D_{pred.}$ [1]
2409	140	4800	9476	0.507	110	564200	538263	1.048	1.555	1.301
2503	139	4800	11553	0.415	109	429606	628961	0.683	1.099	1.286
2504	134	4800	21109	0.227	105	863657	1009994	0.855	1.082	1.195
2511	140	4800	9476	0.507	110	593781	538263	1.103	1.610	1.301
2601	140	6500	9476	0.686	110	350000	538263	0.650	1.336	1.270
1313	110	253800	538263	0.472	140	1600	9476	0.169	0.640	0.748
2109	105	253800	1098905	0.231	133	13373	23502	0.569	0.800	0.698
2502	110	253800	538263	0.472	140	1522	9476	0.161	0.632	0.748
2509	110	362563	538263	0.674	140	1900	9476	0.201	0.874	0.830

Table A.7: S-N data for the block load fatigue tests - Case A2: $R = -1$ [218].

#	σ_{max1} [MPa]	n_1 [1]	N_1 [1] Eq. (5.11)	n_1/N_1 [1]	σ_{max2} [MPa]	n_2 [1]	N_2 [1] Eq. (5.11)	n_2/N_2 [1]	D_{PM} [1]
4506	105	675	987	0.684	64	108244	204519	0.529	1.213
4511	96	511	3183	0.161	58	578688	446393	1.296	1.457
4513	101	511	1661	0.308	61	407966	302152	1.350	1.658
4514	106	511	867	0.590	64	131816	204519	0.645	1.234
4515	109	511	587	0.871	66	141168	157667	0.895	1.766
4517	64	85960	204519	0.420	107	1153	761	1.515	1.936
4518	64	85960	204519	0.420	108	846	668	1.266	1.687
4519	64	85960	204519	0.420	109	745	587	1.270	1.690

Table A.8: S-N data for the block load fatigue tests – Case A3: Variation of the stress ratio [218].

#	R_1 [1]	σ_{max1} [MPa]	n_1 [1]	N_1 [1] Eq. (5.10)	n_1/N_1 [1]	R_2 [1]	σ_{max2} [MPa]	n_2 [1]	N_2 [1] Eq. (5.11)	n_2/N_2 [1]	D_{PM} [1]
4302	0.1	127	25000	73288	0.341	-1	74	48599	54968	0.884	1.225
4303	0.1	126	25000	80905	0.309	-1	74	86452	55688	1.552	1.861
4304	0.1	128	25000	57642	0.434	-1	73	107888	61796	1.746	2.180
4305	0.1	125	25000	94506	0.265	-1	76	74761	42931	1.741	2.006
4310	0.1	131	5000	42244	0.118	-1	80	33883	25514	1.328	1.446
4312	0.1	128	5000	60992	0.082	-1	76	70177	41828	1.678	1.760

#	R_1 [1]	σ_{max1} [MPa]	n_1 [1]	N_1 [1] Eq. (5.11)	n_1/N_1 [1]	R_2 [1]	σ_{max2} [MPa]	n_2 [1]	N_2 [1] Eq. (5.10)	n_2/N_2 [1]	D_{PM} [1]
4307	-1	77	25000	35783	0.699	0.1	128	62044	60992	1.017	1.716
4308	-1	76	25000	41828	0.598	0.1	128	48302	59293	0.815	1.412
4309	-1	76	25000	44639	0.560	0.1	127	46014	71246	0.646	1.206

Table A.9: S-N data for initial loads in fatigue - Scenario B: cyclic initial stresses [201].

Cyclic initial stress	#	N [1]
B3 140MPa	3405	249510
	3508	258060
	3519	228540
	MV	245370
	SD	±15189
B2 120MPa	3401	169430
	3407	117390
	3413	209130
	MV	165317
	SD	±46008
B1 100MPa	3406	195030
	3509	101859
	3606	182726
	MV	159872
	SD	±50616

Table A.10: S-N data for initial loads in fatigue - Scenario C: triangular pulse load [201].

Pulse stress	#	N [1]
C3 140MPa	3512	172197
	3603	104980
	3614	255042
	MV	177406
	SD	±75167
C2 120MPa	3514	70033
	3605	196662
	3616	157799
	MV	141498
	SD	±64869
C1 100MPa	3506	178416
	3510	172682
	3610	160181
	MV	170426
	SD	±9324

Table A.11: S-N data for the creep-recovery-fatigue tests - Case D1 [204].

C120R2000F #	σ_{cr} [MPa]	N [1]
2512	142	414550
2214	131	366554
2208	122	325930
2207	110	446919
2211	100	286297
2210	90	286497
2213	70	298073

Table A.12: S-N data for the creep-recovery-fatigue tests - Case D2 [205].

CxRyF	#	σ_{cr} [MPa]	σ_{max} [MPa]	$N_{exp}(\sigma_{max})$ [1]	$N_{norm}(140MPa)$ [1]
CAF	5406	-	142	315186	418087
	5412	-	141	631042	726789
	3217	-	140	452830	452830
	5405	-	137	546171	357503
	MV			486307	488802
	SD			± 135321	± 163474
C2R0F	5407	91.2	144.0	337854	594467
	3201	91.5	141.3	908304	1091405
	3213	90.9	140.1	720023	730267
	MV			655394	805380
	SD			± 290665	± 256843
C2R2F	5417	90.9	139.8	1014538	986276
	3208	91.8	141.2	676878	801919
	3214	91.3	140.2	1121008	1153132
	MV			937475	980442
	SD			± 231877	± 175679
C2R24F	3207	90.8	138.9	435489	372815
	3210	91.2	140.0	1588153	1588154
	5414	91.2	138.2	1069494	829372
	MV			1031045	930113
	SD			± 577293	± 613901
C24R0F	5409	91.2	141.6	648130	812497
	5413	91.1	141.9	779427	1019389
	3202	90.7	140.4	962695	1018659
	MV			796751	950182
	SD			± 157996	± 119239
C24R2F	5415	90.9	140.6	488030	531198
	3211	91.0	140.0	780515	780515
	3215	91.5	142.6	375208	541728
	MV			547918	617814
	SD			± 209185	± 141002
C24R24F	3206	91.2	140.1	927871	941072
	3209	90.8	145.1	480276	987131
	3212	91.3	141.4	629766	767484
	MV			679304	898562
	SD			± 227872	± 115830

Bibliography

[1] K. L. Reifsnider. Introduction. In K. L. Reifsnider, editor, *Fatigue of Composite Materials*, volume 4 of *Composite Materials Series*, chapter 1, pages 1–9. Elsevier, 1991. ISBN 0-444-70507-4.

[2] W. Thomson (Lord Kelvin). *Elasticity, Heat, Electro-Magnetism*, volume 3 of *Mathematical and Physical Papers*. C. J. Clay and Sons, Cambridge University Press Warehouse, London, 1890.

[3] Albert. Ueber Treibseile am Harz. *Archiv für Mineralogie, Geognosie, Bergbau und Hüttenkunde*, X(1):215–234, 1837.

[4] R. A. Smith. The Versailles railway accident of 1842 and the first research into metal fatigue. In H. Kitigawa and T. Tanaka, editors, *Fatigue 90 - Proceedings 4th Int Conference Fatigue and Fatigue Thresholds*, volume IV, pages 2033–2041, Honolulu, USA, 15-20 July 1990. Materials and Component Engineering Publications (MCEP). ISBN 1-872-136-079.

[5] A. Wöhler. Bericht über die Versuche, welche auf der Königl. Niederschlesisch-Märkischen Eisenbahn mit Apparaten zum Messen der Biegung und Verdrehung von Eisenbahnwagen-Achsen während der Fahrt, angestellt wurden. *Zeitschrift für Bauwesen*, VIII:641–652, 1858.

[6] A. Wöhler. Versuche zur Ermittlung der auf die Eisenbahnwagen-Achsen einwirkenden Kräfte und der Widerstandsfähigkeit der Wagen-Achsen. *Zeitschrift für Bauwesen*, X:583–616, 1860.

[7] A. Wöhler. Ueber die Versuche zur Ermittlung der Festigkeit von Achsen, welche in den Werkstätten der Niederschlesisch-Märkischen Eisenbahn zu Frankfurt a. d. O. angestellt sind. *Zeitschrift für Bauwesen*, XIII:233–258, 1863.

[8] A. Wöhler. Resultate der in der Central-Werkstatt der Niederschlesisch-Märkischen Eisenbahn zu Frankfurt a. d. O. angestellten Versuche über die relative Festigkeit von Eisen, Stahl und Kupfer. *Zeitschrift für Bauwesen*, XVI:67–82, 1866.

[9] A. Wöhler. Ueber die Festigkeits-Versuche mit Eisen und Stahl. *Zeitschrift für Bauwesen*, XX:73–106, 1870.

[10] H. Gerber. Bestimmung der zulässigen Spannungen in Eisen-Constructionen. *Zeitschrift des Bayrischen Architekten- und Ingenieur-Vereins*, VI(6):101–110, 1874.

[11] J. Goodman. *Mechanics Applied to Engineering*. Longman Green, Harlow, UK, 1899.

[12] S. Suresh. *Fatigue of Materials*. Cambridge University Press, 1991. ISBN 0-521-36510-4.

[13] A. Palmgren. Die Lebensdauer von Kugellagern. *Zeitschrift des Vereins Deutscher Ingenieure*, 68:339–341, 1924.

[14] M. A. Miner. Cumulative damage in fatigue. *J Applied Mechanics*, 12:A159–A164, September 1945.

[15] E. Gassner. Festigkeitsversuche mit wiederholter Beanspruchung im Flugzeugbau. *Luftwissen*, 6(2):61–64, 1939.

[16] H. Naubereit and J. Weihert. *Einführung in die Ermüdungsfestigkeit*. Carl Hanser Verlag, 1999. ISBN 3-446-21028-8.

[17] I. M. Daniel and O. Ishai. *Engineering Mechanics of Composite Materials*. Oxford University Press, 1994. ISBN 0-19-507506-4.

[18] M. Kupke. *Entwicklung elektrisch leitfähiger Glasfaserverbundwerkstoffe mittels Kohlenstoff-Nanopartikel*. PhD thesis, TU Hamburg-Harburg, 2001. ISBN 3-89873-165-0.

[19] F. L. Matthews and R. D. Rawlings. *Composite Materials: Engineering and Science*. Chapman & Hall, 1st edition, 1994. ISBN 0-412-55970-6.

[20] P. W. R. Beaumont. The failure of fibre composites: An overview. *J Strain Analysis*, 24(4):1–17, 1989.

[21] W. Michaeli, D. Huybrechts, and M. Wegener. *Dimensionieren mit Faserverbundkunststoffen*. Carl Hanser Verlag, 1995. ISBN 3-446-17659-4.

[22] M. R. Luke. *Experimentelle und numerische Beanspruchungsanalyse an gekerbten CFK-Laminaten unter Zugbeanspruchung*. PhD thesis, Universität Duisburg, Germany, 1997.

[23] A. W. Wharmby and F. Ellyin. Damage growth in constrained angle-ply laminates under cyclic loading. *Composites Science and Technology*, 62:1239–1247, 2002.

[24] J. Petermann, A. Gagel, and S. Hinz. Personal communication. July 2003.

[25] K. Schulte, J. Petermann, and A. Gagel. Darstellung von Degradationsmodellen zur Beschreibung des Ermüdungsverhaltens in Faserverbundwerkstoffen. In *SFB-Kolloquium: Moderne Werkstoffe - Modellierung und Charakterisierung ihrer Schäden*, Stuttgart, Germany, 17.-18. October 2002.

[26] K. Schulte, J. Petermann, A. Gagel, and B. Fiedler. Durability of fibre reinforced composites (FRC). In 6th *International Seminar on Experimental Techniques and Design in Composite Materials*, Vicenza, Italy, 18.-20. June 2003.

[27] A. Gagel and K. Schulte. Non-scalar approach to simulate the mechanical degradation process in fibre-reinforced-polymers (FRPs). In C. E. Bakis, editor, *Composite Materials: Testing and Design, ASTM STP 1436*, pages 238–251. West Conshohocken, PA, 2003.

[28] T. Hobbiebrunken, B. Fiedler, M. Hojo, M. Tanaka, S. Ochiai, and K. Schulte. Analysis of thermal residual stresses and initial matrix failure in CFRP model composites. In *Proceedings of RIAM Symposium*, pages 31–36, Kyushu University, Kasuga, Fukuoka, Japan, 03.-05. March 2003.

[29] T. Hobbiebrunken, B. Fiedler, M. Hojo, S. Ochiai, and K. Schulte. FEM Modellierung der thermischen Eigenspannungen und des Matrixversagens in CFK. In *14. Symposium Verbundwerkstoffe und Werkstoffverbunde*, pages 599–604, Wien, Austria, 02.-04. July 2003.

[30] M. Wevers. *Identification of fatigue failure modes in carbon fibre reinforced composites*. PhD thesis, Katholieke Universiteit Leuven, Belgium, 1987.

[31] M. C. Lafarie-Frenot and F. Touchard. Comparative in-plane shear behaviour of long-carbon-fibre composites with thermoset or thermoplastic matrix. *Composites Science and Technology*, 52:417–425, 1994.

[32] H. L. Cox. The elasticity and strength of paper and other fibrous materials. *British J Applied Physics*, 3:72–79, 1952.

[33] A. Kelly and W. R. Tyson. Tensile properties of fibre reinforced metals: copper/tungsten and copper/molybdenum. *J Mechanics Physics Solids*, 13:329–350, 1965.

[34] B. Fiedler. *Mikromechanische Betrachtung der Lasteinleitung und Lastübertragung in faserverstärkten Polymeren*. PhD thesis, TU Hamburg-Harburg, 1998.

[35] A. A. Konkin. Properties of carbon fibres and fields of their application. In W. Watt and B. V. Perov, editors, *Strong Fibres*, volume 1 of *Handbook of Composites*, chapter VII, pages 241–274. North-Holland, 1985. ISBN 0-444-875050.

[36] D. Hull and T. W. Clyne. *An Introduction to Composite Materials*. Cambridge Solid State Science Series. Cambridge University Press, 2nd edition, 1996. ISBN 0-521-38190-8.

[37] W. Johnson. The structure of PAN based carbon fibres and relationship to physical properties. In W. Watt and B. V. Perov, editors, *Strong Fibres*, volume 1 of *Handbook of Composites*, chapter X, pages 389–444. North-Holland, 1985. ISBN 0-444-875050.

[38] S. C. Bennett and D. J. Johnson. Strucural heterogeneity in carbon fibres. In *Proceedings 5th London Int Carbon and Graphite Conference*, pages 377–386, Imperial College, London, UK, 18.-22. September 1978. Society of Chemical Industry.

[39] J.-S. Tsai and C. J. Wu. Control of Young's modulus of carbon fibre. *J Materials Science Letters*, 13:272–274, 1994.

[40] D. J. Thorne. Manufacture of carbon fibres from PAN. In W. Watt and B. V. Perov, editors, *Strong Fibres*, volume 1 of *Handbook of Composites*, chapter XII, pages 475–494. North-Holland, 1985. ISBN 0-444-875050.

[41] G. W. Ehrenstein. *Polymeric Materials: Structure-Properties-Applications*. Carl Hanser Verlag, 2001. ISBN 3-446-21461-5.

[42] E. Brandau. *Duroplastwerkstoffe: Technologie, Prüfung, Anwendung*. VCH Verlagsgesellschaft, 1993. ISBN 3-527-28575-X.

[43] G. W. Ehrenstein, G. Riedel, and P. Trawiel. *Praxis der thermischen Analyse von Kunststoffen*. Carl Hanser Verlag, 1998. ISBN 3-446-21001-6.

[44] B. Ellis. Introduction to the chemistry, synthesis, manufacture and characterization of epoxy resins. In B. Ellis, editor, *Chemistry and Technology of Epoxy Resins*, chapter 1, pages 1–36. Chapman & Hall, Glasgow, 1st edition, 1993. ISBN 0-7514-0092-5.

[45] R. W. Dyson. *Engineering Polymers*. Chapman & Hall, New York, 1990. ISBN 0-412-02081-5.

[46] J. A. Brydson. *Plastics Materials*. Butterworth-Heinemann, 7th edition, 1999. ISBN 0-7506-4132-0.

[47] E. B. Stark, W. V. Breitigam, R. D. Farris, D. G. Davis, and H. D. Stenzenberger. Resin transfer molding (RTM) of high performance resins. Technical Report SC 1207-01, Resolution Performance Products, USA, November 2001.

[48] W. R. Ashcroft. Curing agents for epoxy resins. In B. Ellis, editor, *Chemistry and Technology of Epoxy Resins*, chapter 2, pages 37–71. Chapman & Hall, Glasgow, 1st edition, 1993. ISBN 0-7514-0092-5.

[49] Hexcel Composites. *Prepreg Technology*, January 1997. Publication FGU 017.

[50] G. Niederstadt. *Ökonomischer und Ökologischer Leichtbau mit faserverstärkten Polymeren: Gestaltung, Berechnung und Qualifizierung*. expert-Verlag, 2nd edition, 1997. ISBN 3-8169-1416-0.

[51] J. M. Whitney. *Structural Analysis of Laminated Anisotropic Plates*. Technomic Publishing, 1987. ISBN 87762-518-2.

[52] M. Katouzian. *On the effect of temperature on creep behaviour of neat and carbon fiber reinforced PEEK and epoxy - A micromechanical approach*. PhD thesis, TU München, Germany, 1994. ISBN 3-18-316318-7.

[53] H.-G. Elias. *An Introduction to Polymer Science*. VCH Verlagsgesellschaft, 1st edition, 1997. ISBN 3-527-28790-6.

[54] W. D. Callister jr. *Materials Science and Engineering: An Introduction*. John Wiley & Sons, 5th edition, 1999. ISBN 0-471-32013-7.

[55] T. Hobbiebrunken. Modellierung und Implementierung der thermomechanischen Eigenschaften und induzierten Mikroschädigungen in Faserverbundwerkstoffen. Diploma thesis, TU Hamburg-Harburg, Germany, 2002. Supervision: K. Schulte, U. Weltin, B. Fiedler, and M. Renner.

[56] H. Eyring. Viscosity, plasticity, and diffusion as examples of absolute reaction rates. *J Chemical Physics*, 4:283–291, April 1936.

[57] J. Koppelmann. Über das dynamische-elastische Verhalten hochpolymerer Stoffe. *Kolloid Zeitschrift*, 144(1-3):12–41, 1955.

[58] O. I. Okoli and G. F. Smith. The effect of strain rate and fibre content on the Poisson's ratio of glass/epoxy composites. *Composite Structures*, 48:157–161, 2000.

[59] R. Knausenberger. *Mechanical behaviour of isotropic and anisotropic materials with nonlinear properties*. PhD thesis, RWTH Aachen, Germany, 1982.

[60] B. Harris. *Engineering Composite Materials*. IOM Communications, 2nd edition, 1999. ISBN 1-86125-032-0.

[61] M. Schlimmer. *Zeitabhängiges mechanisches Werkstoffverhalten: Grundlagen, Experimente, Rechenverfahren für die Praxis*, volume 2 of *Werkstoff-Forschung und -Technik*. Springer Verlag, 1984. ISBN 3-540-13648-7.

[62] R. W. Evans and B. Wilshire. *Introduction to Creep*. IOM Communications, 1993. ISBN 0-901462-64-0.

[63] W. Ehrenstein and B. Sarabi. Numerische Beschreibung und systematische Auswertung des Kriechens verstärkter Polymerwerkstoffe. *Plaste und Kautschuk*, 27(10):573–576, 1980.

[64] B. Sarabi. *Das Anstrengungsverhalten von Polymerwerkstoffen infolge ein- und zweiachsigen Kriechens*. PhD thesis, Gesamthochschule Kassel, 1984.

[65] G. Menges. *Werkstoffkunde: Kunststoffe*. Carl Hanser Verlag, 3rd edition, 1990. ISBN 3-446-15612-7.

[66] W. Retting. Das mechanische Verhalten von Thermoplasten bei mittlerer und hoher Deformation bis zum Bruch. *Rheologica Acta*, 8(3):259–267, 1969.

[67] P. G. Nutting. A study of elastic viscous deformation. In *Proceedings of the 24th Annual Meeting*, volume 21, pages 1162–1171, Asbury Park, New Jersey, USA, 21.-24. June 1921. American Society for Testing Materials.

[68] C. R. Soderberg. The interpretation of creep tests for maschine design. *Transactions American Society Mechanical Engineers (Trans ASME)*, 58(15):733–743, 1936.

[69] L. Prandtl. Ein Gedankenmodell zur kinetischen Theorie der festen Körper. *Zeitschrift für angewandte Mathematik und Mechanik*, 8(2):85–106, April 1928.

[70] D. A. Dillard, D. H. Morris, and H. F. Brinson. Predicting viscoelastic response and delayed failures in general laminated composites. In I.M. Daniel, editor, *Composite Materials; Testing and Design (Sixth Conference), ASTM STP 787*, pages 357–370. American Society for Testing and Materials, 1982.

[71] W. N. Findley, J. S. Lai, and K. Onaran. *Creep and Relaxation of Nonlinear Viscoelastic Materials*. North-Holland Publishing Company, 1976.

[72] J. L. Sullivan. Creep and physical aging of composites. *Composites Science Technology*, 39:207–232, 1990.

[73] L. C. E. Struik. *Physical Aging in Amorphous Polymers and Other Materials.* Elsevier, Amsterdam, 1978. ISBN 0-444-41655-2.

[74] S. F. Wang and A. A. Ogale. Influence of aging on transient and dynamic mechanical properties of carbon fiber/epoxy composites. *SAMPE Quarterly*, 20(2):9–13, 1989.

[75] W. Retting. *Mechanik der Kunststoffe.* Carl Hanser Verlag, 1991. ISBN 3-446-16101-5.

[76] W. Retting and H. M. Laun. *Kunststoff-Physik.* Carl Hanser Verlag, 1991. ISBN 3-446-16235-6.

[77] H. Brinson. Matrix dominated time dependent failure predictions in polymer matrix composites. *Composite Structures*, 47:445–456, 1999.

[78] J. D. Ferry. *Viscoelastic Properties of Polymers.* Wiley & Sons, 3rd edition, 1980. ISBN 0-471-04894-1.

[79] W. R. Cannon and T. G. Langdon. Review: Creep of ceramics. *J Materials Science*, 18:1–50, 1983.

[80] J. Čadek. *Creep in Metallic Materials*, volume 48 of *Materials Science Monographs.* Elsevier, 1988. ISBN 0-444-98916-1.

[81] B. Ilschner. *Hochtemperatur-Plastizität*, volume 23 of *Reine und Angewandte Metallkunde in Einzeldarstellungen.* Springer Verlag, 1973.

[82] G. P. Sendeckyj. Life prediction for resin-matrix composite materials. In K. L. Reifsnider, editor, *Fatigue of Composite Materials*, volume 4 of *Composite Materials Series*, chapter 10, pages 431–483. Elsevier, 1991. ISBN 0-444-70507-4.

[83] R. Talreja. A continuum mechanics characterization of damage in composite materials. *Proceedings Royal Society London A*, 399:195–216, 1985.

[84] R. Talreja. Stiffness properties of composite laminates with matrix cracking and interior delamination. *Engineering Fracture Mechanics*, 25(5/6):751–762, 1986.

[85] K. L. Reifsnider. Damage accumulation and fracture initiation in composite laminates. *SAMPE Quarterly*, pages 39–44, October 1984.

[86] K. L. Reifsnider and W. W. Stinchcomb. A critical element model of the residual strength and life of fatigue loaded composite coupons. In H. T. Hahn, editor, *Composite Materials: Fatigue and Fracture, ASTM STP 907*, pages 298–313. American Society for Testing and Materials, Philadelphia, 1986.

[87] K. L. Reifsnider. Micromechanical modelling of polymeric composites. *Polymer*, 35(23):5035–5040, 1994.

[88] W. W. Stinchcomb and C. E. Bakis. Fatigue behaviour of composite materials. In K. L. Reifsnider, editor, *Fatigue of Composite Materials*, volume 4 of *Composite Materials Series*, chapter 4, pages 105–180. Elsevier, 1991. ISBN 0-444-70507-4.

[89] V. Altstädt. *Hysteresismessungen zur Charakterisierung der mechanisch-dynamischen Eigenschaften von R-SMC*. PhD thesis, Gesamthochschule Kassel, 1987.

[90] W. Hwang and K. S. Han. Fatigue of composites - Fatigue modulus concept and life prediction. *J Composite Materials*, 20:154–165, March 1986.

[91] J. Petermann and K. Schulte. Strain based service time estimation for angle-ply laminates. *Composites Science and Technology*, 62(7-8):1043–1050, 2002.

[92] K. L. Reifsnider and R. Jamison. Fracture of fatigue-loaded composite laminates. *Int J Fatigue*, pages 187–197, October 1982.

[93] K. L. Reifsnider, K. Schulte, and J. C. Duke. Long-term fatigue behavior of composite materials. In T. K. O'Brien, editor, *Long-Term Behavior of Composites; ASTM STP 813*, pages 136–159. American Society for Testing and Materials, Philadelphia, 1983.

[94] D. R. Askeland. *The Science and Engineering of Materials*. PWS Publishing Company, 3rd edition, 1994. ISBN 0-534-93423-4.

[95] H. Schmiedel. *Handbuch der Kunststoffprüfung*. Carl Hanser Verlag, 1992. ISBN 3-446-16336-0.

[96] J. C. Halpin, T. A. Johnson, and M. E. Waddoups. Kinetic fracture models and structural reliability. *Int J Fracture Mechanics*, 8:465–468, 1972.

[97] W. Weibull. A statistical distribution function of wide applicability. *J Applied Mechanics*, 18:293–297, 1951.

[98] L. J. Broutman and S. Sahu. A new theory to predict cumulative fatigue damage in fiberglass reinforced plastics. In *Composite Materials: Testing and Design, ASTM STP 497*, pages 170–188. American Society for Testing and Materials, 1972.

[99] J. M. Whitney. Fatigue characterisation of composite materials. In *Fatigue of Fibrous Composite Materials: ASTM STP 723*, pages 133–151. American Society for Testing and Materials, 1981.

[100] J. R. Schaff and B. D. Davidson. A strength-based wearout model for predicting the life of composite structures. In E. A. Armanios, editor, *Composite Materials: Fatigue and Fracture, ASTM STP 1285*, pages 179–200. American Society for Testing and Materials, 1997.

[101] A. J. Davies and P. T. Curtis. Fatigue life prediction of composite materials - A review. Technical report, DERA, October 1999. DERA/MSS/MSMA2/TR990682.

[102] H. T. Hahn and R. Y. Kim. Fatigue behavior of composite laminate. *J Composite Materials*, 10:156–180, April 1976.

[103] J. Awerbuch and H. T. Hahn. Fatigue and proof-testing of unidirectional graphite/epoxy composite. In K. L. Reifsnider and K. N. Lauraitis, editors, *Fatigue of Filamentary Composite Materials, ASTM STP 636*, pages 248–266. American Society for Testing and Materials, 1977.

[104] R. Y. Kim and W. J. Park. Proof testing under cyclic tension-tension fatigue. *J Composite Materials*, 14:69–79, January 1980.

[105] P. C. Chou and R. Crowman. Residual strength in fatigue based on the strength-life equal rank assumption. *J Composite Materials*, 12:177–194, April 1978.

[106] Z. Hashin and A. Rotem. A fatigue failure criterion for fibre reinforced materials. *J Composite Materials*, 7:448–464, 1973.

[107] P. C. Chou and R. Croman. Degradation and sudden-death models of fatigue of graphite/epoxy composites. In S. W. Tsai, editor, *Composite Materials: Testing and Design, ASTM STP 674*, pages 431–454. American Society for Testing and Materials, 1979.

[108] W. Hwang and K. S. Han. Fatigue of composite materials-damage models and life prediction. In P. A. Lagace, editor, *Composite Materials: Fatigue and Fracture, ASTM STP 1012*, pages 87–102. American Society for Testing and Materials, 1989.

[109] A. Poursartip, M. F. A. Ashby, and P. W. R. Beaumont. The fatigue damage mechanics of a carbon fibre carbon fibre composite laminate: I-Development of the model. *Composites Science and Technology*, 25(3):193–218, 1986.

[110] W. Hwang and K. S. Han. Cumulative damage models and multi-stress fatigue life prediction. *J Composite Materials*, 20:125–153, March 1986.

[111] H. L. Leve. Cumulative damage theories. In A. F. Madayag, editor, *Metal Fatigue: Theory and Design*, pages 170–203. John Wiley & Sons, 1969. SBN 471 56315 3.

[112] M. J. Owen and R. J. Howe. The accumulation of damage in a glass-reinforced plastic under tensile and fatigue loading. *J Physics D*, 5:1637–1649, 1972.

[113] S. M. Marco and W. L. Starkey. A concept of fatigue damage. *Transactions American Society Mechanical Engineers (Trans ASME)*, 76(1):627–632, May 1954.

[114] Z. Hashin. Cumulative damage theory for composite materials: Residual life and residual strength methods. *Composites Science and Technology*, 23:1–19, 1985.

[115] J.-W. Lee, I. M. Daniel, and G. Yaniv. Fatigue life prediction of cross-ply composite laminates. In P. A. Lagace, editor, *Composite Materials: Fatigue and Fracture, Second Volume, ASTM STP 1012*, pages 19–28. American Society for Testing and Materials, Philadelphia, 1989.

[116] I. P. Bond. Fatigue life prediction for GRP subjected to variable amplitude loading. *Composites: Part A*, 30:961–970, 1999.

[117] M. H. Beheshty, B. Harris, and T. Adam. An empirical fatigue-life model for high performance fibre composites with and without impact damage. *Composites: Part A*, 30:971–987, 1999.

[118] M. M. Shokrieh and L. B. Lessard. Progressive fatigue damage modeling of composite materials, part I: Modeling. *J Composite Materials*, 34(13):1056–1080, 2000.

[119] J. N. Yang and D. L. Jones. Effect of load sequence on the statistical fatigue of composites. *American Institute Aeronautics Astronautics (AIAA) Journal*, 18(12):1525–1531, December 1980.

[120] J. N. Yang and D. L. Jones. Load sequence effects on the fatigue of unnotched composite materials. In *Fatigue of Fibrous Composite Materials, ASTM STP 723*, pages 213–232. American Society for Testing and Materials, 1981.

[121] J. L. Lee, K. E. Fu, and J. N. Yang. Prediction of fatigue damage and life for composite laminates under service loading spectra. *Composites Science and Technology*, 56:635–648, 1996.

[122] J. R. Schaff and B. D. Davidson. Life prediction methodology for composite structures. Part I - Constant amplitude and two-stress level fatigue. *J Composite Materials*, 31(2):128–157, 1997.

[123] J. R. Schaff and B. D. Davidson. Life prediction methodology for composite structures. Part II - Spectrum fatigue. *J Composite Materials*, 31(2):158–181, 1997.

[124] S. S. Wang and E. S.-M. Chim. *J Composite Materials*, 17:114–134, 1983.

[125] K. Schulte, H. Nowack, H.-F. Trautmann, and C. Baron. Estimation of the durability of composite materials by means of stiffness reduction. In A. R. Bunsell, P. Lamicq, and A. Massiah, editors, *Proceedings 1st European Conference Composite Materials (ECCM/1)*, pages 51–55, Bordeaux, France, 24.-27. September 1985.

[126] D. Schütz and J. J. Gerharz. Fatigue strength of a fibre-reinforced material. *Composites*, 8(4):245–250, 1977.

[127] M. S. Found and M. Quaresimin. Two-stage fatigue loading of woven carbon fibre reinforced laminates. *Fatigue and Fracture of Engineering Materials and Structures*, 26(1):17–26, 2003.

[128] J. N. Yang and D. L. Jones. Load sequence effects on graphite/epoxy $[\pm 35]_{2S}$ laminates. In T. K. O'Brien, editor, *Long-Term Behaviour of Composites, ASTM STP 813*, pages 246–262. American Society for Testing and Materials, Philadelphia, 1983.

[129] C.-H. Lee and M.-H. R. Jen. Fatigue response and modelling of variable stress amplitude and frequency in AS-4/PEEK composite laminates, part 2: Analysis and formulation. *J Composite Materials*, 34(11):930–953, 2000.

[130] E. K. Gamstedt and B. A. Sjögren. An experimental investigation of the sequence effect in block amplitude loading of cross-ply composite laminates. *Int J Fatigue*, 24:437–446, 2002.

[131] E. L. Robinson and N. Y. Schenectady. Effect of temperature variation on the long-time rupture strength of steels. *Transactions American Society Mechanical Engineers (Trans ASME)*, 74:777–781, July 1952.

[132] F. Sidoroff. Damage mechanics and its application to composite materials. Technical report, Laboratoire de Mechanique des Solides, Ecole Centrale de Lyon, France, 1984.

[133] K. Schulte. Damage development under cyclic loading. In *Proceedings Damage Development and Failure Process in Composite Materials*, Leuven, Belgium, 04.-06. May 1987.

[134] K. Schulte and W. W. Stinchcomb. Damage mechanisms - including edge effects - in carbon fibre-reinforced composite materials. In K. Friedrich, editor, *Application of Fracture Mechanics to Composite Materials*, volume 6 of *Composite Materials Series*, chapter 8, pages 273–325. Elsevier, 1989.

[135] A. Puck. *Festigkeitsanalyse von Faser-Matrix-Laminaten: Modelle für die Praxis*. Carl Hanser Verlag, 1996. ISBN 3-446-18194-6.

[136] B. Budiansky and N. A. Fleck. Compressive failure of fibre composites. *J Mechanics Physics Solids*, 41(1):183–211, 1993.

[137] C. Soutis and D. Turkmen. Influence of shear properties and fibre imperfections on the compressive behaviour of GFRP. *Applied Composite Materials*, 2:327–342, 1995.

[138] C. Soutis. Compressive strength of unidirectional composites: Measurement and prediction. In S. J. Hooper, editor, *Composite Materials: Testing and Design, ASTM STP 1242*, pages 168–176. American Society for Testing and Materials, 1997.

[139] K. Schulte. Compressive static and fatigue loading of continuous fiber-reinforced composites. In S. E. Groves and A. L. Highsmith, editors, *Compression Response of Composite Structures, ASTM STP 1185*, pages 278–305. American Society for Testing and Materials, Philadelphia, 1994.

[140] J. Awerbuch and H. T. Hahn. Off-axis fatigue of graphite/epoxy composite. In *Fatigue of fibrous composite materials, ASTM STP 723*, pages 243–273. American Society for Testing and Materials, 1981.

[141] J. Petermann and A. Plumtree. A unified fatigue failure criterion for unidirectional laminates. *Composites: Part A*, 32(1):107–118, 2001.

[142] J. Petermann, A. Plumtree, and K. Schulte. An analytical model to predict fracture of off-axis unidirectional composites. *Advanced Composites Letters*, 11(5):243–249, 2002.

[143] C. Baron, K. Schulte, and H. Harig. Influence of fibre and matrix failure strain on static and fatigue properties of carbon fibre-reinforced plastics. *Composites Science and Technology*, 29:257–272, 1987.

[144] M. J. Owen. Fatigue processes in fibre reinforced plastics. *Philosophical Transactions Royal Society London A*, 294:535–543, 1980.

[145] C. K. H. Dharan. Fatigue failure mechanisms in a unidirectionally reinforced composite material. In J. R. Hancock, editor, *Fatigue of Composite Materials: ASTM STP 569*, pages 171–188. American Society for Testing and Materials, 1975.

[146] S. M. Jessen and A. Plumtree. Fatigue damage accumulation in pultruded glass/polyester rods. *Composites*, 20(6):559–567, 1989.

[147] R. Talreja. Fatigue of composite materials: damage mechanisms and fatigue-life diagrams. *Proceedings Royal Society London A*, 378:461–475, 1981.

[148] R. D. Jamison, K. Schulte, K. L. Reifsnider, and W. W. Stinchcomb. Characterization and analysis of damage mechanisms in fatigue of graphite/epoxy laminates. In D. J. Wilkins, editor, *Effects of Defects in Composite Materials: ASTM STP 836*, pages 36–51. American Society for Testing and Materials, Philadelphia, 1984.

[149] W. Becker and G. Kress. Stiffness reduction in laminate coupons due to the free-edge effect. *Composite Science and Technology*, 52:109–115, 1994.

[150] R. Prinz. Schadensmechanik faserverstärkter Kunststoffe. In *Schadensmechanik kohlenstoffaserverstärkter Kunststoffe bei Schwingbelastung; DFVLR-Mitt. 87-08*, pages 9–27. Deutsche Forschungs- und Versuchsanstalt für Luft- und Raumfahrt, 1987.

[151] R. B. Pipes and N. J. Pagano. Interlaminar stresses in composite laminates under uniform axial extension. *J Composite Materials*, 4:538–548, October 1970.

[152] A. H. Puppo and H. A. Evensen. Interlaminar shear in laminated composites under generalized plane stress. *J Composite Materials*, 4:204–220, April 1970.

[153] V. Trappe, K.-W. Harbich, and H. Ernst. Intralaminar fatigue behaviour von CFRP. In *European Conference on Spacecraft Structures, Materials & Mechanical Testing*, Toulouse, France, 11.-13. December 2002.

[154] M. J. Salkind. Fatigue of composites. In *Composite Materials: Testing and Desing; ASTM STP 497*, pages 143–169. American Society for Testing and Materials, 1972.

[155] L. Han and M. R. Piggott. Tension-compression and Iosipescu tests on laminates. *Composites: Part A*, 33:35–42, 2002.

[156] V. Trappe and H. Kossira. Über die Größe des Randeinflusses auf ermittelte Werkstoffkennwerte aus Faserverbundwerkstoffen. In *DGLR-Jahrestagung*, pages 54:1–10. Deutsche Gesellschaft für Luft- und Raumfahrt, 1997.

[157] M. Khatibzadeh and M. R. Piggott. The effect of width on the mechanical properties of angle-ply laminates. *Composites Science and Technology*, 58:497–504, 1998.

[158] D. Kujawski. Width effects on the tensile strength and fatigue behaviour of angle-ply laminates. *Int J Fatigue*, 20(8):575–580, 1998.

[159] J. B. Sturgeon. Creep, repeated loading, fatigue and crack growth in ±45° oriented carbon fibre reinforced plastics. *J Materials Science*, 13:1490–1498, 1978.

[160] T. S. Gates. Matrix-dominated stress/strain behaviour in polymeric composites: effects of hold time, nonlinearity, and rate dependency. In E. T. Camponeschi Jr., editor, *Composite Materials: Testing and Design, 11th Volume, ASTM STP 1206*, pages 177–189. American Society for Testing and Materials, 1996.

[161] C. T. Herakovich, R. D. Schroedter III, A. Gasser, and L. Guitard. Damage evolution in $[\pm 45]_s$ laminates with fiber rotation. *Composites Science and Technology*, 60:2781–2789, 2000.

[162] C. T. Sun and C. Zhu. The effect of deformation-induced change of fibre orientation on the non-linear behavior of polymeric composite laminates. *Composites Science and Technology*, 60:2337–2345, 2000.

[163] K. Komai, K. Minoshima, K. Tanaka, and T. Tokura. Effects of stress waveform and water absorption on the fatigue strength of angle-ply aramid fiber/epoxy composites. *Int J Fatigue*, 24:339–348, 2002.

[164] A. Horoschenkoff. *Beitrag zur Charakterisierung des nichtlinear thermoviskoelastischen Kriechverhaltens von Faserverbundwerkstoffen.* PhD thesis, Technische Universität München, Germany, 1995.

[165] M. Katouzian, O. S. Brüller, and A. Horoschenkoff. On the effect of temperature on the creep behavior of neat and carbon fiber reinforced PEEK and epoxy resin. *J Composite Materials*, 29(3):372–387, 1995.

[166] C. C. M. Ma, N. H. Tai, S. H. Wu, S. H. Lin, J. F. Wu, and J. M. Lin. Creep behavior of carbon-fiber-reinforced polyetheretherketone (PEEK) $[\pm 45]_{4S}$ laminated composites. *Composites: Part B*, 28B:407–417, 1997.

[167] T. S. Gates and M. Feldman. Effects of physical aging at elevated temperatures on the viscoelastic creep of IM7/K3B. In R. B. Deo and C. R. Saff, editors, *Composite Materials: Testing and Design, ASTM STP 1274*, pages 7–36. American Society for Testing and Materials, 1996.

[168] T. S. Gates, D. R. Veazie, and L. C. Brinson. Creep and physical aging in a polymeric composite: Comparison of tension and compression. *J Composite Materials*, 31:2478–2505, 1997.

[169] P. Ladevace and E. Le Dantac. Damage modelling of the elementary ply for laminated composites. *Composites Science and Technology*, 43:257–267, 1992.

[170] D. Gamby, M. C. Lafarie-Frenot, A. Vinet, and D. Guedra-Degeorge. The prediction of the long-term mechanical behaviour of aeronautical laminates. *Composites Science and Technology*, 61:439–443, 2001.

[171] A. Schieffer, J.-F. Maire, and D. Lévêque. A coupled analysis of mechanical behaviour and aging for polymer-matrix composites. *Composites Science and Technology*, 62:543–549, 2002.

[172] D. F. Sims and V. H. Brogdon. Fatigue behavior of composites under different loading modes. In K. L. Reifsnider and K. N. Lauraitis, editors, *Fatigue of Filamentary Composite Materials, ASTM STP 636*, pages 185–205. American Society for Testing and Materials, 1977.

[173] G. D. Sims and D. G. Gladman. Effect of test conditions on the fatigue strength of a glass-fabric laminate: Part a - frequency. *Plastics and Rubber: Materials and Applications*, pages 41–48, May 1978.

[174] G. D. Sims and D. G. Gladman. Effect of test conditions on the fatigue strength of a glass-fabric laminate: Part B - specimen condition. *Plastics and Rubber: Materials and Applications*, pages 122–128, August 1980.

[175] C. T. Sun and W. S. Chan. Frequency effect on the fatigue life of a laminated composite. In S. W. Tsai, editor, *Composite Materials: Testing and Design, ASTM STP 674*, pages 418–430. American Society for Testing and Materials, 1979.

[176] C. J. Jones, R. F. Dickson, T. Adam, H. Reiter, and B. Harris. Environmental fatigue of reinforced plastics. *Composites*, 14(3):288–293, 1983.

[177] C. R. Saff. Effect of load frequency and lay-up on fatigue life of composites. In T. K. O'Brien, editor, *Long-Term Behaviour of Composites, ASTM STP 813*, pages 78–91. American Society for Testing and Materials, Philadelphia, 1983.

[178] D. Curtis, D. Moore, B. Slater, and N. Zahlan. Fatigue testing of multi-angle laminates of CF/PEEK. *Composites*, 19(6):446–452, 1988.

[179] E. Dan-Jumbo, S. G. Zhou, and C. T. Sun. Load-frequency effect on fatigue life of IM6/APC-2 thermoplastic composite laminates. In G. M. Newaz, editor, *Advances in Thermoplastic Matrix Composite Materials, ASTM STP 1044*, pages 113–132. American Society for Testing and Materials, 1989.

[180] A. Rotem. Stiffness change of a graphite epoxy laminate under reverse fatigue loading. *J Composites Technology & Research (JCTRER)*, 11(2):59–64, 1989.

[181] A. Rotem and H. G. Nelson. Residual strength of composite laminates subjected to tensile-compressive fatigue loading. *J Composites Technology & Research (JCTRER)*, 12(2):76–84, 1990.

[182] A. Rotem. Tensile and compressive failure modes of laminated composites loaded by fatigue with different mean stress. *J Composites Technology and Research (JCTRER)*, 12(4):201–208, 1990.

[183] A. Rotem. The fatigue behaviour of composite laminates under various mean stresses. *Composite Structures*, 17:113–126, 1991.

[184] C. C. M. Ma, N. H. Tai, G. Y. Wu, S. H. Lin, J. M. Lin, C. L. Ong, Y. C. Chang, and M. F. Sheu. Fatigue behavior of carbon fiber reinforced epoxy composites - $[\pm 45]_{4S}$ laminate under tension-tension and tension-compression fatigue loading test. In *Proceedings 41st International SAMPE Symposium*, pages 474–485, 24.-28. March 1996.

[185] M.-H. R. Jen and C.-H. Lee. Strength and life in thermoplastic composite laminates under static and fatigue loads. Part I: Experimental. *Int J Fatigue*, 20(9):605–615, 1998.

[186] M.-H. R. Jen and C.-H. Lee. Strength and life in thermoplastic composite laminates under static and fatigue loads. Part II: Formulation. *Int J Fatigue*, 20(9):617–629, 1998.

[187] C.-H. Lee and M.-H. R. Jen. Fatigue response and modelling of variable stress amplitude and frequency in AS-4/PEEK composite laminates, Part 1: Experiments. *J Composite Materials*, 34(11):906–929, 2000.

[188] K. Komai, K. Minoshima, K. Tanaka, and H. Hosen. Effects of stress waveform and water absorption on fatigue strength of CF/PEEK. In F. Ellyin and J. W. Provan, editors, *Progress in Mechanical Behaviour of Materials, Volume III: Advance Materials and Modelling of Mechanical Behaviour*, pages 922–927, Victoria, Canada, 16.-21. May 1999.

[189] X. R. Xiao. Modeling of load frequency effect on fatigue life of thermoplastic composites. *J Composite Materials*, 33(12):1141–1158, 1999.

[190] M. Quaresimin. Fatigue of woven composite laminates under tensile and compressive loading. In H. Sol and J. Degrieck, editors, *Proceedings 10th European Conference on Composite Materials (ECCM/10)*, Brugge, Belgium, 03.-07. June 2002.

[191] T. Y. Kam, S. Y. Tsai, and K. H. Chu. Fatigue reliability analysis of composite laminates under spectrum stress. *Int J Solids and Structures*, 34(12):1441–1461, 1997.

[192] C. T. Sun and E. S. Chim. Fatigue retardation due to creep in a fibrous composite. In *Fatigue of Fibrous Composite Materials, ASTM STP 723*, pages 233–242. American Society for Testing and Materials, 1981.

[193] DaimlerChrysler Aerospace Airbus. *DAN 1287; Unidirektionale Kohlenstofffasern vorimprägniert mit Epoxidharz - 180° C härtend*, November 1998. Reference no. 124 206.

[194] J. M. Kenny and A. Trivisano. Chemorheological and dielectric behavior of the epoxy matrix in a carbon fiber prepreg. Technical Paper RP085, NETZSCH Gerätebau GmbH, February 2003. http://www.micromet.com/holometrix/m_techpapers.asp.

[195] Enka AG. *Tenax - Industrial Fibres*, May 1986.

[196] R. E. Smith. Ultrasonic elastic constants of carbon fibers and their composites. *J Applied Physics*, 43(6):2555–2561, 1972.

[197] Hexcel Composites. *Product Data Sheet: 6376*, February 1997. Publication FTA 051.

[198] Deutsche Airbus. *Werkstoff-Handbuch*, February 1992. 75-T-2-0120-1-1.

[199] Artur Krüger: Technik in Kunststoff. *Product Data Sheet: Duraver® Hgw 2372.4*. Barsbüttel, Germany.

[200] UHU GmbH & Co. KG. *Product Data Sheet: UHU® plus endfest 300.* Bühl, Germany.

[201] O. Mohr. Experimentelle Untersuchungen zur Dehnratenabhängigkeit und Auswirkungen von Vorlasten auf die Ermüdungslebensdauer von $[\pm45]_{2S}$ C/EP Laminaten. Term thesis, TU Hamburg-Harburg, Germany, 2003. Supervision: K. Schulte and J. Petermann.

[202] B. Das. The effect of creep on the fatigue properties of angle-ply CFRP. Term thesis, TU Hamburg-Harburg, Germany, 2002. Supervision: K. Schulte and J. Petermann.

[203] C. F. Stange. Einrichtung eines servohydraulischen Prüfstandes und Ermüdungsuntersuchungen and CFK. Term thesis, TU Hamburg-Harburg, Germany, 2002. Supervision: K. Schulte and J. Petermann.

[204] J. Petermann and K. Schulte. Creep prediction and creep-fatigue interaction in angle-ply laminates. In H. Sol and J. Degrieck, editors, *Proceedings 10th European Conference on Composite Materials (ECCM/10)*, pages 192:1–7, Brugge, Belgium, 03.-07. June 2002.

[205] J. Dahl. Experimental investigations on the creep and creep-fatigue interaction of carbon fibre reinforced epoxy laminates. Diploma thesis, TU Hamburg-Harburg, Germany, 2003. Supervision: K. Schulte, G. Bertrand, A. Plumtree and J. Petermann.

[206] S. Hinz. Einfluß von Lastreihenfolgen auf das Ermüdungsverhalten von CFK. Diploma thesis, TU Hamburg-Harburg, Germany, 2001. Supervision: K. Schulte, G. Bertrand, and J. Petermann.

[207] J. Petermann, S. Hinz, and K. Schulte. A nonlinear damage accumulation model for carbon fibre reinforced angle-ply laminates. In H. Sol and J. Degrieck, editors, *Proceedings 10th European Conference on Composite Materials (ECCM/10)*, pages 328:1–7, Brugge, Belgium, 03.-07. June 2002.

[208] W. H. M. van Dreumel and J. L. M. Kamp. Non Hookean behaviour in the fibre direction of carbon-fibre composites and the influence of fibre waviness on the tensile properties. *J Composite Materials*, 11:461–469, October 1977.

[209] T. Ishikawa, M. Matsushima, and Y. Hayashi. Hardening non-linear behaviour in longitudinal tension of unidirectional carbon composites. *J. Material Science*, 20:4075–4083, 1985.

[210] B. Fiedler, M. Hojo, S. Ochiai, K. Schulte, and M. Ochi. Finite-element modeling of initial matrix failure in CFRP under static transverse tensile load. *Composites Science and Technology*, 61:95–105, 2001.

[211] K.-H. Schwalbe. *Bruchmechanik metallischer Werkstoffe.* Carl Hanser Verlag, 1980. ISBN 3-446-12983-9.

[212] W. D. Bascom and S. Y. Gweon. Fractography and failure mechanisms of carbon fiber-reinforced composite materials. chapter 9, pages 351–386. Elsevier, 1989. ISBN 1-85166-296-0.

[213] D. Purslow. Some fundamental aspects of composite fractography. *Composites*, November 1981.

[214] M. J. Hiley. A fractographic study of static and fatigue failures in polymeric composites. Technical report, Defence Evaluation and Research Agency (DERA), 1998. DERA/SMC/SM3/CR980024/1.0.

[215] O. Konur and F. L. Matthews. Effect of the properties of the constituents on the fatigue performance of composites: A review. *Composites*, 20(4):317–328, July 1989.

[216] J. Petermann, S. Hinz, and K. Schulte. Degradation parameters and two-stress block fatigue of angle-ply carbon fibre reinforced epoxy. In P. C. Mc-Keighan and N. Ranganathan, editors, *Fatigue Testing and Analysis Under Variable Amplitude Loading Conditions, ASTM STP 1439*. ASTM International, West Conshohocken, PA, accepted for publication.

[217] J. Petermann and K. Schulte. The effects of creep and fatigue stress ratio on the long term behaviour of angle-ply CFRP. *Composite Structures*, 57(1-4):205–210, 2002.

[218] J. Dahl. Experimental investigations on the static and fatigue behaviour of carbon fibre reinforced epoxy laminates. Term thesis, TU Hamburg-Harburg, Germany, 2002. Supervision: U. Weltin, K. Schulte, A. Plumtree and J. Petermann.

Curriculum Vitae

Name	:	Jörg Petermann
Date of birth	:	03. January 1973
Place of birth	:	Frankfurt/Oder (Germany)
Nationality	:	German

Education

09/1979 - 06/1991	:	Schooling in Frankfurt/Oder, Abitur from *Spezialschule math.-nat.-techn. Richtung Carl Friedrich Gauß*
10/1991 - 09/1998	:	Study of Mechanical Engineering with majors in Mechanics and Materials *Technische Universität Braunschweig University of Waterloo* (Canada) Degree: *Diplom-Ingenieur (Maschinenbau)*

Work experience

10/1995 - 09/1996	:	Alternative civilian service
11/1998 - 03/1999	:	Free-lancing engineer
04/1999 - 07/2003	:	*Technische Universität Hamburg-Harburg* Polymers and Composites Section Research engineer
since 01/2004	:	*Airbus Deutschland GmbH* Engineer for Composite Design Principles

Honours

09/1996 - 08/1997	:	Scholarship of *Deutscher Akademischer Austauschdienst* (DAAD)
03/2002	:	Innovation-Award by *SAMPE Germany*